# Dielectrically Lined Rectangular Waveguides as Wakefield Based Dechirper Structures

Dissertation

zur

Erlangung des akademischen Grades
Doktor-Ingenieur (Dr.-Ing.)
der Fakultät für Informatik und Elektrotechnik
der Universität Rostock

**vorgelegt von**

Franziska Reimann, geboren am 08.08.1989 in Ribnitz-Damgarten
aus Rostock

https://doi.org/10.18453/rosdok_id00002394

# Abstract

In the physics of particle accelerators, light sources and compact accelerators are gaining more and more importance for various fields of science, medicine and industry. This is coupled to increasing demands on the beam quality, like, e.g., the need for ever higher charge densities and pulses in the range of sub-picoseconds.

Another requirement for particle beams, especially in a *lin*ear *ac*celerator (linac) or linac-based X-ray *F*ree *E*lectron *L*aser (FEL), is a small energy width. In fact, the problem of large energy spreads has been present in accelerator science for a long time. In the last years, however, a new concept has been proposed as a counter measure to this problem: the so-called 'dechirper' or 'silencer', a passive, geometrically simple structure based on the use of the interaction between the particle beam and its own wakefield.

The aim of this thesis is to provide a comprehensive study of the general properties of a specific type of dechirper: a rectangular waveguide coated with dielectrics. For this purpose, a semi-analytical model is developed which calculates the wake function inside the dechirper using an eigenmode expansion. As a second step, this model is implemented in the programming language Python and benchmarked against simulations with CST Particle Studio® (CST PS). These studies show that the geometrical simplicity of the chosen dechirper type makes an analytical treatment of the wakefield possible, even though the final computation of the wake function has to be performed numerically. This method has the advantage of delivering the wakefield of a point charge, the so called wake function, as a result. The wake function can be considered a Green's function and enables the calculation of wake potentials of arbitrary bunches by a simple convolution. The programme, named *W*akefield Calculation *I*n *R*ectangular Waveguides Lined with *D*ielectrics (WIzaRD), is then used to perform parameter studies to provide an overview over the influence of variations of the geometrical and dielectric properties on the magnitude of the wakefield. Here it is shown that the most powerful parameters to adjust the magnitude of the wakefield are the length of the dechirper, the total charge of the particle beam that generates the wakefield, and the distance between the upper and lower dielectric in the dechirper, the gap width. Especially the latter enables a tuning of the wakefield after the construction of the dechirper and during experiments, which also makes it possible to turn off the dechirper without removing it from the beamline.

The underlying project work of this thesis has been performed in collaboration with the *H*elmholtz-*Z*entrum *D*resden-*R*ossendorf (HZDR). The ultimate goal of the simulation phase has been providing simulations for the later test of a dechirper prototype at the *E*lectron *L*inac for beams with high *B*rilliance and low *E*mittance (ELBE) facility at the HZDR. Consequently, the geometry of a prototype dechirper is introduced in this thesis. Following this, the results of experiments carried out with this prototype are presented here and compared to simulations performed with the afore-

mentioned semi-analytical programme algorithm. The experiments underline the tuning possibilities of the wakefield that the gap width provides. Comparisons with semi-analytic results show a qualitative agreement between theory and experiments.

# Zusammenfassung

Im Rahmen der Beschleunigerphysik gewinnen neuartige Lichtquellen und kompakte Beschleunigerstrukturen mehr und mehr an Bedeutung für verschiedenste Anwendung in den Bereichen der wissenschaftlichen Forschung, der Medizin und Industrie. Dies ist an steigende Anforderungen an die Qualität der Teilchenstrahlen geknüpft, wie zum Beispiel die Notwendigkeit höherer Ladungsdichten und Pulslängen im Bereich von Sub-Pikosekunden.

Eine weitere Anforderung an Teilchenstrahlen, ganz besonders in Linearbeschleunigern (linacs) und auf linacs basierenden Freien Elektronen Lasern (FELs), ist eine schmale Energiebreite. Tatsächlich ist das Problem von zu hohen Energiebreiten in Teilchenbeschleunigern bereits seit vielen Jahren präsent und bekannt. Erst in den letzten Jahren wurde jedoch ein neuartiges Konzept zur Lösung dieses Problems vorgestellt: der sogenannte „Dechirper" oder „Silencer", ein passives, geometrisch einfaches Bauteil, dessen Anwendung auf der Wechselwirkung zwischen dem Teilchenstrahl und seinem eigenen Wakefeld basiert.

Das Ziel dieser Arbeit ist es, eine umfangreiche Studie zu den Eigenschaften eines bestimmten Dechirper-Typen, dem rechteckigen Wellenleiter mit dielektrischer Beschichtung, zu erstellen. Zu diesem Zweck wird zunächst ein semi-analytisches Model eingeführt, welches das Wakefeld in diesem Dechirper auf Basis einer Eigenmoden-Entwicklung des elektrischen Feldes berechnet. Im zweiten Schritt wird dieses Modell dann in Python implementiert und gegen Simulationen mit CST PS validiert. Diese ersten Studien zeigen, dass die geometrische Einfachheit des gewählten Dechirper-Typen eine analytische Betrachtung des Wakefeldes ermöglicht, auch wenn die finale Berechnung der Wakefunktion numerisch erfolgen muss. Durch diese Methodik kann das Wakefeld einer Punktladung, die sogenannte Wakefunktion, berechnet werden. Dies hat den Vorteil, dass es sich bei der Wakefunktion um eine Green'sche Funktion handelt, was somit die Berechnung von Wakepotentialen beliebiger Strahlformen durch einfache Faltung ermöglicht. Das entwickelte Programm wird dann genutzt, um Parameterstudien durchzuführen, die darüber Auskuft geben sollen, wie und in welchem Maße die Variation geometrischer und dielektrischer Parameter die Stärke des resultierenden Wakefeldes beeinflusst. Hier wird gezeigt, dass die Parameter mit dem größten Einfluss auf das Wakefeld die Länge des Dechirpers und die Gesamtladung des Teilchenpakets sowie der Abstand der oberen und unteren dielektrischen Platte zueinander sind. Gerade der zuletzt genannte Parameter ermöglicht ein Tunen des Wakefeldes nach der Konstruktion und während des Betriebs des Dechirpers. Dies macht es außerdem möglich, den Dechirper auszuschalten ohne ihn aus dem Strahlgang entfernen zu müssen.

Das dieser Arbeit zugrunde liegende Projekt wurde in Zusammenarbeit mit dem *H*elmholtz-*Z*entrum *D*resden-*R*ossendorf (HZDR) durchgeführt. Das finale Ziel der Simulationsphase dieses Projektes war es dabei, den Prototypen eines Dechirpers für den Elektronenbeschleuniger ELBE (*E*lectron *L*inac for beams with high *B*rilliance

and low *E*mittance) am HZDR zu entwickeln und später zu testen. Folglich wird in dieser Arbeit auch die Geometrie dieses Prototypen vorgestellt und Resultate der Experimente an ELBE werden präsentiert und mit Ergebnissen der semi-analytischen Berechnungen aus dem erarbeiteten Programmcode verglichen. Diese Experimente unterstreichen die Justierbarkeit der Wakefeld-Stärke durch ein Einstellen des Plattenabstands. Vergleiche mit den semi-analytischen Simulationen zeigen eine qualitative Übereinstimmung von Theorie und Experiment.

# Danksagung

Die Arbeit an dieser Promotionsschrift hier hat mehrere Jahre in Anspruch genommen, und ohne die Unterstützung der Menschen in meinem Umfeld wäre mir diese Arbeit auf jeden Fall mindestens sehr viel schwerer gefallen. Eine Dankesrede in vokaler Form an alle diejenigen, die mich hierbei begleitet und unterstützt haben, würde ohne Zweifel mindestens 20 Minuten in Anspruch nehmen. In A4-Seiten umgerechnet sind das exakt 42 (mein Sprechtempo mit eingerechnet). Da dies diese Arbeit nur noch länger machen würde, als sie ohnehin schon ist, habe ich diesmal wirklich versucht, mich kurz zu fassen. Mein Dank gilt folgenden Personen:

- Prof. van Rienen für die Möglichkeit, meine Dissertation in ihrer Arbeitsgruppe zu schreiben, die fachliche Unterstützung und die gute Zusammenarbeit,

- Dr. Ulf Lehnert und Prof. Peter Michel vom HZDR, ebenfalls für die fachliche Unterstützung, sowie für das Planen und Bauen des Protypen und die Möglichkeit, ihn am HZDR zu testen,

- Prof. Klinkenbusch und Prof. Kanareykin für das Übernehmen der Zweitgutachten,

- meinem Beta-Leser und ehemaligen Kollegen Dr. Thomas Flisgen für die fachliche Hilfe und Motivation,

- meinen (ehemaligen) Kollegen Johann Heller, Andrea Böhme, Hendrikje Raben, Shahnam Gorgi Zadeh, Dr. Tomasz Galek, Dr. Aleksandar Markovic und Dr. Dirk Hecht für viele fachliche und nicht-fachliche Diskussionen,

- allen anderen (ehemaligen) Mitgliedern der Arbeitsgruppe van Rienen für das großartige Gefühl, ein Teil dieser Arbeitsgruppe gewesen zu sein,

- meinem Lebensgefährten Matthias Clahsen und meiner Familie, auch meinen Großeltern Erika und Gerhard Moritz, für die Motivation und mentale Unterstützung über einen sehr langen Zeitraum hinweg,

- meinen Freundinnen Kathleen Strauch und Julia Schubbe für das gemeinsame Standhalten im Angesicht der Gefahren des Studiums, sowie

- meiner Band und meinen ehemaligen Bandkollegen Hannes Bassen und Martin Splettstößer für eine großartige Zeit bei den Proben, und natürlich

- der Musik, insbesondere dem Metal.

...Und allen, die ich aufgrund von weniger als 42 Seiten Danksagung vergessen haben sollte.

# Thesis Statements

of the dissertation

**Dielectrically Lined Rectangular Waveguides as Wakefield Based Dechirper Structures**

by Franziska Reimann

1. Particle beams with a narrow energy spectrum and short pulse lengths are an essential requirement of future particle accelerators. Typically, short pulse lengths are achieved by magnetic chicanes, which, however, have a negative influence on the energy width of the longitudinal phase space of the beams. To compensate for this, additional measures to reduce the energy width again are needed.

2. Active solutions to reduce the energy width of a particle beam include running the particle beam off-crest in additional, separate acceleration modules. This method is ineffective and expensive because it requires additional space and maintenance efforts.

3. As an alternative, passive solution, wakefield dechirpers can be used. These are geometrically simple waveguide structures with dielectric coatings or riffled walls in which wakefields are generated by the interaction of the structure with the particle beam. The wakefields act back on the beam and serve as a spatially dependent modulation of the energy of the beam.

4. For the application at the Helmholtz-Zentrum Dresden-Rossendorf, a dielectrically lined rectangular waveguide was chosen as the configuration baseline for the design of a dechirper. The advantage of a rectangular structure is the additional experimental degree of freedom gained through the adjustable gap width, the distance between the upper and lower dielectric plates of the dechirper.

5. The eigenmodes of this type of dechirper are the so-called Longitudinal Section Electric and Longitudinal Section Magnetic modes. The computation of these eigenmodes utilises the geometric simplicity of the structure and its similarity to a plain rectangular waveguide, as well as a two-step model for the permittivity of the dielectric plates and the vacuum gap. The eigenmodes can then be computed using a Fourier expansion in the direction of the changing permittivity.

6. The electric field of a point charge inside the dechirper can be determined employing an eigenmode expansion. From this, the longitudinal wake function can be derived. Because the analytic expressions of the eigenmodes are known, an analytic description of the electric field and thus the wake function is also available.

7. The wake function serves as the Green's function for the computation of the wake potentials of arbitrary bunch shapes.

8. Despite the availability of analytic expressions for the eigenmodes and the wake function, both computations rely on series expansions. In a realistic scenario, these series need to be terminated after a finite number of terms. Additionally, the expansion coefficients can only be efficiently computed using numerical means, which renders the overall solution semi-analytical.

9. This semi-analytic solution strategy for the wake function of a rectangular dielectrically lined dechirper is effectively implemented in the Python-based programme WIzaRD.

10. WIzaRD exploits the symmetry of the eigenmodes and their phase velocity, which has to be close to the speed of light for the modes to couple to the beam, to compute a high number of eigenmodes relevant to the wake function in a short period of time. As a next step, it computes the loss factors, which represent the contribution strength of each mode to the wake function. The wake function itself is then computed by a simple weighted summation over these eigenmodes.

11. Wake functions and potentials computed with these methods show a very good convergence and a high agreement with benchmark computations performed with other numerical software.

12. From all geometric parameters of the dechirper structure, the gap width and the length of the waveguide are going to have the largest influence on the strength of the final wakefield. Including the characteristics of the particle bunch, the bunch charge is also going to have a strong influence since the wake function scales linearly with the bunch charge.

13. The geometry of the dechirper prototype and therefore its performance is largely determined by the requirements of the accelerator site and has to be adjusted within the given constraints.

14. The energy-modulating effect of the dechirper is shown in simulations with WIzaRD and experiment performed with a dechirper prototype at the Helmholtz-Zentrum Dresden-Rossendorf.

*I try not to go the obvious route all the time, but sometimes the most obvious is actually the best.*
A. M. Yankovic

# Contents

# List of Acronyms

| | |
|---|---|
| **ATF** | *Accelerator Test Facility* |
| **AWA** | *Argonne Wakefield Accelerator* |
| **BNL** | *Brookhaven National* Accelerator *Laboratory* |
| **CST MWS** | CST Microwave Studio® |
| **CST PS** | CST Particle Studio® |
| **DESY** | *Deutschen Elektronen-Synchrotron* |
| **ELBE** | *Electron Linac* for beams with high *Brilliance* and low *Emittance* |
| **FACET** | Facility for Advanced Accelerator Experimental Tests |
| **FEL** | *Free Electron Laser* |
| **HZDR** | *Helmholtz-Zentrum Dresden-Rossendorf* |
| **LCLS** | *Linac Coherent Light Source* |
| **LEP** | *Large Electron-Positron* Collider |
| **LHC** | *Large Hadron Collider* |
| **linac** | *linear accelerator* |
| **LSE** | *Longitudinal Section Electric* |
| **LSM** | *Longitudinal Section Magnetic* |
| **NGLS** | *Next Generation Light Source* |
| **PEC** | *Perfect Electric Conductor* |
| **PMC** | *Perfect Magnetic Conductor* |
| **PAL** | *Pohang Accelerator Laboratory* |
| **RF** | *radio frequency* |
| **SLAC** | *Stanford Linear Accelerator* |
| **TE** | *Transversal Electric* |
| **TEM** | *Transversal Electro-Magnetic* |
| **TM** | *Transversal Magnetic* |
| **WIzaRD** | *Wakefield* Calculation *In Rectangular* Waveguides Lined with *Dielectrics* |
| **XFEL** | *X*-Ray *Free Electron Laser* |

# List of Symbols

| Symbol | Unit | Description |
| --- | --- | --- |
| $a$ | m | width of rectangular waveguide |
| $\mathbf{A}\left(\mathbf{r}\right)$ | 1 | arbitrary vector field |
| $A_{\mathrm{TE}}$ | V | normalisation factor of TE modes |
| $A_{\mathrm{TM}}$ | Vs/m | normalisation factor of TM modes |
| $A_\lambda$ | Vs | normalisation factor of LSE modes |
| $A_\mu$ | Vm | normalisation factor of LSM modes |
| $b$ | m | height of rectangular waveguide |
| $\underline{\mathbf{B}}\left(\mathbf{r}\right)$ | Vs/m$^2$ | phasor of the magnetic flux density |
| $\underline{\mathbf{B}}_{\mathrm{TE}}\left(\mathbf{r}\right)$ | Vs/m$^2$ | phasor of the magnetic flux density of a TE mode |
| $\underline{\mathbf{B}}_{\mathrm{TM}}\left(\mathbf{r}\right)$ | Vs/m$^2$ | phasor of the magnetic flux density of a TM mode |
| $B_\lambda$ | V/$\left(\mathrm{Ams}^2\right)$ | proportionality factor |
| $\underline{\mathbf{B}}_\lambda\left(\mathbf{r}\right)$ | Vs/m$^2$ | phasor of the magnetic flux density of an LSE mode |
| $\underline{\mathbf{B}}_{\lambda,n\tilde{m}l}\left(\mathbf{r}\right)$ | Vs/m$^2$ | phasor of the magnetic flux density of an LSE mode identified by the triple $(n,\tilde{m},l)$ |
| $\underline{\mathbf{B}}_\mu\left(\mathbf{r}\right)$ | Vs/m$^2$ | phasor of the magnetic flux density of an LSM mode |
| $\underline{\mathbf{B}}_{\mu,n\tilde{m}l}\left(\mathbf{r}\right)$ | Vs/m$^2$ | phasor of the magnetic flux density of an LSM mode identified by the triple $(n,\tilde{m},l)$ |
| $\mathbf{B}\left(\mathbf{r},t\right)$ | Vs/m$^2$ | magnetic flux density |
| $\mathbf{B}_\lambda\left(\mathbf{r},t\right)$ | Vs/m$^2$ | magnetic flux density of an LSE mode |
| $\mathbf{B}_\mu\left(\mathbf{r},t\right)$ | Vs/m$^2$ | magnetic flux density of an LSM mode |
| $\mathbf{B}_\perp\left(\mathbf{r},\mathbf{t}\right)$ | Vs/m$^2$ | transversal part of the magnetic flux density |
| $c$ | m/s | speed of light (in matter) |
| $c_0$ | m/s | speed of light in vacuum |
| $C_\lambda$ | 1/s | proportionality factor |
| $d$ | m | height of dielectrically lined rectangular waveguide up to the bottom of the upper dielectric plate |
| $\underline{\mathbf{D}}\left(\mathbf{r}\right)$ | As/m$^2$ | phasor of electric flux density |
| $\mathbf{D}\left(\mathbf{r},t\right)$ | As/m$^2$ | electric flux density |
| $\underline{\mathbf{D}}_\lambda\left(\mathbf{r}\right)$ | As/m$^2$ | phasor of electric flux density of an LSE mode |
| $E$ | J | energy |
| $\mathbf{e}_i$ | 1 | unit vector in direction $i$ |

| Symbol | Unit | Description |
|---|---|---|
| $\underline{\mathbf{E}}\left(\mathbf{r}\right)$ | V/m | phasor of the electric strength field |
| $E_{high}$ | eV | upper energy limit of a longitudinal phase space |
| $E_{low}$ | eV | lower energy limit of a longitudinal phase space |
| $\underline{\mathbf{E}}_{\mathrm{TE}}\left(\mathbf{r}\right)$ | V/m | phasor of the electric field strength of TE mode |
| $\underline{\mathbf{E}}_{\mathrm{TM}}\left(\mathbf{r}\right)$ | V/m | phasor of the electric field strength of TM mode |
| $E_{\mathrm{wake}}$ | eV | energy modulation introduced by the dechirper |
| $E_{z,E}\left(\mathbf{r}\right)$ | V/m | $z$-component of electric field strength with PEC boundary conditions |
| $E_{z,M}\left(\mathbf{r}\right)$ | V/m | $z$-component of electric field strength with PMC boundary conditions |
| $\underline{\mathbf{E}}_{\lambda}\left(\mathbf{r}\right)$ | V/m | phasor of the electric field strength of an LSE mode |
| $\underline{\mathbf{E}}_{\lambda,n\tilde{m}l}\left(\mathbf{r}\right)$ | V/m | phasor of the electric field strength of an LSE mode identified by the triple $(n,\tilde{m},l)$ |
| $\overline{E_{\lambda,z}}$ | V/m | auxiliary quantity |
| $\underline{\mathbf{E}}_{\mu}\left(\mathbf{r}\right)$ | V/m | phasor of the electric field strength of an LSM mode |
| $\underline{\mathbf{E}}_{\mu,n\tilde{m}l}\left(\mathbf{r}\right)$ | V/m | phasor of the electric field strength of an LSM mode identified by the triple $(n,\tilde{m},l)$ |
| $\overline{E_{\mu,z}}$ | V/m | auxiliary quantity |
| $\mathbf{E}\left(\mathbf{r},t\right)$ | V/m | electric field strength |
| $\mathbf{E}_{\lambda}\left(\mathbf{r},t\right)$ | V/m | electric field strength of an LSE mode |
| $\mathbf{E}_{\mu}\left(\mathbf{r},t\right)$ | V/m | electric field strength of an LSM mode |
| $\mathbf{E}_{\perp}\left(\mathbf{r},\mathbf{t}\right)$ | V/m | transversal part of the electric field strength |
| $f_{\mathrm{ideal}}$ | 1/s | ideal frequency of an LSE/LSM mode with $v_{ph}=c$ |
| $\mathbf{F}\left(\mathbf{r},t\right)$ | $\mathrm{kg\,m/s^2}$ | force |
| $g$ | m | length of a cylindrical cavity |
| $\underline{\mathbf{H}}\left(\mathbf{r}\right)$ | A/m | phasor of the magnetic field strength |
| $\mathbf{H}\left(\mathbf{r},t\right)$ | A/m | magnetic field strength |
| $I$ | 1 | intensity of the recorded energy spectra |
| $j$ | 1 | complex unit |
| $\mathbf{J}\left(\mathbf{r},t\right)$ | $\mathrm{A/m^2}$ | electric current density |
| $k$ | 1/m | wave number |
| $k_0$ | 1/m | wave number in vacuum |
| $k_{0,\mathrm{ideal}}$ | 1/m | ideal wave number of an LSE/LSM mode with $v_{ph}=c$ |
| $k_{0,\lambda}$ | 1/m | wave number of an LSE mode |
| $k_{0,\mu}$ | 1/m | wave number of an LSM mode |
| $k_i$ | 1/m | eigenvalue in $i$-direction |
| $k_{y,m}$ | 1/m | wavenumber of the $m$th Fourier expansion function |

| Symbol | Unit | Description |
|---|---|---|
| $l$ | 1 | mode index in $z$-direction |
| $L$ | m | length of rectangular waveguide |
| $l_{\text{ideal}}$ | 1 | ideal $l$ for an LSE/LSM mode with $v_{ph} = c$ |
| $m$ | 1 | mode index in $y$-direction (corresponds to summation index of Fourier series) |
| $\tilde{m}$ | 1 | index of the eigenmode with the lowest eigenfrequency of a Sturm-Liouville-Problem |
| $n$ | 1 | mode index in $x$-direction |
| $\mathbf{n}$ | 1 | normal vector |
| $\mathbf{p}(\mathbf{r}, t)$ | kg m/s | momentum |
| $P(x)$ | 1 | $x$-dependent part of the separation ansatz |
| $\mathbf{P}_\lambda$ | m | auxiliary matrix used for LSE modes |
| $P_{\lambda, mm'}$ | m | entry in the $m$th row and $m'$th column of $\mathbf{P}_\lambda$ |
| $\mathbf{P}_\mu$ | m | auxiliary matrix used for LSM modes |
| $P_{\mu, mm'}$ | m | entry in the $m$th row and $m'$th column of $\mathbf{P}_\mu$ |
| $\mathbf{q}$ | 1 | vector containing the Fourier expansion coefficients |
| $q$ | As | charge |
| $q_p$ | As | total pulse charge |
| $q_{test}$ | As | test charge |
| $q_{m,\lambda}$ | 1 | $m$th Fourier-sine expansion coefficient for LSE modes |
| $q_{m,\mu}$ | 1 | $m$th Fourier-cosine expansion coefficient for LSM modes |
| $Q(y)$ | 1 | $y$-dependent part of the separation ansatz |
| $Q_\lambda(y)$ | 1 | $y$-dependent part of the separation ansatz for LSE modes |
| $Q_\mu(y)$ | 1 | $y$-dependent part of the separation ansatz for LSM modes |
| $Q_{m,\lambda}(y)$ | 1 | $m$th Fourier-sine series expansion function for LSE modes |
| $Q_{m,\mu}(y)$ | 1 | $m$th Fourier-cosine series expansion function for LSM modes |
| $\mathbf{r}$ | m | position vector |
| $R$ | m | radius of a cylindrical cavity |
| $R(z)$ | 1 | $z$-dependent part of the separation ansatz |
| $s$ | m | relative longitudinal position |
| $t$ | s | time |
| $T_{\max}$ | 1 | evaluation threshold used in WIzaRD |
| $T_{xz}$ | 1/m$^2$ | auxiliary quantity |
| $\mathbf{T}_\lambda$ | 1/m | auxiliary matrix used for LSE modes |
| $T_{\lambda, mm'}$ | 1/m | entry in the $m$th row and $m'$th column of $\mathbf{T}_\lambda$ |

| Symbol | Unit | Description |
|---|---|---|
| $\mathbf{T}_\mu$ | 1/m | auxiliary matrix used for LSM modes |
| $T_{\mu,mm'}$ | 1/m | entry in the $m$th row and $m'$th column of $\mathbf{T}_\mu$ |
| $T^*$ | s | auxiliary quantity |
| $U$ | J | energy |
| $U_\lambda$ | m/s$^2$ | orthogonality factor of electric fields of LSE modes |
| $U_\mu$ | 1/m | orthogonality factor of electric fields of LSM modes |
| $\mathbf{v}$ | m/s | velocity |
| $v_{ph}$ | m/s | absolute value of the phase velocity |
| $V$ | V | voltage |
| $V_c$ | V | cavity voltage |
| $V_\lambda$ | 1/m | orthogonality factor of magnetic flux of LSE modes |
| $V_\mu$ | s$^2$/m | orthogonality factor of magnetic flux of LSM modes |
| $W$ | J | stored energy |
| $\mathbf{W}\left(\mathbf{r},s\right)$ | V/C | wakefield |
| $\mathbf{W}_\perp\left(\mathbf{r},s\right)$ | V/C | transversal wakefield |
| $W_{0,\|}\left(s\right)$ | V/C | longitudinal wake function |
| $W_\|\left(s\right)$ | V/C | longitudinal wakefield |
| $W_{\|,E}\left(s\right)$ | V/C | longitudinal wakefield with PEC boundary conditions |
| $W_{\|,M}\left(s\right)$ | V/C | longitudinal wakefield with PMC boundary conditions |
| $W_{\|,ref}\left(s\right)$ | V/C | reference longitudinal wakefield |
| $W_{i+1}^*$ | 1 | wake function scaled up iteratively usind the length of the dechirper |
| $\beta$ | 1 | ratio of the velocity and the speed of light |
| $\gamma$ | 1 | Lorentz factor |
| $\mathbf{\Gamma}$ | m$^2$ | arbitrary surface |
| $\delta_{i,i'}$ | 1 | Kronecker symbol for index $i$ and $i'$ |
| $\delta p$ | kg m/s | momentum change |
| $\delta(x)$ | 1/m | Dirac distribution |
| $\Delta$ | 1 | measure for the overlap between a computed wake function and a reference |
| $\Delta l$ | 1 | increment of the index $l$ used in WIzaRD |
| $\Delta W$ | J | energy change |
| $\varepsilon$ | As/ (Vm) | permittivity |
| $\varepsilon_0$ | As/ (Vm) | permittivity of free space |
| $\varepsilon_r$ | 1 | relative permittivity |
| $\kappa_{\max}$ | V/C | maximum loss factor in a set of eigenmodes |
| $\kappa_\lambda$ | V/C | loss factor for LSE modes |

| Symbol | Unit | Description |
|--------|------|-------------|
| $\kappa_\mu$ | V/C | loss factor for LSM modes |
| $\lambda$ | 1/m | wavelength |
| $\mu$ | Vs/ (Am) | permeability |
| $\mu_0$ | Vs/ (Am) | permeability of free space |
| $\mu_E$ | eV | centre of a Gaussian energy distribution |
| $\mu_r$ | 1 | relative permeability |
| $\xi$ | m | proportionality factor |
| $\mathbf{\Pi}_{\mathrm{TE}}\left(\mathbf{r}\right)$ | V | Hertzian potential for TE modes |
| $\mathbf{\Pi}_{\mathrm{TM}}\left(\mathbf{r}\right)$ | Vs/m | Hertzian potential for TM modes |
| $\mathbf{\Pi}_\lambda\left(\mathbf{r}\right)$ | Vs | Hertzian potential for LSE modes |
| $\mathbf{\Pi}_{\lambda,E}\left(\mathbf{r}\right)$ | Vs | Hertzian potential for LSE modes and PEC boundary conditions |
| $\mathbf{\Pi}_{\lambda,M}\left(\mathbf{r}\right)$ | Vs | Hertzian potential for LSE modes and PMC boundary conditions |
| $\mathbf{\Pi}_\mu\left(\mathbf{r}\right)$ | Vm | Hertzian potential for LSM modes |
| $\rho\left(\mathbf{r},t\right)$ | As/m$^3$ | electric charge density |
| $\sigma$ | m | r.m.s. length of a particle bunch |
| $\sigma_E$ | eV | standard deviation of a Gaussian energy distribution |
| $\phi_{\mathrm{TE}}\left(\mathbf{r}\right)$ | Vs/m | scalar gauge function for TE modes |
| $\phi_{\mathrm{TM}}\left(\mathbf{r}\right)$ | V | scalar gauge function for TM modes |
| $\phi_\lambda\left(\mathbf{r}\right)$ | Vs/m | scalar gauge function for LSE modes |
| $\phi_\mu\left(\mathbf{r}\right)$ | V | scalar gauge function for LSM modes |
| $\chi_\lambda\left(t\right)$ | 1 | time-dependent electric field expansion coefficient for LSE modes |
| $\overline{\chi_\lambda}$ | 1/s | auxiliary quantity |
| $\chi_{\lambda,E}\left(t\right)$ | 1 | electric field expansion coefficient for LSE modes and PEC boundary conditions |
| $\chi_{\lambda,M}\left(t\right)$ | 1 | electric field expansion coefficient for LSE modes and PMC boundary conditions |
| $\chi_\mu\left(t\right)$ | 1 | time-dependent electric field expansion coefficient for LSM modes |
| $\overline{\chi_\mu}$ | 1/s | auxiliary quantity |
| $\psi\left(s\right)$ | 1/m | normalised bunch shape function |
| $\psi_{\mathrm{DG}}\left(s\right)$ | 1/m | normalised shape function of a double Gaussian pulse |
| $\psi_{\mathrm{F}}\left(s\right)$ | 1/m | normalised shape function of a flat-top pulse |
| $\psi_{\mathrm{G}}\left(s\right)$ | 1/m | normalised shape function of a Gaussian pulse |
| $\psi_p\left(s\right)$ | (As) /m | normalised particle distribution |

| Symbol | Unit | Description |
|---|---|---|
| $\psi_{\mathrm{T}}(s)$ | 1/m | normalised shape function of a triangular pulse |
| $\psi_{\mathrm{TE}}(\mathbf{r})$ | 1 | scalar source function of Hertzian potential for TE modes |
| $\psi_{\mathrm{TM}}(\mathbf{r})$ | 1 | scalar source function of Hertzian potential for TM modes |
| $\psi_{\lambda}(\mathbf{r})$ | 1 | scalar source function of Hertzian potential for LSE modes |
| $\psi_{\mu}(\mathbf{r})$ | 1 | scalar source function of Hertzian potential for LSM modes |
| $\Psi(z, s, t')$ | 1 | auxiliary quantity |
| $\omega$ | 1/s | angular frequency |
| $\boldsymbol{\Omega}$ | m³ | arbitrary domain |
| $\omega_{\lambda}$ | 1/s | angular eigenfrequency of an LSE mode |
| $\omega_{\mu}$ | 1/s | angular eigenfrequency of an LSM |
| $\partial_i$ | 1/m | partial derivative with respect to $i$ |
| $\partial\boldsymbol{\Gamma}$ | m | boundary of an arbitrary surface |
| $\partial\boldsymbol{\Omega}$ | m² | boundary of an arbitrary domain |
| $\nabla$ | 1/m | gradient operator |
| $\nabla_{\perp}$ | 1/m | transversal gradient operator |
| $\nabla^2$ | 1/m² | Laplace operator |
| $\nabla\cdot$ | 1/m | divergence operator |
| $\nabla\times$ | 1/m | curl operator |

# 1 Introduction and Objectives

Since their first appearances in the early $20^{\text{th}}$ century, accelerators have continued to increase in their relevance for multiple fields of science. Furthermore, their prominence and importance in other areas, such as applied medicine and industry, grew as well. With the increasing opportunities that the use of particle accelerators represent in these fields, and the ever growing technological possibilities, the requirements and demands on accelerators also grew. Such requirements include, for example, higher beam energies, shorter pulses, higher charge densities and particle beams with a narrow energy spectrum. The subject of this thesis is a comprehensive study of a comparatively new concept used for the realisation of the last mentioned requirement, the so-called wakefield dechirper (sometimes also referred to as a 'silencer').

The demand for narrow energy width, on the contrary, is not a new one; as methods like the electromagnetic focussing of particle beams are dependent on the energies of the particles. A narrow energy width in this example would lead to a better focussed particle beam after the electromagnetic lens, whereas the focussing of beams with a higher energy width to a specific point is not possible. Methods to counteract the energy spread of particle beams have previously mostly consisted of employing further accelerating structures in which the beam was run off-crest leading to a phase-dependent deceleration of the particles. This method, however, is spatially demanding and costly as it needs additional accelerating modules, which in turn require, e.g., an external power supply and cooling as well as constant maintenance. This in turn involves additional, high production expenses.

A different, passive option which promises to be both cheaper and less spatially demanding, as well as easier to construct, are the aforementioned dechirpers. Two different waveguide profiles have been proposed as basis for dechirpers so far; a rectangular waveguide and a cylindrical one. In these structures, wakefields are generated through the interaction of the particle beam with certain surface conditions. This wakefield then acts back on the particle beam, causing an energy loss for the particles depending on their position in the bunch. Surface conditions that allow for such a wakefield generation are dielectric linings and corrugations.

This thesis focusses on the combination of a rectangular waveguide with dielectric coatings as a dedicated dechirper and aims at a comprehensible study of this structure, focussed primarily on a theoretical inspection of the achievable wakefields. For this purpose, the geometrical simplicity of the dechirper and its similarity with a regular rectangular waveguide is exploited. Employing a two-step-function to model the dielectric linings allows for a derivation of the eigenmodes of the structure, so-called

*L*ongitudinal *S*ection *E*lectric (LSE) and *L*ongitudinal *S*ection *M*agnetic (LSM) modes, in close analogy to the derivation of regular *T*ransversal *E*lectric (TE) and *T*ransversal *M*agnetic (TM) modes in empty waveguides. The analytical expression of the eigenmodes of the dechirper is then used to perform a second expansion of the electric field inside the dechirper in case of a point charge traversing it with the speed of light. From this, the wake function (the wakefield of the point charge) can be derived. In this way, a full analytic expression of the wake function is obtained.

For both expansions, the expansion coefficients need to be computed numerically, rendering the overall solution semi-analytical. This computation is performed within the programme package *W*akefield Calculation *I*n *R*ectangular Waveguides Lined with *D*ielectrics (WIzaRD) developed in the context of this thesis. From the calculation of the wake function, the wake potentials of every arbitrary bunch shape can be computed using a simple convolution with the bunch shape function.

With this programme, studies regarding the influence of the geometrical parameters of the dechirper and the properties of the particle bunch have been performed. These studies, combined with the spatial and technical requirements of the *E*lectron *L*inac for beams with high *B*rilliance and low *E*mittance (ELBE) linear accelerator at the *H*elmholtz-*Z*entrum *D*resden-*R*ossendorf (HZDR), have been employed to determine a suitable dechirper geometry for the use at ELBE. This structure has been designed and built at ELBE, and results from the performed experiments are then compared to theoretical predictions using WIzaRD. One very important property of the dechirper is the tunability of the wakefield when the distance between the upper and the lower dielectric, the gap width, is adjusted. This aspect has been particularly in the focus of the experiments.

In this way, this thesis examines the dielectrically lined rectangular waveguide both theoretically and experimentally in its function as a wakefield dechirper.

## 1.1 Structure of the Thesis

This thesis is structured as follows: This chapter serves as an introduction and motivation into wakefield based dechirping, as well as a distinction of the novel aspects of this work. To illustrate the problem further, the underlying principles of particle acceleration will be given and the necessity for the dechirping of particle beams will be explained. The method presented in this thesis is a so-called passive method of dechirping, and this chapter will also serve as a distinction of these methods to other possibilities of reducing the energy width of the particle beam (referred to as 'active methods', c.f. Section 1.3.1). The state of the art in the field of dechirping will also be depicted and differentiated from the approach presented in the theoretical part of this thesis (c.f. Sections 1.4 and 1.4.1).

In the subsequent Chapter 2, the basic underlying electromagnetic principles of the theoretical part of this thesis will be presented and explained. Here, also the

concept of wakefields will be introduced. An additional part of this chapter will focus on the derivation of eigenmodes in the textbook example of a regular rectangular cavity, which will help illustrating the model derived in Chapter 3. In this chapter, at first, the eigenmodes of the rectangular waveguide with dielectric linings are introduced and derived. From this, the electric field of a point charge traversing the structure at the speed of light will be computed employing an eigenmode expansion. The electric field is then integrated to obtain an analytically closed expression of the wake function inside the dechirper depending on geometric parameters of the structure and characteristics of the eigenmodes.

Chapter 4 introduces a Python-based programme code dedicated to the semi-analytical computation of the eigenmodes of the studied dechirper geometry and the subsequent derivation of the wake function, called WIzaRD. The methods and algorithms this programme is based on will be explained here. Additionally, special properties of the eigenmodes with regards to the wake function are introduced and consequently used to improve the efficiency of WIzaRD. The programme is then benchmarked against CST Particle Studio® (CST PS) and convergence studies with respect to CST PS and the used number of expansion functions in both expansions of the underlying model are presented.

The following Chapter 5 shows parameter studies performed with WIzaRD with respect to the geometrical parameters of the dechirper and the properties of the beam. These studies have been oriented on the dechirper prototype designed at the HZDR and used in Chapter 6 for experiments. These experiments are focussed on a proof of the dechirping principle, as well as on an experimental validation of the results obtained from WIzaRD. Of special interest here was the influence of the gap width of the dechirper on the wake potential, and thus the effect of the dechirper, on the particle beam. The gap width remains adjustable after the building of the dechirper and thus remains a parameter with which the wake potential can be tuned during operation.

Chapter 7 finalises this thesis by summarising this content.

## 1.2 Novel Contributions

To the author's best knowledge, this thesis contains the following scientific novelties:

- The derivation of a full, analytically closed description of the wake function inside the rectangular, dielectrically lined dechirper based on an Fourier expansion of the three-dimensional eigenmodes of the structure and a subsequent eigenmode expansion of the electric field of a point charge. Here, the analytic expressions of the loss factors are of particular importance, as they exclusively depend on geometrical aspects of the structure and on modal characteristics. This will consequently allow for a simple computation of these factors.

- The development and implementation of a Python-based programme that allows for the computation of the wake function inside the dechirper following the derived analytic expression of this quantity. The wake function serves as a Green's function for the computation of the wake potentials of arbitrary bunch shapes and cannot be determined by grid-based numeric schemes.

- The experimental results presented in the final part of this thesis constitute novel contributions as the dechirper in itself is a comparatively new concept. A proof of principle as presented in this thesis, together with a clear proof of the tuning abilities provided by the gap width, support that the observed structure is indeed suited as a dechirper and complement similar experiments performed parallel to this work by a different work group ([1], [2]). Both these experimental successes as well as the limitations of this type of dechirper structure that became apparent during the experiments presented in Chapter 6 can serve as a basis for more extensive, future uses of the dechirper not only at the HZDR but also at other international accelerator sites.

These contributions have previously been published in [3] and [4].

## 1.3 Particle Accelerators

Nowadays, particle accelerators have gained such a large prominence that it is hard to imagine the modern scientific world without them. Their applications have expanded far beyond physics to other areas such as medicine and different industrial branches. Especially in the field of medicine, accelerators are often used in radio therapy and microsurgery, as well as for the sterilisation of medical equipment. In industry, particle accelerators have gained importance for X-ray radiography and material testing and modification, amongst others. With the ever growing technological improvement of accelerators, this importance can only be expected to increase in the coming years.

In the field of physics, particle accelerators have become essential to many different types of studies and applications. The most widely known accelerator laboratory to the general audience particularly in Europe is probably the CERN. Its facilities *L*arge *E*lectron-*P*ositron Collider (LEP) [5] (decommissioned in the year 2000) and *L*arge *H*adron *C*ollider (LHC) [6] have contributed greatly in the verification of the existence of previously theoretically suggested subatomic particles in collision experiments, like for example the Higgs boson [7], and have thus significantly shaped the modern image and understanding of physics. Accelerators are also gaining significance as synchrotron radiation sources (for example PETRA II and its successor, PETRA III [8], located at the *D*eutschen *E*lektronen-*Sy*nchrotron (DESY)) which in turn enable studies in a variety of research areas, like material science, the physics of condensed matter and molecular cell biology, amongst others. *F*ree *E*lectron
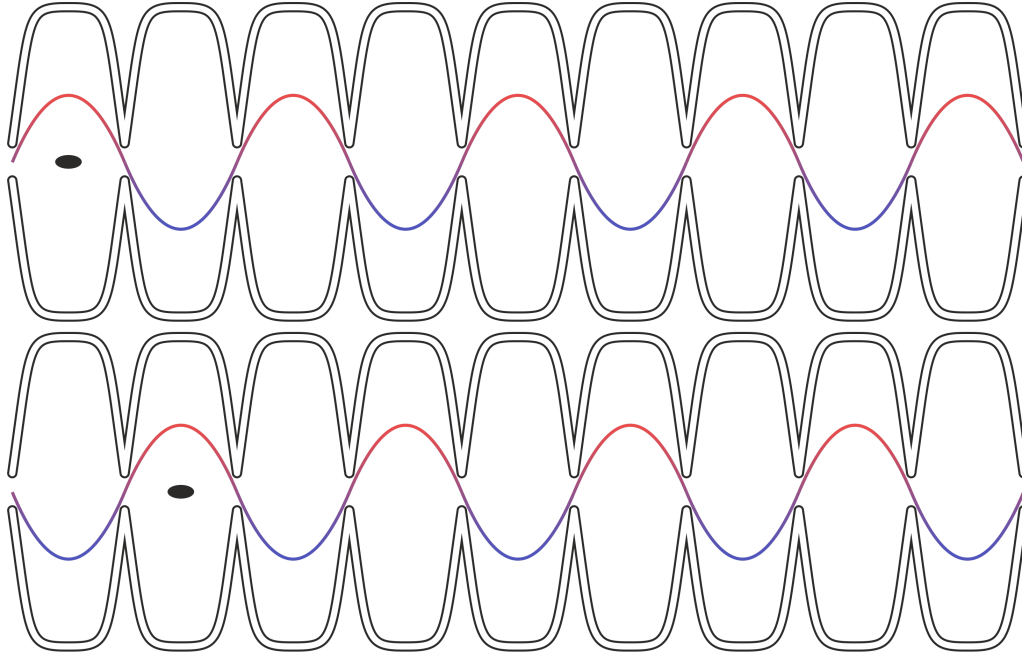
**Figure 1.1:** Schematic overview over the acceleration principle in a 9-cell acceleration cavity employing the resonant electric field of the $\pi$-mode. The particle bunch is on-crest with the accelerating half-wave of the electric field (red) in the first cavity (upper panel). It then traverses into the second cavity, while the field alternates. In this way, the bunch is again on-crest with the accelerating half-wave (lower panel).

*L*aser (FEL)s like the *L*inac *C*oherent *L*ight *S*ource (LCLS) [9] at the *S*tanford *L*inear *A*ccelerator (SLAC) and the European *X*-Ray *F*ree *E*lectron *L*aser (XFEL) at the DESY [10] additionally enable the use of pulses with short wavelengths (from extreme ultra-violet to X-ray) and very short lengths in the range of femto- to attoseconds.

Subject of the experimental part of this thesis is ELBE [11] located at the HZDR. As a standing wave *r*adio *f*requency (RF) *lin*ear *acc*elerator (linac), the acceleration of particles (more specifically, electrons) in this type of structure is based on the sinusoidally varying electric field of the driving mode of the accelerator in a chain of superconducting cavities. A schematic overview of this acceleration principle is shown in Fig. 1.1.

Depending on the phase of the particle bunch relative to the crest of the electric field, the bunch can either be accelerated (red in Fig. 1.1) or decelerated (blue in Fig. 1.1). For an optimal energy gain, the phase of the bunch should coincide with the accelerating crest of the field in one cavity. The electric field is oscillating at the resonance frequency of the 9-cell cavity. During the design process of the unit, this resonant frequency is chosen such that the driving field alternates in the same time that it takes the bunch to travel from one cavity to the next, so that it again

experiences the maximum energy gain from the crest of the alternated field. This process is then repeated for the following cavities in the chain. This field pattern basically amounts to a phase change of exactly $\pi$ between neighbouring cavities. This is why this driving standing electric field is also often referred to as the $\pi$-mode. For a more detailed explanation of the acceleration principle in linacs and other accelerators, see for example [12] or [13].

For further general information on particle accelerators, their applications and underlying principles, see for example [14], or the more recent textbooks [15] and [16].

### 1.3.1 Ultrashort Pulses and Bunch Compression

In the last years, technological advances like photoinjectors (c.f. [17]) have made ultra-short pulses available for a wide variety of applications. Bunches with lengths in the range of sub-picoseconds are required for obtaining high gradients in beam-driven wakefield accelerators (c.f. [18], [19] and [20]), two-beam accelerators (see [21] and [22]) and wavelengths in the X-ray region, as used in the aforementioned FELs.

At ELBE, planned laser-plasma experiments and combined ELBE-laser experiments (for example experiments on Thomson scattering) make an effective interaction between laser and electron pulse necessary. This, in turn, is granted when the phase spaces of both the laser and electron beam exhibit a maximal overlap. For the electron beam in particular this means that an optimal compression of both the length and energy width of the beam is required. In context with the bunch compression procedure used at ELBE this, however, leads to an intrinsic conflict, sketched in Fig. 1.2.

Figure 1.2 shows the acceleration and bunch compression procedure as it is performed, e.g. at ELBE. The upper row shows the longitudinal phase space of the particle bunch; a projection of the energy and time of each particle. Important to note here is that particles which follow the reference particle at $t = 0$ will have $t > 0$; this part of the bunch is usually referred to as the bunch tail, which is depicted in red in the figure. Consequently, the particles which are in front of the reference particle have $t < 0$, this part is referred to as the bunch head (depicted in blue in the figure). This formulation is useful in later chapters though not intuitive: leading particles have positive longitudinal positions, $z > 0$, which corresponds to the proportionality constant between time and position being $-1$, $z \propto -t$.

Figure 1.2 (a) shows the longitudinal phase space before traversing the acceleration module as an ellipse. The particle bunch is injected into the accelerating module off-crest. Depending on the phase of the particles relative to the accelerating wave in the acceleration module, the particles gain more or less energy, which introduces a so-called chirp in the longitudinal phase space (see Fig. 1.2 (b)). This chirp is expressed in a stronger energy gain in the tail of the bunch than in its head, which leads to a rotation of the phase space ellipse. The bunch length, however, is not affected. To compress the bunch in time and to reach the desired ultra-short pulses,
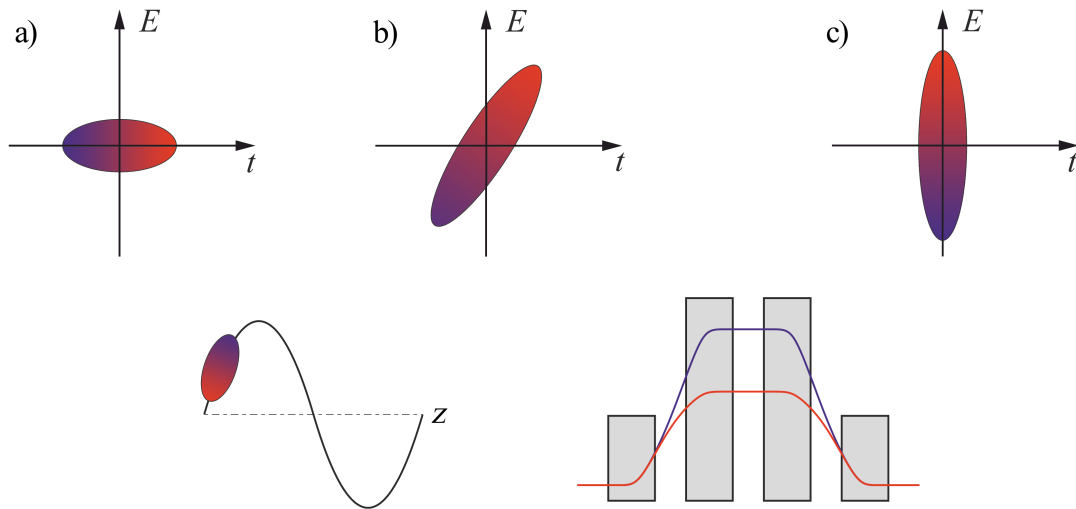
**Figure 1.2:** Schematic overview over the bunch compression using a magnetic chicane, as used at ELBE. The upper row shows the longitudinal phase space of the particle bunch at the different stages of the process; before the acceleration module (a), after the acceleration but before the bunch compression (b) and after the bunch compression (c) in a magnetic chicane composed of four dipoles (grey). The tail of the particle bunch is depicted in red, the head in blue.

the beam is now injected into a magnetic chicane. This structure is composed of four dipoles (grey in Fig. 1.2), which serve as electro-magnetic lenses. Here, particles with a higher energy are deflected less than particles with a lower energy. The deflection angles of the dipoles are adjusted such that the particles nevertheless leave the chicane on the same trajectory. This results in an overall shorter path lengths through the chicane for particles of higher energies: at the end of the chicane, they appear advanced, while particles with lower energies are delayed. This leads to a second rotation of the longitudinal phase space ellipse (Fig. 1.2 (c)). At the end of the chicane, the bunch is thus compressed in time.

However, for this procedure to work, the imprinting of the chirp via the accelerating module (Fig. 1.2 (b)) is absolutely necessary. Additionally, comparing stage (a) and (c) of Fig. 1.2, it becomes apparent that while the pulse length is significantly reduced, the energy width is significantly increased as the chirp 'survives' the chicane, which stands in conflict with the requirements listed above. Figure 1.3 shows the longitudinal phase space plotted from actual data of the ELBE thermionic gun after the first acceleration module (green) and after the magnetic chicane (red). The energy spread is increased from $\approx 30\,\text{keV}$ to $\approx 3\,\text{MeV}$[1].

More specifically, Fig. 1.2 also helps to illustrate one actual problem with beams of high energy spread: the chirp impedes the focussing of the beam. This focussing

---

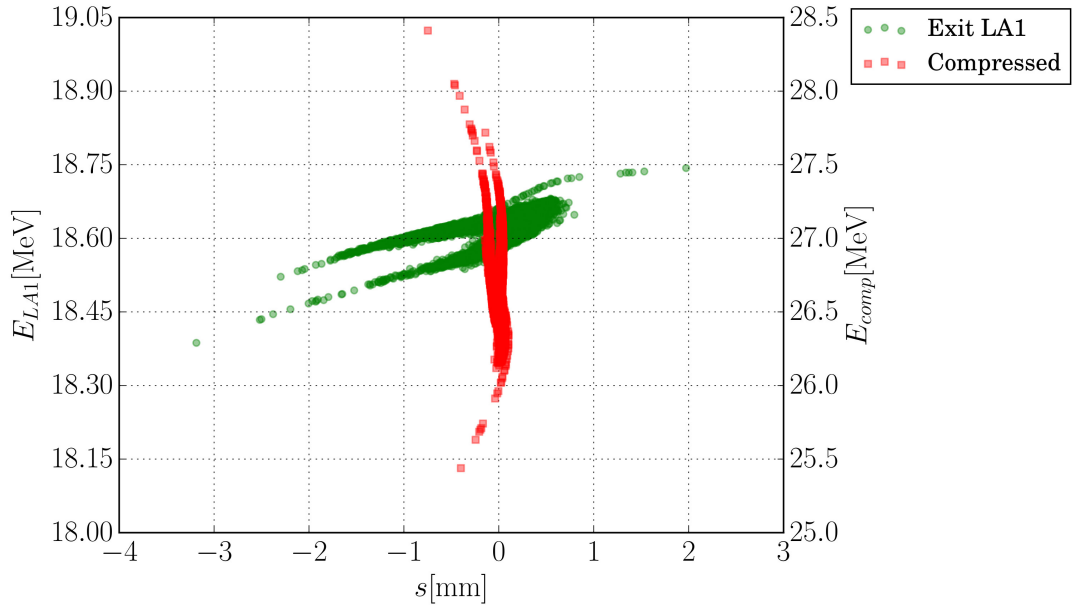[1]Data courtesy of U. Lehnert, HZDR; private correspondence.

**Figure 1.3:** Longitudinal phase space of an exemplary ELBE electron beam, recorded after the first acceleration module (green, left axis) and after the magnetic chicane (red, right axis). The energy spread is significantly increased after the chicane.

is usually performed by further electromagnetic lenses (i.e. quadrupoles), where, like in the magnetic chicane, particles are deflected with respect to their momentum. A focussing of a beam with a significant energy spread to a specific focal point or even plane is thus impossible.

**Active Solutions**

It shall be noted here that this issue is by no means a specific problem of the ELBE facility; but, in fact, known since decades and present at other accelerator facilities world-wide (c.f., for example, [23] and [24]). A feasible and flexible solution to this problem is thus of high interest.

Previous to the consideration of dechirpers for the task of reducing the final energy spread of the bunch, the issue was often solved by running the electron beam off-crest in another, separate acceleration module (c.f. Fig. 1.2 (a) and (b)) which is driven by a mode of a higher frequency than the main acceleration unit ([25], [26]). This method, however, requires a significant amount of additional space for the acceleration module. It is also expensive, its costs are comparable to those of a main acceleration unit. It also requires regular tuning and maintenance, which is again expensive and time-consuming. Furthermore, this solution often can only partly counteract the chirp, which makes this strategy inefficient with regards to the ratio between its cost and the improvements to the beam quality.

**Passive Solutions**

A different concept that fulfils the purpose of reducing the energy spread of a particle beam is the so-called 'dechirper'. Basically, a dechirper is a comparatively simple waveguide structure in which a wakefield is generated through either dielectric coatings or periodic corrugations in the walls of the waveguide. Through the interaction of the wakefield with the bunch generating it, the energy spread of the bunch can be reduced.
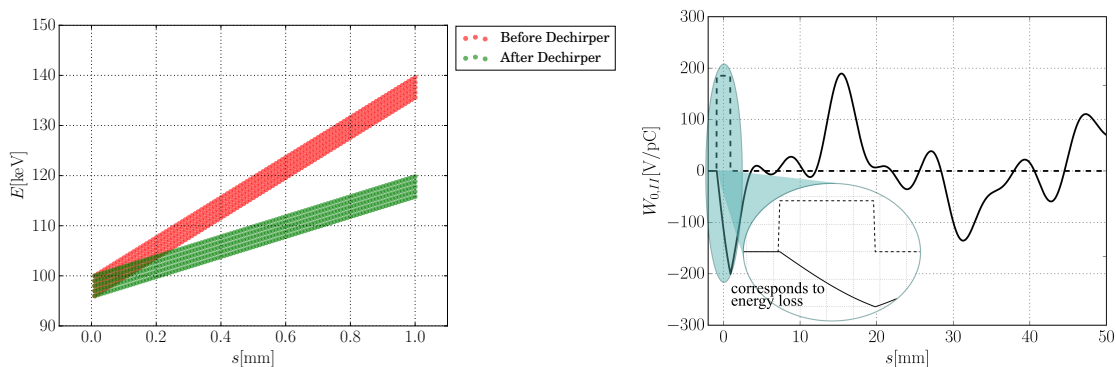


**Figure 1.4:** Overview over the general principle of a wakefield dechirper. Left panel: The longitudinal phase space of an arbitrary bunch with a uniform shape function before (red) and after the dechirper (green). Right panel: The wake potential of the bunch generated in a dechirper. The zoomed-in part of the wake potential along the bunch shape (dashed line) corresponds to an energy loss.

Figure 1.4 depicts the general principle of the dechirper: the left panel shows the longitudinal phase space of an arbitrary pulse with a uniform bunch shape before and after the dechirper. Before the dechirper, the bunch shows an energy chirp between the leading particles at $s = 0$ and the following particles for $s > 0$ (depicted in red). This bunch now passes through a dechirper structure, where a wake potential is generated by an interaction between the beam and the structure (shown in the right panel). Along the pulse shape, this wake potential is nearly linear[2] and corresponds to an energy loss. Depending on the position of the particle in the bunch, this energy loss differs; the particles in the tail of the bunch generally experience a larger energy loss. Overall, this energy modulation counteracts the original chirp of the beam and reduces the energy spread (left panel, shown in green).

This concept is fundamentally different to the previously described active methods, as there is no need for an external excitation of an electromagnetic field inside the structure. What counteracts the energy spread here is the wakefield, which is only generated by an interaction between the dechirper and the beam in the moment

---

[2]This is the case for this specific pulse shape, for more information on the influence of the pulse shape on the wake potential, see Chapter 5.

when the beam passes the structure. To put it very simply, all that this procedure needs to work is the mere presence of the dechirper structure. This is also why this type of method is sometimes called a *passive* solution to contrast it against the previously mentioned active solutions that require external excitation and elaborate tuning of the beam and the driving field.

### 1.3.2 Statement Regarding the Subject of this Thesis

The project work this thesis is based on was a collaboration between the Chair of Electromagnetic Field Theory at the University of Rostock and the HZDR. The underlying task has been the design of a dedicated dechirper structure for ELBE[3].

During the simulation phase, however, it became apparent that due to the novelty of the dechirper as an approach to reduce the energy spread of a particle beam, not only design studies, but also theoretical background work was required to obtain an all-encompassing understanding of the processes within the dechirper and especially the influences of the geometric and dielectric parameters of the structure on the obtainable dechirper effect.

The task thus evolved from a single design study to a complete inspection of a rectangular, dielectrically lined dechirper, starting with an analytical treatment of the generated wakefield. Especially the wake function was of interest here since it serves as a Green's function for bunches of arbitrary shapes, and thus, the following considerations would not be limited to bunches with specific particle distributions.

The underlying problem of this thesis is thus the development of an eigenmode-based model for the analytic expression of the wake function and its subsequent implementation into a simple yet efficient programme code; and the test and validation of both in parameter studies and accompanying experiments performed at ELBE.

## 1.4 State of the Art

The concept of wakefields (explained in more detail in Chapter 2) in itself, is by far not a novelty in the field of accelerator physics (see, e.g., [13] and [27] for textbooks dealing with this subject). The computation of wakefields has played an important role for several decades since, due to their energy modulating nature, wakefields can have a negative and impeding influence on the quality of the particle beam (e.g., by increasing its transversal emittance, c.f. [28]). Another aspect that has been studied with respect to wakefields and their possibly energy-modulating effects is that of a wakefield accelerator, where long range wakefields of electron bunches are used to accelerate secondary bunches of particles (c.f. [29] and [30]).

---

The basis for the study of wakefields in the context of this work is the possibility to derive, with whatever methods should prove most effective, a mathematical description of the wake potential as described in [31] and [32]. Progress on the field of accelerator physics and increasing demands on the beam quality have made precise solutions for the wakefields become necessities. Software like TBCI [33] and MAFIA [34], CST PS [35] (all based on the Finite Integration Technique) and ECHO (for rotationally symmetric structures, [36] and [37]) is dedicated to the computation of the wakefields, mostly wake potentials of Gaussian pulses, inside various types of structures. The programme URMEL-I [38], which is based on the software URMEL [39], also allows for impedance computations. The related software URMEL-T [40] additionally enables the computation of RF fields in the presence of longitudinally invariant dielectric fillings in cylindrical symmetric cavities. In an effort to accurately predict the effects of wakefields on the particle beam, results of these programmes are often combined with particle-tracking algorithms like ELEGANT [41] or ASTRA [42]. The computation and evaluation of these effects play a crucial part in the design process of accelerator structures, as illustrated in [43] for DESY, in [44] for CLIC, and more recently in [45] for SOLEIL, [46] for FERMI@Elettra and in [47] for CXEB, an energy booster planned at the Colorado State University.

However, for structures with comparatively simple geometries, analytic solutions for the resulting wakefields are available. These solutions are often based on a modal analysis of the structure, as the eigenmodes in case of simple geometries are analytically known; which is also the approach used in this thesis. Analytic computations of wakefields in cylindric cavities [48], e.g., are often used as benchmark for numerical software, which is needed to compute the wakefields in more complex, but similar structures like the typical elliptic accelerating cavities. As a substitute benchmark, spherical cavities have been studied, as well [49]. Additional attempts have been made to expand on the analytic expressions of wake fields using the periodicity of the structures, e.g. in [50]. Other analytic studies are often based on computing the impedance (the Fourier transform of the wakefield, c.f. [32]) and deriving the wakefield from there, for example for cylindrical cavities with resistive walls [51] and between parallel resistive plates [52].

These considerations are already closely related to the subject of the dechirper, as all suited dechirper structures are unified in their simplicity and similarity to these basic geometric cavities. The wakefields in dielectrically lined tubes have been reviewed in [53], while still considered as harmful for the quality of the beam. The idea to use the originally considered obstructive effects for the purpose of the reduction of the energy spread came up in 1990 [54], but only gained new attention and momentum when several work groups, mostly seated in the USA, picked up on the idea and started considering the dechirper for use at several accelerator sites around the year 2012.

In its corrupted form, a dechirper was proposed for the *Next Generation Light Source* (NGLS) at SLAC by Bane and Stupakov in that year [55]. In this work, the

corrugated, cylindrical waveguide was reviewed, and single-mode analytical computations of the wakefield were compared to numerical results obtained with ECHO. Special attention was put on the nearly linear dechirp created by a flat-top pulse traversing the dechirper. It has to be mentioned here that the theoretical structure proposed in [55] was about 9 m long. The group continued working on the topic of dechirpers in the following years, and in 2014, a scientific cooperation with a second work group from Berkeley and the *P*ohang *A*ccelerator *L*aboratory (PAL) in Korea, was able to implement a rectangular waveguide with corrugated walls as a dechirper at the PAL-FEL, [56]. The success of the energy spread reduction was experimentally observed and compared to beam dynamics simulation. Additionally, observations of the transversal phase space showed an emittance growth in these directions, which limits the functionality of the dechirper. A similar experiment with a corrugated rectangular waveguide was recently carried out in Shanghai, China, [57]. The results here were compared to theoretical phase spaces obtained by beam dynamics simulations performed with ELEGANT and ASTRA. The wakefield was analytically approximated by a single mode.

On the field of dielectrically lined dechirpers, Craievich [58] suggested the use of a dielectrically lined cylindrical waveguide as a phase space linearizer in 2010 in a prospective study for Elettra. Single and two mode approximations of the wakefield were performed and then used for particle tracking with the specific beam line and bunch characteristics for Elettra. Here, the linearizer structure was suggested for cancelling second order terms in the longitudinal phase space distribution of the particle beam, since the energy modulation induced by the structure is also non-linear using an appropriate bunch shape.

Also in the year 2012, Antipov et al. suggested the use of a dielectrically coated rectangular waveguide as a silencer for the Facility for Advanced Accelerator Experimental Tests (FACET) (c.f. [59]) and reported on first successes of a cylindrical, dielectrically lined dechirper structure at the *A*ccelerator *T*est *F*acility (ATF) at the *B*rookhaven *N*ational Accelerator *L*aboratory (BNL) [60]. In the latter work, the reported dechirp achieved by the cylindrical structure is in the range of a few 10 keV, and the numerical considerations were once again based on a single mode approximation of the wake. Additionally, [60] introduces the idea of using the dechirper and the oscillating nature of the wakefield for microbunching and the generation of Terrahertz radiation. In [1] and [61], the same authors report on tests with an alumina-coated rectangular waveguide at the ATF and show first experimental results for the tuning of the gap width of the dechirper and the resulting adjustment of the final strength of the wakefields (and thus, the dechirp). The numerical considerations in [1] use an eigenmode expansion based approach for the computation of the wakefields, but give no information on the eigenmodes' respective loss factors. Additionally, it is suggested that the number of eigenmodes used for the approximation of the wakefield is dependent on the thickness of the dielectric layer; thin layers enable a single mode approximation, while thick layers require a multi-mode expansion. Further

experiments with a short silicon-lined rectangular dechirper were conducted by this group in 2015, where again the influence of the gap width has been studied, [2].

As a minor intermediate conclusion, it has to be stated here that the experimental aspect of the rectangular dielectrically lined dechirper is still a new concept. This field of study, despite the experiments mentioned above, is far from being saturated with results. Structures of similar geometries like described above more and more become the focus of international accelerator sites, c.f. [62].

The mathematical aspect of wakefields in dielectrically loaded structures has also been the focus of several studies in the last years, at first with regard to analysing the potentially harmful nature of wakefields in accelerator structures. In 1997, Tremaine, Rosenzweig and Schoessow proposed an analytical method for the wakefield computation in dielectrically lined rectangular waveguides based on an expansion in the two-dimensional eigenmodes of the structure [63]. These eigenmodes are LSE and LSM modes as opposed to the more commonly known TE and TM modes of structures without dielectric lining and have been introduced in [64] before. For this, the loaded structure was split into the vacuum and dielectric regions for which Maxwell's equations have been solved separately; this is later combined into complete field distributions of the eigenmodes. The wakefield is then deduced from these eigenmodes by an energy balance method. This procedure has been expanded upon in [65]. Additionally, [65] uses the derived method and implements it in the framework IMPACT-T. Computations with this code were compared to simulations with the software VORPAL and show a high agreement. Both methods also consider transversal wakefields and strongly highlight the contributions of single eigenmodes to the wakefield.

Further extensive mathematical studies on dielectrically lined waveguides have been carried out by Baturin et al. in the same timeframe in which the method presented in this thesis has been developed. In 2012, they presented an optimisation for potential dielectrically lined dechirpers at FACET and the *Argonne Wakefield Accelerator* (AWA) based on a single-mode wakefield approximation for a Gaussian pulse. In this paper, it was suggested that the optimal coating for both structures was diamond ($\varepsilon_r \approx 6$). In 2013, they reported on a rigorous analytical approach contrasting the more often used impedance formulation for the computation of the wakefield inside the rectangular, dielectrically loaded dechirper called Transverse Operator Method [66]. It introduces a spatially dependent relative permittivity to model the dielectric slabs, and directly solves Maxwell's equations in the dechirper in the presence of a point charge without an eigenmode expansion. Based on this method, the programme code RECTANGULAR has been developed. In [67], they generalised this approach for arbitrary cross-sections of the dechirper.

The formalism of LSE and LSM modes has also been used in [68], though here the equivalent circuit method is used to compute a single mode wakefield. Further computations are performed with MAFIA. In [69], this method is expanded to transversal wakefields for beams outside of the centre of the structure using the

Panofsky-Wenzel theorem. Less recent considerations on wakefields in dielectrically lined waveguides include studies on cylindrical structures [70], in which the wake potential of a Gaussian is computed. Here, like in [63], the waveguide is split into a dielectric and a vacuum region, and the analytical solution is deduced for the special cases of an infinitely thick and thin dielectric layer. In [71], an approach for the calculation of the wake function in a structure with multiple, asymmetrically positioned dielectrics with different relative permittivities based on two-dimensional eigenmodes is presented.

The theoretical considerations regarding corrugated dechirpers are omitted here, because they are not of relevance for the structure considered in this thesis. It shall be noted here, however, that some efforts have been made by Bane and Stupakov to connect the theoretical considerations of both corrugated and dielectrically lined structures by calculating effective permittivities and permeabilities from the corrugation parameters in [72].

## 1.4.1 Distinction of the Presented Semi-Analytical Approach

In light of the statements of the last section, it appears appropriate to distinguish the method presented in this thesis against the previously listed analytical approaches for the wakefield computation in dielectrically lined rectangular waveguides.

In this thesis, a rigorous, self-consistent method is presented with which the wake function (i.e. the Green's function) inside the dechirper can be computed. While also focussing on the expansion of the wakefield into the eigenmodes of the structure like in [63] and [65], neither method uses the here presented Fourier-expansion based Rayleigh-Ritz approach to compute the eigenmodes but rather considers the solution in the different sub-sections of the waveguide (i.e. dielectric slabs and vacuum). Additionally, both works do not present a solution for the wake function, instead [65] limits the considerations to charge distributions with a symmetry with respect to the vertical axis of the dechirper.

The idea of using a spatially dependent relative permittivity is similar to the approach presented in [66], which constitutes a rigorous solution to Maxwell's equations in the dechirper structure in presence of a point charge, which then leads to the wake function. Other suggestions for the computation of the wake function have been made in [73], however, these considerations focus on a recreation of the wake function from a wake potential of a longer pulse, and rely on a numerical fitting of a correction function.

The approach presented here is free of assumptions. The modes computed with the suggested approach are three-dimensional eigenmodes compared to the two-dimensional eigenmodes used in [63]; the open boundary in longitudinal direction is not imposed on the modes, it is rather reached by a superposition of the eigenmodes

in a closed structure for *P*erfect *E*lectric *C*onductor (PEC) and *P*erfect *M*agnetic *C*onductor (PMC) boundary conditions employed in longitudinal direction (c.f. Chapter 3.5). The velocity and symmetry conditions of the modes (c.f. Chapter 3.2.2) directly result from the employed model itself and are not previously imposed on the analytical considerations. In this way, an analytically closed formulation of the wake function is found which also includes the loss factors (that have not been considered in neither [63] nor [66]) of the structure.

The algorithm presented here can calculate any arbitrary three-dimensional eigenmode in the structure in the same computational time, regardless of its frequency, since the algorithm is in very large parts free of any spatial or temporal discretisation.

# 2 Introduction of the Underlying Principles

This chapter addresses the general physical and mathematical concepts that a large portion of this thesis is based on. For this purpose, Maxwell's equations are introduced and the general concepts of wakefields, eigenmodes and eigenmode expansions are reviewed. As an example, the eigenmodes of a rectangular cavity are determined analytically.

## 2.1 Maxwell's Equations

Maxwell's equations provide the theoretical foundation of classical electromagnetism. Formulated in the 19$^{\text{th}}$ century, they are based on physical laws originally established by other scientists, but have been improved upon by the eponymous James Clerk Maxwell [74].

Their most commonly used expressions were later reformulated from Maxwell's original statements by Heaviside and Gibbs. The integral representation of Maxwell's equations for a given spatial coordinate $\mathbf{r}$ and a temporal dependence $t$ is

$$\oiint_{\partial\boldsymbol{\Omega}} \mathbf{D}\left(\mathbf{r}, t\right) \cdot \mathrm{d}\mathbf{S} = \iiint_{\boldsymbol{\Omega}} \rho\left(\mathbf{r}, t\right) \mathrm{d}V, \tag{2.1}$$

$$\oiint_{\partial\boldsymbol{\Omega}} \mathbf{B}\left(\mathbf{r}, t\right) \cdot \mathrm{d}\mathbf{S} = 0, \tag{2.2}$$

$$\oint_{\partial\boldsymbol{\Gamma}} \mathbf{E}\left(\mathbf{r}, t\right) \cdot \mathrm{d}\mathbf{s} = -\frac{\mathrm{d}}{\mathrm{d}t} \iint_{\boldsymbol{\Gamma}} \mathbf{B}\left(\mathbf{r}, t\right) \cdot \mathrm{d}\mathbf{S}, \tag{2.3}$$

$$\oint_{\partial\boldsymbol{\Gamma}} \mathbf{H}\left(\mathbf{r}, t\right) \cdot \mathrm{d}\mathbf{s} = \iint_{\boldsymbol{\Gamma}} \left(\frac{\partial}{\partial t} \mathbf{D}\left(\mathbf{r}, t\right) + \mathbf{J}\left(\mathbf{r}, t\right)\right) \cdot \mathrm{d}\mathbf{S}, \tag{2.4}$$

where $\mathbf{D}\left(\mathbf{r}, t\right)$ and $\mathbf{B}\left(\mathbf{r}, t\right)$ represent the electric and magnetic flux densities, respectively; $\mathbf{E}\left(\mathbf{r}, t\right)$ and $\mathbf{H}\left(\mathbf{r}, t\right)$ the electric and magnetic field strengths; $\rho\left(\mathbf{r}, t\right)$ the electric charge density and $\mathbf{J}\left(\mathbf{r}, t\right)$ the electric current density.

Equation (2.1) is referred to as *Gauss' Law*. It states that the total electric flux through the closed boundary $\partial\boldsymbol{\Omega}$ equals the total charge contained in the corresponding arbitrary domain $\boldsymbol{\Omega}$. Similarly, *Gauss' Law for Magnetism* (2.2) equates

the total magnetic flux through $\partial\Omega$ with zero. Equation (2.3), *Faraday's Law of Induction*, states that the negative rate of change of the magnetic flux through an arbitrary surface $\Gamma$ is equal to the integrated electric field along a closed boundary $\partial\Gamma$ of the surface. Again in a similar fashion, (2.4) equates the integration of the magnetic field strength along a closed boundary of the surface $\Gamma$ to the sum of the total electric current and the rate of change of the electric flux through the surface. This relation is labelled *Ampere's Circuital Law with Maxwell's Extension.*

The constitutive equations for linear isotropic materials

$$\mathbf{D}\left(\mathbf{r}, t\right) = \varepsilon_0\varepsilon_r\mathbf{E}\left(\mathbf{r}, t\right) \text{ and}$$
$$\mathbf{B}\left(\mathbf{r}, t\right) = \mu_0\mu_r\mathbf{H}\left(\mathbf{r}, t\right)$$

relate the flux densities to the respective field strengths of the electric and magnetic field. Here, $\varepsilon_0$ is the permittivity of vacuum, while $\varepsilon_r$ is the material-dependent relative permittivity. Both are often combined into a single quantity referred to as permittivity, $\varepsilon = \varepsilon_0\varepsilon_r$. Similarly, the permeability of vacuum $\mu_0$ and the relative permeability $\mu_r$ can be combined into a single quantity, the permeability $\mu = \mu_0\mu_r$. Both the permittivity and the permeability are not necessarily spatially constant. Generally, they represent tensors that account for the material's anisotropy. Additionally, the speed of light in vaccum can be derived from the vacuum permittivity and permeability via

$$c_0^2 = \frac{1}{\varepsilon_0\mu_0}. \tag{2.5}$$

Using Gauss' theorem

$$\iiint \left(\nabla \cdot \mathbf{A}\left(\mathbf{r}\right)\right)\mathrm{d}V = \oiint \left(\mathbf{A}\left(\mathbf{r}\right) \cdot \mathbf{n}\right)\mathrm{d}S, \tag{2.6}$$

and Stokes' theorem

$$\oint \mathbf{A}\left(\mathbf{r}\right)\mathrm{d}\mathbf{\Gamma} = \iint \nabla \times \mathbf{A}\left(\mathbf{r}\right)\mathrm{d}\mathbf{S}, \tag{2.7}$$

where $\mathbf{A}\left(\mathbf{r}\right)$ is an arbitrary vector field, the integral representation of Maxwell's equations can be transferred into the differential representation,

$$\nabla \cdot \mathbf{D}\left(\mathbf{r}, t\right) = \rho\left(\mathbf{r}, t\right), \tag{2.8}$$

$$\nabla \cdot \mathbf{B}\left(\mathbf{r}, t\right) = 0, \tag{2.9}$$

$$\nabla \times \mathbf{E}\left(\mathbf{r}, t\right) = -\frac{\partial}{\partial t}\mathbf{B}\left(\mathbf{r}, t\right), \tag{2.10}$$

$$\nabla \times \mathbf{H}\left(\mathbf{r}, t\right) = \frac{\partial}{\partial t}\mathbf{D}\left(\mathbf{r}, t\right) + \mathbf{J}\left(\mathbf{r}, t\right). \tag{2.11}$$

In these representations, Maxwell's equations form a set of four coupled, ordinary partial differential equations, which are more easily applicable for analytical considerations compared to their integral forms.

### 2.1.1 The Wave and Helmholtz Equations

A strategy to obtain a solution to Maxwell's equations is the derivation of the electric and magnetic wave equations. In the following considerations, it will be assumed that both the permittivity and the permeability are spatially constant[1].

For the electric wave equation, first the curl of Faraday's Law of Induction (2.10), is generated:

$$\nabla \times \nabla \times \mathbf{E}\left(\mathbf{r}, t\right) = -\frac{\partial}{\partial t} \nabla \times \mathbf{B}\left(\mathbf{r}, t\right) = -\frac{\partial}{\partial t} \mu \nabla \times \mathbf{H}\left(\mathbf{r}, t\right).$$

Using Ampere's Law with Maxwell's Extension (2.11), the right hand side of the upper equation can be transformed into

$$\nabla \times \nabla \times \mathbf{E}\left(\mathbf{r}, t\right) = -\frac{\partial}{\partial t} \mu \left(\frac{\partial}{\partial t} \mathbf{D}\left(\mathbf{r}, t\right) + \mathbf{J}\left(\mathbf{r}, t\right)\right).$$

To further simplify this equation, the vector identity

$$\nabla \times \left(\nabla \times \mathbf{A}\right) = \nabla \left(\nabla \cdot \mathbf{A}\right) - \nabla^2 \mathbf{A} \tag{2.12}$$

is used. With this, the left hand side of the upper equation can be rewritten and

$$\nabla \left(\nabla \cdot \mathbf{E}\left(\mathbf{r}, t\right)\right) - \nabla^2 \mathbf{E}\left(\mathbf{r}, t\right) = -\frac{\partial}{\partial t} \mu \left(\frac{\partial}{\partial t} \mathbf{D}\left(\mathbf{r}, t\right) + \mathbf{J}\left(\mathbf{r}, t\right)\right)$$

is obtained. After a few further transformations, the wave equation for electric fields

$$\nabla^2 \mathbf{E}\left(\mathbf{r}, t\right) = \frac{1}{\varepsilon} \nabla \rho \left(\mathbf{r}, t\right) + \varepsilon \mu \frac{\partial^2}{\partial t^2} \mathbf{E}\left(\mathbf{r}, t\right) + \mu \frac{\partial}{\partial t} \mathbf{J}\left(\mathbf{r}, t\right), \tag{2.13}$$

is generated.

Using a similar procedure but starting at Ampere's Law with Maxwell's extension (2.11), the magnetic wave equation can be formulated:

$$\nabla^2 \mathbf{H}\left(\mathbf{r}, t\right) = \varepsilon \mu \frac{\partial^2}{\partial t^2} \mathbf{H}\left(\mathbf{r}, t\right) - \nabla \times \mathbf{J}\left(\mathbf{r}, t\right). \tag{2.14}$$

Given there are no charges and currents present, the equations (2.13) and (2.14) can be simplified into

$$\nabla^2 \mathbf{E}\left(\mathbf{r}, t\right) = \varepsilon \mu \frac{\partial^2}{\partial t^2} \mathbf{E}\left(\mathbf{r}, t\right) \text{ and}$$

$$\nabla^2 \mathbf{H}\left(\mathbf{r}, t\right) = \varepsilon \mu \frac{\partial^2}{\partial t^2} \mathbf{H}\left(\mathbf{r}, t\right).$$

---

[1]In the dechirper structure that is the main focus of this thesis, this is not the case. The assumption is still useful to introduce the general methods and procedures used throughout Chapter 3.

As a last step, the fields are now assumed to exhibit a harmonic time dependence. Introducing phasors, the electric and magnetic field strength can be reformulated using a separation ansatz,

$$\mathbf{E}\left(\mathbf{r}, t\right) = \underline{\mathbf{E}}\left(\mathbf{r}\right) \mathrm{e}^{-j\omega t} \text{ and}$$
$$\mathbf{H}\left(\mathbf{r}, t\right) = \underline{\mathbf{H}}\left(\mathbf{r}\right) \mathrm{e}^{-j\omega t},$$

where $\omega$ is the angular frequency.

Using $\varepsilon\mu = 1/c^2$, where $c$ is the speed of light in matter, the Helmholtz equations

$$\nabla^2 \underline{\mathbf{E}}\left(\mathbf{r}\right) = -\frac{\omega^2}{c^2} \underline{\mathbf{E}}\left(\mathbf{r}\right) \text{ and} \tag{2.15}$$

$$\nabla^2 \underline{\mathbf{H}}\left(\mathbf{r}\right) = -\underbrace{\frac{\omega^2}{c^2}}_{k^2} \underline{\mathbf{H}}\left(\mathbf{r}\right) \tag{2.16}$$

can be derived. Here, $k$ is the wavenumber.

## 2.2 Basic Concepts of Wakefields

Great parts of this section have previously been published in [75] and follow the lines of [32].

### 2.2.1 The Term 'Wakefield'

Outside of accelerator physics, the term 'wake' is mostly known from fluid dynamics, referring to the wave pattern behind an object moving in a liquid (e.g. a ship moving in water). This also comes to mind first when the term is used in everyday language.

In accelerator physics, the word 'wakefield' has a different meaning, as it describes an electromagnetic effect created by charged particles (see next paragraph). However, it is not completely wrong to think of the wakefield as a certain field pattern that follows a charged particle, like water waves excited by a ship.

Wakefields, in the context of accelerator physics, are generated by a charged particle that travels through a metallic vacuum chamber. The self-field of an ultra-relativistic particle ends perpendicular to the highly conductive walls. On the surface of the walls, image charges are created, which turn into the sources of new fields and act back on the particle. In a metallic vacuum chamber without any geometric variation, the image charges travel together with the ultra-relativistic particle. Any geometric variation forces the field lines to bend, since they still need to stay perpendicular to the conductive walls. Then, some parts of the fields (and the energy stored therein) stay behind and consequently trail behind the particle. These fields are denoted wakefields. If a second particle follows the first closely enough, it will still see the
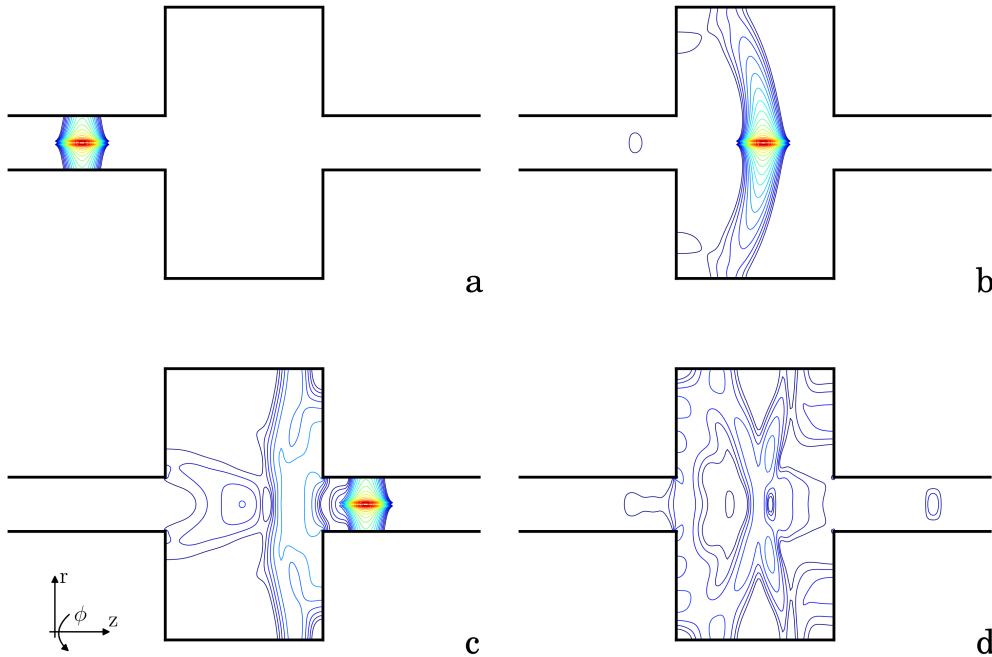
**Figure 2.1:** Electric field lines of a Gaussian pulse travelling through the model pillbox cavity ($R = 5\,\mathrm{cm}$, $g = 10\,\mathrm{cm}$), calculated using the CST STUDIO SUITE®[35]: (a) while entering the structure; (b) traversing the cavity; (c) leaving the structure; (d) after leaving. It can be seen that a part of the electric field remains in the structure even after the bunch has left.

wakefields of the first particle and interact with them. In a bunch of charged particles, the trailing particles of the bunch will see the wakefields of the leading particles and interact with them.

Figure 2.1 illustrates this process. A Gaussian pulse enters a so-called pillbox cavity. A pillbox cavity consists of a cylindrical cavity resonator with round openings that are attached to the beam pipe. The beam axis coincides with the symmetry axis of the pillbox cavity. At the transitions between the cylindrical cavity and the beam pipes, the diameter of the vacuum chamber changes so that a wakefield can be generated—a figurative description would say that part of the self-field of the bunch is 'stripped off' by the geometric changes in the structure. The wakefield remains in the structure and oscillates for some time after the bunch has left. A second particle bunch that traverses the structure would consequently be influenced by the generated wakefield. The pillbox cavity used in Fig. 2.1 has a radius of $R = 5\,\mathrm{cm}$ and a length of $R = 10\,\mathrm{cm}$ and will be used in examples throughout this chapter as an exemplary model.

The word 'wakefield' is usually understood as a general term. More specifically,

the term 'wake potential' is used when considering the wakefield behind a particle bunch, and 'wake function' when the wakefield behind a point charge is considered. These expressions will be explained in more detail in subsequent sections.

## 2.2.2 Basic Concepts of Ultra-Relativistic Wakefields

To understand the underlying principles of wakefields, it is helpful to understand what happens to a point charge $q$ that moves in free space with a velocity close to the speed of light, $v \approx c$.

Owing to the Lorentz contraction, the electromagnetic field of the electron will be shrunk to a thin disk perpendicular to its moving direction. The opening angle of the field travelling with the particle is given by $1/\sqrt{1 - \beta^2} = 1/\gamma$ with the factor $\beta = v/c$. If the velocity approaches the speed of light, the thickness of the disk shrinks further, to a $\delta$-distribution (see Fig. 2.2). This field is strictly radial, i.e. there are no components of the field *behind* or *in front* of the charge, which is also a consequence of the *principle of causality*. Accordingly, in this case, there can be no wakefield behind the electron in free space.

To actually achieve a field and a force behind the field-generating charge, additional mechanisms are required. For example, the image charges and fields created on the waveguide walls are only synchronous with the fields generating them if the walls are perfectly conducting. In resistive or imperfectly conducting walls, the image fields will trail behind the field-generating charge. Other possibilities include obstacles in the beam pipe, e.g. geometric variations (c.f. Fig. 2.1), from which the fields are scattered. Another possibility is to introduce dielectric walls because the speed of light will be lower here than in a vacuum. This means that the fields are 'slowed down', in the sense that travelling waves in these media will have a lower phase velocity and thus trail behind the generating fields.
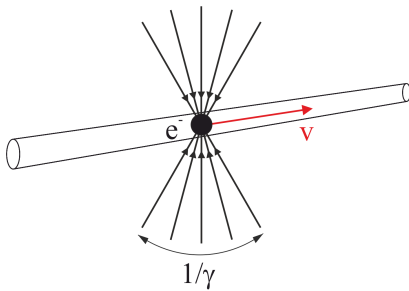


**Figure 2.2:** Radial electric field of an electron moving at the speed of light, contracted to a disc.
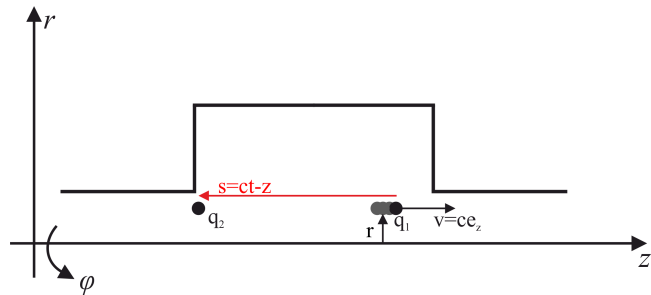
**Figure 2.3:** Field-generating and test charges in a pillbox cavity. The grey dots represent the possibility of a particle bunch generating the wakefield instead of a single charge.

## 2.3 Theoretical Definition of the Wake Potential and Related Quantities

In the following, a field-generating charge $q_1$ located at the three-dimensional coordinate $\mathbf{r}$ is considered. First, the electromagnetic force that this field-generating charge exerts on a test charge $q_2$ that moves at the speed of light along the $z$-axis, $\mathbf{v} = c\,\mathbf{e}_z$, is examined. This force is simply the Lorentz force,

$$\mathbf{F}\left(\mathbf{r}, t\right) = q_2\left(\mathbf{E}\left(\mathbf{r}, t\right) + c\,\mathbf{e}_z \times \mathbf{B}\left(\mathbf{r}, t\right)\right). \tag{2.17}$$

A new variable for the distance between $q_2$ and $q_1$ (see Fig. 2.3) is introduced, so that

$$s = c\,t - z\,,$$

and

$$\mathbf{F}\left(s, t\right) = \mathbf{F}\left(x, y, z = c\,t - s, t\right).$$

The net momentum change $\delta p$ of the test charge due to the Lorentz force will then be

$$\delta p \sim \int \mathbf{F}\left(s, t\right) \mathrm{d}t\,. \tag{2.18}$$

### 2.3.1 The Wake Potential

The concept of wake potentials is related to the concept of the momentum change on a test charge, described before. In the situation described in Fig. 2.3, a pillbox cavity with its transitions between the cylindrical cavity and the beam pipes introduces a radial change of the vacuum chamber and thus wakefields can be generated. Additionally, both charges are assumed to have a transverse offset $\mathbf{r}$ from the centre of the beam pipe, while the movement is still parallel to the $z$-axis. In cylindrical coordinates, the described situation is as shown in Fig. 2.3. In this case, the *three-dimensional wake potential* is defined as

$$\mathbf{W}\left(\mathbf{r}, s\right) = \frac{1}{q_1} \int\limits_{-\infty}^{\infty} \left[\mathbf{E}\left(\mathbf{r}, z, t\right) + c\mathbf{e}_z \times \mathbf{B}\left(\mathbf{r}, z, t\right)\right]_{t=(z+s)/c} \mathrm{d}z\,, \tag{2.19}$$

which is basically an integral over the Lorentz force evaluated on the beam axis and normalised to the field-generating charge. Additionally, time is substituted with $t = z + s/c$. The momentum change of the test charge is related to this via

$$\delta p = q_1 q_2 \mathbf{W}(\mathbf{r}, s)\,. \tag{2.20}$$

Usually, the wake potential is separated into the *longitudinal wake potential* and the *transverse wake potential*.

For the longitudinal wake potential, the projection of the Lorentz force onto the $z$-axis is used:

$$\mathbf{W}\left(\mathbf{r}, s\right) \cdot \mathbf{e}_z = \frac{1}{q_1} \int\limits_{-\infty}^{\infty} \left[\mathbf{E}\left(\mathbf{r}, z, t\right) \cdot \mathbf{e}_z + c\left(\mathbf{e}_z \times \mathbf{B}\left(\mathbf{r}, z, t\right)\right) \cdot \mathbf{e}_z\right]_{t=(z+s)/c} \mathrm{d}z \,.$$

Here, the second term vanishes because $\mathbf{e}_z \cdot \left(\mathbf{e}_z \times \mathbf{B}\left(\mathbf{r}, z, t\right)\right) = 0$. The longitudinal component of the wake potential is thus only dependent on the electric field:

$$W_{\|}\left(\mathbf{r}, s\right) = \frac{1}{q_1} \int\limits_{-\infty}^{\infty} E_z\left(\mathbf{r}, z, \frac{z+s}{c}\right) \mathrm{d}z \,. \tag{2.21}$$

Consequently, the transverse wake potential is only dependent on the transverse components of the electric and magnetic field:

$$\mathbf{W}_{\perp}\left(\mathbf{r}, s\right) = \frac{1}{q_1} \int\limits_{-\infty}^{\infty} \left[\mathbf{E}_{\perp}\left(\mathbf{r}, z, t\right) + c\mathbf{e}_z \times \mathbf{B}_{\perp}\left(\mathbf{r}, z, t\right)\right]_{t=(z+s)/c} \mathrm{d}z \,. \tag{2.22}$$

Both wake potentials are dependent on the distance $s$ between the field-generating charges and the test charge. This distance is measured in the negative longitudinal direction (see Fig. 2.3). This means that a negative distance $s$ corresponds to the case in which the test charge is *in front* of the field-generating charges. Owing to the principle of causality, in this case there can be *no wake potential*. Consequently, this means that:

$$W_{\|}\left(\mathbf{r}, s\right) = 0 \text{ for } s < 0, \text{ and} \tag{2.23}$$
$$\mathbf{W}_{\perp}\left(\mathbf{r}, s\right) = 0 \text{ for } s < 0 \,. \tag{2.24}$$

An example of a longitudinal wake potential of a Gaussian pulse inside a pillbox cavity is shown in Fig. 2.4.

## 2.3.2 The Panofsky–Wenzel Theorem

The Panofsky–Wenzel theorem connects the longitudinal and transverse wake potentials via

$$\mathbf{W}_{\perp}\left(x, y, s\right) = -\nabla_{\perp} \int\limits_{-\infty}^{s} W_{\|}\left(x, y, s'\right) \mathrm{d}s', \tag{2.25}$$

where $\nabla_{\perp}$ is the gradient operator relating only to transversal coordinates.

Therefore, in principle, knowledge of only the longitudinal component of the wake potential is enough, since the transverse component can be constructed from it.
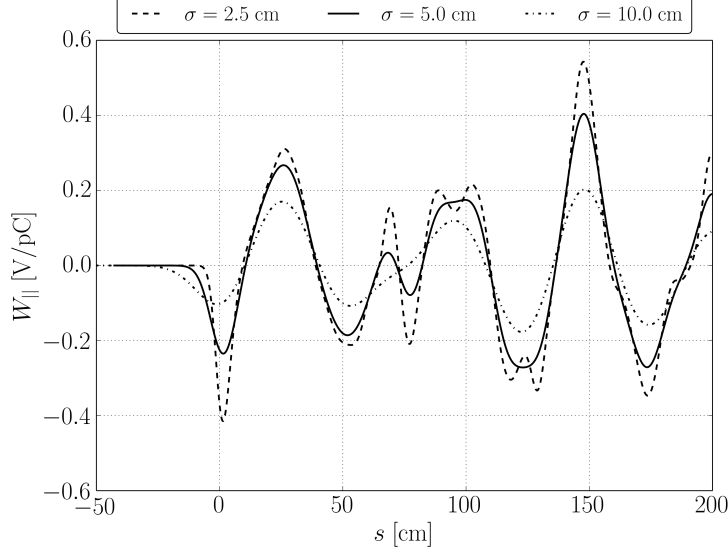
**Figure 2.4:** Longitudinal wake potentials of Gaussian pulses with different pulse width $\sigma$ inside the model pillbox cavity, computed using CST STUDIO SUITE ®[35].

In the following, the proof of this theorem is briefly sketched.

As a starting point, the transverse wake potential from eqn. (2.22) is chosen. Its derivative with respect to $s$ is

$$\frac{\partial}{\partial s}\mathbf{W}_\perp\left(\mathbf{r},s\right) = \frac{1}{q_1}\int_{-\infty}^{\infty}\left[\underbrace{\frac{\partial}{c\partial t}\mathbf{E}_\perp\left(\mathbf{r},z,t\right)}_{T_1} + \underbrace{\mathbf{e}_z\times\frac{\partial}{\partial t}\mathbf{B}_\perp\left(\mathbf{r},z,t\right)}_{T_2}\right]_{t=(z+s)/c}\mathrm{d}z\,,\quad(2.26)$$

where $s = c\,t - z$ and $\partial s = c\partial t$ have been used.

Now $T_1$ and $T_2$ are replaced with more convenient expressions. For term $T_1$, the total derivative of the transverse electric field with respect to $z$ is required. Using $s = c\,t - z$ this reads as

$$\frac{\mathrm{d}}{\mathrm{d}z}\mathbf{E}_\perp\left(\mathbf{r},z,\frac{z+s}{c}\right) = \left(\frac{\partial}{\partial z} + \frac{1}{c}\frac{\partial}{\partial t}\right)\mathbf{E}_\perp\left(\mathbf{r},z,\frac{z+s}{c}\right)\,,$$

where $\mathrm{d}/\mathrm{d}z$ is the total differential with respect to $z$. In equation (2.26), $T_1$ is reformulated as

$$\frac{1}{c}\frac{\partial}{\partial t}\mathbf{E}_\perp\left(\mathbf{r},z,\frac{z+s}{c}\right) = \left(\frac{\mathrm{d}}{\mathrm{d}z} - \frac{\partial}{\partial z}\right)\mathbf{E}_\perp\left(\mathbf{r},z,\frac{z+s}{c}\right)\,.\quad(2.27)$$

Considerations for term $T_2$ start with Faraday's law of induction,

$$\nabla\times\mathbf{E}\left(\mathbf{r},t\right) = -\frac{\partial}{\partial t}\mathbf{B}\left(\mathbf{r},t\right)\,.$$

Computing the cross product of this equation with the beam axis leads to

$$\mathbf{e}_z \times \frac{\partial}{\partial t} \mathbf{B}\left(\mathbf{r}, t\right) = -\mathbf{e}_z \times \left(\nabla \times \mathbf{E}\left(\mathbf{r}, t\right)\right) = \frac{\partial}{\partial z} \mathbf{E}_\perp \left(\mathbf{r}, t\right) - \nabla_\perp E_z \left(\mathbf{r}, t\right) . \qquad (2.28)$$

Inserting (2.27) and (2.28) into equation (2.26) results in

$$\frac{\partial}{\partial s} \mathbf{W}_\perp \left(\mathbf{r}, s\right) = \frac{1}{q_1} \int\limits_{-\infty}^{\infty} \left( \left( \frac{\mathrm{d}}{\mathrm{d}z} - \frac{\partial}{\partial z} \right) \mathbf{E}_\perp \left(\mathbf{r}, z, \frac{z+s}{c}\right) \right.$$
$$\left. + \left( \frac{\partial}{\partial z} \mathbf{E}_\perp \left(\mathbf{r}, z, \frac{z+s}{c}\right) - \nabla_\perp E_z \left(\mathbf{r}, z, \frac{z+s}{c}\right) \right) \right) \mathrm{d}z .$$

This is reformulated as

$$\frac{\partial}{\partial s} \mathbf{W}_\perp \left(\mathbf{r}, s\right) = \frac{1}{q_1} \int\limits_{-\infty}^{\infty} \frac{\mathrm{d}}{\mathrm{d}z} \mathbf{E}_\perp \left(\mathbf{r}, z, \frac{z+s}{c}\right) - \nabla_\perp E_z \left(\mathbf{r}, z, \frac{z+s}{c}\right) \mathrm{d}z .$$

At the waveguide walls, PEC boundary conditions are assumed so that the tangential electric field vanishes there. This simplifies equation (2.26) to

$$\frac{\partial}{\partial s} \mathbf{W}_\perp \left(\mathbf{r}, s\right) = -\frac{1}{q_1} \int\limits_{-\infty}^{\infty} \nabla_\perp \mathbf{E}_z \left(\mathbf{r}, z, \frac{z+s}{c}\right) \mathrm{d}z ,$$

which is equivalent to

$$\frac{\partial}{\partial s} \mathbf{W}_\perp \left(\mathbf{r}, s\right) = -\nabla_\perp W_\| \left(\mathbf{r}, s\right) .$$

Integrating the last statement over $s$ leads to equation (2.25).

## 2.3.3 The Fundamental Theorem of Beam Loading

This section follows the lines of [12].

Up to this point, the definition of wakefields only included cases with $s > 0$. For $s < 0$, it was concluded from the principle of causality that there can be no wakefield, and thus $\mathbf{W}\left(\mathbf{r}, s\right) = \mathbf{0}$.

The remaining case of $s = 0$ shall now be considered, which had been excluded before. For this, a different example situation will be considered first: two particles with equal charge $q$ and a distance of a half wavelength, $\lambda/2$, between them are moving along the same axis, at the same speed. The first charge enters a previously empty cavity with no internal electric fields or stored energy (see Fig. 2.5). The charge will induce surface charges, electric fields, and voltages in the cavity,

$$V_i = -\int_C \mathbf{E}\left(\mathbf{r}, t\right) \mathrm{d}\mathbf{l} ,$$
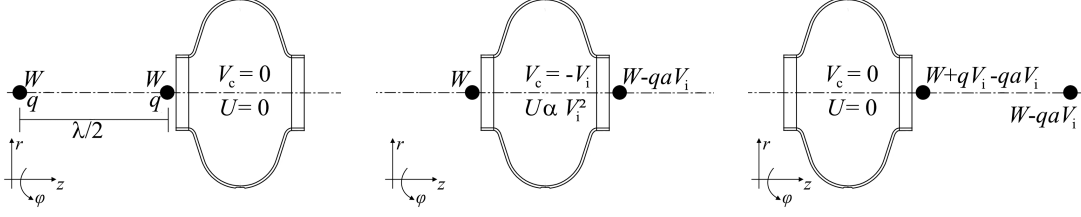
**Figure 2.5:** Left panel: Two charges separated by a distance $\lambda/2$ travelling along the same beam axis at the same speed are about to enter a previously empty elliptic cavity. Middle panel: The first charge has traversed the cavity and induced an image voltage of $-V_i$ in the cavity. Right panel: Both charges have left the cavity. The total energy change in the cavity is 0, while both charges have lost energy, owing to the image fields they experienced. From this, the proportionality factor $a$ can be calculated.

where the voltage is defined as a line integral over the electric field along a closed path $C$.

This induced voltage is referred to as $-V_i$. This induced voltage is left in the cavity, even after the first charge left. From the law of energy conservation, it can be infered that energy must be left behind in the cavity. However, the first charge will also 'see' a fraction $a$ of its own induced voltage while in the cavity,

$$V_1 = -aV_i \, .$$

This corresponds to an energy loss of the first particle,

$$\Delta W_1 = qV_1 = -qaV_i \, .$$

Thus, with the first particle in the cavity, the net cavity voltage is $V_c = -V_i$, while the stored energy $U$ will be proportional to this voltage squared, $U \propto V_i^2$. This situation is shown in the middle panel of Fig. 2.5.

When the second particle arrives in the cavity, the voltage induced by the first particle will have changed phase by $\pi$ owing to the distance between the two particles. Thus, the induced voltage from particle 1 is now $+V_i$. The second particle, however, will *also* induce a voltage in the cavity of $-V_i$. The net cavity voltage will be

$$V_c = +V_i - V_i = 0 \, .$$

Particle 2 will also lose energy according to

$$\Delta W_2 = \underbrace{qV_i}_{\text{from particle 1}} - \underbrace{qaV_i}_{\text{from own induced voltage}} \, .$$

Since the net energy of the cavity must remain 0, the energy changes of particle 1 and 2 have to compensate each other (see right panel of Fig. 2.5),

$$\Delta W_1 + \Delta W_2 = 0 \, ,$$
$$qV_i - qaV_i - qaV_i = 0 \, .$$

This leads directly to

$$a = \frac{1}{2}.$$

From this, the *fundamental theorem of beam loading* can directly be derived: a moving charge will experience (or 'see') half of its own induced voltage.

For the case of the wake potential, this implies that, for $s = 0$, when the field-generating and test charges are virtually at the same place, the wake potential must be multiplied by $1/2$. Thus, the final definition of the longitudinal wake potential is:

$$W_{\parallel}(\mathbf{r}, s) = \frac{1}{q_1} \int\limits_{-\infty}^{\infty} E_z\left(\mathbf{r}, z, \frac{z+s}{c}\right) \mathrm{d}z \begin{cases} 0 & \text{for } s < 0, \\ \frac{1}{2} & \text{for } s = 0, \\ 1 & \text{for } s > 0. \end{cases} \qquad (2.29)$$

## 2.4 The Eigenmodes of an Empty Rectangular Cavity

In the following section, the procedure for the determination of the eigenmodes of empty rectangular cavities shall be introduced. The clarification of this approach as well as concepts and terms connected to it will greatly help the derivation of the LSE and LSM modes in Chapter 3.2 and simplify the explanations made at this later point.

A sketch of the geometry of a rectangular cavity can be found in Fig. 2.6. The internal space of the cavity is supposed to consist of vacuum ($\varepsilon_r = 1$). PEC conditions are assumed on all boundaries. This gives rise to the condition that the tangential electric field and the normal magnetic field at these boundaries need to be zero. In Fig. 2.6, the PEC boundary in $z$-direction is omitted for reasons of easier comprehensibility.

### 2.4.1 The General Concept of Eigenmodes

The term 'eigenmode' describes a general concept that is not inherently and exclusively linked to electromagnetism, but present in many parts of physics. In fact, some of the more common and widely spread examples of eigenmodes originate from other fields, especially mechanics and atomic physics. Especially examples from the field of mechanics are also often more intuitive than examples of electromagnetic eigenmodes. Because of that, these examples shall be described shortly before returning to the actual subject of this thesis.

The probably most intuitive example are mechanical vibrations. A rope fixed on both ends and exposed to mechanical stress (e.g., via pulling it into one direction) will lead to vibrations, visible in harmonic displacements of the rope in form of a sinusoidal oscillation. Due to the fixation on both ends, this will in an idealised case
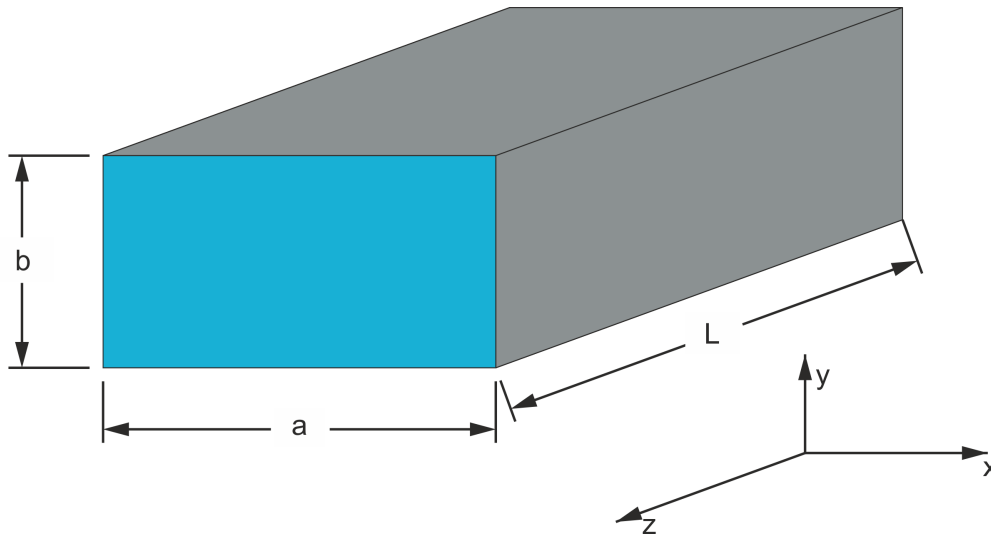
**Figure 2.6:** General sketch of the dimensions of a rectangular waveguide. For reasons of comprehensibility, the PEC walls in *z*-direction are omitted in the sketch, though they are present in the final model.

lead to a *standing wave* with a fixed frequency in contrast to a *travelling wave* in the case of no fixation[2]. Important is that an excitation of the system (pulling the rope) leads to an oscillation in which all parts of the system oscillate with the same frequency.

In an electromagnetic context, eigenmodes follow a similar concept. The term describes here distinct distributions of the electric and magnetic field inside a cavity or waveguide. These field patterns represent, just like in the mechanical case, standing waves with fixed frequencies, often referred to as *eigenfrequencies*. The boundaries provided in the case of vibrations by fixed ends are the terminating walls of the cavity or waveguide in this case, which impose certain conditions on the electric and magnetic field depending on their nature. Waveguides and cavities can be distinguished in so far as that cavities are limited by walls in all three spatial dimensions while waveguides are open in one dimension (most often the longitudinal direction). This leads to the differentiation between so-called 3D-eigenmodes in the case of cavities and 2D-eigenmodes in case of waveguides. This takes into account that for 3D-eigenmodes, the walls only allow for standing waves in all three spatial dimension, while in the case of 2D-eigenmodes, the typical patterns of the standing waves can only be exhibited in the two (transversal) directions which are limited by the walls of the structure, whereas the mode will behave like a travelling wave in the third direction.

---

[2]Exciting a travelling wave in the case of a rope with two fixed ends is still technically possible, though not considered here for the sake of simplicity in this more graphic explanation of waves and modes.

In general, for simple cavities without any form of dielectric linings it is distinguished between three types of eigenmodes: TE modes, TM modes and *T*ransversal *E*lectro-*M*agnetic (TEM) modes. For TE modes it is characteristic that their electric fields do not possess a longitudinal component, i.e. in $z$-direction in the most commonly used cases. TM modes, respectively, do not feature a magnetic field component in longitudinal direction. The third type, TEM modes, does not possess neither an electric nor a magnetic field component in longitudinal direction. Their occurrences, however, are limited to geometries in which two isolated conductors exist, such as in coaxial cables. Therefore, they play no role for the considerations in this work and will be omitted in the following.

Because they present such a basic principle in a wide variety of fields of physics, further and more detailed information on eigenmodes can be found in any textbook dealing with the foundations and general concepts of physics. As one example dealing with general physics, [76] shall be named here. More specific information about eigenmodes in the context of electromagnetism can, amongst others, be found in [64] or [77].

## 2.4.2 The Empty Rectangular Cavity

**Maxwell's Equations for the Empty Rectangular Cavity**

The following considerations are made with regard to the model presented in Fig. 2.6, assuming that its lower left corner of the front face is located at the origin.

If not directly excited and thus visible or measurable in an experiment, eigenmodes still exist as underlying mathematical concepts. Here, the eigenmodes of a cavity or waveguide are the intrinsic solutions to Maxwell's equations inside the structure without any further charge or current present ($\rho\left(\mathbf{r}, t\right) = 0, \mathbf{J}\left(\mathbf{r}, t\right) = \mathbf{0}$), assuming an isotropic material with $\mu = \mu_0$ and a harmonic time-dependence that results from the assumption that the structure is closed and lossless. This simplifies Maxwell's equations to

$$\nabla \cdot \underline{\mathbf{D}}\left(\mathbf{r}\right) = \varepsilon_0 \nabla \cdot \underline{\mathbf{E}}\left(\mathbf{r}\right) = 0, \tag{2.30}$$

$$\nabla \cdot \underline{\mathbf{B}}\left(\mathbf{r}\right) = 0, \tag{2.31}$$

$$\nabla \times \underline{\mathbf{E}}\left(\mathbf{r}\right) = j\omega\underline{\mathbf{B}}\left(\mathbf{r}\right), \tag{2.32}$$

$$\nabla \times \underline{\mathbf{B}}\left(\mathbf{r}\right) = -j\frac{\omega}{c_0^2}\underline{\mathbf{E}}\left(\mathbf{r}\right), \tag{2.33}$$

with $\omega$ representing the angular frequency of the mode, and the underlined quantities indicating phasors. Both TE and TM modes represent solutions to this specific set of Maxwell's equations under PEC boundary conditions. It is easier to derive their expressions separately due to the different requirements concerning the $z$-components of their respective electric and magnetic fields.

The PEC boundary conditions for the phasors of the electric fields and magnetic flux densities read

$$\underline{E}_x \left( \mathbf{r} \right) = 0 \text{ for } y = 0, b \text{ and } z = 0, L, \tag{2.34}$$

$$\underline{E}_y \left( \mathbf{r} \right) = 0 \text{ for } x = 0, a \text{ and } z = 0, L, \tag{2.35}$$

$$\underline{E}_z \left( \mathbf{r} \right) = 0 \text{ for } x = 0, a \text{ and } y = 0, b \text{ and} \tag{2.36}$$

$$\underline{B}_x \left( \mathbf{r} \right) = 0 \text{ for } x = 0, a, \tag{2.37}$$

$$\underline{B}_y \left( \mathbf{r} \right) = 0 \text{ for } y = 0, b, \tag{2.38}$$

$$\underline{B}_z \left( \mathbf{r} \right) = 0 \text{ for } z = 0, L. \tag{2.39}$$

**Solution Procedure for TM Modes**

Due to Gauss's Law for Magnetism (2.31), the magnetic flux density of a TM mode can generally be expressed as the curl of a suited potential $\mathbf{\Pi}_{\text{TM}} \left( \mathbf{r} \right)$,

$$\underline{\mathbf{B}}_{\text{TM}} \left( \mathbf{r} \right) = \nabla \times \mathbf{\Pi}_{\text{TM}} \left( \mathbf{r} \right). \tag{2.40}$$

This automatically fulfils (2.31), since the divergence of a curl is always zero.

In the specific case of TM modes, the magnetic flux density has no longitudinal component, $\underline{B}_{\text{TM},z} \left( \mathbf{r} \right) = 0$. In this case, it is efficient to choose the potential $\mathbf{\Pi}_{\text{TM}}$ parallel to the $z$-axis,

$$\mathbf{\Pi}_{\text{TM}} \left( \mathbf{r} \right) = A_{\text{TM}} \psi_{\text{TM}} \left( \mathbf{r} \right) \mathbf{e}_z. \tag{2.41}$$

Here, $A_{\text{TM}}$ is a normalisation factor and $\psi_{\text{TM}} \left( \mathbf{r} \right)$ is a scalar source function.

More specifically, the components of the electric fields and magnetic flux densities can now be defined with regard to the source function $\psi_{\text{TM}} \left( \mathbf{r} \right)$. Using equation (2.41) and plugging it into eqn. (2.40) yields the magnetic flux density

$$\underline{\mathbf{B}}_{\text{TM}} \left( \mathbf{r} \right) = A_{\text{TM}} \begin{pmatrix} \partial_x \\ \partial_y \\ \partial_z \end{pmatrix} \times \begin{pmatrix} 0 \\ 0 \\ \psi_{\text{TM}(\mathbf{r})} \end{pmatrix} = A_{\text{TM}} \begin{pmatrix} \partial_y \psi_{\text{TM}} \left( \mathbf{r} \right) \\ -\partial_x \psi_{\text{TM}} \left( \mathbf{r} \right) \\ 0 \end{pmatrix}, \tag{2.42}$$

where $\partial_i$ are the shortened notations for the partial derivates $\partial/\partial i$ with respect to the variable $i = x, y, z$.

The electric field can now be obtained using the upper equation and inserting it into (2.33),

$$\underline{\mathbf{E}}_{\text{TM}} \left( \mathbf{r} \right) = j \frac{c_0^2}{\omega} \nabla \times \underline{\mathbf{B}}_{\text{TM}} \left( \mathbf{r} \right) = j A_{\text{TM}} \frac{c_0^2}{\omega} \begin{pmatrix} \partial_x \partial_z \psi_{\text{TM}} \left( \mathbf{r} \right) \\ \partial_y \partial_z \psi_{\text{TM}} \left( \mathbf{r} \right) \\ -\left( \partial_x^2 + \partial_y^2 \right) \psi_{\text{TM}} \left( \mathbf{r} \right) \end{pmatrix}. \tag{2.43}$$

From comparing eqn. (2.40) to eqn. (2.32) it can be inferred that the electric field and the potential have to be proportional to one another apart from the gradient of an arbitrary scalar function $\phi_{\text{TM}} \left( \mathbf{r} \right)$,

$$\underline{\mathbf{E}}_{\text{TM}} \left( \mathbf{r} \right) = j\omega \mathbf{\Pi}_{\text{TM}} \left( \mathbf{r} \right) + \nabla \phi_{\text{TM}} \left( \mathbf{r} \right). \tag{2.44}$$

For the continuation of the solutions of Maxwell's equations inside the rectangular cavity, the eqs. (2.40) and (2.44) are now inserted into eqn. (2.33), resulting in

$$\nabla \times \left( \nabla \times \mathbf{\Pi}_{\mathrm{TM}} \left( \mathbf{r} \right) \right) = \underbrace{\frac{\omega^2}{c_0^2}}_{k_0^2} \mathbf{\Pi}_{\mathrm{TM}} \left( \mathbf{r} \right) - j \frac{\omega}{c_0^2} \nabla \phi_{\mathrm{TM}} \left( \mathbf{r} \right).$$

Using identity (2.12), the term on the left hand side can be reformulated. The up until now undefined but arbitrary scalar potential $\phi_{\mathrm{TM}}$ can then be specified using the gauge $\phi_{\mathrm{TM}} \left( \mathbf{r} \right) = j \frac{c_0^2}{\omega} \nabla \cdot \mathbf{\Pi}_{\mathrm{TM}} \left( \mathbf{r} \right)$. With this, two parts of the resulting equation will eliminate each other. The remaining parts constitute the Helmholtz equation for TM modes,

$$\nabla^2 \mathbf{\Pi}_{\mathrm{TM}} \left( \mathbf{r} \right) + k_0^2 \mathbf{\Pi}_{\mathrm{TM}} \left( \mathbf{r} \right) = \mathbf{0}. \tag{2.45}$$

With the definition used here, the potential $\mathbf{\Pi}_{\mathrm{TM}}$ is referred to as an electric Hertzian potential [64][3].

Since $\nabla^2$ is a scalar operator and $\mathbf{\Pi}_{\mathrm{TM}}$ only constitutes of a $z$-component, the Helmholtz equation can be rewritten in terms of the source function $\psi_{\mathrm{TM}}$. Assuming a non-trivial solution with $A_{\mathrm{TM}} \neq 0$, this leads to

$$\frac{\partial^2}{\partial x^2} \psi_{\mathrm{TM}} \left( \mathbf{r} \right) + \frac{\partial^2}{\partial y^2} \psi_{\mathrm{TM}} \left( \mathbf{r} \right) + \frac{\partial^2}{\partial z^2} \psi_{\mathrm{TM}} \left( \mathbf{r} \right) + k_0^2 \psi_{\mathrm{TM}} = 0, \tag{2.46}$$

where $\nabla^2$ has been split into its components.

To solve equation (2.46) further, the separation approach is used. For this, it is assumed that

$$\psi_{\mathrm{TM}} \left( x, y, z \right) = P \left( x \right) Q \left( y \right) R \left( z \right). \tag{2.47}$$

Plugging this ansatz into equation (2.46), excluding any of the trivial cases in which $\psi_{\mathrm{TM}} = 0$ and dividing by $\psi_{\mathrm{TM}}$, this leads to

$$\frac{1}{P \left( x \right)} \frac{\mathrm{d}^2}{\mathrm{d} x^2} P \left( x \right) + \frac{1}{Q \left( y \right)} \frac{\mathrm{d}^2}{\mathrm{d} y^2} Q \left( y \right) + \frac{1}{R \left( z \right)} \frac{\mathrm{d}^2}{\mathrm{d} z^2} R \left( z \right) + k_0^2 = 0.$$

If the squared wavenumber $k_0^2$ is now also split according to $k_0^2 = k_x^2 + k_y^2 + k_z^2$, this partial differential equation can be separated into three ordinary differential equations,

$$\frac{\mathrm{d}^2}{\mathrm{d} x^2} P \left( x \right) + k_x^2 P \left( x \right) = 0, \tag{2.48}$$

$$\frac{\mathrm{d}^2}{\mathrm{d} y^2} Q \left( y \right) + k_y^2 Q \left( y \right) = 0, \tag{2.49}$$

$$\frac{\mathrm{d}^2}{\mathrm{d} z^2} R \left( z \right) + k_z^2 R \left( z \right) = 0, \tag{2.50}$$

---

[3]In a source-free region with $\mu_r = 1$ and $\varepsilon_r \neq 1$, the right hand side of the Helmholtz equation will yield the dielectric polarization. For a detailed explanation of the terminology, see [64].

which can readily be solved employing PEC boundary conditions.

If the electric field has the form presented in equation (2.43), the function $P(x)$ has to comply with the requirement $P(x = 0, a) = 0$ to fulfil the boundary condition (2.35). From the set of general solutions that obey the symmetry of eqn. (2.48), the function that fulfils this condition is the sine, so that

$$P(x) = \sin(k_x x).$$

The eigenvalue $k_x$ can also be specified using the boundary conditions, since

$$P(x = a) = \sin(k_x a) = 0$$

requires $k_x a$ to be any positive integer multiple of $\pi$. With this, the solution to equation (2.48) can be written down as

$$P(x) = \sin\left(\frac{n\pi}{a}x\right) \text{ with } n = 1, 2, 3..., \tag{2.51}$$

and $k_x = n\pi/a$.

An equivalent line of argument can be made for $Q(y)$, leading to

$$Q(y) = \sin\left(\frac{m\pi}{b}y\right) \text{ with } m = 1, 2, 3..., \tag{2.52}$$

and $k_y = m\pi/b$.

For $R(z)$, the conditions (2.34) and (2.35) combined with equation (2.43) lead to the requirement

$$\left.\frac{\mathrm{d}}{\mathrm{d}z}R(z)\right|_{z=0,L} = 0.$$

This is fulfilled if

$$R(z) = \cos\left(\frac{l\pi}{L}y\right) \text{ with } l = 0, 1, 2, 3..., \tag{2.53}$$

and $k_z = l\pi/L$.

With this, the scalar source function of the Hertzian potential can be defined as

$$\psi_{\mathrm{TM}}(x, y, z) = \sin(k_x x)\sin(k_y y)\cos(k_z z). \tag{2.54}$$

The electric and magnetic field distributions can now be specified using equation (2.42) and (2.43). The angular eigenfrequency $\omega$ relates to the wavenumber according to

$$\omega = c_0 k_0 = c_0\sqrt{k_x^2 + k_y^2 + k_z^2}. \tag{2.55}$$

**Solution Procedure for TE Modes**

A similar approach is used to determine the field distributions of the electric fields and magnetic flux densities of TE modes.

Here, it is exploited that due to Gauss' Law in the cavity (2.30), the electric field can be expressed via

$$\underline{\mathbf{E}}_{\text{TE}}(\mathbf{r}) = \nabla \times \mathbf{\Pi}_{\text{TE}}(\mathbf{r}). \tag{2.56}$$

Here, the magnetic Hertzian potential[4],

$$\mathbf{\Pi}_{\text{TE}}(\mathbf{r}) = A_{\text{TE}}\psi_{\text{TE}}(\mathbf{r})\,\mathbf{e}_z, \tag{2.57}$$

is also chosen to be parallel to the $z$-axis such that the $z$-component of the electric field automatically vanishes. The quantities $A_{\text{TE}}$ and $\psi_{\text{TE}}(\mathbf{r})$ are a normalisation constant and the scalar source function of the Hertzian potential, respectively.

With this definition, the components of the electric field can be specified with respect to the source function as

$$\underline{\mathbf{E}}_{\text{TE}}(\mathbf{r}) = A_{\text{TE}} \begin{pmatrix} \partial_x \\ \partial_y \\ \partial_z \end{pmatrix} \times \begin{pmatrix} 0 \\ 0 \\ \psi_{\text{TE}}(\mathbf{r}) \end{pmatrix} = A_{\text{TE}} \begin{pmatrix} \partial_y\psi_{\text{TE}}(\mathbf{r}) \\ -\partial_x\psi_{\text{TE}}(\mathbf{r}) \\ 0 \end{pmatrix}. \tag{2.58}$$

This can be inserted into equation (2.32), yielding a more specific expression for the magnetic flux density,

$$\underline{\mathbf{B}}_{\text{TE}}(\mathbf{r}) = -j\frac{1}{\omega}\nabla \times \underline{\mathbf{E}}_{\text{TE}}(\mathbf{r}) = -jA_{\text{TE}}\frac{1}{\omega} \begin{pmatrix} \partial_x\partial_z\psi_{\text{TE}}(\mathbf{r}) \\ \partial_y\partial_z\psi_{\text{TE}}(\mathbf{r}) \\ -\left(\partial_x^2 + \partial_y^2\right)\psi_{\text{TE}}(\mathbf{r}) \end{pmatrix}. \tag{2.59}$$

The Helmholtz equation for TE modes is derived in a similar manner as before for the TM modes. At first, a relation between the Hertzian potential and the magnetic flux density is determined using equation (2.33), where both sides compared lead to

$$\underline{\mathbf{B}}_{\text{TE}}(\mathbf{r}) = -j\frac{\omega}{c_0^2}\mathbf{\Pi}_{\text{TE}}(\mathbf{r}) + \nabla\phi_{\text{TE}}(\mathbf{r}), \tag{2.60}$$

where $\phi_{\text{TE}}(\mathbf{r})$ is an arbitrary scalar function.

The equations (2.60) and (2.56) are now inserted into eqn. (2.32) and the left hand side is transformed using vector algebra analogously like in the case of TM modes. At this point, the gauge $\phi_{\text{TE}}(\mathbf{r}) = -j/\omega\nabla \cdot \mathbf{\Pi}_{\text{TE}}(\mathbf{r})$ is chosen. The resulting Helmholtz equation for TE modes is

$$\nabla^2\mathbf{\Pi}_{\text{TE}}(\mathbf{r}) + k_0^2\mathbf{\Pi}_{\text{TE}}(\mathbf{r}) = \mathbf{0}. \tag{2.61}$$

---

[4]In a source-free region with $\mu_r \neq 1$ and $\varepsilon_r = 1$, the right hand side of the resulting Helmholtz equation for TE modes will yield the magnetisation. For a more detailed explanation of the terminology, see [64].

Using the definition of the Hertzian potential in equation (2.57), this automatically leads to the partial differential equation for $\psi_\mathrm{TE}$ analogous to eqn. (2.46). The separation approach (2.47) is used again, and following the same steps and arguments made in the previous section on TM modes, the three ordinary differential equations (2.48), (2.49) and (2.50) are once more the result of the transformation of the Helmholtz equation.

However, the PEC boundaries impose different conditions on the functions $P(x)$, $Q(y)$ and $R(z)$. Combining the requirements given in the equations (2.34) and (2.35) with the definitions in (2.58) it can be deduced that the following conditions need to be met by the three separated functions,

$$\frac{\mathrm{d}}{\mathrm{d}x}P(x)\bigg|_{x=0,a}=0,$$

$$\frac{\mathrm{d}}{\mathrm{d}y}Q(y)\bigg|_{y=0,b}=0,$$

$$R(z=0,L)=0.$$

With these conditions, the solution of the equations (2.48), (2.49) and (2.50) for the case of TE modes can be written down as

$$P(x)=\cos\left(\frac{n\pi}{a}y\right) \text{ with } n=0,1,2,3..., \tag{2.62}$$

$$Q(y)=\cos\left(\frac{m\pi}{b}y\right) \text{ with } m=0,1,2,3..., \tag{2.63}$$

$$R(z)=\sin\left(\frac{l\pi}{L}y\right) \text{ with } l=1,2,3.... \tag{2.64}$$

Therefore, the source function of the Hertzian potential reads

$$\psi_\mathrm{TE}(x,y,z)=\cos(k_x x)\cos(k_y y)\sin(k_z z). \tag{2.65}$$

Inserting this into eqn. (2.58) and eqn. (2.32) yields the expression for the electric and magnetic field distributions of TE modes. The eigenfrequency of a TE mode is $\omega=c_0\sqrt{k_x^2+k_y^2+k_z^2}$, analogous to the eigenfrequencies of TM modes.

### Normalisation

Up until now, the electric fields and magnetic flux densities of both mode types have not been normalised, i.e., the factors $A_\mathrm{TM}$ and $A_\mathrm{TE}$ are still undefined.

Generally, determining these factors will not change the behaviours of the field distributions, only their amplitudes. Most often, the modes are normalised to the energy stored in the mode, i.e.

$$U=\frac{1}{2}\iiint\limits_V \left(\varepsilon_0 \left|\underline{\mathbf{E}}(\mathbf{r})\right|^2 + \frac{1}{\mu_0}\left|\underline{\mathbf{B}}(\mathbf{r})\right|^2\right)\mathrm{d}z\mathrm{d}y\mathrm{d}x.$$

Solving this integral for both TE and TM modes and transforming the result in dependency of the unknown factors will lead to expressions for the normalisation constants in dependence of the energy. Most commonly, the energy stored in the mode is then set to $U = 1\,\mathrm{J}$ and the normalisation constants are defined further. Theoretically, other normalisation like a normalisation to a field amplitude of one are also conceivable. In praxis, however, they are seldom used.

### 2.4.3 Eigenmode Expansions

For later applications, it shall be noted here that one significant advantage of knowing the eigenmodes of a structure is that they form a complete, orthogonal set of basis functions. This means that the electric and magnetic field inside the observed structures can be expanded in a series of eigenmodes even in the presence of charges and currents. This allows for a solution strategy to Maxwell's equations even in cases in which it would usually be complicated or impossible to solve them. Additionally, the analytic expressions of eigenmodes are often known, which at least allows for the derivation of an analytic expression of the fields.

On the other hand, the description of fields via an expansion into the eigenmodes of the structure is in all practical cases an approximation. Eigenmode expansions, as a form of regular series expansions like the Fourier- or Taylor-series, are only analytically correct and accurate if infinitely many expansion functions are used, given that the expansion converges. If the series is terminated after a finite number of terms, which is always the case in a practical scenario, the expression becomes a mere approximation of the accurate results.

# 3 The Analytical Model

The foundation of all considerations regarding rectangular dechirpers lined with dielectrics in this work is a completely analytical model for the wake function inside these waveguides. In this chapter, the derivation of the analytical description of the eigenmodes of these structures is presented. Subsequently, these expressions are then used to derive the electric field of a point charge moving through the guide. From this, an approximation-free analytical model for the wake function is deduced.

The derivations presented in this chapter have also been submitted for publication in [78], and have been presented in a similar fashion in [3].

## 3.1 Dielectrically Lined Rectangular Waveguides

A general layout of a dielectrically lined rectangular waveguide is shown in Fig. 3.1. The guide itself is composed of a highly conductive material, e.g. copper or aluminium, and is lined symmetrically with two identical dielectric slabs at the top and bottom of the guide. Theoretically, the only requirement on the slabs is that their relative permittivity is larger than one; while practically the chosen materials must be suitable for the use in vacuum as well. The particle beam, here electrons, passes the structure right through its centre.
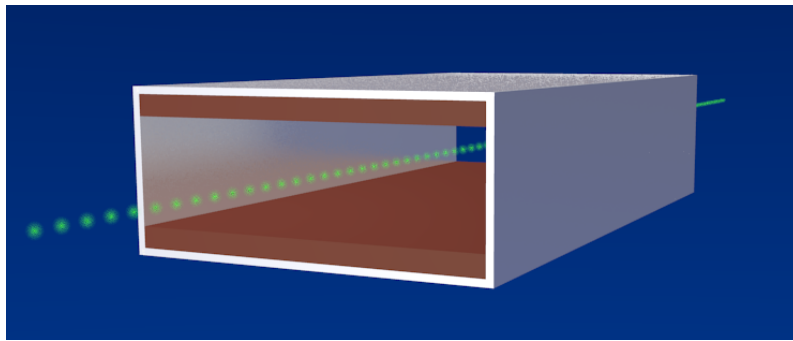


**Figure 3.1:** General layout of a dielectrically lined rectangular waveguide used for passive wakefield dechirping. The electron beam is indicated in green.

Compared to cylindrical waveguides, a rectangular structure has the advantage of a higher flexibility: while the radius of the cylinder is a quantity that cannot be adjusted once the structure is in production, a rectangular layout still allows for a later tuning. To achieve this, the waveguide is build in a way so that the

upper conducting plate with the corresponding dielectric is left unconnected to the remaining guide and is thus movable. This allows for an adjustment of the gap widths between the dielectric plates after production. Consequently, this also allows for an adjustment of the wakefield.

For the use at ELBE, an adjustable structure like the one described in Fig. 3.1 was constructed. The outer aluminium guide has a total length of 80 cm with an adjustable gap width in the range of $0.5 - 3.5$ cm. The dielectric plates will consist of the glass ceramic MACOR[1], with a thickness of 3.0 mm and a relative permittivity of 6.0. MACOR is suited for the use in ultra-high vacuum and comparatively easy and cheap to acquire. This makes the material ideal for feasibility studies.

Next to these technical advantages, the rectangular dielectrically lined dechirper opens up the possibility of an analytic examination of the wakefield due to its geometric simplicity. From a mathematical point of view, the insertion of dielectric slabs into the otherwise textbook example of the open, rectangular waveguide, presents a comparatively minor change in geometry. This similarity is used for an analytic determination of the eigenmodes of the structure. These eigenmodes can be used as basic functions for an expansion of the electric field generated by a single point charge inside such a waveguide. Calculating the longitudinal wakefield from the electric field leads to the possibility of gaining an analytical Green's function in form of the point charge wakefield. This can then be used to determine the wakefield of a variety of differently shaped bunches by means of simple convolutions, instead of performing a complete numerical simulation for every shape.

In total, the geometric simplicity of the structure provides the possibility of gaining a fundamental insight in the dechirping qualities of the chosen layout, which should not be left unexploited.

## 3.2 Eigenmode Calculations

### 3.2.1 The General Model

For all following analytic calculations, the model shown in Fig. 3.2 is used to represent the dielectrically lined rectangular waveguide. The guide is considered to be composed entirely of PEC with a length $L$, width $a$ and height $b$. The thickness of the walls is irrelevant. The dielectric slabs have a thickness of $b - d$ (where $d$ gives the height of the lower edge of the upper dielectric) and a relative permittivity of $\varepsilon_r > 1$, which is not further specified at this point to grant a maximum adaptability of the model. The material between the dielectric slabs is considered to be vacuum.

It shall be noted here that, for calculation purposes, the model is *completely* enclosed in PEC. This, on the first glance, seems to be in conflict with the beam indi-

---

[1]The name, most likely, comes from the term '*ma*chineable glass-ceramic' and their initial distributor, the company *Cor*ning Inc.

cated in Fig. 3.1, because the beam requires the structure to be open in $z$-direction. Yet, a mathematical model of an open dechirper requires the assumption that the structure is infinitely long. The actual length of the dechirper is not fixed at this point and might not differ from the other dimensions of the structure in a way that justifies assuming it is, in fact, infinite compared to, e.g., the gap width, which would render the whole assumption already a strong approximation. Additionally, a closer inspection shows that wakefields in an open waveguide can be expanded in a series of eigenmodes of the closed waveguide, see Chapter 3.5.
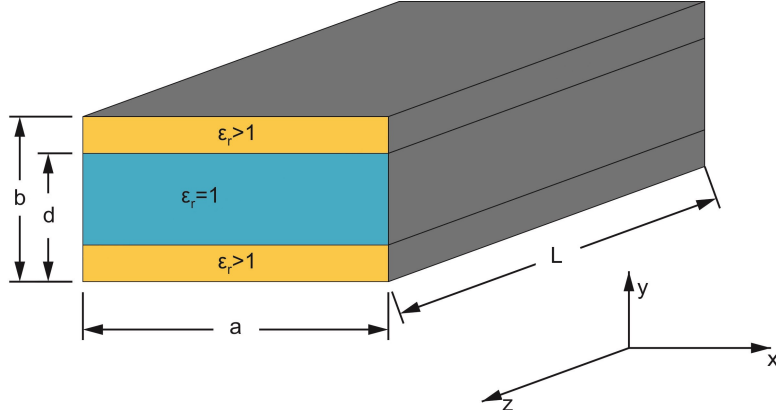


**Figure 3.2:** General sketch of the dimensions of a dielectrically lined rectangular waveguide. For reasons of comprehensibility, the PEC walls in $z$-direction are omitted in the sketch, though they are present in the final model.

Figure 3.2 shows that the only difference to the textbook problem of the rectangular waveguide without slabs is the change in permittivity in $y$-direction. In $x$- and $z$-direction the permittivity stays constant, while in $y$-direction it changes according to

$$\varepsilon_r(y) = \begin{cases} \varepsilon_r, & 0 < y \leq b - d \\ 1, & b - d < y < d \\ \varepsilon_r, & d < y \leq b \end{cases} . \tag{3.1}$$

First of all, Maxwell's equations have to account for the $y$-dependency of the permittivity:

$$\nabla \cdot \mathbf{D}(\mathbf{r}, t) = \varepsilon_0 \nabla \cdot (\varepsilon_r(y)\mathbf{E}(\mathbf{r}, t)) = \rho(\mathbf{r}, t), \tag{3.2}$$

$$\nabla \cdot \mathbf{B}(\mathbf{r}, t) = 0, \tag{3.3}$$

$$\nabla \times \mathbf{E}(\mathbf{r}, t) = -\frac{\partial}{\partial t}\mathbf{B}(\mathbf{r}, t), \tag{3.4}$$

$$\nabla \times \mathbf{B}(\mathbf{r}, t) = \mu_0 \mathbf{J}(\mathbf{r}, t) + \mu_0 \varepsilon_r(y)\varepsilon_0 \frac{\partial}{\partial t}\mathbf{E}(\mathbf{r}, t). \tag{3.5}$$

Consequently, this leads to the speed of light also being $y$-dependent, $c(y)^2 = (\varepsilon_0 \varepsilon_r(y)\mu_0)^{-1} = c_0^2 \varepsilon_r(y)^{-1}$, with $c_0$ representing the speed of light in vacuum.

## 3.2.2 The Eigenmodes of Lined Waveguides

The presence of the dielectric slabs causes that the eigenmodes of the lined waveguide are not simply TE or TM modes. Instead, the set of eigenmodes inside the lined waveguide needs to account for the changing permittivity in $y$-direction.

The eigenmodes of general rectangular waveguides lined with dielectric slabs (not just specifically in the form shown in Fig. 3.2) are introduced in [64] as LSE and LSM modes (c.f. also [79]). These two types are characterised by the lack of an electric field component in the direction of the change of the permittivity (for LSE modes) and the lack of a magnetic field component in this direction (for LSM modes), respectively. In the special case depicted in Fig. 3.2, this means $E_y = 0$ for LSE modes, and $B_y = 0$ for LSM modes.

The general process of calculating these modes is also shown in [64], however, only for a structure loaded with just one dielectric slab and also only in two dimensions. It shall be expanded upon here. Following the derivation in [64], the calculation of the eigenmodes for the structure in Fig. 3.2 is shown in the next sections.

### Maxwell's Equations

As presented in Section 2.4, for eigenmode calculations a structure with no external charges or currents ($\rho(\mathbf{r}, t) = 0, \mathbf{J}(\mathbf{r}, t) = \mathbf{0}$) and a harmonic time-dependence of the fields are assumed. However, in this specific case, the $y$-dependence of the relative permittivity needs to be taken into account. This changes Maxwell's equations to

$$\nabla \cdot \underline{\mathbf{D}}(\mathbf{r}) = \varepsilon_0 \nabla \cdot (\varepsilon_r(y)\underline{\mathbf{E}}(\mathbf{r})) = 0, \tag{3.6}$$

$$\nabla \cdot \underline{\mathbf{B}}(\mathbf{r}) = 0, \tag{3.7}$$

$$\nabla \times \underline{\mathbf{E}}(\mathbf{r}) = j\omega\underline{\mathbf{B}}(\mathbf{r}), \tag{3.8}$$

$$\nabla \times \underline{\mathbf{B}}(\mathbf{r}) = -j\frac{\omega}{c_0^2}\varepsilon_r(y)\underline{\mathbf{E}}(\mathbf{r}). \tag{3.9}$$

Again, according to the model presented in Fig. 3.2, the structure is limited by PEC boundary conditions in all three coordinate directions.

For the application in a subsequent chapter, the curl-curl equation of the electric field is generated and reformulated to create a general, Helmholtz-like equation. Therefore, eqn. (3.9) is inserted into the curl of eqn. (3.8) yielding

$$\nabla \times \nabla \times \underline{\mathbf{E}}(\mathbf{r}) = \underbrace{\frac{\omega^2}{c_0^2}}_{k_0^2} \varepsilon_r(y)\underline{\mathbf{E}}(\mathbf{r})$$

with $k_0$ representing the wavenumber in vacuum.

It can be deduced from eqn. (3.6) that $\nabla \cdot \underline{\mathbf{E}}(\mathbf{r}) = -\varepsilon_r^{-1}(y)\underline{\mathbf{E}}(\mathbf{r})\nabla\varepsilon_r(y)$, which is then inserted in the upper equation.

The final result for the general equation then reads:

$$\nabla^2 \underline{\mathbf{E}}\left(\mathbf{r}\right) = -k_0^2 \varepsilon_r \underline{\mathbf{E}}\left(\mathbf{r}\right) - \nabla \cdot \left( \frac{1}{\varepsilon_r(y)} \underline{\mathbf{E}}\left(\mathbf{r}\right) \nabla \varepsilon_r(y) \right). \tag{3.10}$$

**LSM Modes**

From the fact that $\underline{B}_{\mu,y}\left(\mathbf{r}\right) = 0$ for LSM modes (indexed with $\mu$) it can be deduced that the magnetic field can be described as the curl of a vector purely oriented in $y$-direction,

$$\underline{\mathbf{B}}_\mu\left(\mathbf{r}\right) = -\frac{\omega}{c_0^2} \nabla \times \mathbf{\Pi}_\mu\left(\mathbf{r}\right), \tag{3.11}$$

where $\mathbf{\Pi}_\mu\left(\mathbf{r}\right) = A_\mu \psi_\mu\left(\mathbf{r}\right) \mathbf{e}_y$ is a so-called Hertzian potential (c.f. Section 2.4), $\psi_\mu\left(\mathbf{r}\right)$ a scalar source function and $A_\mu$ is a normalisation constant. It shall be noted here that the prefactor is chosen purely for convenience; the final fields would usually be normalised anyway so that the factor here plays no role.

The introduction of this potential brings along the advantage that the problem of solving Maxwell's equations for six components (three from each the electric and the magnetic field, respectively) can be reduced to solving a Helmholtz-like equation for the Hertzian potential, so for just one component. Both magnetic field, and in turn, the electric field, can be deduced from $\mathbf{\Pi}_\mu\left(\mathbf{r}\right)$. Using eqn. (3.8), the electric field can be determined as

$$\nabla \times \underline{\mathbf{E}}_\mu\left(\mathbf{r}\right) = j\omega \underline{\mathbf{B}}_\mu\left(\mathbf{r}\right) = k_0^2 \nabla \times \mathbf{\Pi}_\mu\left(\mathbf{r}\right),$$

and is, thus, up to the gradient of a scalar function $\Phi_\mu\left(\mathbf{r}\right)$, proportional to the Hertzian potential,

$$\underline{\mathbf{E}}_\mu\left(\mathbf{r}\right) = k_{0,\mu}^2 \mathbf{\Pi}_\mu\left(\mathbf{r}\right) + \nabla \Phi_\mu\left(\mathbf{r}\right). \tag{3.12}$$

The Helmholtz-like equation for the Hertzian potential can now be derived from eqn. (3.9) by inserting eqs. (3.11) and (3.12):

$$\nabla \times \underline{\mathbf{B}}_\mu\left(\mathbf{r}\right) = -j\frac{\omega}{c_0^2} \nabla \times \nabla \times \mathbf{\Pi}_\mu\left(\mathbf{r}\right) = -j\frac{\omega}{c_0^2} \varepsilon_r(y) \underline{\mathbf{B}}_\mu\left(\mathbf{r}\right)$$

$$\nabla \times \nabla \times \mathbf{\Pi}_\mu\left(\mathbf{r}\right) = \varepsilon_r(y) k_{0,\mu}^2 \mathbf{\Pi}_\mu\left(\mathbf{r}\right) + \nabla \varepsilon_r(y) \Phi_\mu\left(\mathbf{r}\right) - \Phi_\mu\left(\mathbf{r}\right) \nabla \varepsilon_r(y).$$

At this point, further specifications are made by choosing a suitable gauge for the up to now arbitrary function $\Phi_\mu\left(\mathbf{r}\right)$. The gauge $\nabla \varepsilon_r(y) \Phi_\mu\left(\mathbf{r}\right) = \nabla\left(\nabla \cdot \mathbf{\Pi}_\mu\left(\mathbf{r}\right)\right) \rightarrow$ $\Phi_\mu\left(\mathbf{r}\right) = \varepsilon_r^{-1}(y) \nabla \cdot \mathbf{\Pi}_\mu\left(\mathbf{r}\right)$ is used, and with it the upper equation simplifies to the final version of the Helmholtz-like basic equation:

$$\mathbf{0} = \nabla^2 \mathbf{\Pi}_\mu\left(\mathbf{r}\right) + \varepsilon_r(y) k_{0,\mu}^2 \mathbf{\Pi}_\mu\left(\mathbf{r}\right) - \varepsilon_r^{-1}(y) \nabla \cdot \mathbf{\Pi}_\mu\left(\mathbf{r}\right) \nabla \varepsilon_r(y). \tag{3.13}$$

With the chosen gauge, the electric field representation in eqn. (3.12) can be simplified into

$$\underline{\mathbf{E}}_\mu\left(\mathbf{r}\right) = \varepsilon_r(y) \nabla \times \nabla \times \mathbf{\Pi}_\mu\left(\mathbf{r}\right). \tag{3.14}$$

To determine the Hertzian potential, the product ansatz is used for the source function $\psi_\mu(\mathbf{r}) = P(x)Q_\mu(y)R(z)$, comparable to the case of the empty waveguide in Section 2.4. Employing PEC boundary conditions in $x$- and $z$-direction leads directly to $P(x) = \sin(k_x x)$ and $R(z) = \sin(k_z z)$, with $k_x = n\pi/x$, $k_z = l\pi/L$ and $n, l = 0, 1, 2...$. Thus, the Hertzian potential reads now

$$\mathbf{\Pi}_\mu(\mathbf{r}) = A_\mu \sin(k_x x) \sin(k_z z) Q_\mu(y) \mathbf{e}_y.$$

Note that this behaviour can only be justified because in $x$- and $z$-direction, the structure is comparable to a regular, empty rectangular waveguide. In $y$-direction, there is the change in the permittivity that affects $Q_\mu(y)$, making it impossible to determine this function straight away.

Instead, the ansatz for the Hertzian potential is now inserted into the Helmholtz-like equation (3.13). Because $\mathbf{\Pi}_\mu(\mathbf{r})$ is proportional to $\mathbf{e}_y$, it is sufficient to look at the $y$-component:

$$0 = \underbrace{\frac{\partial^2}{\partial x^2}\psi_\mu(\mathbf{r})}_{-k_x^2\psi_\mu(\mathbf{r})} + \frac{\partial^2}{\partial y^2}\psi_\mu(\mathbf{r}) + \underbrace{\frac{\partial^2}{\partial z^2}\psi_\mu(\mathbf{r})}_{-k_z^2\psi_\mu(\mathbf{r})} + \varepsilon_r(y)k_{0,\mu}^2\psi_\mu(\mathbf{r}) - \varepsilon_r^{-1}(y)\frac{\mathrm{d}}{\mathrm{d}y}\varepsilon_r(y)\frac{\partial}{\partial y}\psi_\mu(\mathbf{r}).$$

Excluding the trivial cases in which $P(x) = 0$ or $R(z) = 0$, the upper equation is now divided by $P(x)R(z)$, leading to

$$0 = \frac{\mathrm{d}^2}{\mathrm{d}y^2}Q_\mu(y) - \varepsilon_r^{-1}(y)\frac{\mathrm{d}}{\mathrm{d}y}\varepsilon_r(y)\frac{\mathrm{d}}{\mathrm{d}y}Q_\mu(y) + \left(\varepsilon_r(y)k_{0,\mu}^2 - k_x^2 - k_z^2\right)Q_\mu(y).$$

This equation is then rearranged into a more convenient representation:

$$-\frac{\mathrm{d}}{\mathrm{d}y}\left(\frac{1}{\varepsilon_r(y)}\frac{\mathrm{d}}{\mathrm{d}y}Q_\mu(y)\right) + \frac{1}{\varepsilon_r(y)}\left(k_x^2 + k_z^2\right)Q_\mu(y) = k_{0,\mu}^2 Q_\mu(y), \qquad (3.15)$$

which can be solved to get an expression for $Q_\mu(y)$.

The boundary conditions for the electric field are used now to create boundary conditions for $Q_\mu(y)$ accordingly, leading to $\left.\frac{\mathrm{d}Q_\mu(y)}{\mathrm{d}y}\right|_{y=0,b} = 0$.

These conditions together with eqn. (3.15) form a Sturm-Liouville problem (c.f. [80]) for $Q_\mu(y)$ to the eigenvalues $k_{0,\mu}^2$ and the weighting function 1. This automatically implies that the solutions of the Sturm-Liouville problem fulfil the orthogonality relation

$$\int_0^b Q_{\mu,m}(y)Q_{\mu,m'}(y)\mathrm{d}y = \xi\delta_{m,m'}, \qquad (3.16)$$

which will be of use further on for the overall orthogonality of the LSM modes. Here, $\delta_{m,m'}$ indicates the Kronecker delta. Additionally, $\xi$ is a proportionality factor that has the value 1 in this case, but the unit [m] and is introduced for consistency.

To solve the Sturm-Liouville problem, it is at first multiplied by $Q_\mu(y)$ and integrated over the computational domain (i.e. the dimensions of the structure):

$$-\int_0^b Q_\mu(y)\frac{\mathrm{d}}{\mathrm{d}y}\left(\frac{1}{\varepsilon_r(y)}\frac{\mathrm{d}}{\mathrm{d}y}Q_\mu(y)\right)\mathrm{d}y + \int_0^b \frac{1}{\varepsilon_r(y)}\left(k_x^2+k_z^2\right)Q_\mu^2(y)\mathrm{d}y = k_{0,\mu}^2\int_0^b Q_\mu^2(y)\mathrm{d}y.$$

The first term is then integrated by parts and the boundary conditions are used to obtain the final integral relation:

$$\int_0^b \frac{1}{\varepsilon_r(y)}\left[\left(\frac{\mathrm{d}}{\mathrm{d}y}Q_\mu(y)\right)^2+\left(k_x^2+k_z^2\right)Q_\mu^2(y)\right]\mathrm{d}y = k_{0,\mu}^2\int_0^b Q_\mu^2(y)\mathrm{d}y. \tag{3.17}$$

A straight-forward analytical solution of this equation is very difficult. Nonetheless, the unknown function $Q_\mu(y)$ can be expanded into a set of known functions, and the solution of eqn. (3.17) limited to the determination of the expansion coefficients. Here, the Fourier-cosine series $Q_\mu(y) = \sum_{m=0}^\infty q_{\mu,m}Q_{\mu,m}(y) = \sum_{m=0}^\infty q_{\mu,m}\cos(\frac{m\pi}{b}y)$ is chosen as the basic expansion, since the given cosine already satisfies the boundary conditions for $Q_\mu(y)$. This choice finalises the Hertzian potential as

$$\mathbf{\Pi}_\mu(\mathbf{r}) = \sin(k_x x)\sum_{m=0}^\infty q_{\mu,m}\cos(k_{y,m}y)\sin(k_z z)\mathbf{e}_y, \tag{3.18}$$

with $k_{y,m} = m\pi/b$, where only the expansion coefficients $q_{\mu,m}$ remain to be determined.

Inserting the Fourier-cosine series into eqn. (3.17) and rearranging the resulting equation yields

$$0 = \sum_{m=0}^\infty\sum_{m'=0}^\infty\left[T_{\mu,mm'} - k_{0,\mu}^2 P_{\mu,mm'}\right]q_{\mu,m}q_{\mu,m'}, \tag{3.19}$$

introducing the auxiliary quantities

$$T_{\mu,mm'} = \int_0^b \frac{1}{\varepsilon_r(y)}\left[\frac{\mathrm{d}Q_{\mu,m}(y)}{\mathrm{d}y}\frac{\mathrm{d}Q_{\mu,m'}(y)}{\mathrm{d}y}+\left(k_x^2+k_z^2\right)Q_{\mu,m}(y)Q_{\mu,m'}(y)\right]\mathrm{d}y$$

$$\tag{3.20}$$

$$P_{\mu,mm'} = \int_0^b Q_{\mu,m}(y)Q_{\mu,m'}(y)\mathrm{d}y.$$

Equation (3.19) is fulfilled if

$$0 = \sum_{m=0}^\infty\left[T_{\mu,mm'} - k_{0,\mu}^2 P_{\mu,mm'}\right]q_{\mu,m}\ \ \text{for all } m' = 0,1,2.... \tag{3.21}$$

The solution to this set of equations gives the correct analytical result for the expansion coefficients of the Fourier-cosine series. Note, however, that this is not feasible in a realistic attempt to obtain a solution. Instead, the series needs to be terminated after a *finite* number of functions, which renders the final solution a mere *approximation* of the correct analytical solution. Ending the series after $N$ functions sets up a system of $N$ equations, which can be represented by the matrix equation,

$$
\left[ \begin{pmatrix} T_{\mu,11} & T_{\mu,12} & \cdots & T_{\mu,1s} \\ T_{\mu,21} & T_{\mu,22} & \cdots & T_{\mu,2s} \\ \vdots & \vdots & \ddots & \vdots \\ T_{\mu,m1} & T_{\mu,m2} & \cdots & T_{\mu,mm'} \end{pmatrix} - k_{0,\mu}^2 \begin{pmatrix} P_{\mu,11} & P_{\mu,12} & \cdots & P_{\mu,1s} \\ P_{\mu,21} & P_{\mu,22} & \cdots & P_{\mu,2s} \\ \vdots & \vdots & \ddots & \vdots \\ P_{\mu,m1} & P_{\mu,m2} & \cdots & P_{\mu,mm'} \end{pmatrix} \right] \mathbf{q} = \mathbf{0},
$$
(3.22)

where $\mathbf{T}_\mu$ and $\mathbf{P}_\lambda$ are symmetric matrices containing the integrals specified above and $\mathbf{q}$ is the vector containing the expansion coefficients.

**LSE Modes**

In contrast to LSM modes, for LSE modes (indexed with $\lambda$) $\underline{E}_{\lambda,y}(\mathbf{r}) = 0$, while $\underline{B}_{\lambda,y}(\mathbf{r}) \neq 0$. Consequently, while still using Hertzian potentials, a different ansatz is employed here:

$$
\mathbf{E}_\lambda(\mathbf{r}) = \omega \nabla \times \mathbf{\Pi}_\lambda(\mathbf{r}),
$$
(3.23)

where $\mathbf{\Pi}_\lambda(\mathbf{r}) = A_\lambda \psi_\lambda(\mathbf{r}) \, \mathbf{e}_y$ is the Hertzian potential and the prefactor is chosen for convenience.

This choice for the electric field needs to fulfil Gauss' Law (3.6). Inserting eqn. (3.23) into eqn. (3.6) yields

$$
\begin{aligned}
\nabla \cdot \underline{\mathbf{D}}_\lambda(\mathbf{r}) &= (\nabla \varepsilon_r(y)) \, \underline{\mathbf{E}}_\lambda(\mathbf{r}) + \varepsilon_r(y) \nabla \cdot \underline{\mathbf{E}}_\lambda(\mathbf{r}) \\
&= \omega \varepsilon_r(y) \nabla \cdot (\nabla \times \mathbf{\Pi}_\lambda(\mathbf{r})) = 0.
\end{aligned}
$$

Here, the orthogonality of the gradient of the permittivity (which only has a $y$-component) with the electric field (which has no $y$-component) is exploited along with general vector algebra.

Inserting equation (3.23) into eqn. (3.8) yields an expression for the magnetic field in terms of the Hertzian potential:

$$
\mathbf{B}_\lambda(\mathbf{r}) = -j \nabla \times \nabla \times \mathbf{\Pi}_\lambda(\mathbf{r}).
$$
(3.24)

A different way of obtaining the magnetic field is to rewrite eqn. (3.9) with eqn. (3.23) and comparing both sides of the equation, resulting in

$$
\mathbf{B}_\lambda(\mathbf{r}) = -j \left( k_{0,\lambda}^2 \varepsilon_r(y) \mathbf{\Pi}_\lambda(\mathbf{r}) + \nabla \Phi_\lambda(\mathbf{r}) \right),
$$
(3.25)

with arbitrary $\nabla\Phi_\lambda(\mathbf{r})$. Equating (3.24) with equation (3.25) and using vector algebra to eliminate the double curl yields

$$-j\left(\nabla\left(\nabla\cdot\mathbf{\Pi}_\lambda(\mathbf{r})\right) - \nabla^2\mathbf{\Pi}_\lambda(\mathbf{r})\right) = -j\left(k_{0,\lambda}^2\varepsilon_r(y)\mathbf{\Pi}_\lambda(\mathbf{r}) + \nabla\Phi_\lambda(\mathbf{r})\right).$$

The gauge $\Phi_\lambda(\mathbf{r}) = \nabla\cdot\mathbf{\Pi}_\lambda(\mathbf{r})$ is then employed, resulting in the final Helmholtz-like equation for LSE modes:

$$\mathbf{0} = \nabla^2\mathbf{\Pi}_\lambda(\mathbf{r}) + k_{0,\lambda}^2\varepsilon_r(y)\mathbf{\Pi}_\lambda(\mathbf{r}). \tag{3.26}$$

The equation is again solved by employing the product ansatz for the Hertzian potential, $\psi_\lambda(\mathbf{r}) = P(x)Q_\lambda(y)R(z)$. Using boundary conditions in $x$- and $z$-direction (c.f. Section 2.4) directly leads to the solutions for $P(x)$ and $R(z)$, respectively, so that the Hertzian potential can be further specified as

$$\mathbf{\Pi}_\lambda(\mathbf{r}) = A_\lambda\cos(k_x x)\cos(k_z z)Q_\lambda(y),$$

with $k_x$ and $k_z$ identical to the LSM case.

The determination of $Q_\lambda(y)$ follows along the same lines as for the LSM modes. First of all, by inserting the last equation into (3.26), dividing the resulting formulation by $\psi_\lambda(\mathbf{r})$ and rewriting it, the Sturm-Liouville form is obtained:

$$\varepsilon_r(y)k_{0,\lambda}^2 Q_\lambda(y) = -\frac{\mathrm{d}^2}{\mathrm{d}y^2}Q_\lambda(y) + \left(k_x^2 + k_z^2\right)Q_\lambda(y). \tag{3.27}$$

Using the PEC boundaries on the electric field again the boundary conditions for $Q_\lambda(y)$ can be established as $Q_\lambda(y)|_{y=0,b} = 0$, which completes the Sturm-Liouville problem. The eigenvalues of this problem are again $k_{0,\lambda}^2$, while the weighting function in this case is the permittivity $\varepsilon_r(y)$. The orthogonality of the eigenfunctions follows directly from the Sturm-Liouville problem and can therefore be stated as

$$\int\limits_0^b Q_{\lambda,m}(y)Q_{\lambda,m'}(y)\varepsilon_r(y)\mathrm{d}y = \xi\delta_{m,m'}, \tag{3.28}$$

which will be used later to establish the general orthogonality relations of the LSE modes.

To solve equation (3.27), it is first of all multiplied by $Q_\lambda(y)$ and integrated over the computational domain. The term containing the second derivative is then integrated by parts and the boundary conditions are used to obtain the intermediate result:

$$k_{0,\lambda}^2\int\limits_0^b \varepsilon_r(y)Q_\lambda^2(y)\mathrm{d}y = \int\limits_0^b\left[\left(\frac{\mathrm{d}}{\mathrm{d}y}Q_\lambda(y)\right)^2 + (k_x^2 + k_z^2)Q_\lambda^2(y)\right]\mathrm{d}y. \tag{3.29}$$

The unspecified function $Q_\lambda(y)$ is again expanded, this time using the Fourier-sine series $Q_\lambda(y) = \sum_{m=0}^{\infty} q_{\lambda,m} Q_{\lambda,m}(y) = \sum_{m=1}^{\infty} q_{\lambda,m} \sin(\frac{m\pi}{b}y)$. This finalises the representation of the Hertzian potential as

$$\mathbf{\Pi}_\lambda(\mathbf{r}) = A_\lambda \cos(k_x x) \sum_{m=1}^{\infty} q_{\lambda,m} \sin(k_{y,m}y) \cos(k_z z)\mathbf{e}_y. \qquad (3.30)$$

Inserting the expansion of $Q_\lambda(y)$ into eqn. (3.29) and introducing similar auxiliary terms like in the last chapter delivers

$$0 = \sum_{m=0}^{\infty} \sum_{m'=0}^{\infty} \left[ T_{\lambda,mm'} - k_{0,\lambda}^2 P_{\lambda,mm'} \right] q_{\lambda,m} q_{\lambda,m'}, \qquad (3.31)$$

with the auxiliary quantities

$$
\begin{aligned}
T_{\lambda,mm'} &= \int_0^b \left[ \frac{\mathrm{d}Q_{\lambda,m}(y)}{\mathrm{d}y} \frac{\mathrm{d}Q_{\lambda,m'}(y)}{\mathrm{d}y} + \left( k_x^2 + k_z^2 \right) Q_{\lambda,m}(y) Q_{m'}(y) \right] \mathrm{d}y \\
&\qquad\qquad\qquad\qquad\qquad\qquad\qquad\qquad\qquad\qquad\qquad\qquad\qquad (3.32) \\
P_{\lambda,mm'} &= \int_0^b \varepsilon_r(y) Q_{\lambda,m}(y) Q_{\lambda,m'}(y) \mathrm{d}y.
\end{aligned}
$$

The expansion needs to be terminated after $N$ terms, so that the final system of equations, just like in the case of LSM modes, reads as

$$0 = \sum_{m=0}^{N} \left[ T_{\lambda,mm'} - k_{0,\lambda}^2 P_{\lambda,mm'} \right] q_{\lambda,m} \quad \text{for all } m' = 0,1,2...N, \qquad (3.33)$$

or in matrix form

$$\left[ \mathbf{T}_\lambda - k_{0,\lambda}^2 \mathbf{P}_\lambda \right] \mathbf{q} = \mathbf{0}. \qquad (3.34)$$

**The Solution Strategy**

The general matrix equations (3.22) and (3.33) are identical. The only changes are the definitions of the matrices $\mathbf{T}_{\lambda,\mu}$ and $\mathbf{P}_{\lambda,\mu}$, while both are symmetric in both cases. In theory, a solution to the systems of equations established in the previous sections is possible. Though in reality, of course, this might only be feasible for a small number of expansion functions. Given the approximative nature of the solution, a reasonably large number of basic functions is needed to grant a result satisfiably close to the correct analytic solution of the Sturm-Liouville problems.

Thus, the only option to keep the accuracy high is by solving eqs. (3.22) and (3.33) numerically, rendering the overall result *semi-analytical*, while the general representation of the eigenmodes remains analytically correct.

For this purpose, a Python-based [81] programme called WIzaRD was developed, which will be introduced in detail in Chapter 4. In Fig. 3.3 and 3.4 the electric field strengths of the LSM and LSE modes with the lowest eigenfrequencies of a test structure are shown, both calculated using WIzaRD.
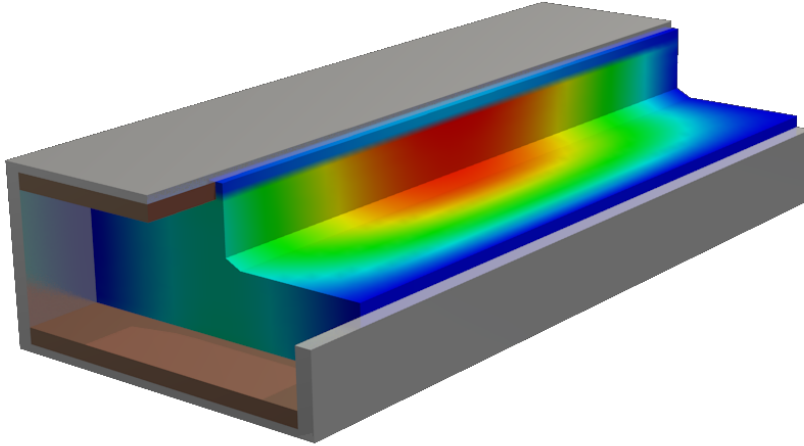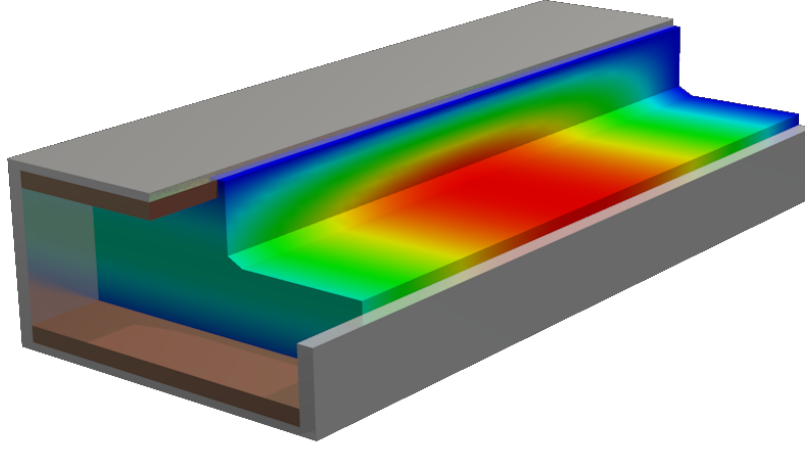


**Figure 3.3:** Absolute value of the electric field strength of the LSM mode with the lowest eigenfrequency in a test waveguide cut open at $x = a/2$ and $y = b/2$ for clarity.

It shall be noted here that, due to the symmetry of the structure, the eigenmodes exhibit symmetry (or antisymmetry) as well. Put into praxis this means that either all even or odd expansion coefficients are 0. Thus, the number of basis functions that are used to represent the final mode is effectively halved.

**Orthogonality Relations**

LSE and LSM modes form a complete, orthogonal set of eigenmodes, making it possible to expand any given field into a weighted sum of these modes.

It should be mentioned here that while the magnetic fields are orthogonal in the conventional sense (with $i = \mu, \lambda$),

$$\int\limits_{-\infty}^{\infty} \underline{\mathbf{B}}_i\left(\mathbf{r}\right) \cdot \underline{\mathbf{B}}_{i'}\left(\mathbf{r}\right) \mathrm{d}V = A_i^2 V_i \delta_{i,i'}, \tag{3.35}$$

the electric fields are orthogonal with respect to the permittivity function:

$$\int\limits_{-\infty}^{\infty} \varepsilon_r(y) \underline{\mathbf{E}}_i\left(\mathbf{r}\right) \cdot \underline{\mathbf{E}}_{i'}\left(\mathbf{r}\right) \mathrm{d}V = A_i^2 U_i \delta_{i,i'}. \tag{3.36}$$

**Figure 3.4:** Absolute value of the electric field strength of the LSE mode with the lowest eigenfrequency in a test waveguide cut open at $x = a/2$ and $y = b/2$ for clarity.

These relations ensure the orthogonality between LSE and LSM modes as well as between the products of LSE and LSM modes, which is crucial for further considerations. The detailed proof of these relations is given in Appendix A.

## 3.3 Electric Field Expansion

The analytical description of the eigenmodes is now used to determine the electric field of a single point charge with the charge and current densities

$$\rho\left(\mathbf{r}, t\right) = q\delta\left(x - \frac{a}{2}\right)\delta\left(y - \frac{b}{2}\right)\delta\left(z - ct\right), \tag{3.37}$$

$$\mathbf{J}\left(\mathbf{r}, t\right) = c\rho\left(\mathbf{r}, t\right)\mathbf{e}_z, \tag{3.38}$$

and thus passing the structure in positive $z$-direction through $x = a/2$ and $y = b/2$ at the speed of light. In this case, Maxwell's equations read like eqs. (3.2) - (3.5).

The general methodology of such an expansion can be found, e.g. in [31]. The aim of the eigenmode expansion is, just like before with the Fourier expansions, the determination of the expansion coefficients $\chi_\lambda\left(t\right)$ and $\chi_\mu\left(t\right)$ in

$$\mathbf{E}(\mathbf{r}, t) = \sum_\lambda \chi_\lambda(t)\underline{\mathbf{E}}_\lambda(\mathbf{r}) + \sum_\mu \chi_\mu(t)\underline{\mathbf{E}}_\mu(\mathbf{r}). \tag{3.39}$$

Here, the time dependence of the field is completely moved to the unknown expansion coefficients $\chi_\lambda\left(t\right)$ and $\chi_\mu\left(t\right)$, while the spatial part of the electric field is a superposition of the electric phasors of the LSE and LSM modes of the structure.

To determine the coefficients, Maxwell's equations are solved within the structure. Therefore, the curl-curl equation of the electric field is generated:

$$\nabla \times \nabla \times \mathbf{E}\left(\mathbf{r}, t\right) = -\frac{\partial}{\partial t} \nabla \times \mathbf{B}\left(\mathbf{r}, t\right).$$

Next, eqn. (3.5) is inserted and the double curl is reformulated using vector algebra:

$$\nabla \cdot \left(\nabla \cdot \mathbf{E}\left(\mathbf{r}, t\right)\right) - \nabla^2 \mathbf{E}\left(\mathbf{r}, t\right) = -\mu_0 \frac{\partial}{\partial t} \mathbf{J}\left(\mathbf{r}, t\right) - \mu_0 \varepsilon_0 \varepsilon_r \frac{\partial^2}{\partial t^2} \mathbf{E}\left(\mathbf{r}, t\right).$$

Due to the $y$-dependence of the permittivity, the divergence of the electric field derived from eqn. (3.2) reads

$$\nabla \cdot \mathbf{E}\left(\mathbf{r}, t\right) = \frac{\rho\left(\mathbf{r}, t\right)}{\varepsilon_r(y)\varepsilon_0} - \frac{1}{\varepsilon_r(y)} \mathbf{E}\left(\mathbf{r}, t\right) \cdot \nabla \varepsilon_r(y).$$

This is now inserted into the curl-curl equation, leading to

$$\begin{aligned}
\nabla\left(\frac{\rho\left(\mathbf{r}, t\right)}{\varepsilon_r(y)\varepsilon_0}\right) + \mu_0 \frac{\partial}{\partial t} \mathbf{J}\left(\mathbf{r}, t\right) = {} & \nabla^2 \mathbf{E}\left(\mathbf{r}, t\right) - \frac{1}{c_0^2}\varepsilon_r(y)\frac{\partial^2}{\partial t^2}\mathbf{E}\left(\mathbf{r}, t\right) \\
& + \nabla \cdot \left(\frac{1}{\varepsilon_r(y)}\mathbf{E}\left(\mathbf{r}, t\right) \cdot \nabla \varepsilon_r(y)\right).
\end{aligned} \tag{3.40}$$

The electric field on the right-hand side of this equation is now reformulated using the eigenmode expansion (3.39):

$$\begin{aligned}
\nabla\left(\frac{\rho\left(\mathbf{r}, t\right)}{\varepsilon_r(y)\varepsilon_0}\right) + \mu_0 \frac{\partial}{\partial t} \mathbf{J}\left(\mathbf{r}, t\right) = {} & \sum_{\lambda,\mu}\chi_{\lambda,\mu}\left(t\right)\nabla^2\underline{\mathbf{E}}_{\lambda,\mu}\left(\mathbf{r}\right) - \frac{1}{c_0^2}\varepsilon_r(y)\sum_{\lambda,\mu}\underline{\mathbf{E}}_{\lambda,\mu}\left(\mathbf{r}\right)\frac{\partial^2}{\partial t^2}\chi_{\lambda,\mu}\left(t\right) \\
& + \sum_{\lambda,\mu}\chi_{\lambda,\mu}\left(t\right)\nabla \cdot \left(\frac{1}{\varepsilon_r(y)}\underline{\mathbf{E}}_{\lambda,\mu}\left(\mathbf{r}\right) \cdot \nabla \varepsilon_r(y)\right).
\end{aligned}$$

Next, the general Helmholtz-like equation for both eigenmodes (3.10) is applied to the first term on the right-hand side:

$$\begin{aligned}
\nabla\left(\frac{\rho\left(\mathbf{r}, t\right)}{\varepsilon_r(y)\varepsilon_0}\right) + \mu_0 \frac{\partial}{\partial t} \mathbf{J}\left(\mathbf{r}, t\right) = {} & -\frac{1}{c_0^2}\varepsilon_r(y)\sum_{\lambda,\mu}\omega_{\lambda,\mu}\chi_{\lambda,\mu}(t)\underline{\mathbf{E}}_{\lambda,\mu}\left(\mathbf{r}\right) \\
& -\sum_{\lambda,\mu}\chi_{\lambda,\mu}(t)\nabla \cdot \left(\frac{1}{\varepsilon_r(y)}\underline{\mathbf{E}}_{\lambda,\mu}\left(\mathbf{r}\right) \cdot \nabla \varepsilon_r(y)\right) \\
& -\frac{1}{c_0^2}\varepsilon_r(y)\sum_{\lambda,\mu}\underline{\mathbf{E}}_{\lambda,\mu}\left(\mathbf{r}\right)\frac{\partial^2}{\partial t^2}\chi_{\lambda,\mu}(t) \\
& +\sum_{\lambda,\mu}\chi_{\lambda,\mu}(t)\nabla \cdot \left(\frac{1}{\varepsilon_r(y)}\underline{\mathbf{E}}_{\lambda,\mu}\left(\mathbf{r}\right) \cdot \nabla \varepsilon_r(y)\right)
\end{aligned}$$

After cancelling out the two equal terms and writing $\frac{\partial^2}{\partial t^2}\chi_{\lambda,\mu}(t) = \ddot{\chi}_{\lambda,\mu}(t)$, the final form of the curl-curl equation reads as

$$-\nabla\left(\frac{\rho(\mathbf{r},t)}{\varepsilon_r(y)\varepsilon_0}\right) - \mu_0\frac{\partial}{\partial t}\mathbf{J}(\mathbf{r},t) = \frac{1}{c_0^2}\varepsilon_r(y)\left(\sum_{\lambda}\left(\chi_\lambda(t)\,\omega_\lambda^2 + \ddot{\chi}_\lambda(t)\right)\underline{\mathbf{E}}_\lambda(\mathbf{r})\right.$$
$$\left. + \sum_{\mu}\left(\chi_\mu(t)\,\omega_\mu^2 + \ddot{\chi}_\mu(t)\right)\underline{\mathbf{E}}_\mu(\mathbf{r})\right). \tag{3.41}$$

At this point, the orthogonality relations from Section 3.2.2 are employed. For this, eqn. (3.41) is first of all multiplied by $\underline{\mathbf{E}}_{\lambda'}(\mathbf{r})$ and then integrated over the cavity volume (c.f. Fig. 3.2). Due to the orthogonality of the modes, all terms dependent on $\underline{\mathbf{E}}_\mu(\mathbf{r})$ vanish, while the integral over the terms dependent on $\underline{\mathbf{E}}_\lambda(\mathbf{r})$ will yield $A_\lambda^2 U_\lambda \delta_{\lambda,\lambda'}$. Thus, the resulting equation reads as:

$$\chi_\lambda(t)\,\omega_\lambda^2 + \ddot{\chi}_\lambda(t) = -\frac{c_0^2}{A_\lambda^2 U_\lambda}\left(\int\nabla\left(\frac{\rho(\mathbf{r},t)}{\varepsilon_r(y)\varepsilon_0}\right)\underline{\mathbf{E}}_{\lambda'}(\mathbf{r})\,\mathrm{d}V\right.$$
$$\left. + \int\mu_0\frac{\partial\mathbf{J}(\mathbf{r},t)}{\partial t}\underline{\mathbf{E}}_{\lambda'}(\mathbf{r})\,\mathrm{d}V\right). \tag{3.42}$$

In the same manner, multiplying (3.41) by $\underline{\mathbf{E}}_{\mu'}(\mathbf{r})$ and integrating over the volume of the cavity and using the orthogonalities to cancel out terms dependent on $\underline{\mathbf{E}}_\lambda(\mathbf{r})$, the source equation to solve for $\chi_\mu(t)$ is

$$\chi_\mu(t)\,\omega_\mu^2 + \ddot{\chi}_\mu(t) = -\frac{c_0^2}{A_\mu^2 U_\mu}\left(\int\nabla\left(\frac{\rho(\mathbf{r},t)}{\varepsilon_r(y)\varepsilon_0}\right)\underline{\mathbf{E}}_{\mu'}(\mathbf{r})\,\mathrm{d}V\right.$$
$$\left. + \int\mu_0\frac{\partial\mathbf{J}(\mathbf{r},t)}{\partial t}\underline{\mathbf{E}}_{\mu'}(\mathbf{r})\,\mathrm{d}V\right). \tag{3.43}$$

For an exact solution of the integrals on the right-hand side, the reader is referred to Appendix B. At this point, it shall be sufficient to state that the solution of the integrals basically amounts to an evaluation of the electric field components of the modes and their derivatives on the beam axis, while the $z$-coordinate is transferred from space to time using the speed of light. With this, the differential equations for the coefficients read

$$\chi_\lambda(t)\,\omega_\lambda^2 + \ddot{\chi}_\lambda(t) = -\frac{q\omega_\lambda c_0^2}{A_\lambda U_\lambda \varepsilon_0}k_x k_z \sin\left(\frac{n\pi}{2}\right)\sum_{m=1}^{N}q_{\lambda,m}\sin\left(\frac{m\pi}{2}\right)\sin\left(k_z c_0 t\right) \tag{3.44}$$

and

$$\chi_\mu(t)\,\omega_\mu^2 + \ddot{\chi}_\mu(t) = -\frac{qc_0^2}{A_\mu U_\mu \varepsilon_0}k_z^2 \sin\left(\frac{n\pi}{2}\right)\sum_{m=1}^{N}q_{\mu,m}k_{y,m}\sin\left(\frac{m\pi}{2}\right)\sin\left(k_z c_0 t\right). \tag{3.45}$$

Both equations (3.44) and (3.45) are second order ordinary differential equations of the form $f(t)\omega^2 + \ddot{f}(t) = O(t)$, for which a general solution can be found using the variation of constants. This general solution is

$$f(t) = \frac{1}{\omega} \int_0^T O(t') \sin\left(\omega\left(t - t'\right)\right) \mathrm{d}t'.$$

The term $T = \min\left(t, L/c_0\right)$ indicates the upper boundary of the integral, meaning that the evaluation can be truncated at $L/c_0$ because at this point, the charge leaves the cavity and does not contribute to the electric field any longer.

Using this strategy, eqs. (3.44) and (3.45) can be solved, and the final expansion coefficients can be written down as:

$$\chi_\lambda(t) = -\frac{q k_x k_z c_0^2}{A_\lambda U_\lambda \varepsilon_0} \sin\left(\frac{n\pi}{2}\right) \sum_{m=1}^{N} q_{\lambda,m} \sin\left(\frac{m\pi}{2}\right)$$

$$\cdot \int_0^T \sin\left(k_z c_0 t'\right) \sin\left(\omega_\lambda\left(t - t'\right)\right) \mathrm{d}t', \tag{3.46}$$

$$\chi_\mu(t) = -\frac{q k_z^2 c_0^2}{A_\mu U_\mu \omega_\mu \varepsilon_0} \sin\left(\frac{n\pi}{2}\right) \sum_{m=1}^{N} q_{\mu,m} k_{y,m} \sin\left(\frac{m\pi}{2}\right)$$

$$\cdot \int_0^T \sin\left(k_z c_0 t'\right) \sin\left(\omega_\mu\left(t - t'\right)\right) \mathrm{d}t'. \tag{3.47}$$

## 3.4 The Longitudinal Wakefield

With the knowledge of the time-dependent electric field $\mathbf{E}(\mathbf{r}, t)$ generated by the point charge inside the dielectrically lined rectangular waveguide, it is now possible to determine an analytic expression for the wakefield (for more information, see e.g. [32]).

The wakefield is evaluated acting on another point-like test charge following the generating charge in a distance $s$ (c.f. Fig. 3.5) according to

$$W_{0,\|}(s) = \frac{1}{q_{\text{test}}} \int_0^L E_z\left(\frac{a}{2}, \frac{b}{2}, z, \frac{(z+s)}{c}\right) \mathrm{d}z. \tag{3.48}$$

The wake function thus is an integral over the longitudinal component of the electric field (the $z$-component in this case), evaluated at the beam axis ($x = a/2$ and $y = b/2$), and is dependent on the distance between the two charges.
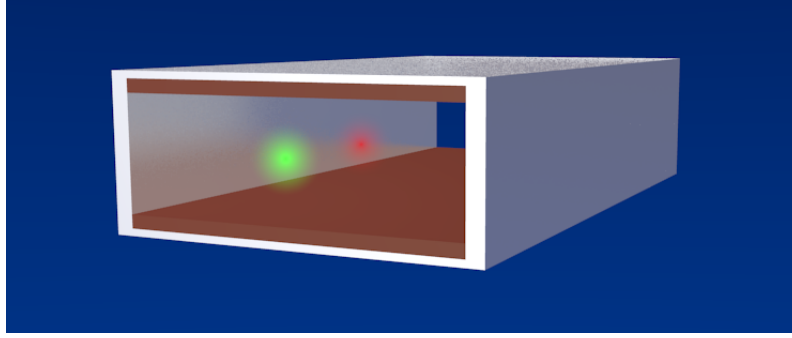
**Figure 3.5:** Field generating charge (green) and test charge (red) inside a dielectrically lined rectangular waveguide.

Using the field expansion (3.39) in eqn. (3.48), the wakefield can be rewritten as

$$W_{0,||}(s) = \frac{1}{q_{\text{test}}} \int_0^L \left( \sum_{\lambda,\mu} \chi_{\lambda,\mu} \left( \frac{z+s}{c_0} \right) \underline{E_{\lambda,\mu,z}} \left( \frac{a}{2}, \frac{b}{2}, z \right) \right) \mathrm{d}z, \qquad (3.49)$$

which is basically a sum over the contributions of each mode to the wakefield. Since all components of the given equation are known analytically, the wakefield integration can be carried out symbolically.

However, inserting eqs. (3.46) and (3.47) into the upper equation and using the complete expressions for the electric fields of the modes would lead to unmanageably long terms, where most parts are constant anyway and are not relevant for the integration itself.

Therefore, the auxiliary quantities

$$\overline{\chi_\lambda} = -\frac{q k_x k_z c_0^2}{A_\lambda U_\lambda \varepsilon_0} \sin\left(\frac{n\pi}{2}\right) \sum_{m=1}^N q_{\lambda,m} \sin\left(\frac{m\pi}{2}\right), \qquad (3.50)$$

$$\overline{\chi_\mu} = -\frac{q k_z^2 c_0^2}{A_\mu U_\mu \omega_\mu \varepsilon_0} \sin\left(\frac{n\pi}{2}\right) \sum_{m=1}^N q_{\mu,m} k_{y,m} \sin\left(\frac{m\pi}{2}\right), \qquad (3.51)$$

$$\overline{E_{\lambda,z}} = -A_\lambda \omega_\lambda k_x \sin\left(\frac{n\pi}{2}\right) \sum_{m=1}^N q_{\lambda,m} \sin\left(\frac{m\pi}{2}\right), \qquad (3.52)$$

$$\overline{E_{\mu,z}} = -A_\mu k_z \sin\left(\frac{n\pi}{2}\right) \sum_{m=1}^N q_{\mu,m} k_{y,m} \sin\left(\frac{m\pi}{2}\right) \qquad (3.53)$$

are introduced. With them, expression (3.49) can be simplified to

$$W_{0,\|}(s) = \frac{1}{q_{test}} \sum_{\lambda,\mu} \overline{\chi_{\lambda,\mu}} \overline{E_{\lambda,\mu,z}}.$$

$$\int_0^L \int_0^{T^*} \sin\left(k_z c_0 t'\right) \sin\left(\omega_{\mu,\lambda}\left(\frac{z+s}{c_0} - t'\right)\right) dt' \cos\left(k_z z\right) dz, \tag{3.54}$$

where $T^* = \min\left(\frac{(z+s)}{c_0}, \frac{L}{c_0}\right)$.
The general challenge here is the evaluation of

$$I(s) = \int_0^L \int_0^{T^*} \sin\left(k_z c_0 t'\right) \sin\left(\omega_{\mu,\lambda}\left(\frac{z+s}{c_0} - t'\right)\right) dt' \cos\left(k_z z\right) dz,$$

which is considered in detail in Appendix C. At this point, it shall be sufficient to state the integral as

$$I(s) = -\frac{c_0^2 k_z \omega_{\lambda,\mu}\left(2 - 2e^{jl\pi}\cos\left(k_{0,\lambda,\mu}L\right)\right)\cos\left(k_{0,\lambda,\mu}s\right)}{\left(c_0 k_z - \omega_{\lambda,\mu}\right)^2 \left(c_0 k_z + \omega_{\lambda,\mu}\right)} \begin{cases} 1 & \text{for } s > 0 \\ \frac{1}{2} & \text{for } s = 0 \\ 0 & \text{for } s < 0 \end{cases}. \tag{3.55}$$

Important to note here is that the only term dependent on $s$ is $\cos(k_{0,\lambda,\mu}s)$; everything else are constants and geometric parameters or mode characteristics.

Combining this result with eqs. (3.50) - (3.53), the prefactors

$$\kappa_\lambda = -\frac{c_0^4 \omega_\lambda k_x^2 k_z^2 \sin^2\left(\frac{n\pi}{2}\right)\left(\sum_m q_{\lambda,m}\sin\left(\frac{m\pi}{2}\right)\right)^2 \left(2 - 2e^{jl\pi}\cos\left(k_{0,\lambda}L\right)\right)}{\varepsilon_0 U_\lambda \left(c_0 k_z - \omega_\lambda\right)^2 \left(c_0 k_z + \omega_\lambda\right)}$$

$$\kappa_\mu = -\frac{c_0^4 k_z^4 \sin^2\left(\frac{n\pi}{2}\right)\left(\sum_m q_{\mu,m} k_{y,m}\sin\left(\frac{m\pi}{2}\right)\right)^2 \left(2 - 2e^{jl\pi}\cos\left(k_{0,\mu}L\right)\right)}{\varepsilon_0 U_\mu \left(c_0 k_z - \omega_\mu\right)^2 \left(c_0 k_z + \omega_\mu\right)}.$$

are generated. Using these, the final expression for the wakefield reads

$$W_{0,\|}(s) = \left(\sum_\lambda \kappa_\lambda \cos\left(k_{0,\lambda}s\right) + \sum_\mu \kappa_\mu \cos\left(k_{0,\mu}s\right)\right) \begin{cases} 1 & \text{for } s > 0 \\ \frac{1}{2} & \text{for } s = 0 \\ 0 & \text{for } s < 0 \end{cases}. \tag{3.56}$$

This expression shows that the wakefield in the case of an electric field resulting from a mode expansion is generally a superposition of contributions from each mode. The contribution strength of the modes is summarised in $\kappa_\lambda$ and $\kappa_\mu$ (often called 'loss

factors' to signalise that they basically indicate how much energy of the generating particle is stored in the respective mode). Both are only dependent on geometric constants and mode characteristics. Thus, detailed knowledge of the electric fields, while vital for the derivation of the wakefield, is eventually unnecessary for the wake function. Additionally, several other properties of the wakefield can be deduced from the analytic descriptions of the loss factors:

1. Both loss factors are proportional to $\sin\left(\frac{n\pi}{2}\right)$, which is zero if $n$ is even. Thus, neither LSE nor LSM modes with an even $n$ in their wavenumber $k_x$ contribute to the wakefield.

2. Additionally, $\sin\left(\frac{m\pi}{2}\right)$ is zero if $m$ is even, as well. Since, as stated in Section 3.2.2, either all $m$ are even or odd, depending on the symmetry of the mode, it can be stated that all modes where the entirety of $m$ is even do not contribute to the final wakefield.

3. For LSE modes, the loss factor is proportional to $k_x^2 k_z^2$. Thus, it vanishes for either $k_x = 0$ or $k_z = 0$. Both cases therefore deliver a loss factor that is zero and do not contribute to the final strength of the wakefield. This can be utilised to specify the case differentiation in Appendix A.

Using these symmetry conditions, the loss factors can be represented as

$$\kappa_\lambda = -\frac{4}{\varepsilon_0 a L} \frac{k_x^2 k_z^2}{k_x^2 + k_z^2} \left(\sum_{\text{odd } m} q_{\lambda,m} \sin\left(\frac{m\pi}{2}\right)\right)^2 \frac{\left(2 - 2e^{jl\pi}\cos\left(k_{0,\lambda}L\right)\right)}{\left(k_{0,\lambda}^2 - k_z^2\right)^2} \tag{3.57}$$

$$\kappa_\mu = -\frac{4}{\varepsilon_0 a L} \frac{k_z^4}{k_{0,\mu}\left(k_x^2 + k_z^2\right)} \left(\sum_{\text{odd } m} q_{\mu,m} k_{y,m} \sin\left(\frac{m\pi}{2}\right)\right)^2 \\ \cdot \frac{\left(2 - 2e^{jl\pi}\cos\left(k_{0,\mu}L\right)\right)}{\left(k_{0,\mu}^2 - k_z^2\right)^2}. \tag{3.58}$$

**The Longitudinal Wake Potential**

The longitudinal wake function serves as a Green's function for the determination of the longitudinal wakefield of any form of arbitrarily shaped particle bunch (then called wake potential). This means that the wake potential of any particle bunch can simply be calculated by convolving the wake function with the respective bunch shape function,

$$W_{||}(s) = \int_{-\infty}^{\infty} \psi\left(s - s'\right) W_{0,||}\left(s'\right) \mathrm{d}s'. \tag{3.59}$$

Here, $\psi(s)$ is the normalised bunch shape function. For a Gaussian bunch, this function, e.g., is

$$\psi(s) = \frac{1}{\sqrt{2\pi\sigma^2}} \exp\left(-\frac{s-s_0}{2\sigma^2}\right), \tag{3.60}$$

where $s_0$ is the centre of the Gaussian pulse and $\sigma$ is the corresponding r.m.s. bunch length.

### 3.4.1 A Remark on Normalisation

In Chapter 3.2, the normalisation constants for both LSE and LSM were not defined further.

A normalisation mathematically amounts to the multiplication of a quantity with a constant factor $A_{\lambda,\mu}$ (most often this factor is smaller than one), which is in this case included in the expressions for the electric and magnetic fields. The orthogonality relations, due to the scalar product of the fields in the integral, then automatically scale with $A_{\lambda,\mu}^2$, as described in the previous sections.

Resulting from the manner in which they have been determined, also the expansion coefficients of the electric field expansion in Section 3.3 scale with the normalisation constant. Following eqs. (3.46) and (3.47), this scaling goes with $A_{\lambda,\mu}^{-1}$.

The total product of an expansion function and an expansion coefficient, which is important for the loss factors, is thus scaling with $A_{\lambda,\mu}^{-1} \cdot A_{\lambda,\mu} = 1$. A determination of the normalisation constants is therefore not necessary if the fields are later used in a series expansion.

## 3.5 A Closer Observation of the Longitudinal Boundary Conditions

As introduced in section 3.2, for the eigenmode calculation the structure was considered to be completely enclosed in PEC. This is in conflict with the situation shown in Fig. 3.1, as the presence of the beam requires the structure to be open in $z$-direction. This discrepancy may have effects on the final wakefield that have not been considered yet and may even be an over-simplification. This may, in turn, lead to the used model becoming inapplicable for a realistic scenario. That this, however, is *not* the case here shall be proven now.

The proof is based on the concept of the superposition of waves: A three-dimensional eigenmode as presented in Section 3.2 is basically a standing wave in all three dimensions. On the other hand, the eigenmode of a longitudinally open structure would only be a standing wave in the transversal directions, whereas in the longitudinal direction it would be represented by a free or travelling wave. A fundamental concept of electrical field theory is that a travelling wave can be represented as a sum of

two standing waves [82], weighted with the according transmission and reflection coefficients. These two standing waves need to

1. be of the same eigenfrequency, and

2. differ in their boundary conditions such that one is terminated by PEC and the other by PMC.

Consequently, the eigenmodes of the longitudinally open structure can be calculated by superimposing the already known three-dimensional eigenmodes for PEC boundary conditions with the eigenmodes for PMC boundary conditions in longitudinal direction only (the transversal boundaries can remain as PEC). Thus, it is necessary to investigate the effects of changing the longitudinal boundaries from PEC to PMC.

First, all modes are generally a combination of sines and cosines. Switching from PEC to PMC basically means exchanging the one-dimensional function $R(z)$ for its derivative or vice versa, what amounts to exchanging sine and cosine (and the sign) in the Hertzian potentials. For example, the Hertzian potential of an LSE mode changes according to

$$\mathbf{\Pi}_{\lambda,E}(\mathbf{r}) = A_\lambda \cos(k_x x) \cos(k_z z) Q_\lambda(y) \mathbf{e}_y \text{ for PEC,}$$
$$\mathbf{\Pi}_{\lambda,M}(\mathbf{r}) = -A_\lambda \cos(k_x x) \sin(k_z z) Q_\lambda(y) \mathbf{e}_y \text{ for PMC.}$$

It is important to note here that there is *no* change in the behaviour in neither transversal component. The Helmholtz-like equation (3.13) is not influenced by the change in the boundary conditions, as well. To solve the Helmholtz-like equations, the actual behaviour of the Hertzian potential in longitudinal direction is only relevant with respect to its second derivative. The behaviour of the second derivative compared to the original function, however, is identical for sine and cosine, $\frac{\mathrm{d}}{\mathrm{d}z}R(z) = -k_z^2 R(z)$. Consequently, all the source equations on which the determination of the coefficients of the Fourier expansion are based *do not* change with a switch in the boundary conditions. Thus, the eigenfrequencies of the calculated fields remain identical, and condition 1. is fulfilled. Note that, however, the expressions for the fields *do* change, e.g. the longitudinal component of the electric field of an LSE mode is

$$\underline{E}_{z,E}(\mathbf{r}) = -k_z \sin(k_x x) Q(y) \cos(k_z z) \text{ for PEC,}$$
$$\underline{E}_{z,M}(\mathbf{r}) = k_z \sin(k_x x) Q(y) \sin(k_z z) \text{ for PMC.}$$

This will consequently influence the derivation of the coefficients of the eigenmode expansion of the electric field, described in Section 3.3. Basically, it leads to the same sine - cosine exchange in equations (3.44) and (3.45). Again for LSE modes,

this would mean that the expansion coefficients will change according to

$$\chi_{\lambda,E}(t) = -C_\lambda \int\limits_0^T \sin(k_z c_0 t') \sin\left(\omega_\lambda (t - t')\right) \mathrm{d}t' \text{ for PEC},$$

$$\chi_{\lambda,M}(t) = C_\lambda \int\limits_0^T \cos(k_z c_0 t') \sin\left(\omega_\lambda (t - t')\right) \mathrm{d}t' \text{ for PMC},$$

where $C_\lambda$ is the proportionality factor containing the remaining contributions.
To generate the total electric field of the point charge, though, the coefficients and the electric fields of the modes are multiplied. This, firstly, compensates for the change in the sign. For the wakefield, the longitudinal electric field is then integrated again. The resulting wakefield contributions per mode then read (for LSE modes)

$$W_{\parallel,E}(s) = B_\lambda \int\limits_0^L \cos(k_z z) \int\limits_0^T \sin(k_z c_0 t') \sin\left(\omega_\lambda (t - t')\right) \mathrm{d}t' \mathrm{d}z \text{ for PEC},$$

$$W_{\parallel,M}(s) = B_\lambda \int\limits_0^L \sin(k_z z) \int\limits_0^T \cos(k_z c_0 t') \sin\left(\omega_\lambda (t - t')\right) \mathrm{d}t' \mathrm{d}z \text{ for PMC},$$

with $B_\lambda$ indicating a proportionality factor again.

Evaluating these integrals leads to the exact *same* result. Consequently, a dielectrically lined rectangular waveguide with PMC boundaries in longitudinal direction has the exact same wakefield as the same waveguide using PEC boundary conditions.

The aforementioned superposition of two standing waves to represent a travelling wave could, for example, be carried out for the electric fields. So, to generate the open boundary case, the electric fields for both the PEC and the PMC case would be superimposed, and then integrated to gain the longitudinal wakefield. Both integrations would however lead to the same wakefield, making the superposition in this case all but unnecessary. Thus, due to the PEC and the PMC case both generating eigenmodes with the same eigenfrequencies and the same total wakefields, the open boundary case can be represented using PEC boundaries in longitudinal direction alone.

Note that this is *only* true for the wakefield; as the electric fields and also the magnetic fields of both cases are different from each other.

# 3.6 Summary

In this chapter, it has been shown that the wakefield generated by a point charge inside a rectangular, dielectrically lined waveguide can be expanded in a series of eigenmodes. These eigenmodes are LSE and LSM modes, and can, in turn, be determined using a Rayleigh-Ritz method based on Fourier expansion.

The eigenmodes were calculated for a structure completely enclosed in PEC. It was shown that this treatment is sufficient, even though in an actual application of the dielectrically lined rectangular waveguide as a wakefield dechirper, the structure would have to be open in $z$-direction. The reason for this is proven to be the invariance of the wakefield with respect to an exchange of boundary conditions from PEC to PMC in $z$-direction. A superposition of these two wakefields would deliver the result for open boundary conditions.

# 4 The Programme Package WIzaRD

In this chapter, the programme package WIzaRD is presented as the numerical approach to solve the analytical problem shown in Chapter 3. This consideration is divided into the tasks of eigenmode and wakefield computations. The underlying principles of the implementation are discussed as well as further assumptions and conditions that can be exploited to increase the efficiency of the programme package. WIzaRD is then benchmarked against the commercial software CST STUDIO SUITE ® [35].

## 4.1 The General Solution Strategy for Wake Function Calculations

The set of problems presented in the previous chapter is obviously divided into eigenmode computations and the calculation of the loss factors. Both issues contain series expansions: the eigenmode computation is only possible due to a Fourier expansion of the $y$-component of the respective Hertzian potentials. Moreover, the basis for the loss factor calculations is the expansion of the electric field into a set of eigenmodes.

As discussed before, this has the consequence that the series expansions need to be terminated after a finite number of basis functions, rendering the overall result an approximation. Even so, analytic expressions of the eigenmodes and the wake function are available. Additionally, if the set of expansion functions is chosen in a suitable way, these approximations still show a very high accuracy.

As seen from the equations (3.57) and (3.58), the loss factors themselves are only dependent on mode characteristics and geometrical parameters of the structure, which is another advantage. This enables the wake function calculation with knowledge that can purely be gained from an observation of the eigenmodes of the structure, with no necessity to compute an electric field as an intermediate step.

Consequently, the first step to calculate the wake function in a certain type of dechirper is the computation of its eigenmodes. For this, at first the geometry needs to be set using the parameters introduced in Fig. 3.2. Then, specific eigenmodes can be computed solving the matrix equations (3.22) and (3.34). This will result in knowledge about the expansion coefficients of the Fourier series, and thus, all requirements to solve eqns. (3.57) and (3.58) are met. Using equation (3.56), the wake function can then be calculated.

The given set of problems is implemented in the programming language Python [81]. Next to the high performance of programmes written in this language, one major advantage of Python is the availability of a high number of specific modules which work together seamlessly and, in this case, enable combining the efficiency of matrix calculations with the accuracy of a symbolic evaluation of integrals.

## 4.2 Eigenmode Computations

In the following section, the focus solely lies on the eigenmode computation with Python and the methods and modules used for it.

The quantities important for the later computation of the wake function are the frequency of the eigenmode as well as the Fourier expansion coefficients from which, theoretically, the electric and magnetic field distributions can be derived.

It shall be emphasised once more that all considerations for the eigenmodes are made for the 3D case in which the structure is closed in all three spatial dimensions and terminated by PEC.

### 4.2.1 The Algorithm for Computing the Eigenmodes

#### The General Approach

As already stated before, the determination of the eigenmodes of a dechirper is done by solving the equations (3.22) and (3.34). Both of these equations are eigenvalue equations corresponding to the eigenvalue $k_0^2$, the total wavenumber squared.

The entries of the matrices $\mathbf{T}_\lambda$, $\mathbf{T}_\mu$, $\mathbf{P}_\lambda$ and $\mathbf{P}_\mu$ are defined in the equations (3.20) and (3.32) as integrals depending mostly on the Fourier expansion functions and their derivatives. However, also the one-dimensional wavenumbers $k_x$ and $k_z$ appear in the definition of $\mathbf{T}_\lambda$ and $\mathbf{T}_\mu$.

All four integrals can be solved analytically for the chosen Fourier expansion coefficients. The resulting general functions will give the matrix entries in dependence on $m$ and $m'$, $k_x$ and $k_z$. Special attention needs to be paid to the $\mathbf{T}_\mu$ and $\mathbf{P}_\lambda$, since both are additionally dependent on the changing relative permittivity (its value as well as the coordinates of the jumps). Especially this more complicated behaviour makes it more effective to determine an analytically correct expression for the integrals *once* and then evaluate them by simply plugging in parameters instead of computing the integrals anew for every new combination of parameters possible.

The size of the resulting matrices is dependent on the number of expansion coefficients chosen. Selecting $N$ Fourier expansion functions will result in matrices of the size $N \times N$. Due to the nature of the integrals that make up the matrices' entries, the matrices will be symmetric, real-valued, sparse and will exhibit a full rank. Accordingly, the matrices possess $N$ real-valued eigenvalues corresponding to $N$ different wavenumbers $k_0^2$ and $N$ different eigenmodes. Since for all the eigenmodes

arising from one specific matrix configuration $k_x$ and $k_z$ remain unchanged, these eigenmodes will only differ in their behaviour in $y$-direction. Analogously to TE and TM modes, the total one-dimensional eigenvalue in $y$-direction shall be defined as

$$k_y^2 = k_0^2 - k_x^2 - k_z^2. \tag{4.1}$$

However, due to the behaviour in $y$-direction being defined via a Fourier series, an extraction of a single $m$ that corresponds to $k_y$ like in the case of TE and TM modes, where $k_y = m\pi/b$, is not possible here. This also makes a simple identification of the eigenmodes via the triple of integers $(n, m, l)$ impossible. For TE and TM modes, this triple specified the number of half-waves the fields of the eigenmodes would exhibit in $x$-, $y$- and $z$-direction and made both a simple referencing and identification of modes from their respective field patterns possible.

To preserve this intuitive nomenclature for LSE and LSM modes, a substitute identifier $\tilde{m}$ for the behaviour in $y$-direction shall be introduced here. As stated before, the eigenvalue equations (3.22) and (3.34) each possess $N$ different eigenvalues corresponding to different eigenvectors and thus eigenmodes. To specify a single mode, one of these eigenvalues has to be selected. The identifier $\tilde{m}$ is chosen such that in an ascending list of eigenvalues corresponding to the same problem defined by $k_x$ and $k_z$, $\tilde{m} = 0$ refers to the eigenvalue with the lowest total wavenumber and thus to the eigenmode with the lowest eigenfrequency. Subsequently, $\tilde{m} = 2$ refers to the mode with the second lowest eigenfrequency, and $\tilde{m} = N - 1$ to the mode with the highest frequency that is calculable from the given matrix equation. As a consequence, to calculate the $(N + 1)$th eigenfrequency of a set of solutions defined by $k_x$ and $k_z$, also $N + 1$ expansion functions are needed.

**The Implementation in Python**

In practice, this set of problems is solved using Python's modules *SymPy* [83] and *NumPy* [84]. The schematic of this procedure is visualised in Fig. 4.1.

As a first step, the geometry is specified in a single file that stores all unchanging geometrical parameters as well as the chosen number of Fourier expansion functions. This file is then used as input for all further procedures.

*SymPy* has the advantage of being able to process symbolic expressions. In this work, it is used to store the general solutions of the integrals (3.20) and (3.32) which have previously been analytically solved by using Mathematica [85]. The resulting symbolic expressions are then evaluated and transferred into a *NumPy* array by choosing $k_x$ and $k_z$ for the selected set of modes. The eigenvalue equations (3.22) and (3.34) are then solved by first generating the system matrices $\mathbf{P}_{\lambda,\mu}^{-1}\mathbf{T}_{\lambda,\mu}$ and then solving the eigenvalue equation

$$\mathbf{P}_{\lambda,\mu}^{-1}\mathbf{T}_{\lambda,\mu}\mathbf{q} = k_{0,\lambda,\mu}^2\mathbf{q}.$$
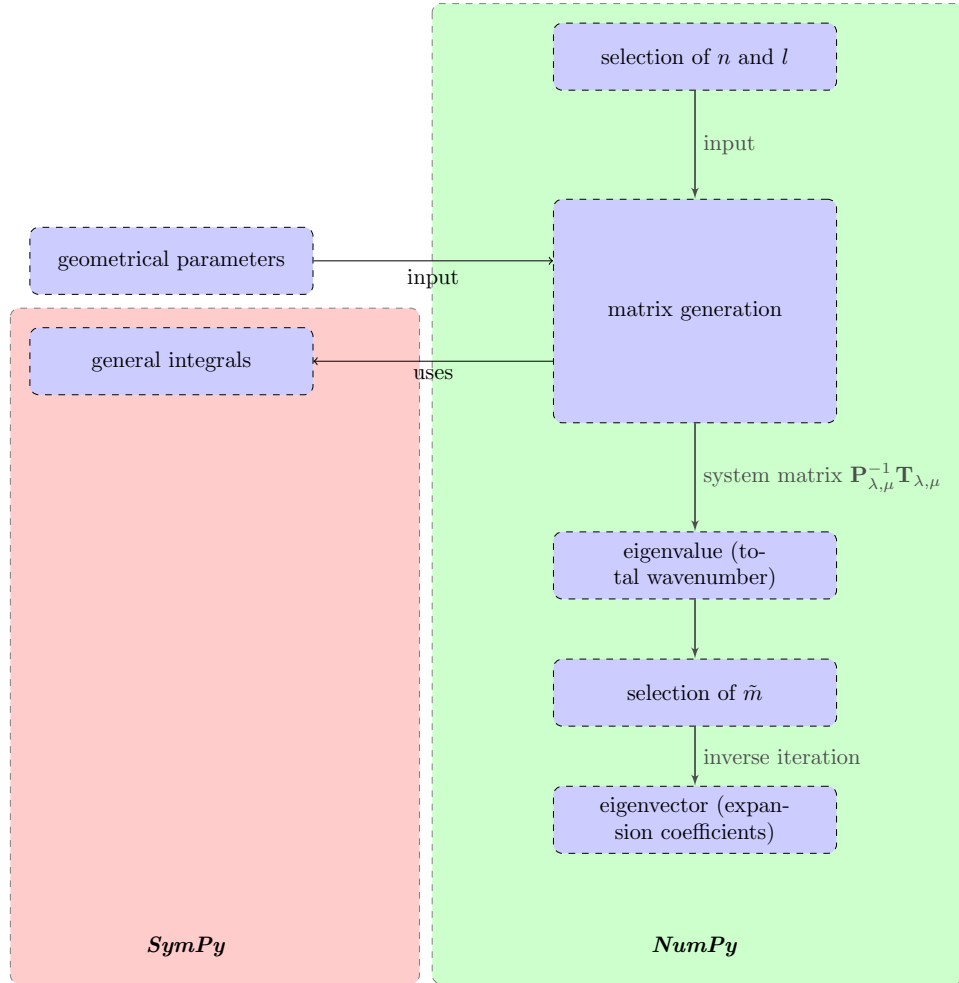
**Figure 4.1:** Schematic of the mode calculation procedure.

This is done by plainly using the native *NumPy* commands for eigenvalue determination.

As a next step, by specifying $\tilde{m}$ a single eigenmode is selected, for which the eigenvector is then calculated using the inverse iteration scheme (c.f. [86]). In this variant of the power method, the eigenvector corresponding to a known eigenvalue can iteratively be determined by the update scheme

$$\mathbf{q}_{i+1} = \left(\mathbf{P}_{\lambda,\mu}^{-1}\mathbf{T}_{\lambda,\mu} - k_{0,\lambda,\mu}\mathbf{I}\right)\mathbf{q}_i,$$

where $i$ indicates the iteration step.

In WIzaRD, the initial vector $\mathbf{q}_0$ is chosen such that all entries are set to zero apart from the $(\tilde{m}+1)$th entry, which is set to 1. This vector is then updated a fixed number of times, where due to the fast convergence of the inverse iteration scheme even a small number of steps like, e.g., 25 are enough.

| *Type* | $n$ | $\tilde{m}$ | $l$ | $q_{1,\lambda,\mu}$ | $q_{2,\lambda,\mu}$ | ... | $q_{N,\lambda,\mu}$ |
|--------|-----|-------------|-----|---------------------|---------------------|-----|---------------------|
| LSM | 1 | 1 | 1 | $q_{1,\mu}$ | $q_{2,\mu}$ | ... | $q_{N,\mu}$ |

**Table 4.1:** Structure of the result vector storing relevant information about the eigenmodes later used to compute the wake function with exemplary entries for the $LSM_{1,1,1}$ mode.

The generated eigenvector then corresponds to the expansion coefficients for the chosen mode. Together with information about the mode type, the triple $(n, \tilde{m}, l)$ and the eigenfrequency of the mode, the coefficients are then stored in another vector (c.f. Table 4.1). This single vector has stored all necessary information about a unique identification of a single mode, and is all that is needed to determine the field distributions of the mode and their later contribution to the wake function.

## 4.2.2 Analysis of the Field Distributions of LSE and LSM Modes

In this section, the electric field and magnetic flux density distributions of LSE and LSM modes are going to be analysed and compared to analytical expectations and results simulated with CST Microwave Studio® (CST MWS).

For this, a model structure with the following geometrical parameters is introduced:

$$a = 5\,\text{cm},$$
$$b = 1.8\,\text{cm},$$
$$d = 1.5\,\text{cm},$$
$$L = 20\,\text{cm},$$
$$\varepsilon_r = 6.$$

This geometry is very similar to the structure later used as the prototype dechirper for ELBE; however, it is only one fourth of the length of the prototype to simplify and speed up computations. Additionally, an intermediate gap widths of $2d - b = 1.2\,\text{cm}$ is chosen.

For this dechirper, the lowest LSE and LSM modes shall now be visualised. Therefore, it is first of all necessary to explicitly state the analytic formulations of the electric field strength and the magnetic flux density of these modes.

For LSE modes, the electric field is derived from the equations (3.23) and (3.30),

$$\underline{\mathbf{E}}_\lambda\left(\mathbf{r}\right) = A_\lambda \omega_\lambda \begin{pmatrix} k_z \cos(k_x x) \sum\limits_{m=1}^{N} q_{\lambda,m} \sin(k_{y,m}y) \sin(k_z z) \\ 0 \\ -k_x \sin(k_x x) \sum\limits_{m=1}^{N} q_{\lambda,m} \sin(k_{y,m}y) \cos(k_z z) \end{pmatrix}. \tag{4.2}$$

Here, $k_x = k_z = 0$ results in a trivial solution and is thus excluded. The magnetic flux density can be derived from equation (3.24), resulting in

$$
\underline{\mathbf{B}}_\lambda\left(\mathbf{r}\right) = jA_\lambda \begin{pmatrix} k_x \sin(k_x x) \sum_{m=1}^{N} q_{\lambda,m} k_{y,m} \cos(k_{y,m} y) \cos(k_z z) \\ -(k_x^2 + k_z^2) \cos(k_x x) \sum_{m=1}^{N} q_{\lambda,m} \sin(k_{y,m} y) \cos(k_z z) \\ k_z \cos(k_x x) \sum_{m=1}^{N} q_{\lambda,m} k_{y,m} \cos(k_{y,m} y) \sin(k_z z) \end{pmatrix}. \tag{4.3}
$$

The mode with the lowest eigenfrequency is always the mode with the lowest possible combination of the indices $(n, \tilde{m}, l)$. For LSE modes, the modes with $\tilde{m} = 0$ do not exist.

On the contrary, the cases $n = 0$ and $l = 0$ are allowed, but mutually exclusive. For the chosen geometry, however, $k_z$ for $l = 1$ will be smaller than $k_x$ for $n = 1$ since $L > a$, which is why the mode with $n = 0$ will overall result in the smaller eigenfrequency. The mode in question is thus the one with $(n = 0, \tilde{m} = 1, l = 1)$, from now on referred to as LSE$_{0,1,1}$ analogously to the common notation for TE and TM modes. Using these specifications, the expressions (4.2) and (4.3) simplify to

$$
\underline{E}_{\lambda,011,x}\left(\mathbf{r}\right) = A_{\lambda,011}\omega_{\lambda,011}\frac{\pi}{L} \sum_{m=1}^{N} q_{\lambda,m} \sin(k_{y,m} y) \sin\left(\frac{\pi}{L}z\right), \tag{4.4}
$$

for the electric field and

$$
\underline{\mathbf{B}}_{\lambda,011}\left(\mathbf{r}\right) = jA_{\lambda,011} \begin{pmatrix} 0 \\ -\left(\frac{\pi}{L}\right)^2 \sum_{m=1}^{N} q_{\lambda,m} \sin(k_{y,m} y) \cos(\frac{\pi}{L}z) \\ \frac{\pi}{L} \sum_{m=1}^{N} q_{\lambda,m} k_{y,m} \cos(k_{y,m} y) \sin\left(\frac{\pi}{L}z\right) \end{pmatrix}, \tag{4.5}
$$

for the magnetic flux density.

For LSM modes, the magnetic flux density can be derived from (3.11) and (3.18). The resulting field is

$$
\underline{\mathbf{B}}_\mu\left(\mathbf{r}\right) = -jA_\mu \frac{\omega_\mu}{c_0^2} \begin{pmatrix} -k_z \sin(k_x x) \sum_{m=0}^{N} q_{\mu,m} \cos(k_{y,m} y) \cos(k_z z) \\ 0 \\ k_x \cos(k_x x) \sum_{m=0}^{N} q_{\mu,m} \cos(k_{y,m} y) \sin(k_z z) \end{pmatrix}, \tag{4.6}
$$

where $k_x \neq 0$ and $k_z \neq 0$ need to be fulfilled to exclude a trivial solution. The electric

field can be derived from the magnetic flux density as

$$\underline{\mathbf{E}}_\mu\left(\mathbf{r}\right) = A_\mu\frac{1}{\varepsilon_r(y)}\begin{pmatrix} -k_x\cos(k_xx)\sum\limits_{m=0}^{N}q_{\mu,m}k_{y,m}\sin(k_{y,m}y)\sin(k_zz) \\ (k_x^2+k_z^2)\sin(k_xx)\sum\limits_{m=0}^{N}q_{\mu,m}\cos(k_{y,m}y)\sin(k_zz) \\ -k_z\sin(k_xx)\sum\limits_{m=0}^{N}q_{\mu,m}k_{y,m}\sin(k_{y,m}y)\cos(k_zz) \end{pmatrix}. \qquad (4.7)$$

Here, the eigenmode with the lowest frequency corresponds to $(n=1, \tilde{m}=0, l=1)$; it will be denoted as the $\text{LSM}_{1,0,1}$ mode. The fields resulting from this specification are

$$\underline{\mathbf{E}}_{\mu,101}\left(\mathbf{r}\right) = A_{\mu,101}\frac{1}{\varepsilon_r(y)}\begin{pmatrix} -\frac{\pi}{a}\cos\left(\frac{\pi}{a}x\right)\sum\limits_{m=0}^{N}q_{\mu,m}k_{y,m}\sin(k_{y,m}y)\sin\left(\frac{\pi}{L}z\right) \\ \left(\frac{\pi^2}{a^2}+\frac{\pi^2}{L^2}\right)\sin\left(\frac{\pi}{a}x\right)\sum\limits_{m=0}^{N}q_{\mu,m}\cos(k_{y,m}y)\sin\left(\frac{\pi}{L}z\right) \\ -\frac{\pi}{L}\sin\left(\frac{\pi}{a}x\right)\sum\limits_{m=0}^{N}q_{\mu,m}k_{y,m}\sin(k_{y,m}y)\cos\left(\frac{\pi}{L}z\right) \end{pmatrix},$$

$$(4.8)$$

and

$$\underline{\mathbf{B}}_{\mu,101}\left(\mathbf{r}\right) = -jA_{\mu,101}\frac{\omega_{\mu,101}}{c_0^2}\begin{pmatrix} -\frac{\pi}{L}\sin\left(\frac{\pi}{a}x\right)\sum\limits_{m=0}^{N}q_{\mu,m}\cos(k_{y,m}y)\cos\left(\frac{\pi}{L}z\right) \\ 0 \\ \frac{\pi}{a}\cos\left(\frac{\pi}{a}x\right)\sum\limits_{m=0}^{N}q_{\mu,m}\cos(k_{y,m}y)\sin\left(\frac{\pi}{L}z\right) \end{pmatrix}. \qquad (4.9)$$

In WIzaRD, these eigenmode field distributions can be calculated utilising *SymPy* once more, which allows for a direct implementation of the definitions in eqs. (4.2), (4.3), (4.6) and (4.7). Then, with the expansion coefficients and frequencies calculated with the scheme shown in Fig. 4.1, the fields are specified. This allows for a deeper analysis of the fields along one-dimensional axis, on cutting planes and as a full 3D field plot. For the $\text{LSE}_{0,1,1}$ and the $\text{LSM}_{1,0,1}$ mode, the absolute electric fields (normalised to a maximum amplitude of $1\,\text{V/m}$) along the $y$-axis for $x=a/2$ and $z=L/2$ are shown in the figures 4.2 and 4.3 (for 50 expansion coefficients of the Fourier series and 28,000 tetrahedral mesh cells in CST MWS). Analytically, the behaviours can be predicted from the equations (4.4) and (4.8) as

$$\underline{E}_{\lambda,011,x}\left(\frac{a}{2},y,\frac{L}{2}\right) \propto \sum_{m=1}^{N}q_{\lambda,m}\sin(k_{y,m}y),$$

$$\underline{E}_{\mu,101,y}\left(\frac{a}{2},y,\frac{L}{2}\right) \propto \frac{1}{\varepsilon(y)}\sum_{m=0}^{N}q_{\mu,m}\cos(k_{y,m}y).$$
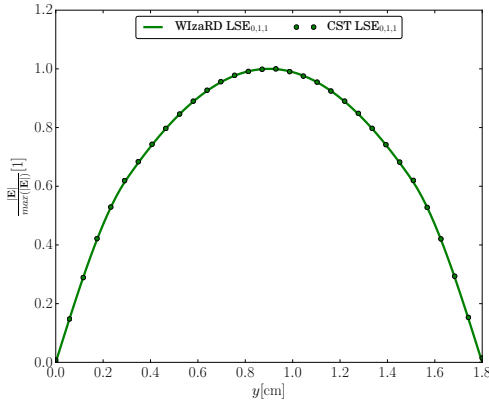
**Figure 4.2:** Normalised absolute electric field of the $LSE_{0,1,1}$ mode at the coordinates $x = a/2$ and $z = L/2$. The result computed with WIzaRD is compared to a simulation from CST MWS. The results computed with both methods agree very well. The average relative difference between both methods is $< 1\%$.
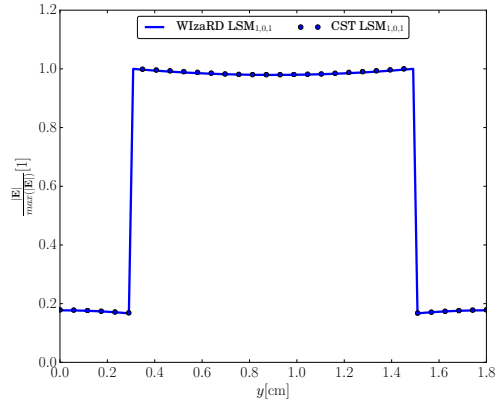
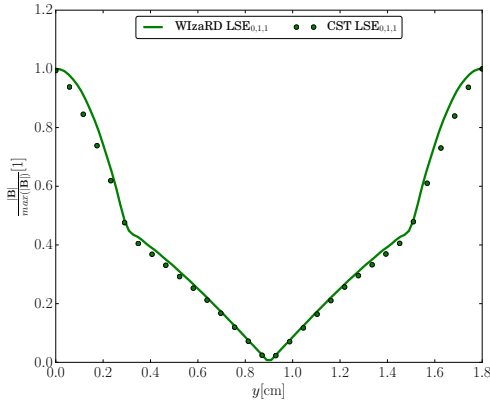**Figure 4.3:** Normalised absolute electric field of the $LSM_{1,0,1}$ mode at the coordinates $x = a/2$ and $z = L/2$. The result computed with WIzaRD is compared to a simulation from CST MWS. Both methods agree very well overall, however, the jump resulting from the step-like behaviour of the permittivity in the CST MWS version suffers from the finite grid resolution. The average relative difference between both methods is $< 1\%$

Basically, these projections on the $y$-axis reflect the behaviour of purely the Fourier expansion series. Additionally, it can be expected that the $LSM_{1,0,1}$ mode will show a step-like behaviour at the transitions between dielectric and vacuum, as the electric field is inversely proportional to the relative permittivity. And in fact, this behaviour can easily be seen in Fig. 4.3. In this case, the comparison to CST MWS also clearly shows the advantages of using a symbolic-based implementation style like *SymPy*: the jump in the permittivities is difficult to resolve with a finite grid spacing, or requires a high number of grid points to be resolved sharply. On the other hand, a symbolic computation can utilise the Heaviside-function like in equation (3.1), which results in a sharply defined jump.

Similar considerations can be made for the magnetic flux densities. Here, however, it is more advantageous to select the projection axis at $x = a/4$ and $z = L/2$, since at $x = a/2$, the resulting fields would be zero along the complete $y$-axis. At the chosen locations, the magnetic flux densities of the $LSE_{0,1,1}$ and the $LSM_{1,0,1}$ show

the following behaviours derived from the equations (4.5) and (4.9):

$$\underline{B}_{\lambda,011,z}\left(\frac{a}{4}, y, \frac{L}{2}\right) \propto \sum_{m=1}^{N} q_{\lambda,m} k_{y,m} \cos(k_{y,m} y),$$

$$\underline{B}_{\mu,101,z}\left(\frac{a}{4}, y, \frac{L}{2}\right) \propto \sum_{m=0}^{N} q_{\mu,m} \cos(k_{y,m} y).$$

From these expressions it can be seen that basically, $\underline{B}_{\mu,101,z}\left(\frac{a}{4}, y, \frac{L}{2}\right)$ shows a similar behaviour to $\underline{E}_{\mu,101,y}\left(\frac{a}{2}, y, \frac{L}{2}\right)$ and is thus directly proportional to the Fourier expansion series. However, it is not directly dependent on the relative permittivity function. This can also clearly be seen from comparing the figures 4.5 and 4.3; the normalised absolute electric and magnetic flux densities do look identical apart from the dependence of the electric field on the inverse relative permittivity, which causes the jump.

According to the upper simplifications, $\underline{B}_{\lambda,011,z}\left(\frac{a}{4}, y, \frac{L}{2}\right)$ should be dependent on the derivative of the Fourier expansion series. Additionally, there is no direct dependence on the relative permittivity visible in the analytic expressions. However, Fig. 4.4 clearly shows that the permittivity still influences the overall behaviour, seen in the dents that are visible between 0 and 3 mm and 15 and 18 mm in the graphical display of the magnetic flux density on the chosen axis. The reason for this is even with no clear proportionality of the fields to the relative permittivity, the Fourier expansion coefficients were still computed from the matrix equations (3.22) and (3.34), where some of the matrices do depend on the relative permittivity and thus indirectly influence the expansion coefficients and the final Fourier series.

### 4.2.3 Convergence Studies

As already stated in Chapter 3, both series expansions used for the wake function computations are only analytically correct as long as an infinite number of expansion functions is chosen. Should the series expansion be terminated after a finite number of terms, which in all realistic scenarios has to be the case, a series expansion only represents an approximation. The accuracy of this approximation is strongly dependent on the number of expansion functions used.

To assess the accuracy of the Rayleigh-Ritz expansion method for LSE and LSM modes, convergence studies regarding the eigenmodes of the previously introduced model structure have been conducted. Two criteria have been of importance here: first, the convergence of the eigenfrequencies calculated with WIzaRD towards a certain value for an increasing number of Fourier expansion functions, and second, the agreement with and convergence to the numerically obtained eigenfrequencies (computed with CST MWS).
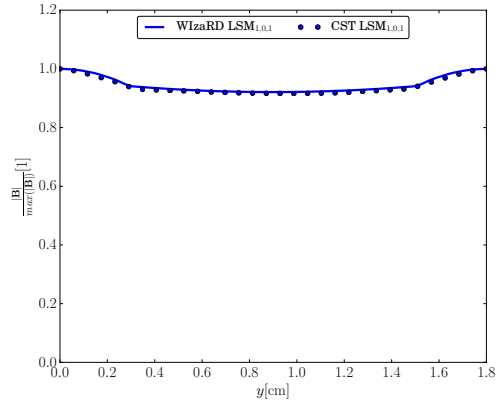
**Figure 4.4:** Normalised absolute magnetic flux density of the $LSE_{0,1,1}$ mode at the coordinates $x = a/4$ and $z = L/2$. The result computed with WIzaRD is compared to a simulation from CST MWS. The results computed with both methods agree well. Despite no clear dependence on the relative permittivity in the analytic expression, the magnetic flux density is clearly dependent on it, seen in the dents that the plotted field displays between 0 and 3 mm and 15 and 18 mm. Compared to the electric fields, the relative difference between both methods is higher here, though still $< 5\,\%$

**Figure 4.5:** Normalised absolute magnetic flux density of the $LSM_{1,0,1}$ mode at the coordinates $x = a/4$ and $z = L/2$. The result computed with WIzaRD is compared to a simulation from CST MWS. Both methods agree very well. According to the analytic expressions the magnetic flux density at this location shows a similar behaviour like the electric field displayed in 4.3 apart from the dependence on the relative permittivity function, which can be clearly seen from comparing the two graphs. The average relative difference between both methods is again $< 1\,\%$

For this purpose, the $LSE_{0,1,1}$ and $LSM_{1,0,1}$ modes of the model structure have been considered. In the case of the $LSM_{1,0,1}$ mode, the eigenfrequencies computed with WIzaRD for an increasing number of expansion functions are shown in Table 4.2.

Table 4.2 also contains the eigenfrequency computed with the eigenmode solver of CST MWS and 28,000 tetrahedral mesh cells[1] as a reference. Already from the numerical values alone it can be seen that while the results obtained with WIzaRD and the result from CST MWS lie very close together, they differ in the range of approximately a few percent. Additionally, it can be seen that the agreement between both values increases slightly for a larger number of expansion functions taken. This behaviour is visualised in Fig. 4.6.

A similar behaviour can be observed for the $LSE_{0,1,1}$ mode. The eigenfrequencies

---

[1]This number has been decided upon in a convergence study that will not be regarded further here.

| $N_{exp}$ [1] | f [GHz] |
|---|---|
| 5 | 2.61510802 |
| 10 | 2.61029354 |
| 15 | 2.60910998 |
| 20 | 2.60889413 |
| 25 | 2.60840116 |
| 30 | 2.60811633 |
| 35 | 2.60789646 |
| 40 | 2.60778679 |
| 45 | 2.60766262 |
| 50 | 2.60762101 |
| $f_{CST}$ | 2.606801 |

**Table 4.2:** Eigenfrequencies of the $LSM_{1,0,1}$ mode of the model structure computed with WIzaRD and an increasing number of Fourier expansion functions $N_{exp}$. The eigenfrequency computed with CST MWS (28,000 tetrahedral mesh cells) is displayed for comparison.

computed with WIzaRD converge to a certain value and show a high conformity with the CST MWS result, however, after reaching a minimum at 15 expansion functions, the agreement between both methods does in fact decrease again with an increasing number of expansion functions used (see Table 4.3 and Fig. 4.7). This behaviour of an increasing difference between the CST MWS and the WIzaRD result is, however, entirely uncritical. First, it is still very low (in the range of less than one percent). Second, since CST MWS is a numerical solver, the result calculated with it is an approximation as well, and can only be used as a reference, but should not be confused with the correct result. The computed eigenfrequency in CST MWS is also dependent on the type of mesh and the number of mesh cells, which has to be high enough so that the eigenmodes can be accurately calculated. The differing values of the frequencies computed with WIzaRD should therefore be taken as a quantitative confirmation of the effectiveness of the algorithms and programming of WIzaRD's mode computation rather than as a qualitative indicator of the accuracy of the method. The true, analytically correct eigenvalues remain unknown and can only be estimated. It has to be assumed, however, that due to being derived from two series expansions, the semi-analytic frequencies will eventually converge to the true analytic value.

Other aspects that have to be looked into are the accuracy and convergence of higher order modes. It will be shown later on that to accurately compute the wake function, especially eigenmodes with a high index $l$ have to be taken into account (c.f. Section 4.3.2), while both $n$ and $\tilde{m}$ can remain comparatively low. For this purpose, the convergence of the $LSM_{1,0,l}$ and $LSE_{0,1,l}$ modes have been plotted in
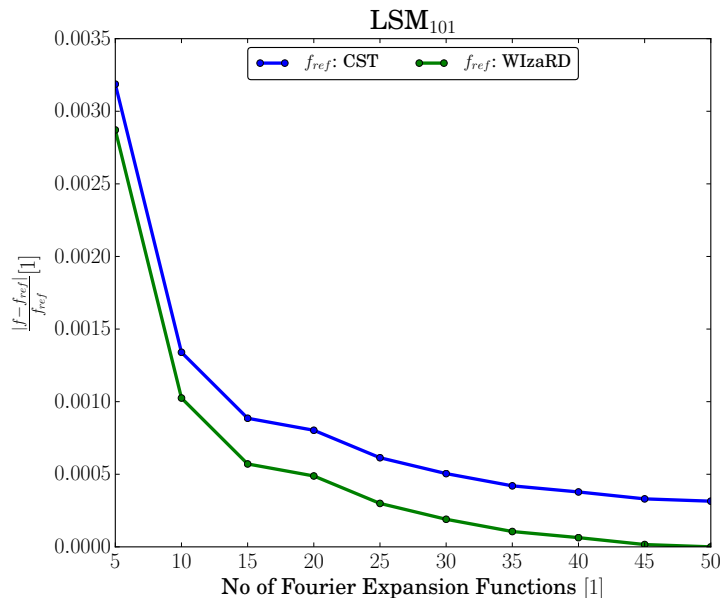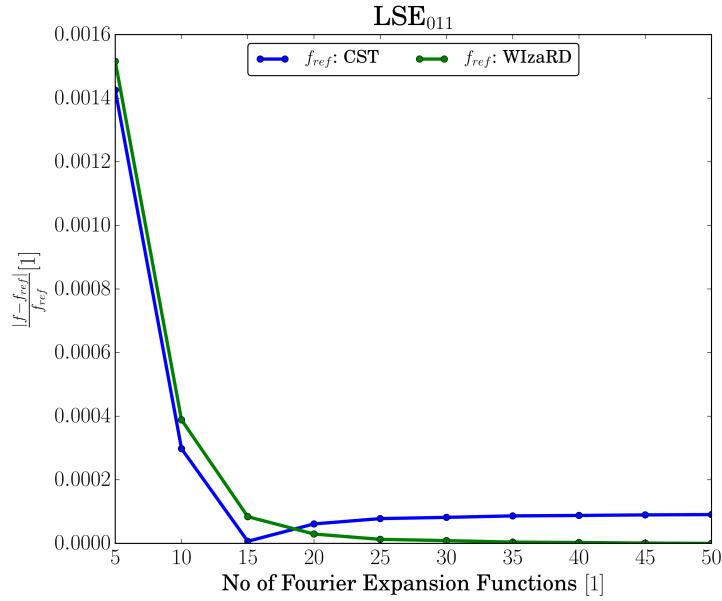
**Figure 4.6:** Relative difference of the eigenfrequency of the $LSM_{1,0,1}$ mode for an increasing number of Fourier expansion functions compared to a reference frequency $f_{ref}$ (blue: $f_{ref}$ calculated with WIzaRD and 50 expansion functions, green: calculated with CST MWS and 28,000 mesh cells). Both curves converge to a certain percentage ($< 0.01\%$ for CST MWS and $\ll 0.001\%$ for WIzaRD) with an increasing number of basis functions used.

Fig. 4.8 for an increasing number of expansion functions and $l = 1, 10, 100, 500$. It can be seen from both panels that while higher order modes generally need more expansion functions to obtain a converged result, the differences between the computed frequencies and the reference values quickly drop below 1%. For the observed LSM modes, this happens already at 15 expansion functions, for LSE modes even already above 10 expansion functions. Both numbers are still very low, and, on the greater scope of computing the wake function and thus a high number of modes, allow for the solution of the given eigenvalue problem in less than a second with WIzaRD[2].

When considering higher order modes, another difference between WIzaRD and CST MWS becomes apparent. The computation of eigenmodes in CST MWS needs at the very least an estimate of the expected frequency range. Additionally, computing solely higher order modes, e.g. the $LSM_{1,0,100}$ mode is difficult in nearly every solver setting as it, at the very least, requires an estimate for the frequency, as well. Modes with high frequencies also require a fine spatial grid spacing and thus a high number of mesh cells which will make the simulations computationally expensive.

---

[2]As a 'rule of thumb' it can be said that for 30-35 Fourier expansion functions, WIzaRD can calculate approximately 1,000 eigenmodes in one hour.

| $N_{exp}$ [1] | f [GHz] |
|---|---|
| 5 | 7.16928125 |
| 10 | 7.16120933 |
| 15 | 7.15902971 |
| 20 | 7.15863916 |
| 25 | 7.15851930 |
| 30 | 7.15945779 |
| 35 | 7.15845779 |
| 40 | 7.15844791 |
| 45 | 7.15843551 |
| 50 | 7.15842827 |
| $f_{CST}$ | 7.159077 |

**Table 4.3:** Eigenfrequencies of the $LSE_{0,1,1}$ mode of the model structure computed with WIzaRD and an increasing number of Fourier expansion functions $N_{exp}$. The eigenfrequency computed with CST MWS (28,000 tetrahedral mesh cells) is displayed for comparison.

This would be similar for any kind of discretisation method, as well. However, in WIzaRD, a mode can be solely calculated from the triple $(n, \tilde{m}, l)$ and the distinguishing between LSE and LSM modes. There is no grid spacing involved, and consequently, computing a higher order mode is exactly as computationally expensive as computing a lower order mode. This allows for a much faster computation of a very high number of modes up to a comparable accuracy, which is important for the later determination of the longitudinal wake potential following the eigenmode expansion ansatz.

## 4.3 Wake Function Computations

In this section, the computational aspects of the wake function calculation based on the eigenmodes are considered. Additionally, algorithms for an efficient sorting of eigenmodes and conditions that limit the number of modes that need to be calculated are introduced.

### 4.3.1 Calculating the Loss Factors

According to equation (3.56), the wake function can be calculated employing a superposition of simple cosines using the eigenmodes' eigenfrequencies and weighting them with the loss factors (3.57) and (3.58). The loss factors, in turn, are only dependent on geometric information about the dechirper structure, which are known from the start, and on the properties stored in the result vector of the eigenmode

**Figure 4.7:** Relative difference of the eigenfrequency of the $LSE_{0,1,1}$ mode for an increasing number of Fourier expansion functions compared to a reference frequency $f_{ref}$ (blue: $f_{ref}$ calculated with WIzaRD and 50 expansion functions, green: calculated with CST MWS and 28,000 mesh cells). Both curves converge to a certain percentage ($\approx 0.001\%$ for CST MWS and $\ll 0.001\%$ for WIzaRD) with an increasing number of basis functions used, however, the conformity between WIzaRD and CST MWS slightly drops after reaching a maximum at 15 expansion functions.

computation. All that remains to be done in WIzaRD is to distinguish between the eigenmode types, collect the necessary information from the result vectors of the mode computation and plug them into the expression (3.57) and (3.58). This can readily be implemented using *NumPy* and *SymPy*.

A number of result vectors for a number of eigenmodes is then combined into a result array, where a column is added at the end of the array that stores the calculated loss factors (c.f. Table 4.4).

| Type | $n$ | $\tilde{m}$ | $l$ | $q_{1,\lambda,\mu}$ | $q_{2,\lambda,\mu}$ | ... | $q_{N,\lambda,\mu}$ | $\kappa_{\lambda,\mu}$ |
|------|-----|-----|-----|------|------|-----|------|------|
| LSM | 1 | 1 | 1 | $q_{1,\mu}$ | $q_{2,\mu}$ | ... | $q_{N,\mu}$ | $\kappa_{\mu}$ |
| LSE | 1 | 2 | 4 | $q_{1,\lambda}$ | $q_{2,\lambda}$ | ... | $q_{N,\lambda}$ | $\kappa_{\lambda}$ |

**Table 4.4:** Structure of the result array, now updated to store the loss factors, as well (indicated in green).
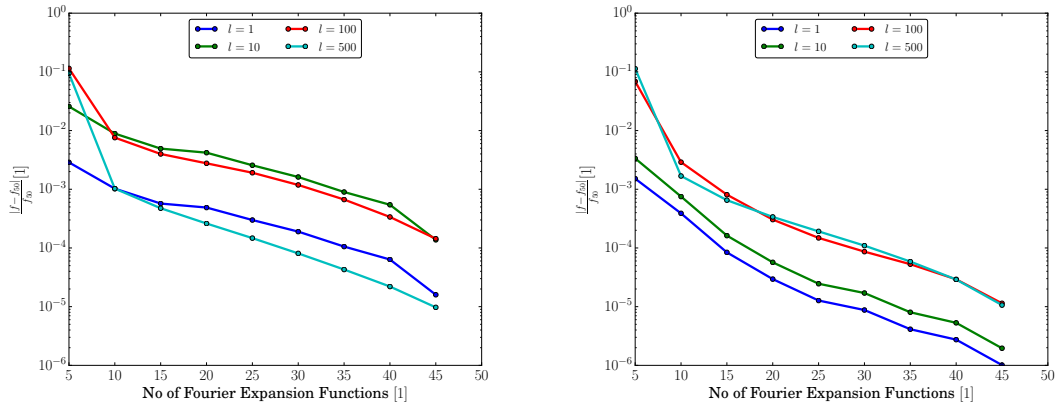
**Figure 4.8:** Semi-logarithmic plot of the relative difference of the eigenfrequencies of different $LSM_{1,0,l}$ (left panel) $LSE_{0,1,l}$ modes (right panel) for an increasing number of Fourier expansion functions compared to the result obtained with 50 basis functions. Modes with a higher $l$ show less conformity with fewer expansion functions, however, above 10 expansion functions used, the difference between the computed frequencies drops below 1% for every mode.

## Mode Sorting

Computations of the wake function by a set of eigenmodes need the set of modes to be sorted in some form to make the superposition of the wake function less arbitrary. Especially terminating the series expansion after a certain number of eigenmodes needs to obey a certain regularity or order, which can be granted if the modes are sorted by ascending frequency. In that manner, using 100 eigenmodes to approximate the wake function will not refer to 100 arbitrary modes, but to the 100 eigenmodes with the lowest eigenfrequencies.

One difference of WIzaRD, if compared to CST MWS for example, is that it needs the input of the triple $(n, \tilde{m}, l)$ to calculate the properties of a mode. While this is not a disadvantage in itself, it results in WIzaRD being unable to calculate a number of modes according to their eigenfrequencies in ascending order without further considerations.

If the eigenfrequencies would be easily predictable like in the case of TE and TM modes (c.f. equation (2.55)), this sorting of modes could be done by a suited algorithm that iterates through combinations of $n$, $\tilde{m}$ and $l$ and sorts the resulting eigenfrequencies in ascending order without actually having to calculate the eigenmodes. As a second step, the generated list of modes in ascending order could then be used as a basis to compute the actual mode properties and then the loss factors.

Since, however, the expressions of the eigenfrequency of LSE and LSM modes are not as simple and depend internally also on the Fourier expansion coefficients, both

the mode computations and the sorting according to their eigenfrequency need to be done simultaneously. Here it is important to be as efficient as possible, since the eigenmode calculation is the most computationally expensive subroutine of WIzaRD.

The first important aspect that can be exploited here is the fact that also for LSE and LSM modes, a triple $(n', \tilde{m}', l')$ indicates a mode with a higher frequency than a mode denoted with the triple $(n, \tilde{m}, l)$ if either of the three indices is larger than for the mode it is compared to; so either $n' > n$, $\tilde{m}' > m$ or $l' > l$. This is readily provable for $n$ and $l$, as the wave numbers

$$k'_x = \frac{n'\pi}{a} > \frac{n\pi}{a} = k_x \text{ if } n' > n,$$
$$k'_z = \frac{l'\pi}{L} > \frac{l\pi}{L} = k_z \text{ if } l' > l,$$

also increase for increasing $n$ and $l$. For $\tilde{m}$, it was already chosen such that a higher $\tilde{m}$ would indicate a mode with a higher frequency. Since this is the case, starting with the eigenmodes that have the lowest eigenfrequencies and subsequently increasing the indices will also make sure that modes with increasing frequencies are calculated.

According to the considerations made in the previous section, the lowest possible eigenmodes are the $LSM_{1,0,1}$ mode and the $LSE_{0,1,1}$ mode. However, according to the specifications made in Chapter 3.4, only modes with odd $n$ and odd $\tilde{m}$ contribute to the wake function due to symmetry reasons. Calculating modes with even $n$ and $\tilde{m}$ is thus not necessary, and skipping these modes entirely will safe computational effort. Since zero can be considered an even number here, the eigenmodes with the lowest eigenmodes that will be needed for the wake function computation are the $LSM_{1,1,1}$ mode and the $LSE_{1,1,1}$ mode.

Increasing either index of either mode will result in a mode with a higher eigenfrequency. Also resulting from the considerations in Chapter 3.4, it is unnecessary to increase $n$ and $\tilde{m}$ in steps of 1, as all even indices can be skipped here. Thus, $n$ and $\tilde{m}$ will be increased by 2 to generate higher order modes.

Thus, theoretically, each of the basis modes indicated by the triple $(1, 1, 1)$ leads to three higher order modes, one for increasing either index: the modes denoted by the triples $(3, 1, 1)$, $(1, 3, 1)$ and $(1, 1, 2)$. However, it is still unclear which of these modes, in turn, has the lowest eigenfrequency. Depending on the geometry and the relation between $a$ and $L$, a statement can be made regarding whether an increase in $n$ or $l$ will lead to the mode with the higher frequency. On the other hand, such an assessment cannot easily be made for the increase in $\tilde{m}$ due to no concrete formulation for $k_y$ being available. The only way of reliably determining which of these modes has the lowest frequency is actually calculating it.

Additionally, it can be deduced that this method of successively increasing the indices of a mode will quickly give rise to a vast number of higher order modes that need to be considered, since for every chosen mode, three indices can be increased to generate a higher order mode.
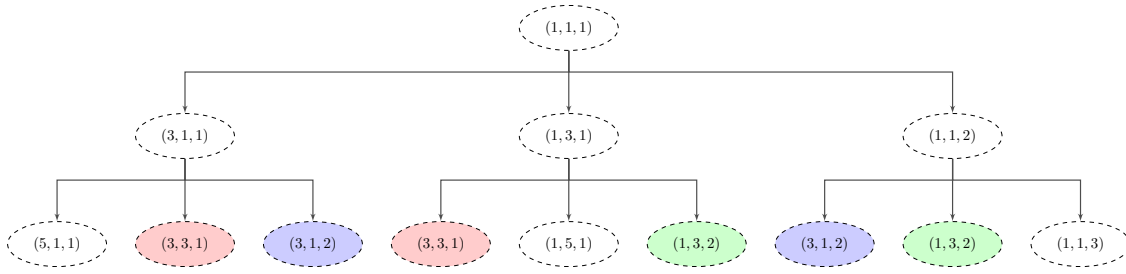
**Figure 4.9:** Tree diagram of the successive increasing of mode indices, exemplary for the triple ($n = 1, \tilde{m} = 1, l = 1$) for two steps. Each mode gives rise to three successively following higher order modes, from which several, however, denote identical modes (marked with colours).

This is shown in Fig. 4.9. It can also be seen from this schematic that simply increasing the indices might lead to overlapping cases: the triple $(3, 3, 1)$ (marked red in the figure), for example, can either be generated by first increasing $n$ and then increasing $\tilde{m}$, or vice versa.

To avoid having to compute modes several times due to these ambiguous cases, WIzaRD uses a mode pool: here, all triples of indices for which the eigenfrequency has already been calculated are stored. If a new triple is considered, it can first be compared to the pool to guarantee that the mode is, indeed, new, and has not already been considered before.

The practical approach to the mode sorting is thus as follows: First, the two basis modes $\text{LSE}_{1,1,1}$ and $\text{LSM}_{1,1,1}$ are computed. All of their relevant properties (the result vectors displayed in Table 4.1) are stored in the mode pool. The pool is then sorted with respect to ascending frequencies, so that the first mode in the pool has then to be the lowest eigenmode that needs to be considered for this structure. This mode is then moved to the result array with all its properties. The indices of this mode are then increased successively, and the three resulting modes for $n + 2$, $\tilde{m} + 2$ and $l + 1$ are calculated and moved to the pool. The pool is sorted in ascending order with respect to the frequencies again and then, the first mode of the pool is moved to the result array. The indices of this mode are again increased successively and the generated indices of the higher order modes are compared to the indices of the modes already in the pool. Only if the modes are not already in the pool, the properties of the mode are computed. Once the new modes are found, the pool is again sorted and the lowest mode is moved to the result array and so on. This circle of computations can then be readily broken off if the desired number of modes has been calculated. This procedure is schematically shown in Fig. 4.10[3]. The resulting array of modes stored together with their properties is then expanded by another

---

[3]This approach will later be refined using the velocity condition and it will also be slightly altered to make the programming more efficient. The general sorting algorithm and procedure using the pool, however, will stay the same.
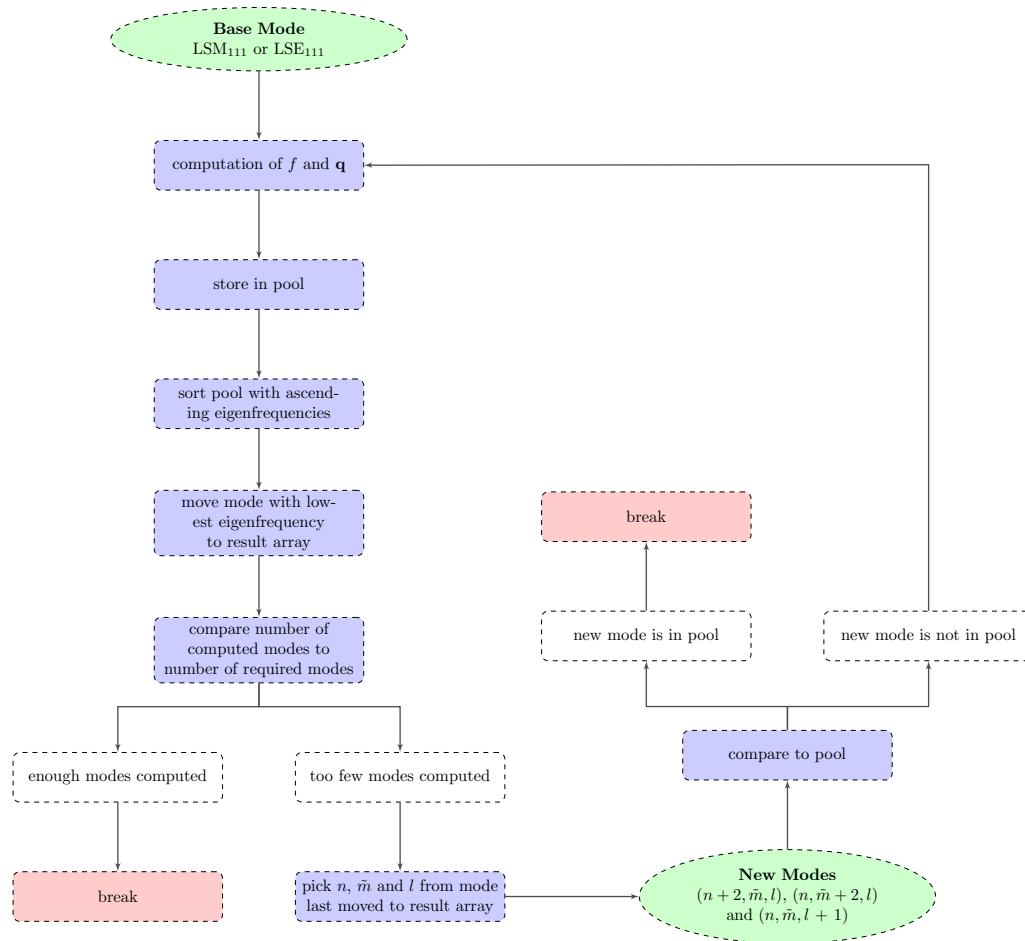
**Figure 4.10:** Schematic overview of the general mode sorting algorithm.

column where the calculated loss factor is stored, like displayed in Table 4.4.

## 4.3.2 Loss Factor Analyses

To guarantee the efficiency of WIzaRD, the accuracy of the computations performed with it needs to be balanced with the computational demand. A number of conditions and properties can be used to drastically reduce the computational effort. First, as stated in Section 3.4, due to their symmetry a large number of modes do not contribute to the wake function. In WIzaRD, this is employed by simply not calculating these modes, which are anticipated to not contribute to the wake function due to their wavenumbers in $x$-, $y$- and $z$-direction.

A second condition that can be exploited derives from the modes' different phase velocities and strongly influences the value of the loss factors.

**The Velocity Condition**

According to the equations (3.57) and (3.58), the final expressions of the loss factors are both indirectly proportional to the term $k_{0,\lambda,\mu}^2 - k_z^2$. The wave number of the respective eigenmode can be transformed such that it depends on the eigenfrequency of the mode

$$k_{0,\lambda,\mu}^2 - k_z^2 = \frac{\omega_0^2}{c_0^2} - k_z^2.$$

The considerations made for the loss factor calculation are based on a point charge moving in longitudinal direction. The phase velocity of the modes can be expressed as

$$v_{ph} = \frac{w_0}{k_z},$$

and thus the denominator of both (3.57) and (3.58) can be rewritten as

$$k_{0,\lambda,\mu}^2 - k_z^2 = \omega_0^2 \left( \frac{1}{c_0^2} - \frac{1}{v_{ph}^2} \right).$$

After some further transformations, it can be deduced that

$$k_{0,\lambda,\mu}^2 - k_z^2 = \frac{\omega_0^2}{c_0^2 v_{ph}^2} \left( v_{ph}^2 - c_0^2 \right).$$

This expression approaches 0 if $v_{ph} \to c_0$, which has also been reported in [65]. Since the loss factors are indirectly proportional to this expression, it can be concluded that the loss factors can be expected to reach significantly higher values should the phase velocity of the eigenmode in question approach the speed of light.

This behaviour can be seen in Fig. 4.11. In the left panel, the loss factors of some of the LSM modes of the model structure are plotted against their longitudinal wave number $k_z$. The modes are distinguished by $n$ and $\tilde{m}$, effectively parting them into different series of modes. In the figure it can be seen that each of these series of increasing $k_z$ possesses a maximum value in form of a peak-like behaviour. Compared to the phase velocities, plotted on the right panel in form of the frequency over the longitudinal wave number, these peaks coincide with the modes which exhibit a phase velocity close to the speed of light (dashed line). Additionally the figure shows that there is no single mode with a phase velocity equal to the speed of light, i.e. the graphs do not show single, sharp maxima. Instead, the maxima are broader, meaning a number of modes exhibit phase velocities around (but not equal to) the speed of light. This is due to the numerical calculation of the modes, and results in more eigenmodes having a large influence on the wakefield than just a single one. Additionally, the condition $v_{ph} = c_0$ would also lead to $k_{0,\lambda,\mu} = k_z$ and thus to an infinite loss factor because the denominators in the equations (3.57) and (3.58) would be zero. This is not possible in practise.
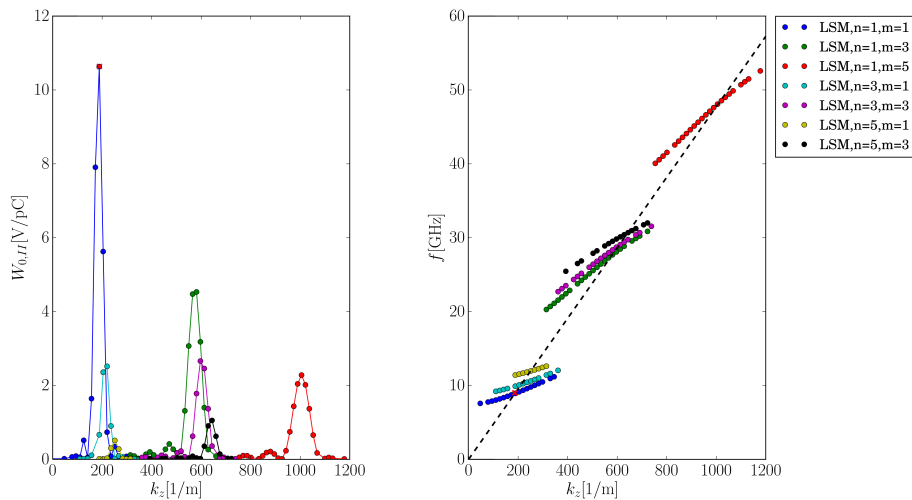
**Figure 4.11:** Left panel: Loss factors of different LSM modes of the model structure modes plotted against their wave number in $z$-direction. Right panel: Frequencies of the same modes plotted against their wave number in $z$-direction and compared to the speed of light (dashed line). All modes are distinguished by their indices $n$ and $\tilde{m}$. Comparing both panels it can be seen that the highest values of the loss factors correspond to the modes with phase velocities close to the speed of light. For convenience, the first of these correspondences is marked with a red x symbol.

That this velocity condition directly results from the loss factor calculations without further previous assumptions supports the functionality of the applied model. This behaviour is advantageous in two different ways for computations with WIzaRD: First and foremost, eigenmodes with phase velocities far lower or far larger than the speed of light are obviously not going to deliver high loss factors compared to the modes which mainly contribute to the wake function and thus, can be excluded from calculations. Second, also visible in Fig. 4.11, there is a high number of modes with loss factors far lower than the ones which contribute most. One example would be the last modes of the $n = 1$, $\tilde{m} = 5$ series in the figure (red). The mode that apparently contributes the most to the wake function is one of the $n = 1$, $\tilde{m} = 1$ series (blue), with a loss factor approximately four times larger than for the last modes of the $n = 1$, $\tilde{m} = 5$ series. These large differences between the highest contributions to the lowest contributions to the wake function can be exploited, too; to make the final superposition of the wake function computationally more effective. For this, an additional filter can be used to eliminate all modes which have insignificant loss factors compared to the largest contributions to the wake function. This is done in WIzaRD by employing a threshold (c.f. Section 4.4.1); in most cases it has been shown to be enough to include modes which have loss factors within a range of three orders of magnitude from the mode that contributes the most. This filtering algorithm has also been used on the data Fig. 4.11 is based on.

### 4.3.3 Using the Velocity Condition to Improve WIzaRD

To exploit the condition that only modes with a phase velocity close to the speed of light contribute to the wake function, the scheme presented in Fig. 4.10 needs to be modified.

Here, one of the most important deductions from the loss factor analysis is that the modes can be distinguished into series with the same $n$ and $\tilde{m}$ and that from these series only a small number of modes with certain $l$ are going to contribute to the wake function. The mode with the highest contribution is going to be the mode where $k_z = l\pi/L$ is closest to $k_0$. If this mode can be determined, a fixed number of modes with higher and lower $l$ can be computed additionally to increase the accuracy of the superimposed wake function.

Theoretically, this procedure is similar to determining the root of the problem $k_0 = k_z$, and a simple method like the bisection method (c.f., [87]) would suffice to solve it. However, this is not strictly necessary since the actual root of the problem can also be represented analytically: In the hypothetical case that $k_z = k_0$, the phase velocity of the mode would equal the speed of light. In that case, in the right panel of Fig. 4.11, the frequency of the mode would be located directly on the dashed line indicating the speed of light. This corresponding, 'ideal' frequency of the mode (the root of $k_z = k_0$) can be determined as

$$k_{0,\text{ideal}} = k_z$$
$$c_0\omega_{\text{ideal}} = \frac{l_{\text{ideal}}\pi}{L}$$
$$f_{\text{ideal}} = \frac{c_0 l_{\text{ideal}}}{2L}, \tag{4.10}$$

where it is not guaranteed that $l_{\text{ideal}}$ is an integer.

A simple solution of $k_0 = k_z$ and a later approximation of $l_{\text{ideal}}$ with an integer is, however, also not possible. The reason for this is that varying $l$ will also change the matrix equations (3.22) and (3.34) from which the expansion coefficients of the Fourier expansions are determined by changing the system matrices. The influence of this on the total wavenumber cannot be estimated a priori, such that the determination of the mode with an index $l$ closest to $l_{\text{ideal}}$ becomes an iterative problem for a series of $n$ and $\tilde{m}$.

To solve this problem, a similar approach like the bisection method is employed. A starting index $l_1$ is set (in the beginning, this is $l_1 = 1$), and a second index $l_2$ is chosen in a distance $\Delta l$ to $l_1$. For this second index, the eigenfrequency and the Fourier expansion coefficients are calculated as it has been described in Section 4.2.1. This frequency $f_2$ is then compared to the 'ideal' frequency of a mode with the given $l_2$ and a phase velocity equal to the speed of light,

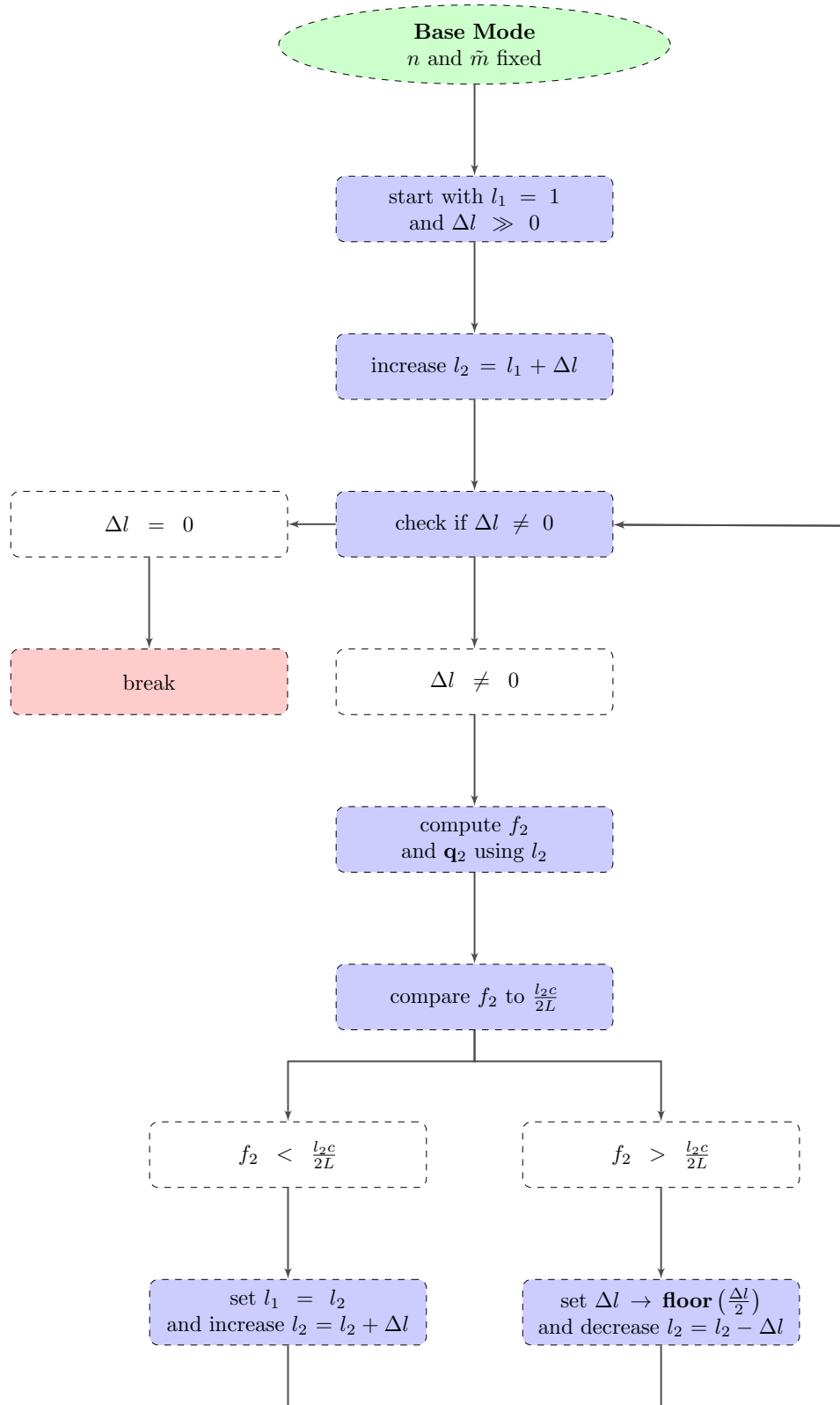$$f_{\text{ideal}} = \frac{c_0 l_2}{2L}. \tag{4.11}$$

**Figure 4.12:** Schematic overview of the algorithm used to determine the eigenmode with the phase velocity closest to the speed of light.

If $f_2 < f_{\text{ideal}}$, the frequency $f_2$ lies below the dashed line in Fig. 4.11, which means that the phase velocity is lower than the speed of light. Since the frequency is monotonously increasing with the index $l$, $l_2$ needs to be increased to approach the speed of light. Therefore, in this case, the interval between $l_1$ and $l_2$ is shifted by $+\Delta l$, and the procedure is repeated.

If $f_2 > f_{\text{ideal}}$, the frequency $f_2$ is above the dashed line in Fig. 4.11, the phase velocity is higher than the speed of light. In this case, the upper limit of the integral needs to be decreased. Here, $l_2$ is shifted by floor $(\Delta l/2)$, where floor indicates that $\Delta l/2$ is rounded down to the next integer value (to guarantee that $l_1$ and $l_2$ remain integers at all times).

This procedure is then repeated until the stepsize $\Delta l$ reaches zero. A schematic display of this method is presented in Fig. 4.12.

Test runs of WIzaRD show that for practical purposes, it is reasonable to choose the stepsize large (usually $\Delta l = 1000$), since apart from the eigenmodes with low $n$ and $\tilde{m}$, all series of transversal indices show modes with a phase velocity close to the speed of light for very high $l$ ($l = 400 - 1000$ for most modes in Fig. 4.11).

After WIzaRD has found the modes of a series denoted by the indices $n$ and $\tilde{m}$ which exhibit the phase velocity closest to the speed of light, it additionally calculates a number of modes above and below the determined $l$. This accounts for the broader peak structure displayed in the left panel of Fig. 4.11, so for modes with a comparatively high loss factor and thus a high contribution to the wake function. In total, only a fraction of the modes in a series denoted by $n$ and $\tilde{m}$ have to be calculated in that way, which significantly reduces the computational effort. All others can safely be assumed to have far too high or low phase velocities to couple to the beam.

To implement this algorithm into WIzaRD, the schematic procedure shown in Fig. 4.10 has to be modified accordingly. The updated diagram can be found in figure 4.13. The first modification is not to address a single mode by the triple $(n, \tilde{m}, l)$, but a series of modes by $n$ and $\tilde{m}$. For this series, the mode with the phase velocity closest to the speed of light is determined, and this mode is then stored in the pool. The indices $n$ and $\tilde{m}$ are then successively increased just as before, and the created higher order modes are compared to the pool. If they are already stored, nothing is done. If not, the mode with the highest loss factor is found by the described algorithm and this mode is then also stored inside the pool.

When modes have been added to the pool, it is again sorted by ascending frequencies, and the mode with the lowest frequency is moved to the result array. A fixed number of modes with higher and lower $l$ are then computed and stored in the result array as well. In this way, only the modes with the highest loss factors are stored inside the pool, which reduces its size significantly. Additionally, a higher number of modes relevant to the wake function can be computed in a smaller fraction of time.

To optimise the later wake function calculation, an additional filter sorts out modes with insignificant contributions to the wake function.
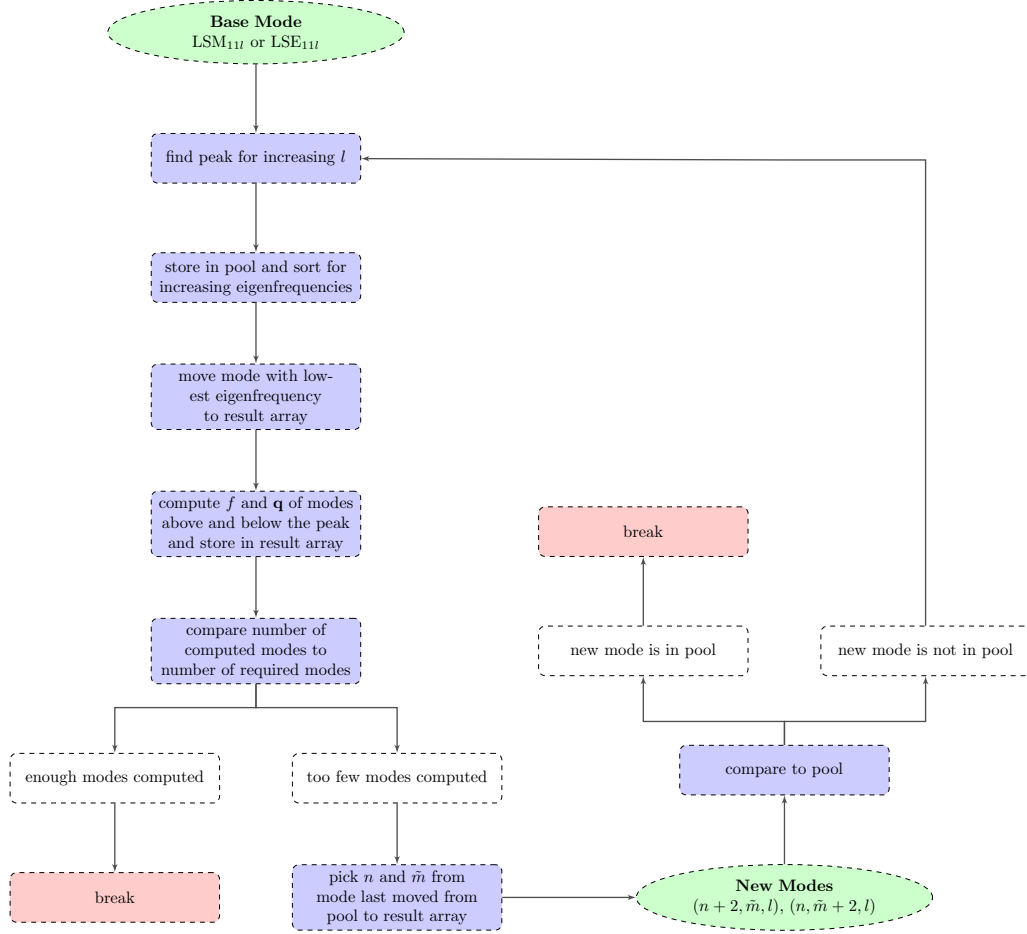
**Figure 4.13:** Updated general mode calculation algorithm of WIzaRD focussing on the computation of modes relevant to the wake function.

## 4.3.4 Green's Function Calculations

Once the loss factors are determined for a number of eigenmodes of increasing eigenfrequencies, the wake function can be determined by using equation (3.56). The capabilities of *SymPy* allow for a symbolic implementation of (3.56), including the case differentiation. This symbolic representation is then numerically evaluated using *NumPy* and the loss factors stored in the result vector of the mode analysis. The total wavenumber is also extracted from this array.

Up until this point, no spatial discretisation has been used to compute either the eigenmodes or the loss factors, and the repeated use of *SymPy* makes the use of discretisation for this step unnecessary as well.

An exemplary Green's function (wake function) for the model structure used throughout this section can be found in Fig. 4.14. The case differentiation of the wake function with respect to the position of the field generating charge and the test

charge can be also seen from the figure: If $s < 0$, the wake function is set to 0 in the *SymPy* implementation, resulting in a sharp jump at $s = 0$. The value at $s = 0$ is multiplied by $1/2$ to obey the fundamental theorem of beam loading, though this is not easily visible in the figure. In Fig. 4.14, 35 Fourier expansion functions were
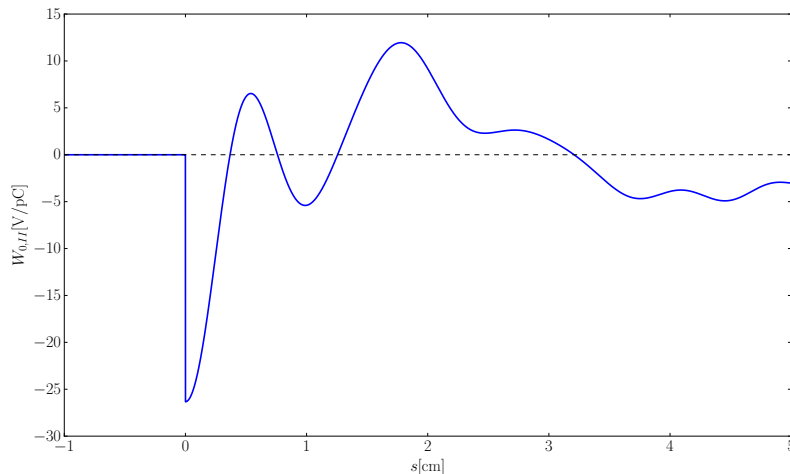


**Figure 4.14:** Wake function of the model structure calculated with WIzaRD. The wake function was generated using 35 Fourier expansion functions per eigenmode and a total number of 408 eigenmodes.

used to calculate the eigenmodes, and 408 modes were superimposed for the wake function calculation. This can be considered a moderately accurate approximation in terms of the number of eigenmodes used (a closer inspection of the accuracy of WIzaRD with respect to the number of eigenfunctions used can be found in the next sections). Should the number of eigenmodes used prove insufficient, the work procedure of WIzaRD allows for the additional calculations of more modes. For this purpose it is only necessary to store the pool in a separate file, so that it simply needs to be read in by the mode calculating subroutine and used as a basis for a repetitive cycle of the procedure shown in Fig. 4.13.

## 4.4 Wakefield Convergence Studies

In this section, the convergence of the wake function, and later the wake potentials for a number of Gaussian particle beams, will be considered. Again, two different reference values for calculations done with WIzaRD are important here, the first being the overall convergence of WIzaRD itself, the second one being the convergence with respect to results computed with CST PS.

## 4.4.1 Wake Function Convergence

This section is going to use the wake function of the exemplary structure introduced in this chapter.

### Convergence with Respect to the Number of Eigenmodes

As explained in the previous section, WIzaRD is implemented in a way such that only the eigenmodes with the potentially highest contribution to the wake function (i.e. the ones with a phase velocity close to the speed of light) are calculated. Additionally, a filter that can be run separately can be used to sort out the modes with the comparatively lowest contributions. This filter operates using a threshold of the ratio of the loss factor of a mode compared to the highest loss factor calculated for the structure

$$\frac{\kappa_{\lambda,\mu}}{\kappa_{\max}} = T_{\max},$$

where the value for the threshold, $T_{\max}$, can be chosen freely. If not stated otherwise, this threshold is set to $T_{\max} = 10^{-3}$, so a deviation from the maximum value of three orders of magnitude is allowed. This has proven sufficient in a great number of structures observed.

A first indicator of the wake functions convergence with regard to the number of eigenmodes taken into consideration is the number of eigenmodes after the filter is applied. For the example examined in the following, the eigenmodes of the model structure have been determined in blocks of 700 modes (i.e. 20 series of different $n$ and $\tilde{m}$ with 35 modes each). After each block of modes, the loss factors have been calculated and then the mode filter has been applied.

| $\mathbf{N_c}$ | $\mathbf{N_f}$ |
|---:|---:|
| 700 | 138 |
| 1,400 | 231 |
| 2,100 | 256 |
| 2,800 | 327 |
| 3,500 | 390 |
| 4,200 | 402 |
| 4,900 | 408 |
| 5,600 | 408 |
| 6,300 | 408 |
| 7,000 | 408 |

**Table 4.5:** Number of eigenmodes of the model structure computed with WIzaRD ($N_c$) compared to the number of modes after filtering ($N_f$).

Table 4.5 shows how many of the calculated modes passed the filter with an applied

threshold of three orders of magnitude. It can be seen that while at first, each new block of eigenmodes computed also has a significant contribution to the eigenmodes passing the filter, the number of 'new' modes after filtering with each added block decreases significantly between 3,500 and 4,900 source modes and then stagnates. This behaviour strongly hints at a lessened contribution of higher order modes to the wake function. Figure 4.15 visualises this in the left bar diagram, showing the number of new modes passing the filter compared to the maximum number of modes used to calculate the wake function (408).
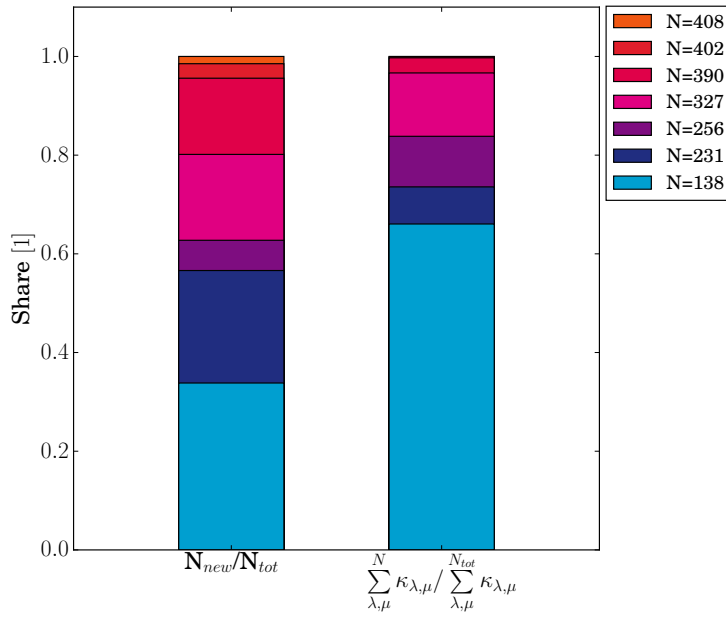


**Figure 4.15:** Left bar diagram: Number of new modes compared to the maximum/total number of modes passing the filter. Right bar diagram: Contribution of the modes passing the filter to the wake function at $s = 0$ normalised to the wake function at $s = 0$ and the total number of 408 modes considered

The right bar diagram in Fig. 4.15 additionally shows the significance of the calculated modes for the wake function. For this diagram, the wake function is evaluated at $s = 0$ for an increasing number of modes used for computations. This specifies equation (3.56) as

$$W_{||}(s) = \frac{1}{2} \sum_{\lambda,\mu} \kappa_{\lambda,\mu}.$$

The result is then normalised to the value of the wake function at $s = 0$ and 408 modes taken into consideration. This diagram gives insight into the overall strength of the summed up loss factors in the computed and filtered blocks. It shows that for this model, more than 60% of the value of the wake function at $s = 0$ comes from modes of the first block, so modes of a comparatively low order and frequency, but

it also shows that the contributions of the following blocks of higher order modes are not negligibly small. Even the contribution of the last six modes (the 402nd to 408th modes) is in the range of a few percent. However, for a good estimation of the strength of the wake function at $s = 0$ with more than 80% accordance to the converged result, 256 modes after filtering are sufficient. This corresponds to the calculation of a total number of 2,100 modes, which can be done on a regular desktop PC in about two hours.
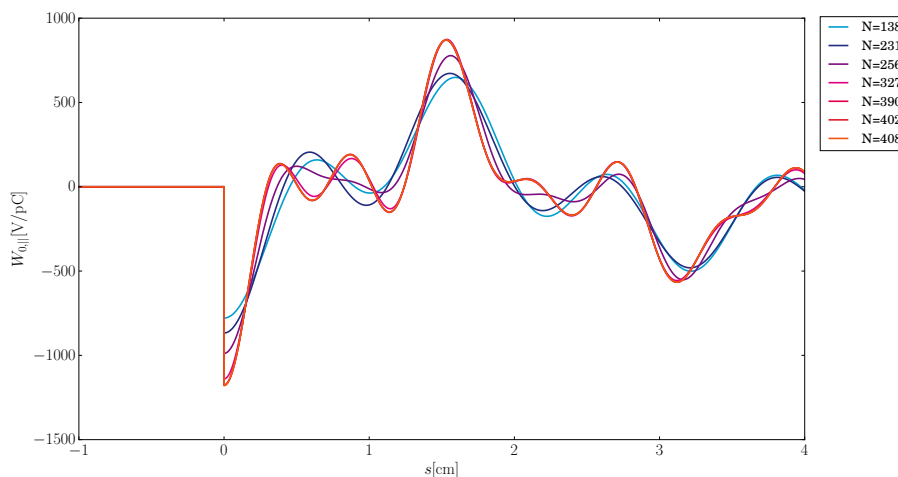


**Figure 4.16:** Wake function of the model structure for an increasing number of eigenmodes used for the superposition.

In the greater scope of the full wake function it becomes apparent that considering higher order modes is essential for the accuracy of the wake function. Figure 4.16 shows the wake function of the model structure for increasing the numbers of modes used for the computation in the same sequence as above. The behaviour shown in the right diagram of Fig. 4.15 is here visible, too, at $s = 0$. What is more important here, however, is the behaviour of the wake function over $s^4$, which differs drastically for a low number of eigenmodes used (138, 231, 256) compared to the maximum number of eigenmodes, 408. Starting with the use of $N = 327$ eigenmodes, the computed wake functions start to resemble each other more closely, and it can clearly be seen that the following wake functions converge to the wake function for the maximum number of eigenmodes. 327 modes after filtering correspond to the calculation of a total number of 2,800 modes, and compared to the right diagram in Fig. 4.15, this means an agreement of $\approx 90\%$ for the value of the wake function at $s = 0$.

---

[4]The interval used in Fig. 4.16 is with $[-1\,\mathrm{cm}, 5\,\mathrm{cm}]$ small compared to the length of the waveguide. Since for the later use as a dechirper mostly short-ranged wakefields are of interest, it is sufficient to examine a region close to $s = 0$, though.

## 4.4.2 Wake Potential Computations

As it has been stated in the previous chapter in equation (3.59), the wake potential of an arbitrary bunch shape can be determined via a convolution of the bunch shape function with the wake function. The wake potentials are determined in WIzaRD by using a spatially discrete convolution of the *SciPy* module. For this step, it is also necessary to project the computed wake function onto a spatial grid, since a symbolic convolution might be possible in theory using *SymPy*, put to practise this, however, is impractical due to the long computational times and the high computational effort for a symbolic convolution. This is the first step in the chain of computational steps in WIzaRD that makes a spatial grid for the wake function necessary.

In this section, two different Gaussian bunches (3.60) centred around $s_0 = 0$ are going to be considered for further convergence studies, one with $\sigma = 3\,\mathrm{mm}$ and another with $\sigma = 0.3\,\mathrm{mm}$.

The results obtained with WIzaRD are then compared to the results computed with CST PS, whenever possible.

**Qualitative Comparisons**

At first, the wake potentials of the Gaussian bunch with $\sigma = 3\,\mathrm{mm}$ are going to be examined for an increasing number of eigenmodes used for the computation of the wake function. The sequence in which the number of modes are increased is the same that was used before, resulting from the filtering of subsequent blocks with 700 modes of increasing eigenfrequencies calculated. Figure 4.17 shows the resulting
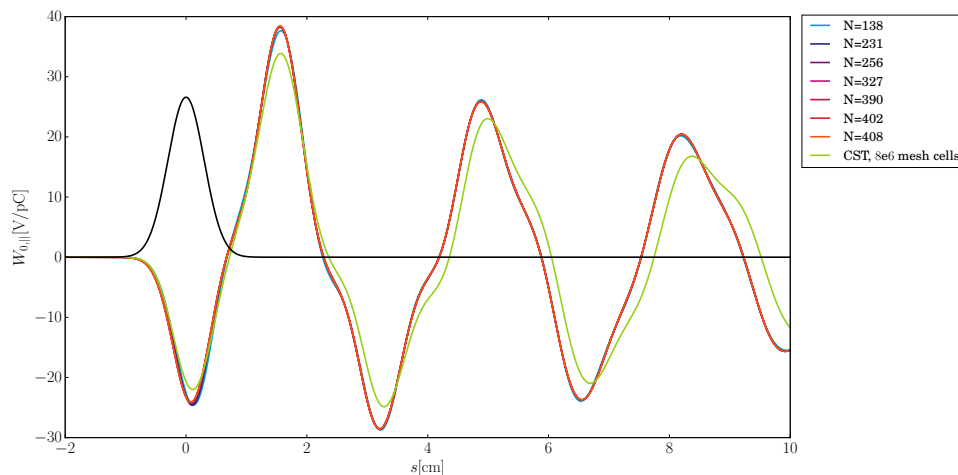


**Figure 4.17:** Wake potential of Gaussian bunch with $s_0 = 0$ and $\sigma = 3\,\mathrm{mm}$ for the model structure for an increasing number of eigenmodes used for the superposition of the wake function. The result is compared to the wake potential computed with CST PS. The shape function of the particle beam is shown in black.

wake potentials compared to the result obtained by using CST PS with $\approx 8{,}000{,}000$ hexahedral mesh cells. The shape function of the bunch is plotted in black. It can be seen in the figure that the overall agreement between the different wake potentials computed with WIzaRD seems to increase. While for the Green's function shown in Fig. 4.16 the differing number of eigenmodes used for the superposition of the wake function also result in an overall differing behaviour of the wake functions, all wake potentials computed with WIzaRD in Fig. 4.17 exhibit the same overall behaviour, only subjected to minor fluctuations. This clearly has to be the result of the convolution: the used Gaussian pulse is with $\sigma = 3\,\mathrm{mm}$ comparatively broad, and the convolution effectively smoothes the rapidly oscillating behaviour of the original wake function.

In comparison to CST PS there are differences in both the magnitude of the extrema and the position of the zeros of the wake potential. The result obtained with CST PS shows extrema that are lower than their WIzaRD counterparts by a few V/pC. The position of the zeros is shifted towards slightly higher $s$ for the CST PS result, and this shift increases towards zeros that are located further away from $s = 0$. In analogy to a regular sine or cosine oscillation, it could be said that the wake potential calculated with CST PS has a slightly lower amplitude and a slightly higher frequency, resulting in the increasing disagreement in the positions of the zeros compared to the WIzaRD result. This difference, however, only becomes critical for positions further away from $s = 0$. In the example used here and in every case considered for the dechirper, the beam will be operated in the single bunch mode or with a very low beam current to grant a high distance between the bunches. This means that only the short range wake potential in direct proximity of the bunch itself is important for the considerations of the dechirper. In the proximity of the bunch (plotted in black in Fig. 4.17), the only relevant difference between the CST PS and the WIzaRD result is the slightly different magnitude of the first extremum, since the first zero of both results match well.

For a smaller Gaussian bunch with $\sigma = 0.3\,\mathrm{mm}$, the calculation of the wake potential with CST PS becomes more complicated. The reason for this is that the small bunch lengths compared to the length of the structure makes a very fine spatial resolution of the grid in $z$-direction necessary. The resulting number of grid cells is too high to be handled on the same desktop PC that was used for the WIzaRD computations and was thus omitted. This also highlights another advantage that WIzaRD has over CST PS - due to the computation of the Green's function wakefield, it is possible to derive any form of wake potential by a simple convolution. These convolutions are not limited by the size of the bunch and even bunches with a small length compared to the dimensions of the structure are possible. Additionally, as is going to be investigated in the following chapter, the wake potentials of other beam shapes, such as double Gaussians or flat-top pulses, can also be derived from the wake function calculated in WIzaRD, while CST PS only allows for the computation of wake potentials of Gaussian bunches.
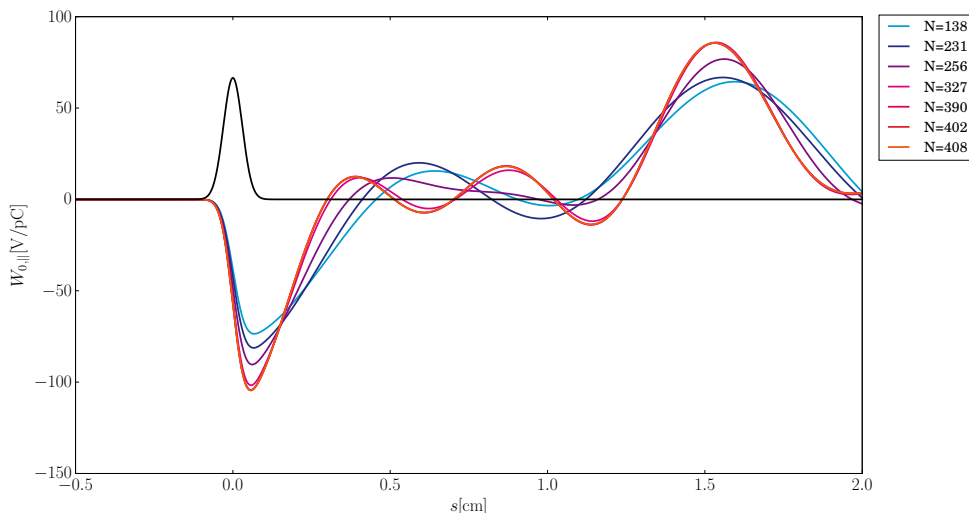
**Figure 4.18:** Wake potential of Gaussian bunch with $s_0 = 0$ and $\sigma = 0.3\,\mathrm{mm}$ for the model structure for an increasing number of eigenmodes used for the superposition of the wake function. The shape function of the particle beam is shown in black.

Figure 4.18 shows the wake potentials for a Gaussian bunch with $\sigma = 0.3\,\mathrm{mm}$ calculated from the wake function of the model structure and the same sequence of increasing the number of eigenmodes. The smoothing due to the convolution with a bunch shape carries less weight here due to the smaller bunch lengths, so that the differences in the overall behaviour of the wake potential depending on the used number of eigenmodes are still easily visible. In fact, if not due to Fig. 4.18 displaying only the interval $[-0.5\,\mathrm{cm}, 2.0\,\mathrm{cm}]$ (compared to $[-1.0\,\mathrm{cm}, 4.0\,\mathrm{cm}]$ in Fig. 4.16), the wake potential of this Gaussian bunch would exhibit a very similar, if scaled, behaviour compared to the original wake function. Consequently, like in Fig. 4.16, it can easily be seen that the result up until $N = 256$ eigenmodes has not converged and shows greater discrepancies towards the result computed with the maximum number of eigenmodes used, the result computed with $N = 408$ eigenmodes.

Important to note for both bunches, however, is that due to the behaviour of the wake function at $s = 0$, the wake potential will for this example always display a negative slope over the length of the bunch. This is independent from the actual length of the bunch, which is a result from the convolution and will be observed in more detail at a later point. This negative slope corresponds to an energy loss over the beam, which is what finally will give rise to the effect of the dechirper.

### Quantitative Comparisons

A purely visual comparison of the wake functions and potentials for different numbers of eigenmodes is a weak criterion to judge the accuracy of the simulation. The

convergence studies conducted here would greatly benefit from a numerical figure of merit.

Therefore, the quantity

$$\Delta = 1 - \frac{\int\limits_0^L \left| W_{||}\left(s\right) - W_{||,ref}\left(s\right) \right| \mathrm{d}s}{\int\limits_0^L \left| W_{||,ref}\left(s\right) \right| \mathrm{d}s} \tag{4.12}$$

is introduced. This basically measures the difference of the wake potentials' areas in relation to the area of the reference wake potential $W_{||,ref}\left(s\right)$ (either the potential computed with CST PS or the WIzaRD result with the highest number of eigenmodes). This is now evaluated numerically for the wake function and potentials discussed previously using the trapezoidal rule to determine the integrals.
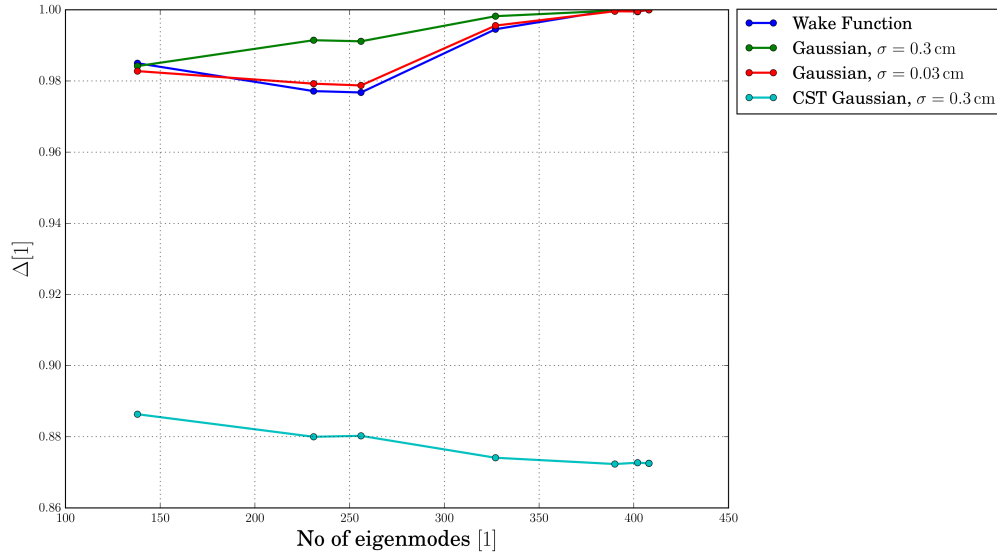


**Figure 4.19:** Accuracy of different wake functions and potentials for the model structure and different references. The reference wake function/potential is the WIzaRD example for the highest number of eigenmodes unless stated otherwise (light blue curve, CST PS).

Figure 4.19 shows the accuracy with respect to equation (4.12) for the wake function of the model structure and the derived wake potentials for Gaussian bunches with $\sigma = 0.3\,\mathrm{mm}$ and $\sigma = 3\,\mathrm{mm}$ as well as the convergence to the CST PS result for the Gaussian bunch with $\sigma = 3\,\mathrm{mm}$.

It can be seen in the figure that the accuracy of WIzaRD computations compared to CST PS is considerably lower than the accuracy of WIzaRD computations compared to each other. It ranges between $\approx 87\%$ and $\approx 89\%$, and even decreases with for an increasing number of eigenmodes used for the WIzaRD computations. This also goes

together with Fig. 4.17, where the visual difference between the CST PS and the WIzaRD example are easily visible. A reason for this discrepancy is the increasing shift in the position of the zeros of the CST PS example.

The accuracies of the examples calculated with WIzaRD, on the contrary, vary between $\approx 97\%$ and $> 99\%$, even for the wake function and the wake potential of the $\sigma = 0.3$ mm Gaussian pulse. The accuracies overall increase with an increasing number of eigenmodes used for the superposition of the wake function. Additionally, going together with the observations from the last section, the accuracy of the $\sigma = 3$ mm Gaussian pulse wake potential (green) is overall slightly higher due to the bunch length of the Gaussian pulse smoothing out the more rapid oscillation of the wake function.
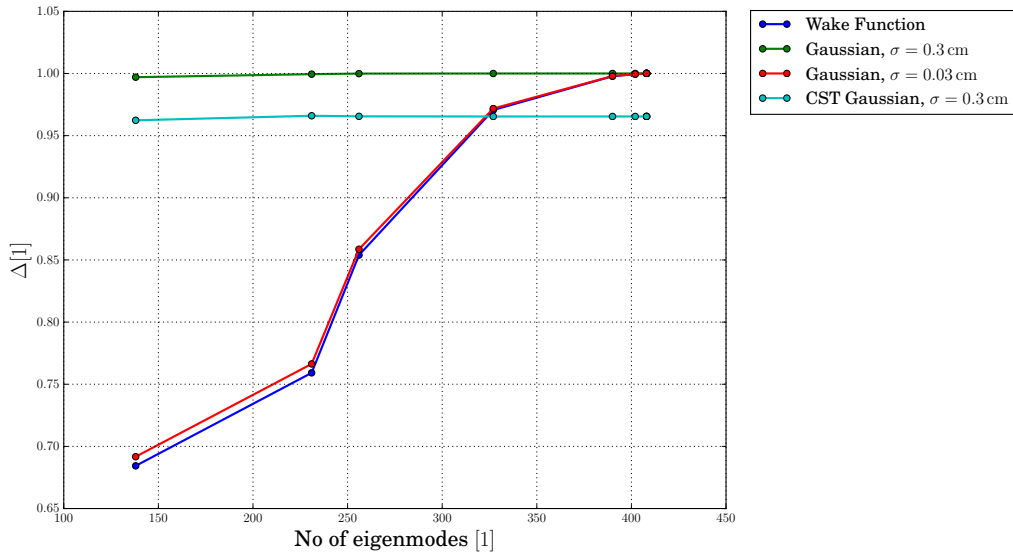


**Figure 4.20:** Accuracy of different wake functions and potentials for the section $-3\sigma < s < 3\sigma$, computed for the model structure and different references. The reference wake function/potential is the WIzaRD example for the highest number of eigenmodes unless stated otherwise (light blue curve, CST PS).

Figure 4.20 shows a second convergence study with respect to equation (4.12) and for the same wake functions and potentials used in the previous figure, this time, however, limited to the section $-3\sigma < s < 3\sigma$, so the area directly around the particle bunch as the area most important for the operation of the dechirper. Here it becomes even clearer that the wake potentials of the broader bunch with $\sigma = 3$ mm (green) do not vary much for an increasing number of eigenmodes because the convolution smoothed out the high oscillations and differences of the original wake function (blue). Both, the wake function and the wake potential of the smaller Gaussian pulse (red) show a significant increase in accuracy with an increasing number of eigenmodes, starting with an accuracy of $< 70\%$, but reaching more than

95% using 256 eigenmodes (filtered; 2,800 unfiltered). While the wake potential of smaller Gaussian pulse shows always a little better accuracies than the wake function, both curves behave very similarly and lie close together. Additionally, the curve of the wake potential of the broader Gaussian pulse compared to CST PS (light blue) shows a significantly greater accuracy (always > 95%) than in Fig. 4.19, where it had been computed over the complete length of the dechirper. This confirms that the discrepancies result from the increase in the shift of the zeros of the wake potential calculated with CST PS compared to the WIzaRD version. The smaller section observed in this figure, on the other hand, only includes the first zero of both versions, which still lie very close together. In other words, the shift is of less importance in this example and thus for the observation of short-range wakefields.

### 4.4.3 Wake Potential Convergence with Regards to the Number of Fourier Expansion Functions

With the underlying routines of selective mode calculations, mode sorting and filtering in WIzaRD, the convergence analysis of the wake function or wake potentials for an increasing number of Fourier expansion functions used is difficult. The reason for this is that changing the number of Fourier expansion functions for the eigenmode calculations will also change, obviously, the eigenfrequency, which has also been shown before. WIzaRD is optimised in a way that the mode calculation is implemented such that only modes relevant to the wake function with ascending frequencies are calculated. A slight shift in the eigenfrequencies, due to a different number of Fourier expansion functions used for their calculation, can change the order in which the eigenmodes are calculated. It can also change which mode will be found to have the phase velocity closest to the speed of light, and lastly, it will change the loss factors.

This is why calculating a fixed number of modes with the optimised version of WIzaRD is *not* guaranteed to lead to the same modes being calculated for two different setting for the Fourier expansions. If, e.g., 2,800 modes are calculated with 25 Fourier expansion functions, these are not necessarily the same 2,800 modes which are computed if 30 Fourier expansion functions have been used. The change of the number of Fourier expansion functions will also change a number of other parameters, that in the current operation of WIzaRD cannot be kept constant while still maintaining its efficiency.

A convergence study of the wake function or wake potentials with respect to the number of Fourier expansion functions has thus to be handled with care. It is done here for the model structure used in this chapter. The previously used 25 expansion functions have been increased in steps of 5 until 50 Fourier expansion functions have been used for the eigenmode computation. The number of modes used for each wake function was determined by looking at the number of modes after the filtering with a

threshold of $10^3$ and stopping to compute new modes once this number did not change any longer (i.e. once only irrelevant modes were added in further calculations). This obviously resulted in a differing number of eigenmodes used for each wake function in the following study.
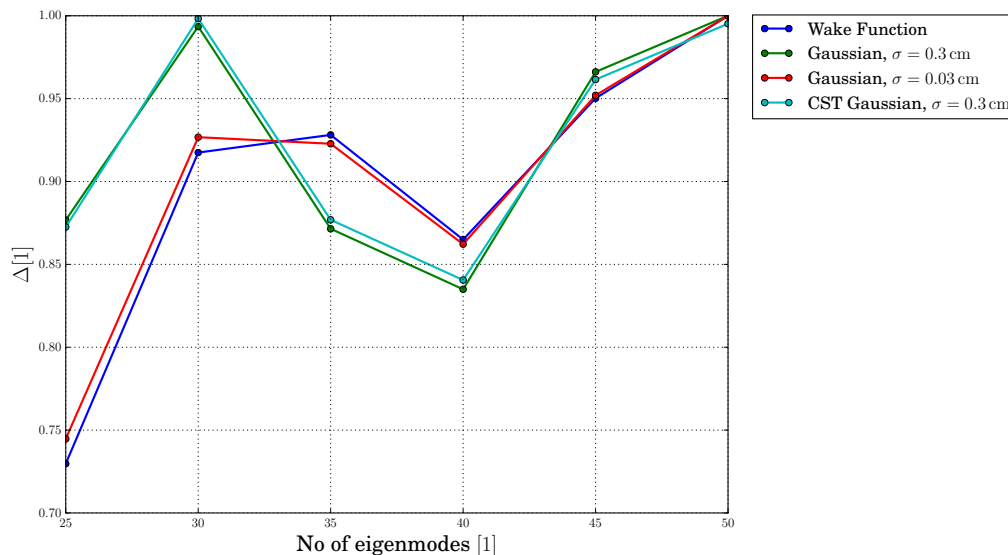


**Figure 4.21:** Accuracy of different wake functions and potentials for the section, computed for the model structure and different references. The reference wake function/potential is the WIzaRD example for the highest number of Fourier expansion functions unless stated otherwise (light blue curve, CST PS).

Figure 4.21 shows the convergence analysis for the wake function, the wake potentials of Gaussian bunches with $\sigma = 0.3\,\mathrm{mm}$ and $\sigma = 3\,\mathrm{mm}$ compared to the WIzaRD result for 50 Fourier expansion functions, and the wake potential of a Gaussian bunch with $\sigma = 3\,\mathrm{mm}$ compared to a completely numerical result from CST PS. The graphic shows that the behaviour for an increasing number of Fourier expansion functions is not monotonous. In fact, the highest accuracy is reached for the Gaussian pulse with $\sigma = 3\,\mathrm{mm}$ for both references at 30 Fourier expansion functions ($\gg 95\%$). For the wake function and the Gaussian pulse with $\sigma = 0.3\,\mathrm{mm}$, the result for 45 Fourier expansion function ($\approx 95\%$) has the highest agreement with the reference wakefield, whereas the result for 35 expansion function is not significantly worse ($\approx 93\%$).

No extrapolation can be done using this data, and no predictions can be made as to which number of Fourier expansion functions delivers the most accurate result due to reasons stated above. Even so, Fig. 4.21 can still be understood as a pointer as to which number of Fourier expansion functions appears to be the most suited and efficient for further computations. At 30 Fourier expansion functions, all four graphs show an agreement of more than 90 % with the reference value. Increasing

this number further will either make the accuracy drop or at least stop to increase significantly. Additionally, computations with 30 Fourier expansion functions are still very fast. The wake function computation for this case can be done in about five hours on a regular desktop PC with a sufficient number of eigenmodes used. For 50 Fourier expansion functions, this time is easily tripled, while the accuracy gain is clearly not, even if the convergence study from above needs to be treated with care. Increasing the number of Fourier expansion functions used above the value of 30 is therefore not efficient.

Additional studies with other dechirper geometries have shown that indeed, 25 - 35 Fourier expansion functions for the wake function computations deliver highly accurate results compared to the references (either CST PS or more computationally expensive WIzaRD results) and can usually be done in about the same time. So while Fig. 4.21 most certainly cannot give a clear idea about the convergence behaviour of wake functions with regards to the number of Fourier expansion functions, it still shows that using 30 expansion functions is a safe and efficient choice for further computations.

## 4.5 Summary

In this chapter, the programme package WIzaRD has been introduced together with the general algorithms and routines for the eigenmode calculation and selection. Additionally, the symmetry and velocity conditions have been explained and used for a further gain in efficiency of the programme package WIzaRD. Benchmarks against purely numerical solvers such as CST and convergence studies demonstrate that both series expansions can be cut off after a reasonably low number of expansion functions while still maintaining a high accuracy of the results.

All points considered, the greatest advantage of the model described is that it presents a possibility to obtain an analytical description of the Green's function wakefield. This is mainly possible because of the comparative simplicity of the structure, and it enables a fast calculation of a multitude of wakefields of different bunch shapes by means of a simple convolution. Additionally, for the use in beam tracking software like, e.g., ELEGANT [41], the input of the wakefield of a point charge is necessary. Employing purely numerical software this is usually emulated by using the wakefield of a very short Gaussian bunch, which is intrinsically inaccurate and introduces a systematic error right from the beginning. Adopting a semi-analytical approach, this specific error can be avoided, making this method preferable due to the feasible stopping criteria of the expansions.

# 5 Parameter Studies with WIzaRD

In this chapter, the influence of the geometrical parameters of the dechirper on the wake function will be studied. Additionally, in a second step, the wake potentials of different bunches will be calculated to study the influence of the bunch characteristics on the wake potential and gain a first perspective insight into the principle of operation of the dechirper with regards to different beam situations.

For this purpose, the model structure used in the previous chapter will be slightly modified, such that now

$$a = 5 \, \text{cm},$$
$$b = 1.8 \, \text{cm},$$
$$d = 1.5 \, \text{cm},$$
$$L = 80 \, \text{cm},$$
$$\varepsilon_r = 6.$$

Compared to the model structure in Chapter 4, this dechirper is four times as long and is identical to the prototype build and operated at ELBE. A more technical and detailed explanation on why these values were chosen can be found in Chapter 6. For the moment, this structure will merely serve as a basis for the parameter variations.

## 5.1 Geometrical Parameters

In this section, the main focus of the parameter studies are the geometrical characteristics of the dechirper, i.e. the length and width of the structure, the properties of the dielectric coating (thickness and material, i.e. relative permittivity) and the gap width between the two dielectric plates.

The wake function is always, if not noted otherwise, evaluated and compared at the position $s = 0$. This is the point at which, no matter the actual shape of the wake function or potential, the absolute value of the wakefield is always comparable to other examples studied in this chapter. The absolute value of the wake function at this point is also what will later have a large influence on the absolute value of the wake potential for an arbitrary bunch shape.

As the overall strength of the wake function is dependent on the loss parameters (3.57) and (3.58). Despite having an analytic expression for them at hand, though, a prediction of the behaviour of the wake function for a variation of the geometry based off of these expressions is difficult and hardly feasible. The middle term in both

expressions is dependent on the expansion coefficients of the Fourier expansion, which are analytically unknown. For a very small number of Fourier expansion functions these coefficients could still be expressed analytically by solving the underlying matrix equations, but this is not reasonable due to low numbers of Fourier expansion functions not delivering the accuracy needed for these parameter studies. It is thus hard to predict how a change of parameters will influence the expansion coefficients analytically. Since in that way, the behaviour of one term in the expression of the loss parameters remains unknown, a full analytic calculation of the expected behaviour of the wake function for variations of the geometry of the dechirper is hardly reasonable.

### 5.1.1 Length of the Dechirper

The first parameter to be studied in this section is the length of the dechirper. The length of the dechirper coincides with the propagation direction of the particle beam and therefore can safely be assumed to have a large influence on the overall wake function. Different sources show that a linear behaviour of the strength of the wake function with an increase in length can be expected. Indeed, it can even be assumed that doubling the length of the dechirper will also double the maximum strength of the wake function, c.f. e.g. [55].

Additionally, the length is, like in the case of ELBE (c.f. Chapter 6), the parameter most susceptible to become subject to the spatial limitations of the accelerator site. It thus becomes crucial to know how much such spatial requirements actually can limit the achievable maximum strength of the wake function so that these can be balanced out by the other properties of the dechirper, if possible.

For this study, the length of the dechirper has been varied between $0.10 \, \text{m}$ and $4.0 \, \text{m}$ in non-equidistant steps.

Figure 5.1 shows the values of the longitudinal wake function at $s = 0$ for increasing dechirper lengths (blue). The values have been computed with WIzaRD and are compared to a fit with a linear function performed with Python (red). Apart from the very first value at $L = 0.1 \, \text{m}$, all data points align nearly perfectly to the fitted function. Additionally, in Fig. 5.2, it can be seen that not only the value at $s = 0$, but the whole wake function scales with the length. The position of the zeros and the overall behaviour of the wake function stays the same with an increase in the length of the dechirper, merely the absolute values of the local extrema are scaled up. The expression of the fitted linear function is

$$W_{0,\parallel}\left(s = 0, L\right) = -497.5268 \frac{\text{V}}{\text{pC} \cdot \text{m}} \cdot L - 5.7446 \frac{\text{V}}{\text{pC}}.$$

Denoting the first value as an outlier (not depicted in Fig. 5.1) changes this expression only very slightly to

$$W_{0,\parallel}\left(s = 0, L\right) = -499.2780 \frac{\text{V}}{\text{pC} \cdot \text{m}} \cdot L - 1.8852 \frac{\text{V}}{\text{pC}}.$$
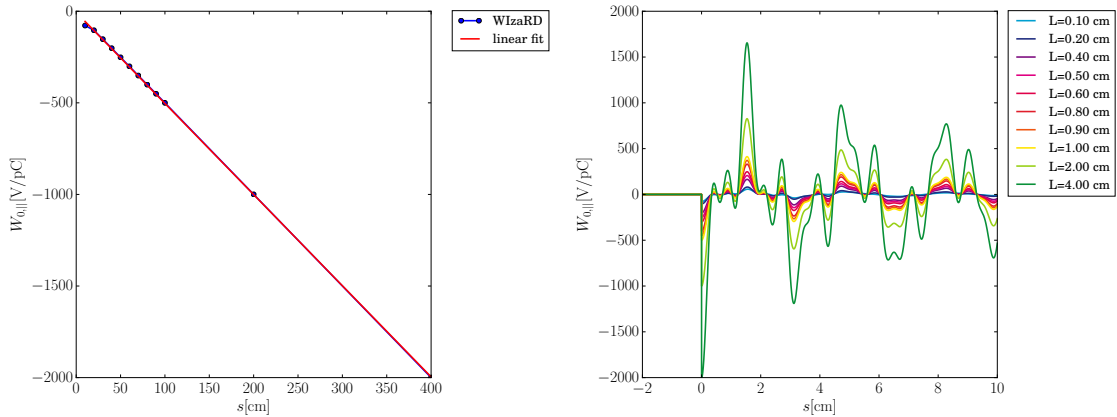
**Figure 5.1:** Longitudinal wake function at $s = 0$ calculated with WIzaRD for various dechirper lengths (blue) compared to a linear fit (red) of the data points performed with Python. The behaviour of the strength of the wake function with the length of the dechirper is clearly linear.

**Figure 5.2:** The linear behaviour of the wake function with an increase in the dechirper length manifests itself in a clear scaling of the total wake function, i.e. the overall shape of the wake function and the positions of the zeros do not vary with an increase in length, though the absolute values of the local extrema do.

From both linear fits it can already be deduced that scaling the length of the dechirper by an arbitrary factor $A$ will also scale the resultant strength of the wake function by nearly the same factor. Reason for this is that the products of the functions' slopes with the inserted length is much larger than the vertical intersect of both functions for dechirper lengths larger than a few centimetres.

To confirm this behaviour, table 5.1 contains the actual data points of the longitudinal wake functions at $s = 0$ computed by WIzaRD (middle column) compared to a value $W^*$ (third column) that is gained from scaling up the previous entry with respect to the length of the dechirper,

$$W^*_{i+1} = \frac{L_{i+1}}{L_i} W_{0,||,i}(0).$$

Again, apart from the very first value (here for $L = 0.2\,\mathrm{m}$) the values actually computed by WIzaRD and the values gained by scaling up the previous WIzaRD result match very well.

Following these studies, it can be concluded that the initially assumed linear behaviour of the wake function with the length of the dechirper can be seen and reinforced by the calculations done with WIzaRD. This is important in two ways: First, it establishes the variation of the length of the dechirper as a comparatively easy way to increase (or decrease, if needed) the effect of the dechirper; and it also shows that a simple scaling of the wake function with respect to the length is enough

| $L$ [m] | $W_{0,\|}(0)$ [V/pC] | $W^*$ [V/pC] |
|---|---|---|
| 0.10 | $-77.9875$ | $-$ |
| 0.20 | $-103.8499$ | $-155.9750$ |
| 0.30 | $-152.5166$ | $-155.77485$ |
| 0.40 | $-201.8129$ | $-203.3555$ |
| 0.50 | $-251.6977$ | $-252.2661$ |
| 0.60 | $-300.9559$ | $-302.0372$ |
| 0.70 | $-351.0260$ | $-351.1152$ |
| 0.80 | $-400.5592$ | $-401.1726$ |
| 0.90 | $-450.4429$ | $-450.6291$ |
| 1.00 | $-500.0755$ | $-500.4921$ |
| 2.00 | $-999.6559$ | $-1000.9844$ |
| 4.00 | $-1999.9136$ | $-2001.9684$ |

**Table 5.1:** Values of the longitudinal wake function at $s = 0$ calculated with WIzaRD for various dechirper lengths (middle column), the underlying data points of Fig. 5.1. The third column shows the values for the longitudinal wake function at this point as they could have been expected by scaling the previous data point with respect to the length. Apart from scaled value at $L = 0.2$ m, both columns match very well.

to calculate the wake function of a different dechirper. For future dechirper projects, this basically makes parameter studies with respect to the length obsolete, the results can simply be scaled.

Second, and more important, though, is that the linear behaviour of the wakefield with the length of the dechirper is a well-known phenomenon also studied for different dechirper types, like circular structures with corrugations [55]. That WIzaRD is able to replicate this behaviour nearly perfectly substantiates the used algorithms and programming structures introduced in the previous chapters once more and thus also provides a benchmark for the validity of the following parameter studies, where there are no previous studies to compare to.

## 5.1.2 Width of the Dechirper

There are no previous studies that describe the behaviour of the wake function of a dielectrically lined rectangular waveguide with an increase in the width of the dechirper. Consequently, only predictions and assumptions can be made regarding the outcome of this parameter study.

Since the width coincides with one of the transversal directions of the wakefield, and for the longitudinal wake function only the point $a/2$ is of significance, it can be expected that the effect of varying the width of the structure will only have a small influence on the strength of the wake function. Intuitively, it can even be assumed

that for larger widths of the structure less changes to the wake function will happen when the width is increased even further, since the only area in which the fields have a big influence on the wake function is the one close to the beam. For larger widths, greater parts of the dechirper are further away from the beam.

For this study, the width of the dechirper has been varied between $1.0\,\mathrm{cm}$ and $15.0\,\mathrm{cm}$ in non-equidistant steps.
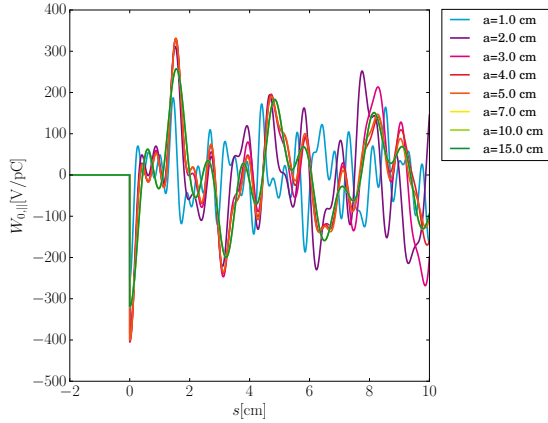


**Figure 5.3:** Total wake functions for an increasing width of the dechirper. In contrast to the behaviour for an increasing dechirper length in Fig. 5.2, the wake function does not simply scale up with an increase in the studied parameter.
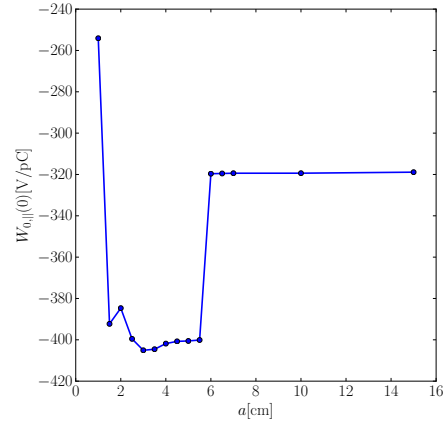
**Figure 5.4:** Longitudinal wake function at $s = 0$ calculated with WIzaRD for various dechirper widths. The graph shows a local extremum between 3 and 5 cm. For larger widths, the absolute value of the longitudinal wake function at $s = 0$ changes only insignificantly.

Figure 5.3 shows the different wake functions of the dechirper for varying the width of the structure. It becomes apparent that in contrast to the variation of the length of the dechirper, the wake function is this case is not simply scaled with respect to the width. The overall behaviour of the wake function, the positions of the extrema and zeros change drastically in this parameter study. This means that in this scenario the wake functions are only comparable at $s = 0$. Since for the purposes of the later application of the dechirper at ELBE only the short-range wakefields are important, such a comparison appears sufficient.

The comparison of the values of the wake functions at $s = 0$ are shown in Fig. 5.4. In this figure it can be seen that for small widths, widening the structure will result in an increase in the absolute value of the wake function at $s = 0$ until a maximum strength is reached between 3 and 6 cm. After that, the absolute value decreases again. For larger width, Fig. 5.4 shows that, indeed, no significant gain or loss can be reached by further increasing the width. For practical applications this means that there is nothing to be gained from a very wide dechirper. Instead, there is apparently an optimal width that corresponds to the maximum absolute value of

the wake function strength at $s = 0$. In the case of the structure build at ELBE, the chosen width of 5 cm lies in that optimal range.

## 5.1.3 The Dielectric Coating

The generation of a wakefield inside the considered structures is only possible due to the dielectric coatings and the lower propagation velocity of electromagnetic waves inside these materials. The dielectric is thus the most important distinguishing characteristic of these types of dechirper. Two parameters play a role here; first, the actual material of the dielectric and thus its relative permittivity, and second the thickness of the coating. On the flipside, however, choosing the appropriate material and thickness is also highly dependent on outside factors: There is no continuous spectrum of relative permittivities to choose from, instead, a selection of a suitable coating for the designated purpose is limited to which materials are practically available and in which thicknesses these materials can be manufactured.

This naturally also puts constraints on the parameter studies performed for these two characteristics. Without going into the technical aspects (c.f. Chapter 6 for more information on this topic), for this study it showed to be sufficient to observe the range of permittivities between 2 and 20, which correspond to materials like FR4 and a number of easily available glass ceramics, but also encompass diamond which has been suggested as a coating material for a dechirper already in [59]. The range with the most practical applicability here is within a few millimetres of thickness, such that the dielectric coating can actually be handled like a separate and solid plate that is later mounted to the metallic waveguide. Smaller thicknesses far below 1 mm require different preparations that were not considered as a solution for ELBE, like thermal evaporation for very thin dielectric films.

Figure 5.5 actually shows that with an increase in the relative permittivity, the maximum absolute value of the wake function at $s = 0$ decreases. This means that to achieve a dechirper effect as high as possible, materials of low relative permittivities, like FR4 (where the permittivity varies depending on the composition and the fabricator, but is generally $\varepsilon_r \approx 5$), diamond (with $\varepsilon_r \approx 6$) and some ceramics with low permittivities, while ceramics with higher permittivities between 15 and 20 are less favourable considering their comparatively lower maximum absolute values for the wake function at $s = 0$.

Considering the thickness of the material, Fig. 5.6 shows no clear regular or periodic behaviour with an increase in thickness, apart from an overall tendency that indicates that higher thicknesses are more likely to result in lower maximum absolute values at $s = 0$. This indicates that thinner coatings seem to be favourable, though in any case, a parameter study should be conducted once the other parameters have been set to ensure an optimal gain. It is worth mentioning, however, that the chosen material thickness of 3 mm coincides with a local extremum in the graph displayed in Fig. 5.6 and thus, for this particular structure, with the most favourable material
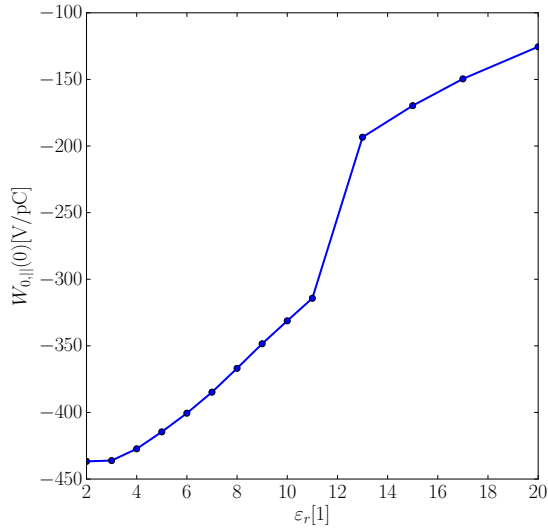
**Figure 5.5:** Longitudinal wake function at $s = 0$ calculated with WIzaRD for various relative permittivities, i.e. different coating materials. At $s = 0$, the absolute value of the wake function decreases with an increase in the relative permittivity.
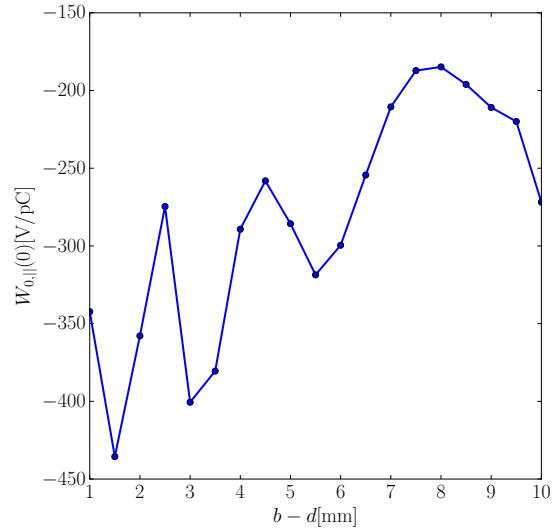
**Figure 5.6:** Longitudinal wake function at $s = 0$ calculated with WIzaRD for an increasing thickness of the dielectric coating. No regular or periodic behaviour can be read off the graph apart from an overall decreasing tendency of the wake function strength at $s = 0$.

thickness.

## 5.1.4 The Gap Width

Likely the most important advantage of a rectangular dechirper is the possibility to tune the gap width between the upper and lower dielectric after the structure itself is built. This additional degree of freedom, it can be presumed, will make it possible to adjust the wakefield during the operation of the dechirper and will thus allow for an exact tuning of the dechirper to the situation at the operation site. It can generally be assumed that smaller gap widths correspond to higher effects of the dechirper; i.e. to higher maximum strength of the wakefield. In addition to this, it is imaginable that a large gap width, and thus a high distance between the dielectrica, will significantly reduce the influence of the dechirper on the beam. This would open up the possibility of using this increased gap width to deactivate the dechirper fully while the structure does not have to be taken out of the beam line completely, which would be a large practical advantage.

In a realistic scenario, the gap width of the dechirper will be limited by outer circumstances, e.g. the mechanics that drive the dielectric plates and the surrounding vacuum chamber in the beam line. Another factor are the characteristics of the beam,

which means that the gap width cannot be smaller than the transversal width of the beam to avoid the dechirper cutting into the beam. For the scenario at ELBE, this means that the minimum achievable gap width lies at about 6 mm, while the mechanical drives and the vacuum chamber will limit the maximum gap width to about 35 mm. This is also the range in which the parameter study will be conducted to stay close to the realistic scenario at ELBE.
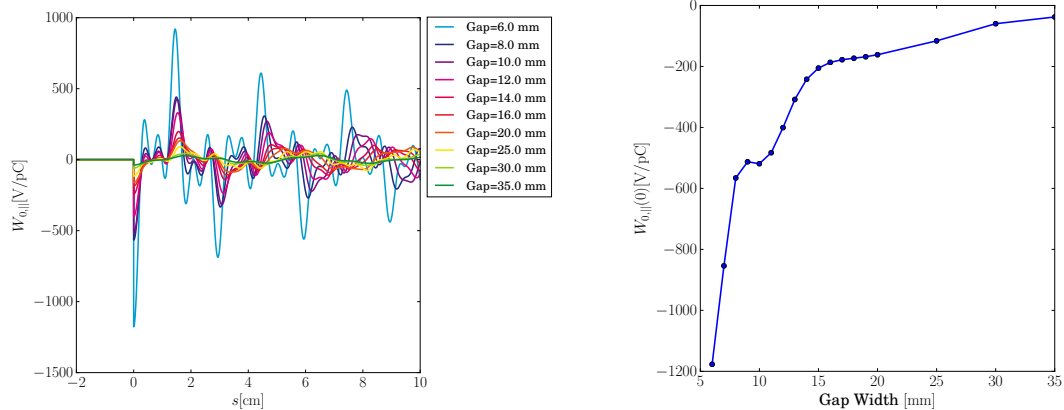


**Figure 5.7:** Total wake functions for an increasing gap width of the dechirper. The wake function does not simply scale up with an increase in the studied parameter; the positions of the extrema and zeros clearly change for the selected examples.

**Figure 5.8:** Longitudinal wake function at $s = 0$ calculated with WIzaRD for various gap widths of the dechirper. The reduction of the maximum absolute value of the wake function with an increase in the gap width is much stronger for lower gap widths and seems to approach 0 for larger gap widths.

Figure 5.7 shows how the behaviour of the wake function changes with varying the gap width of the dechirper. From the figure it can be observed that changing the gap width of the dechirper will also change the overall behaviour of the wake function, i.e. the position and number of extrema and zeros. It can also be seen that the absolute value of comparable extrema at roughly the same position $s$ decreases significantly with an increase in the gap width. This behaviour is shown in more detail in Fig. 5.8, again for the extremum at $s = 0$, since this is the only point where a reliable comparison can be made. This figure shows the indeed drastic reduction of the maximum absolute value of the wake function at $s = 0$, from nearly $-1200\,\mathrm{V/pC}$ for 6 mm to less than $-100\,\mathrm{V/pC}$ for a gap width of 35 mm. It can also be seen that for lower gap widths, the slope of the resulting curve displayed in Fig. 5.8 is larger, meaning the decrease in the strength of the wake function at $s = 0$ is larger here for the same increase in gap width than for overall larger gap widths. The curve seems to slowly approach zero, but due to the decreasing slope it can safely be assumed that another drastic increase in the gap width would be needed to reduce the strength of the wake function at $s = 0$ much further. Theoretically, it can even be assumed that

this behaviour is asymptotic, and that the wakefield will only ever not be present at all without a dechirper. For practical purposes, however, it is sufficient to know that even a comparatively small increase in the gap width (just by about 30 mm) will already significantly reduce the influence of the wakefield on the particle beam due to the much lower absolute value of the wake function for these cases.

## 5.1.5 Conclusion

In this section, the influence of several geometrical parameters of the dechirper on the maximum absolute value of the wake function at $s = 0$ have been shown. First, the linearity of the increase in the maximum absolute value of the wake function with an increase in the length of the dechirper could be observed, which also served as a benchmark of the accuracy of the model used and implemented in WIzaRD.

As a second parameter, the width of the dechirper has been studied. Most important about these results is that after a certain width is reached, the absolute value of the wake function at $s = 0$ will stay the same even for a continued increase in the width of the dechirper. This is very relevant for a practical realisation of the dechirper, as the maximum width can be limited by outer influences, e.g. a vacuum chamber that contains the dechirper.

Both the material and the thickness of the dielectric have been shown to affect the wake function as well when varied. Here, smaller relative permittivities proved to be preferable because they yielded overall higher absolute values of the wake function at $s = 0$. Thinner dielectric plates also appear to be more advantageous, though the behaviour of the absolute value of the wake function at $s = 0$ with an increasing dielectric thickness is not smooth but shows irregular jumps at certain thicknesses.

However, both the material of the coating and its thickness have only a relatively small influence on the final wakefield when compared to the effect of the gap width. Next to the length of the dechirper, this parameter is the one that has the largest influence on the strength of the wake function at $s = 0$. For example, in Fig. 5.6 the absolute value of the wake function at $s = 0$ varies between $\approx -200$ V/pC and $\approx -400$ V/pC for the observed thicknesses. A variation of the absolute value of the wake function in the same range can also be achieved by simply reducing the gap width of the dechirper from 15 mm to 12 mm (c.f. Fig. 5.8). On the other hand, the gap width can easily be adjusted after the dechirper is already built, which results in an additional degree of freedom during the operation of the dechirper. In other words, it shows that any losses in the maximum wake function strength that may arise from technical limitations on the dielectric and its thickness can easily be balanced out by adjusting the gap width (and also, the length of the dechirper), which makes the planning and realisation of the dechirper simpler and more flexible.

## 5.2 Bunch Characteristics

While the wake function will stay unaffected by the characteristics of the bunch, the wake potential as the convolution of the wake function with the bunch shape function, c.f. equation (3.59), will be influenced by the characteristics of the bunch. There are two possible quantities here that play a role: the bunch charge and the bunch shape, i.e. the length and actual form of the particle distribution.

This section is dedicated to determining the influence of these two additional characteristics on the wake potential.

### 5.2.1 Bunch Charge

To be completely accurate it has to be said that the bunch charge has no effect on the wake potential itself, as the wakefield is normalised with the charge of the test bunch, c.f. equation (2.19). However, in later studies of the effect of the wake function on the particle bunch the bunch charge is used to transform the wakefield into an energy modulation,

$$E_{\text{wake}} = q_p W_{||}, \tag{5.1}$$

where the energy is given in eV and $q_p$ is the total charge of the pulse. Since this energy modulation is the primary function of the dechirper and thus the main aspect of these considerations, it nevertheless makes sense to look at the influence of the bunch charge at this point.

From the upper equation it also becomes apparent how this modulation will look like with a variation of the bunch charge: an increase in the bunch charge will lead to a linear increase in the energy modulation due to the wake potential, i.e. doubling the bunch charge will also double the energy modulation. This behaviour makes the bunch charge a powerful influence on the eventual strength of the dechirper effect; one that can, in theory, be used to balance out losses that arise from technical limitations of the other parameters like the gap width or the dechirper length. On the other hand, small variations to the bunch charge will already introduce a possibly visible change in the strength of the energy modulation, i.e. also natural fluctuation in the bunch charge will have an effect on the performance of the dechirper. The range of these fluctuations is determined by the technical aspects of the accelerator site, and the scope of the influence on the dechirper is also dependent on the wakefield characteristics, i.e. the maximum achievable effect of the dechirper. This aspect will be looked into in more detail in Section 6.1.

### 5.2.2 Bunch Shape

The shape of the particle bunch can readily be assumed to have a significant influence on the wake potential and thus also on the effect of the dechirper. The wake

potential of a certain particle bunch is determined from the wake function via a single convolution[1],

$$W_{||}(s) = \int_{-\infty}^{\infty} \psi\left(s - s'\right) W_{0,||}\left(s'\right) \mathrm{d}s'.$$

Here, $\psi(s)$ is the shape function of the particle bunch, or, in other words, the particle distribution. An important characteristic of this function it that it needs to be normalised to 1,

$$\int_{-\infty}^{\infty} \psi\left(s\right) \mathrm{d}s = 1.$$

The charge distribution of a particle bunch consisting only of one type of particles with a total charge $q_p$ derives from this, for example, as

$$\psi_p\left(s\right) = q_p \psi\left(s\right),$$

where the total charge, correspondingly, is

$$\int_{-\infty}^{\infty} \psi_p\left(s\right) \mathrm{d}s = \int_{-\infty}^{\infty} q_p \psi\left(s\right) \mathrm{d}s = q_p.$$

In this section, four different particle distributions are going to be studied. Basis of all of these particle distributions is a Gaussian bunch with an r.m.s. length of $\sigma = 0.3\,\mathrm{mm}$, located at $\mu = 0$,

$$\psi_{\mathrm{G}}\left(s\right) = \frac{1}{\sqrt{2\pi\sigma^2}} \mathrm{e}^{\left(-\frac{1}{2}\frac{(s-\mu)^2}{\sigma^2}\right)}. \tag{5.2}$$

For a Gaussian distribution, 99.7% of all particles lie within a range of $\pm 3\sigma$ around the mean, which implies an approximate bunch length of $6\sigma$. Accordingly, the r.m.s. length for this example study has been chosen to reflect the achievable pulse length at ELBE. The choice of the mean value of the distribution does not have a significant influence on the wake potential, though it is technically also not completely arbitrary. Since the particle distribution is given with respect to the coordinate $s$, which is measured relative to a reference particle, the choice of the mean basically determines the position of this reference particle within the bunch. For wake potentials, it was assumed until now that the reference particle is the first particle in the bunch. This would imply for the particle distribution that it cannot encompass negative $s$, so the bunch has to start at $s = 0$ and moves only in positive direction.

---

[1]This is the same expression as eqn. (3.59). It is repeated here to allow for a more convenient reading of the following analysis.

For the Gaussian pulse, this would imply that the mean has to be chosen such that the Gaussian is zero, or close to zero, at $s = 0$. Due to the asymptotic behaviour of the Gaussian, this is not achievable, though it can be approximated (the mean could, e.g. be chosen as $\mu = 3\sigma$ in correspondence with assuming that the pulse has a length of $6\sigma$). But since other pulses will be derived from this Gaussian distribution for this parameter study, it is more convenient to choose $\mu = 0$ and thus fix all pulses in the centre. Here, the reference particle is *not* the first particle in the bunch, it is rather located in the centre of the bunch. While not completely accurate, for the resulting wake potential this will only introduce a displacement of the whole potential in $s$. Since, however, for this study, only the behaviour of the wake potential relative to the particle bunch is of interest, such a displacement plays no role.

The second particle bunch profile that is going to be observed is a combination of two different Gaussian pulses, referred to as a double Gaussian here. For this, the pulse in equation (5.2) is superimposed with a second Gaussian with a far smaller r.m.s. length and a different mean, $\sigma^* = 0.3\sigma$ and $\mu^* = -1.25\sigma$. These values have been chosen arbitrarily, only keeping to the rule that the base Gaussian has to be the term mainly influencing the overall approximated length of the superimposed pulse. This basically means $\mu^* - 3\sigma^* > -3\sigma$, which is fulfilled here: $-1.25\sigma - 3 \cdot 0.3\sigma = -2.15\sigma > -3\sigma$. Consequently, the expression of the double Gaussian can be formulated as

$$\psi_{\text{DG}}(s) = \frac{1}{2}\left(\frac{1}{\sqrt{2\pi\sigma^2}}\mathrm{e}^{\left(-\frac{1}{2}\frac{s^2}{\sigma^2}\right)} + \frac{1}{\sqrt{2\pi\left(0.3\sigma\right)^2}}\mathrm{e}^{\left(-\frac{1}{2}\frac{(s+1.25\sigma)^2}{(0.3\sigma)^2}\right)}\right). \tag{5.3}$$

As a third profile, a uniform distribution of particles along the length of the pulse is chosen. This form is often referred to as a flat-top or rectangular pulse. There is a variety of possibilities to express this pulse; e.g. via partially defined functions mathematically or simply an *if*-clause in Python. For computational purposes, a superposition of Heaviside-distributions $\Theta$ was chosen here. As a total pulse length of $6\sigma$ was assumed, and to obtain the same symmetry as for the single Gaussian, the flat-top pulse was centred on $s = 0$ as well. The final expression for the used flat-top pulse is

$$\psi_{\text{F}}(s) = \frac{(\Theta(s + 3\sigma) + \Theta(-s + 3\sigma) - 1)}{6\sigma}, \tag{5.4}$$

which has already been normalised to 1 by dividing the function by its area, $6\sigma$.

The fourth and last pulse that has been chosen is a triangular pulse, i.e. a pulse with a linearly rising flank for $s < 0$ and a linearly descending flank with the same absolute slope for $s > 0$. This pulse is easily expressed by an inverted absolute value function centred on $s = 0$ that is shifted upwards such that it has zeros at $s = -3\sigma$ and $s = 3\sigma$, $\psi_T^*(s) = -|s| + 3\sigma$. This is then multiplied by the flat-top pulse which serves as a window function cutting off the negative function values and limiting the

pulse length. The resulting function value at $s = 0$ is $3\sigma$, and by simple geometric considerations, the area under the function is $3\sigma \cdot 3\sigma = 9\sigma^2$. The complete expression of the normalised triangular pulse is thus

$$\psi_{\mathrm{T}}(s) = \frac{(\Theta(s + 3\sigma) + \Theta(-s + 3\sigma) - 1) \cdot (-|s| + 3\sigma)}{9\sigma^2}. \tag{5.5}$$

These four pulses have then been used to derive four different wake potentials from the wake function of the model dechirper. Here, only the behaviour of the wake potential over the length of the pulse is of interest, where basically two things play a role for the later dechirping: first, the maximum absolute value of the wake potential as it determines the maximum energy loss of the particles in the bunch, and second, the form of the slope of the wake potential over the pulse, which can be assumed to have a significant influence on the dechirped phase space of the pulse. Since the wake potential, by its very nature, is a convolution of the wake function and the bunch shape, two assumptions can be made regarding the different wake potentials:

1. The maximum absolute value of the wake potentials will not show a strong dependence on the bunch shape. The convolution basically measures the overlap of the areas under the wake function and under the bunch shape. The maximum absolute value over the length of the bunch is reached when the bunch and the wake function overlap fully for the first time. Since all pulse shapes have to be normalised and thus the area below their respective functions is 1, the maximum overlap of all bunch shapes should be very similar at the very least.

2. The slope will strongly depend on the bunch shape. The flat-top pulse is the most likely to generate a uniform slope or the wake potential, while the slopes of all other pulses will most likely not be uniform but reflect the behaviour of the bunch.

Figure 5.9 shows the wake potentials for the model dechirper calculated for the above-described bunch shapes and in dashed lines the corresponding normalised particle distributions. It can be seen that indeed, the maximum absolute value of all potentials along the bunches is comparable, always at $\approx -350\,\mathrm{V/pC}$. These maxima are reached at the end of the pulses.

The other expectations regarding the form of the slopes can also be verified using Fig. 5.9. For the uniform pulse (green), the slope of the wake potential over the length of the bunch is at a first glance linear, at closer inspection, though, it shows to have a slight curvature which simply results from the non-linearity of the wake function in the considered region (c.f., e.g. Fig. 5.2). No matter this slight curvature, however, the uniform bunch is the pulse shape that grants to most uniform slopes and thus can be expected to grant the most uniform energy loss over the particle bunch.
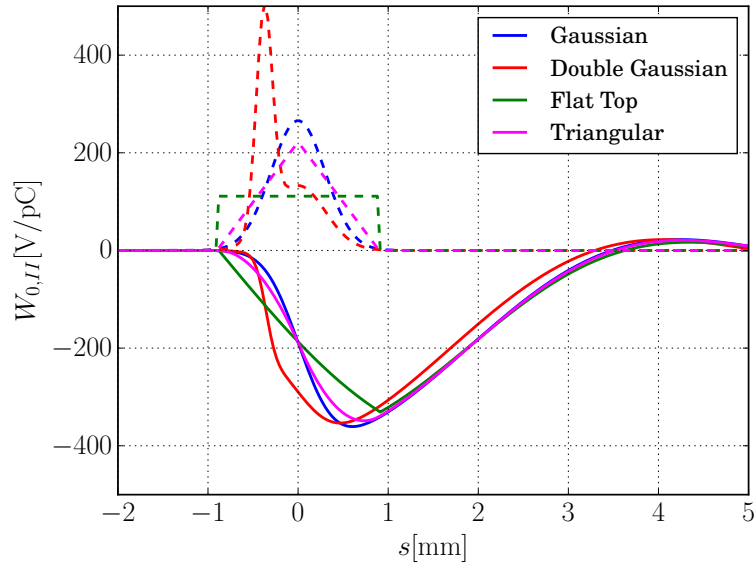
**Figure 5.9:** Wake potentials (solid lines) of different bunch shapes (dashed lines) of the same length derived from a convolution with the wake function of the model structure. It can be seen that the maximum absolute value of the wake potential over the length of the bunches is very similar for the different distributions, while the slopes radically differ.

The Gaussian pulse creates a wake potential with a slope that is curved all over the length of the bunch. The wake potential has an inflection point where the Gaussian has its maximum (i.e. at $s = 0$) and shows a steep, nearly uniform slope in the region around this inflection point. This corresponds to the region in which the slope of the Gaussian pulse has the highest absolute value since these are the regions in which the overlap of the pulse and the wake function increases the fastest. Around the beginning and end of the bunch, where the Gaussian pulse goes over into the asymptotic approach to zero, the wake potential shows a more distinct curvature.

The wake potential of the triangular pulse is similar to the one created by the Gaussian pulse. It also shows an inflection point at $s = 0$, but overall a softer, more steady slope than the wake potential of the Gaussian pulse. For example at the beginning of the bunch the wake potential of the triangular pulse shows lower absolute values than the wake potential of the Gaussian pulse at the same distance $s$. It can be seen from the pulse shapes that in this region at the beginning of the bunch, the triangular pulse encloses a larger area under its curve compared to the Gaussian bunch, but after the maximum at $s = 0$, the steeper slope of the Gaussian leads to a now larger area under the curve of the Gaussian and thus to a weaker overall wake potential of the triangular pulse in the second half of the bunch.

For the double Gaussian, the two superimposed single Gaussians are visible in the wake potential as two regions of clearly different slopes: a steeper region at the

beginning of the pulse resulting from the Gaussian with the smaller r.m.s. length and a region with a smaller overall slope corresponding to the Gaussian with the original, larger r.m.s. length. In both of these regions a change of the internal curvature in an inflection point corresponding to the two local extrema of the Gaussians can be conjectured, for the second Gaussian centred on $s = 0$ it is visible more easily.

These observations all coincide with the initial expectation that the bunch shapes will reflect in different behaviours of the wake potentials. These different behaviours will also have an influence on the phase space of the particle bunch, which will be studied in the following section.

## 5.2.3 Phase Space Computations for Various Bunch Shapes and Gap Widths

Similar findings like presented in this section have previously been published in [4].

As mentioned before in equation (5.1), the energy shift introduced by the dechirper is proportional to the wake potential and the proportionality factor is the total charge of the pulse. This means that the form of the energy shift results directly from the particle distribution and, by implication, has nothing to do with the initial energy distribution of the particle bunch, and neither with the total energy of the pulse. This means for the following phase space studies the energy distribution of the particle bunch can be chosen arbitrarily. For the phase space of the test bunch in these studies 1,000 particles were created and randomly assigned a position according to the particle distributions introduced in the previous sections, and an energy according to a fixed energy distribution. This distribution has been chosen such that the effect of the dechirper is most easily visible for a total charge of

$$q_p = 100\,\mathrm{pC},$$

which is the maximum achievable bunch charge of the ELBE thermionic gun that has been available for the experiments. More specifically, a Gaussian with a standard deviation of

$$\sigma_E = 1.6\bar{6}\,\mathrm{keV},$$

and a mean of

$$\mu_E = 5\,\mathrm{keV},$$

has been chosen. This Gaussian was then imprinted with an energy chirp. This chirp has been introduced as a uniform increase in energy starting from

$$E_{low} = 100\,\mathrm{keV},$$

at the head of the bunch and ending at

$$E_{high} = 220\,\mathrm{keV},$$

at its tail. The total energy width of the bunch is thus 120 keV. The resulting position-dependent energy variation was then added to the original energy distribution and stored for all particles of the bunch.

The initial phase space created in this way is now modulated using the wake potentials of the different bunch shapes studied in the previous section. For this purpose, the wake potentials are calculated discretely over $s$ by performing the convolution in eqn. (3.59) numerically. The resulting potentials are then interpolated using *SciPy* and a one-dimensional, linear interpolation. This is done to guarantee that for every randomly assigned particle position of the initial phase space an energy shift can be calculated from the wake potentials and the total charge of the bunch. This energy change is then added to the initial energy of the particle. This procedure is additionally performed for several gap widths to show the different behaviours of the dechirper in these cases. Exemplary, the gap widths 6 mm, 12 mm and 35 mm have been chosen. The resulting phase spaces for the initial particle distributions and the dechirped bunches are shown in the following figures.
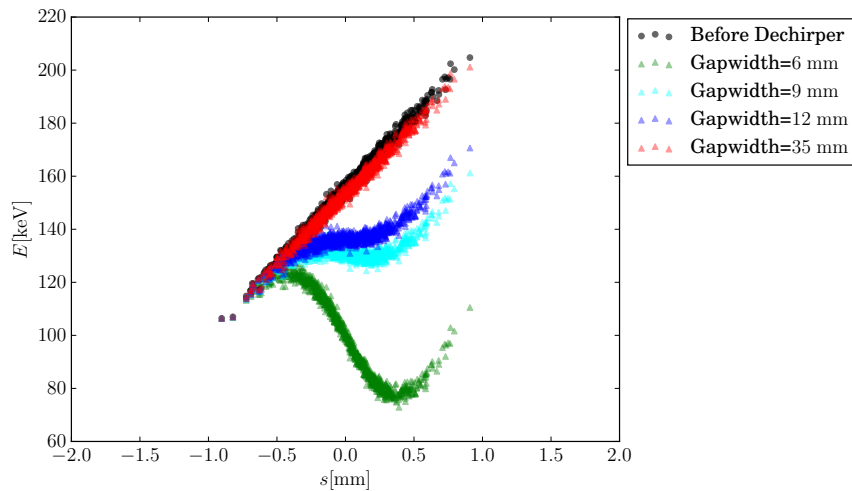


**Figure 5.10:** Phase space of a particle bunch with the example initial energy distribution and a Gaussian particle distribution before and after the model dechirper with varying gap widths. The overall energy reduction caused by the dechirper is, as intended, stronger at the tail of the bunch than at its head. The curvature of the wake potential shown in Fig. 5.9 is clearly visible in the curved, wave-like behaviour of the phase space after dechirping. Increasing the gap width from 6 mm to 9 mm significantly reduces the effect of the dechirper. An increase of the gap width to 12 mm further reduces the effect of the dechirper, increasing it even further to 35 mm nearly completely negates it.

In Fig. 5.10, the dechirping effect of the structure on the model Gaussian with the given energy distribution is shown. The progressively stronger energy modulation with increasing gap width is clearly visible, as is the non-linear behaviour of this effect with respect to the gap width. For a gap width of 35 mm, the effect of the

dechirper on the phase space of the particle bunch is nearly negligible; just a slight modulation of the energy in the range of a few keV can be seen. This modulation is, as could be expected from Fig. 5.9, stronger at the tail of the bunch than at the head. A reduction of the gap width to 12 mm increases the effect of the dechirper. The curvature of the wake potential, also seen in Fig. 5.9, is clearly imprinted on the formerly linear energy chirp. In the central region of the bunch between $-0.5$ mm and $0.5$ mm, the nearly uniform slope of the wake potential of the Gaussian pulse nearly compensates for the initial chirp, leading to a minimal energy width of $\approx 20$ keV in this region. This does not, however, include the head and tail of the bunch, which due to the curvature of the Gaussian pulse increase the total energy width to $\approx 80$ keV for the total pulse. Decreasing the gap width even further to 6 mm again significantly increases the effect of the dechirper, so much in fact that it overcompensates the initial chirp and leads to a new chirp in the opposite direction, where the tail of the bunch has a lower energy than its head. This new phase space has now an energy width of $\approx -60$ keV. The non-linear behaviour of the reduction of the gap width can easily be deduced from the phase space example at a gap width of 9 mm: while it is the central gap width between the other examples at 6 mm and 12 mm, the effect of the dechirper is just slightly stronger here than for the 12 mm example. For a linear scaling of the effect of the dechirper with the gap width, it would be expected that the phase space at a gap width of 9 mm lies in between the other examples of 6 mm and 12 mm. This shows again clearly the influence of the gap width on the overall effect of the dechirper and the power of the tuning: within a range of just 3 cm of gap width, the initial energy chirp of the bunch can be either nearly left uninfluenced up to already significantly overcompensated by the dechirper. Due to their similar wake potentials, the dechirped phase space for the triangular pulse would be very similar and is thus omitted here.

Figure 5.11 shows a similar study conducted for the double Gaussian particle distribution. The effect of the dechirper with varying gap widths is again clearly visible, from a nearly negligible effect at 35 mm to a very strong overcompensation of the initial chirp at 6 mm gap width. The behaviour of the wake potentials is again imprinted on the phase space after the dechirper. In the case of the 6 mm gap width it leads to a valley of nearly constant energy after the dechirper in the region between about $-0.3$ mm to $0.3$ mm, which coincides with the second of the two Gaussians and subsequently the flatter part of the slope of the wake potential. Like for the single Gaussian, though, the head and tail of the bunch deviate vastly from this valley, which overall increases the energy width of the dechirped phase space to $\approx -50$ keV. And even if the mentioned valley does have a very low local energy width, the mean energy nevertheless was clearly reduced to just $\approx 60$ keV. For the middle gap width of 12 mm this valley is discernible as well, but the overall energy of the phase space after the dechirper is still determined by the initial chirp and still $\approx 75$ keV, which does not significantly differ from the single Gaussian, as was expected due to the comparable maximum absolute values of the wake potentials over the bunch length.
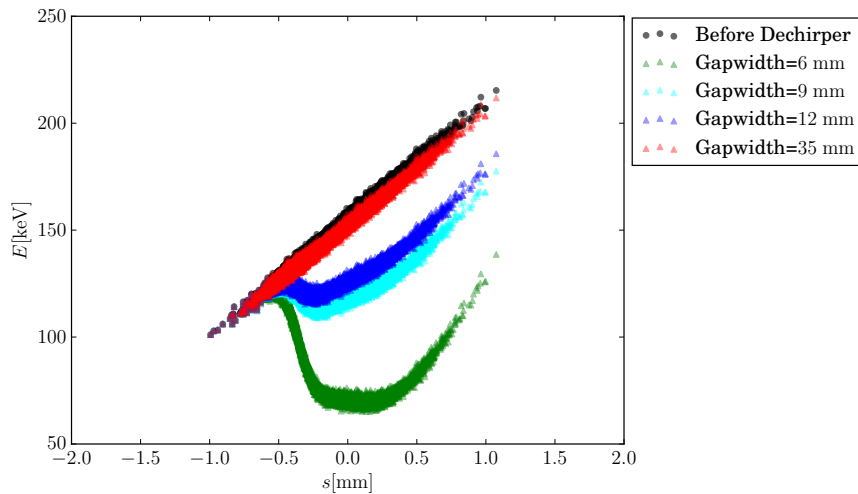
**Figure 5.11:** Phase space of a particle bunch with the example initial energy distribution and a double Gaussian particle distribution before and after the model dechirper with varying gap widths. Similar to the single Gaussian, the curvature of the wake potential is clearly visible in the behaviour of the phase space after dechirping. In this case, the behaviour of the wake potential of the double Gaussian leads to a valley-like region in the centre of the dechirped phase space. An increase in the gap width again significantly reduces the effect of the dechirper.

In Fig. 5.12, the effect of the dechirper with varying gap widths on a uniform particle bunch is shown. Again, the influence of the gap is easily visible; for 35 mm the dechirper has hardly any effect on the energy distribution, while for 6 mm, the effect is the strongest. Due to the uniform pulse and the wake potential displayed in Fig. 5.9, the dechirped pulses show the least curvature here. For the two larger gap widths, nearly no curvature is discernible, though for a gap of 6 mm width it is easily visible. As stated in the previous section, this curvature results from the non-linearity of the wake function and has nothing to do with the shape of the pulse itself. What does have an influence on this curvature, and thus on the wake potential, is the length of the pulse compared to the length of the first flank of the wake function. From Fig. 5.14 it can be seen that the first rising flank (between $s = 0$ and the first local maximum) of the wake function of the model structure for a gap width of 6 mm is $\approx 3$ mm long and comparatively steep, while for the lower gap widths, this flank is flatter and a little longer. For the wake potential, which, again, is determined by a convolution of the wake function with the pulse shape, especially the region between $s = 0$ and the length of the pulse, which is 1.8 mm here, is relevant. For this pulse, this coincides with nearly the total length of the first flank of the wake function, and thus, all non-linearities in that region will influence the wake potential.

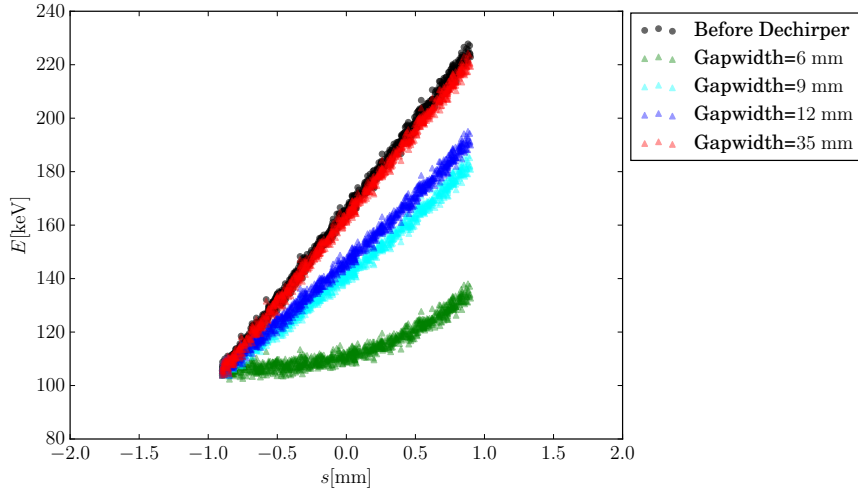To mitigate this effect, it makes sense to reduce the length of the pulse compared

**Figure 5.12:** Phase space of a particle bunch with the example initial energy distribution and a uniform particle distribution with a total length of $6\sigma = 1.8\,\text{mm}$ before and after the model dechirper with different gap widths. The scaling of the effect of the dechirper with an increase in gap width is clearly visible. Additionally, despite the uniform particle bunch and in accordance to Fig. 5.9, the dechirped phase space for the lowest gap width clearly shows a curvature.

to the length of the first flank for the wake function. In Fig. 5.13 this is done by reducing the length of the uniform pulse to a tenth of its previous value, $0.18\,\text{mm}$. This shorter pulse will result in a smaller region of the wake function playing a role for the wake potential (if the considerations are limited to short range wake potentials). In this smaller region, no matter the gap width, the value of the wake function will not change that drastically compared to the larger region that becomes interesting for longer pulses. As a result, the phase space will be dechirped much more uniformly as seen in Fig. 5.13: here, for the lowest gap width, the initial chirp has been fully compensated. The energy width of $\approx 10\,\text{keV}$ of the pulse is here merely the result of the initial random energy distribution that was chosen for the generation of the model pulses, but the imprinted chirp of the initial bunch has been balanced out by the effect of the wake potential and thus, the dechirper.

### 5.2.4 Conclusion

Apart from the bunch charge that serves as a scaling factor for the strength of the wake potential, the length and the shape of the particle bunch have both a significant influence on the effect of the dechirper. Here the form of the pulse is not, or only minimally, important for the maximum dechirp over the pulse the structure is able to generate. This is due to the wake potential being influenced by the normalised particle distribution and the maximum of the wake potential over the
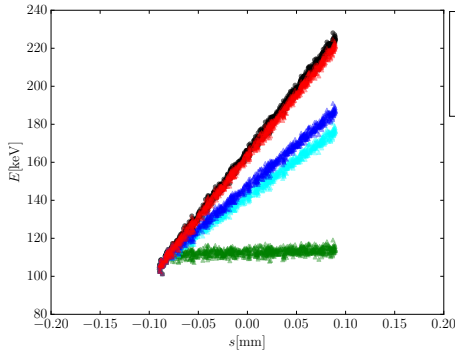
**Figure 5.13:** Phase space of a particle bunch with the same initial characteristics as in 5.12, but a total length of 0.18 mm before and after the model dechirper with different gap widths. Compared to the longer bunch, the curvature in the dechirped phase spaces is no longer discernible. In fact, in this case, the dechirper position with the lowest gap width is able to fully compensate the initial chirp.
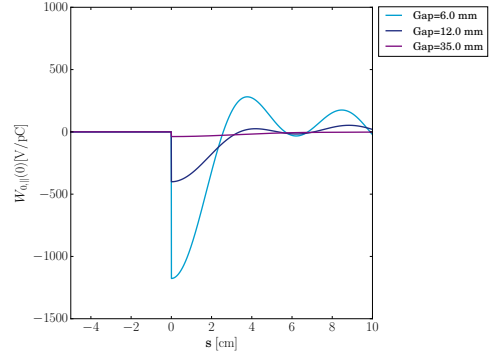
**Figure 5.14:** Close-up of the wake function of the model dechirper for the gap widths 6, 12 and 35 mm around $s = 0$. The first rising flank of the wake functions starting at $s = 0$ is the steepest for the lowest gap width.

bunch coinciding with the maximum overlap of the areas of the wake function in the region of the pulse and the bunch. However, the shape of the bunch greatly influences the form of the slope of the wake potential over the pulse. The pulse that generates the most uniform slope of the wake potential over the length of the bunch is the flat-top pulse, though even here the non-linear behaviour of the wake function will create a slight curvature of the wake potential. This effect can be mitigated by choosing a pulse length that is short compared to the length of the first flank of the wake function. Other pulse shapes, like the Gaussian or double Gaussian, show a significantly more curved wake potentials, though with smaller regions within the pulse where the slope is nearly uniform.

These potentials have different effect on the model phase space. For a linear initial chirp like chosen in this section, a strong effect of the dechirper (which is achievable for low gap widths) will easily imprint on the dechirped phase space. A complete compensation of such a linear chirp is naturally only possible with a more or less linear slope of the wake potential, and could be achieved for the model energy distribution for a very short flat-top pulse and the smallest possible gap width of 6 mm. Consequently, though, for different initial chirps, e.g. for a more wave-like chirp, other pulse shapes are more suited to compensate for the chirp and flatten the energy distribution as much as possible. For the wave-like chirp, a Gaussian pulse, e.g. might deliver more promising results.

# 6 Dechirper Experiments at ELBE

After the geometrical parameters of the dechirper had been agreed on with the HZDR, the prototype and the corresponding vacuum chamber were planned and built directly at the HZDR. During the second half of the year 2016, the dechirper was integrated into the beam line and was then available for experiments.

The following chapter will deal with the experiments carried out at ELBE in 2016. For this, the dechirper prototype will at first be described in detail. Spatial and technical limitations of the accelerator site will also be taken into account before the experimental results will be compared to expectations and results obtained with WIzaRD.

## 6.1 The Dechirper Prototype Used at ELBE

In this section, the parameter choice for the dechirper prototype used at ELBE will be illustrated in detail. Two aspects are of interest in this regard: the geometrical parameters, limited purely by spatial and technical characteristics of the accelerator site; and the parameters of the dielectric coating, which are influenced by material characteristics and manufacturing limitations and availability.

### 6.1.1 Spatial Requirements at the Accelerator Site and Geometric Parameters of the Dechirper

As mentioned already in the previous sections, the geometry of the final dechirper prototype has been subject to a number of limitations due to the situation at ELBE. First and foremost, the length of the dechirper could not exceed 80 cm, as this corresponds to the largest amount of free space in the beam line at the accelerator site.

Second, the dechirper had to be inserted into the beam line within a cylindrical vacuum chamber. This chamber has a diameter of 10 cm, which limits the width of the dechirper and the maximum achievable gap width. The vacuum chamber also holds mechanical drives that allow for a tuning of the distance between the two dielectric plates even after the dechirper has been taken into operation. These drives also make it possible to close the dechirper entirely (i.e. such that the dielectrics lie directly on top of each other) and bring the closed dechirper towards one side of the vacuum chamber and thus remove it from the beam path entirely. For the geometry of the dechirper, it holds that the wider the structure is, the more the gap width will

be limited. A width of 5 cm has been chosen. As seen in Fig. 5.4, at this width the achievable maximum value of the dechirp at $s = 0$ is nearly maximal. Additionally, starting at 6 cm, the wake function strength remains unchanged if the width of the dechirper is increased even further.

The width of the dechirper also influences the experiments in another way. To simplify the geometry and the construction process, the terminating walls in $x$-direction have been left out in the prototype (c.f. Fig. 6.1). The necessary electric termination in this transversal direction is instead provided by the vacuum chamber. This represents a deviation from the original, completely rectangular, semi-analytic model that WIzaRD cannot account for. Comparative studies conducted with CST PS, however, show that this differing termination makes little to no difference for the final wake potential. The parameter study in Fig. 5.4 hints at this behaviour, too: a simple way to interpret the curved termination resulting from the vacuum chamber is to assume that the width of the dechirper varies between 5 cm and 10 cm along $y$-direction, and Fig. 5.4 shows that apart from the jump occurring around 6 cm, the width does not influence the wake function in that range. A sufficiently wide vacuum chamber, as used in this prototype, should therefore be comparable to the situation considered in the semi-analytical model.
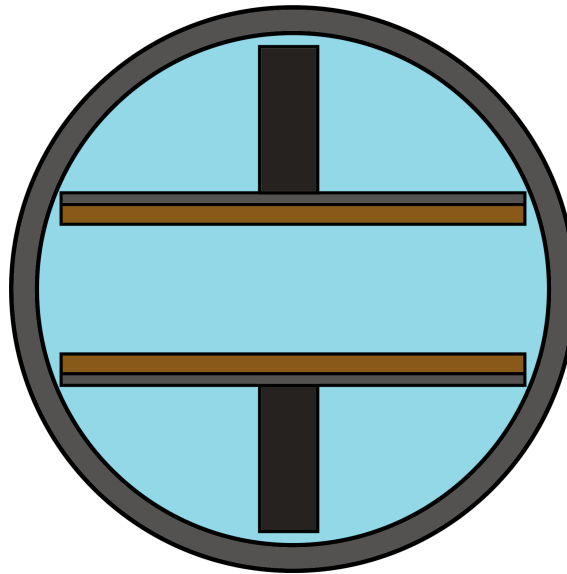


**Figure 6.1:** Schematic profile of the dechirper prototype inside the vacuum chamber. The terminating walls of the analytical model have been left out in one transversal direction. The necessary termination is provided by the chamber walls instead.

Under these conditions and taking the mechanical drives into consideration, the maximum achievable gap width at ELBE was limited to 35 mm.

## 6.1.2 The Material of the Dielectric Coating

The choice of the coating material and its parameters is likewise subject to limitations of different natures. Here, first and foremost, the material needs to be suited for the use in ultra-high vacuum. Under the low pressure inside the beam line, even solid materials can release gases that in turn contaminate the vacuum and increase the pressure inside the accelerator. This process is generally referred to as outgassing.

Additionally, especially the thickness of the chosen material strongly depends on the manufacturing and processing possibilities. Moreover, in all previous studies conducted with both CST PS and WIzaRD, lower dielectric constants resulted in higher achievable strengths of the wakefield (c.f. Fig. 5.5). This was taken into account during the design process of the dechirper.

Initially, FR4[1] was considered as a dielectric coating. As a composite material consisting of amongst others of epoxy resin and woven glass fabric reinforcements, FR4 is often used in circuit boards and had already previously been applied at ELBE for other purposes. It is easy to produce in various thicknesses, comparatively cheap and easy to process further. Additionally, while the dielectric constant varies for different compositions, it is most often found to be in the range between $\varepsilon_r = 4$ and $\varepsilon_r = 5$ (c.f. [88]) and thus relatively low. However, first ultra-high vacuum tests with a sample of the material designated for the use on the dechirper showed that the outgassing of this material was greater than initially assumed and it is thus unsuited for the use on the dechirper.

As substitute materials especially glass-ceramics were considered due to their low propensity for outgassing. In the end, MACOR was chosen for the dielectric coating. It is also a composite material made up of mainly silica and various metal oxides and is known to be a good thermal insulator with very little outgassing. It can be produced in a variety of forms and thicknesses. Its dielectric constant is $\varepsilon_r = 6$ (c.f. [89]) for the used sample, which is slightly higher than for FR4, but still comparatively low (other ceramic materials have higher dielectric constants up onto $\varepsilon_r \approx 20$). This is also comparable to the permittivity of diamond ($\varepsilon_r \approx 5.7$, [90]), which has been proposed as a material for the coating of dielectrically lined dechirpers in [59] and [91]. Samples of the used material were tested at ELBE and met the ultra-high vacuum requirements.

The samples of MACOR used for the dechirper prototype at ELBE have a thickness of $3\,\mathrm{mm}$ due to manufacturing limitations. For similar reasons, two single plates in the given dimensions ($80\,\mathrm{cm} \times 5\,\mathrm{cm}$) proved to be unobtainable. Therefore, instead of using two single plates as the dielectric coating, five shorter plates per side with a length of $16\,\mathrm{cm}$ each were used to emulate the total length of the dechirper. This was done by mounting the single plates with metallic clamps in a row. These metallic clamps also connected the upper and lower dielectric with the necessary electric termination in $y$-direction, in this case, aluminium plates. This splitting of a single

---

[1]The letters FR stand for 'flame retardant' and refer to the low flammability of the material.

plate into five smaller plates is assumed to have little to no influence on the final wakefield.

### 6.1.3 Consequences for the Wake Potential

The geometric and dielectric properties of the dechirper can therefore be summarised as:

- length $L = 80\,\text{cm}$,

- width $a = 5\,\text{cm}$,

- permittivity of the coating $\varepsilon_r = 6$,

- coating thickness $b - d = 3\,\text{mm}$,

- gap width adjustable up to $35\,\text{mm}$.

Figures 6.2 and 6.3 show the prototype of the dechirper used at ELBE during construction and after incorporation into the beamline. The model structure used in
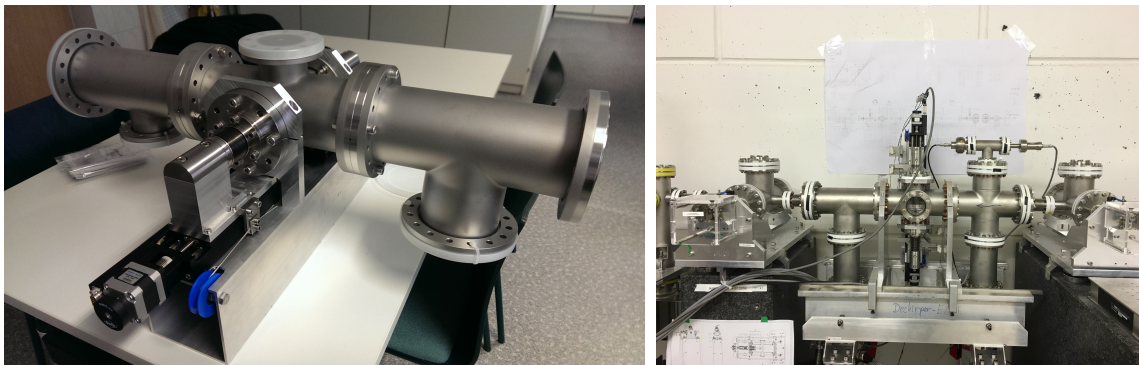


**Figure 6.2:** Vacuum chamber of the dechirper prototype operated at ELBE during construction. Courtesy of U. Lehnert, HZDR.

**Figure 6.3:** Vacuum chamber and dechirper integrated into the beam line at ELBE. Courtesy of U. Lehnert, HZDR.

Chapter 5 assumes a gap width of $12\,\text{mm}$ as a start for further investigations. This corresponds to an opening that is least likely to cut into the beam in transversal direction and thus leads to no beam loss, yet can still be considered as a small gap width with a resultingly high effect of the dechirper. According to table 5.1, the wake function strength at $s = 0$ in this case is $-400.5592\,\text{V/pC}$, which also limits the wake potential for an arbitrary bunch shape to this value. Of course, should a lower gap width be achievable, the maximum possible amplitude of the wake function will increase.

It should also be mentioned that at the maximum achievable gap width of 35 mm, there will still be a wakefield generated inside the dechirper. Figures 5.10 to 5.13 however show that these effects are very small and will thus be neglected during this chapter. The state of the maximally opened dechirper will be regarded as the state of a 'turned off' dechirper. While it is technically possible to mechanically remove the dechirper fully from the beam path, this is not a desirable solution as it additionally makes it necessary to fully close the dechirper. In a series of experiments this would make a new adjustment of the beam inside the dechirper necessary for every new setting, as it is crucial that the beam passes directly through the centre of the dechirper. It is technically simpler to adjust the beam to the centre once and then use this configuration for as many experiments as possible without having to remove the dechirper from the beam path entirely.

## 6.2 Experimental Conditions

### 6.2.1 The General Aim of the Experiments

The option to tune the dechirper after construction due to the adjustable gap width has always been one of the most important aspects in the design choice of the dechirper for the HZDR. Since the very first stages of the planning process, the experimental proof of the dependence of the wake potential and thus the dechirp on the gap width has been decided on as the most important part of the tests with the prototype. Additionally, variations of the bunch charge will also influence the final dechirp, though not the wake potential, which is why they are also suited as experimental degrees of freedom.

These aspects in mind, the focus of the experiments carried out at the HZDR was quickly set on

1. a proof of the general working principle of the dechirper,

2. an experimental proof of the influence of the gap width on the dechirp, and

3. studies regarding the influence of the bunch charge on the final effect of the dechirper.

Additionally, the effect of the dechirper on the particle bunch can also be calculated numerically using WIzaRD, and therefore, both experiment and semi-analytical prediction will be compared to each other. This promises an additional experimental validation of the functionality of WIzaRD.

## 6.2.2 Experimental Limitations and Compensating Measures

The measured quantity in the experiments conducted at ELBE was the energy spectrum of the particle beam. From these spectra, the average energy of the particles (i.e. the energy average with respect to the intensity displayed in the spectrum) and the corresponding standard deviations were computed. The dechirper effect, as shown in the previous sections, basically amounts to an overall energy loss and a narrowing of the energy width of the beam. In the energy spectrum, this would correspond to

1. a decrease of the average energy of the beam, and

2. a decrease of the standard deviation of the spectrum.

Depending on the gap width of the dechirper and the bunch charge, these changes will be more or less pronounced.

The studied bunches during the experiments were generated by a thermionic particle gun. Here, the maximum achievable pulse charge was limited to $\approx 100\,\mathrm{pC}$. Taking Table 5.1 into account once more, the maximum achievable dechirp for this case, a gap width of $12\,\mathrm{mm}$ and the given maximum bunch charge is

$$-400.56\,\frac{\mathrm{V}}{\mathrm{pC}} \cdot 100\,\mathrm{pC} = -40{,}056\,\mathrm{V},$$

which corresponds to an energy loss of $\approx -40\,\mathrm{keV}$ that the particles of the bunch can maximally experience.

This is very small compared to the usual chirp of the ELBE beam during normal operation, which is in the range of several MeV (c.f. Fig. 1.3). Without any experiments, it can therefore be predicted that the prototype will not be enough to compensate the usual energy chirp of the ELBE beam, which is already accounted for by the technical and spatial limitations of the accelerator site.

The small effect of the prototype compared to the usual chirp at ELBE poses another experimental challenge here: the variations in the dechirp created by adjusting the gap width are also small compared to the initial chirp. It is thus harder to differentiate between and consequently identify the effects of the dechirper and varying the gap width, respectively, and, e.g., natural fluctuations of the beam caused by the gun. This challenge, however, is also easy to work around. The chirp at the ELBE facility is imprinted on the particle beam within a magnetic chicane used to shorten the spatial bunch length before the bunch passes the second accelerator module (c.f. Fig. 1.2). Both the chicane and the second module can be deactivated, so that it becomes possible to use a particle bunch without an initial chirp during the experiments. This has the advantage that the effect of the dechirper is measured directly, and not in correlation with the initial chirp of the beam.
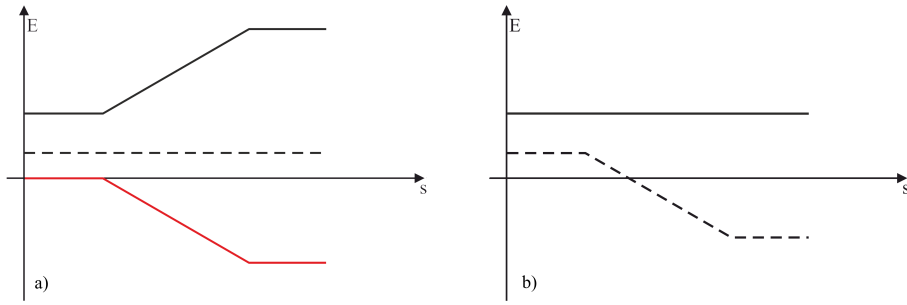
**Figure 6.4:** Exemplary phase space of two particle beams, one with an initial chirp (solid line) and one without (dashed line) (displayed in panel (a)). The schematic effect of the dechirper is shown in read, and is basically added to the phase spaces of the particle beam. Panel (b) shows the resulting phase spaces after the dechirper: While energy width of the initially chirped beam is compensated, the dechirper imprints its own energy width onto the initially unchirped beam.

On the other hand, this also changes the objective of the experiments. Figure 6.4 shows schematic phase spaces for an initially unchirped beam (dashed line) and an initially chirped beam (black, solid line), as well as a schematic dechirp (red). The acting of the dechirper on the particle beam can generally be understood as a summation of the phase space profile and the dechirp. This means that while the energy width of the intially chirped is compensated by the dechirp, the initially unchirped beam is imprinted with the profile of the dechirp. A similar effect is the overcompensation of the initial chirp, which can also be seen in the test phase spaces in the figures 5.10 to 5.13. This means that for the given situation of an unchirped beam, the objectives of the experiments have to be adjusted. The general energy loss of the particles is not affected by whether or not the beam is initially chirped, so that the first objective still remains to measure a general decrease in the average energy of the spectrum of the particle bunch. However, instead of narrowing the energy width of the spectrum, the dechirper will imprint the bunch with its own phase space profile, and thus *widen* the spectrum. Therefore, the *standard deviation of the energy spectrum will **increase***. This is technically the inverse effect of what the dechirper ideally should accomplish, but it will serve as a proof of principle just as well.

Another limitation resulting from the circumstances at ELBE is that next to the energy spectrum, neither the longitudinal phase space, nor the particle distribution of the bunch, nor the bunch length could be measured directly. While this is not detrimental to the experiments themselves as the effect of the dechirper can still be deduced from the energy spectra, it nevertheless complicates the comparisons to the semi-analytically expected effects of the dechirper. The particle distribution and bunch length, as shown in the previous sections, are fundamental for the numerical derivation of the wake potential from the wake function. Not knowing these quanti-

ties makes an accurate prediction of the effect of the dechirper on the particle bunch impossible as the correct wake potential remains unknown. Both the bunch length and also an approximated particle distribution could be reconstructed from measured data using phase-space tomography methods, though these still remain only approximations and cannot replace actual measured data which will consequently overall negatively influence the comparisons that can be made between the experiments and the semi-analytical predictions.

# 6.3 Experimental Results

## 6.3.1 Evaluation of Raw Measured Data and Variations of the Bunch Charge

**Average Energy and Standard Deviation of the Energy Spectra**

The effect of the dechirper on the energy spectra of different bunches was observed in three experimental sessions in the second half of the year 2016. As a first step, in this subsection the raw experimental data for selected experimental series were analysed. The only alteration of the initial data is that the evaluated window of the original energy spectra is tightened to a region of interest.

To differentiate and compare the results for the different bunches, each particle bunch will be identified by the date of the respective experimental session, a consecutive number denoting the different experimental series per day, and the bunch charge.

The first pulse that is going to be analysed here is the bunch 1008_1_54, measured on August 10 at 54 pC. The normalised intensities of the energy spectra measured for varying gap width are shown in Fig. 6.5. In this plot, the intensities are represented by a colourmap and plotted over the energy and the gap width. The upper limit of the gap width is 35 mm for technical reasons. The lower limit, 6 mm, has been found to be the closest position that the two dechirper plates can have without cutting transversally into the beam. For this depiction, the data has been interpolated over gap widths that have not been measured (e.g. between 30 mm and 35 mm because the expected changes to the spectrum introduced by the dechirper are only minimal in this range). The figure shows a shift of the non-zero areas of the spectra towards lower energies for low gap widths. Additionally, a general broadening of the spectra for these gap widths can also be surmised, though both effects clearly only appear in a range of a few 10 keV.

For a closer inspection of the effect of the dechirper on the pulse, the average energy and the standard deviation of the spectra are calculated. To see the actual effect compared to the 'opened' dechirper at 35 mm more clearly, the average energy and the standard deviation of this case are taken as a reference for the evaluation.
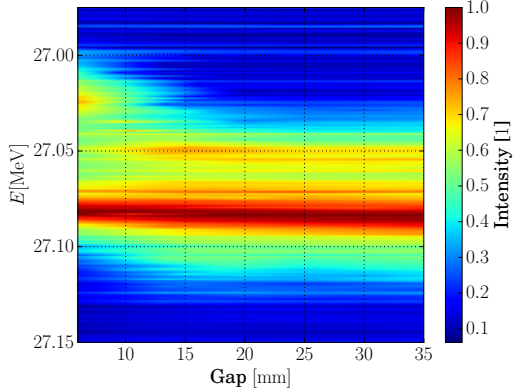
**Figure 6.5:** Normed intensities of the energy spectra of the particle bunch 1008_1_54 for different gap width of the dechirper. A broadening of the width of the spectrum for lower gap widths of the dechirper is visible. The general energy reduction induced by the dechirper can be seen in a shift of the non-zero areas of the spectra towards lower energies for lower gap width. Both effects are only minimal.
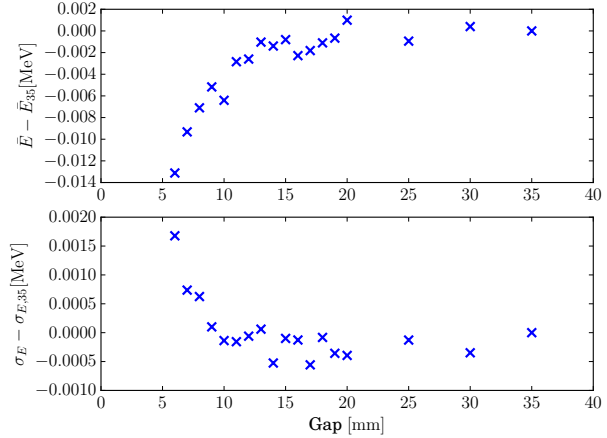
**Figure 6.6:** Average energies (top) and standard deviations (bottom) of the energy spectra of the particle bunch 1008_1_54 for different gap width of the dechirper compared to the open dechirper. As predicted, the closing of the dechirper leads to a decrease of the average energy, and, as the inverse dechirper effect is measured, to an increase in the standard deviations of the spectra.

Figure 6.6 shows clearly the expected behaviour of both the average energy and the standard deviation compared to the reference measurement. The average energy decreases for a decreasing gap width by a total of 13 keV, which is in the same range as the effect reported in [60] for a similar dechirper, while the standard deviation increases by 1.5 keV. Both effects are clearly not linear, and get significantly stronger for lower gap width, a behaviour also reported in [1] and [2]. This is in accordance with the previous prediction and parameter analyses shown in the last chapter. However, both effects are also very small, only in the range of a few keV, which, to a certain degree, has also been expected.

The same effects could be verified in several other experimental sessions, shown as a second example for the bunch 2508_1_56 in the Figures 6.7 and 6.8. In Fig. 6.7, both explained effects can also be seen more clearly: the increase of the energy width of the pulse is visible in the second high intensity region at $\approx 26.93$ MeV that starts to appear for gap widths smaller than 10 mm. An observation of the first high intensity region at $\approx 26.97$ MeV shows that this region shifts towards lower energies for low gap widths, which again confirms the general energy-reducing effect of the dechirper.
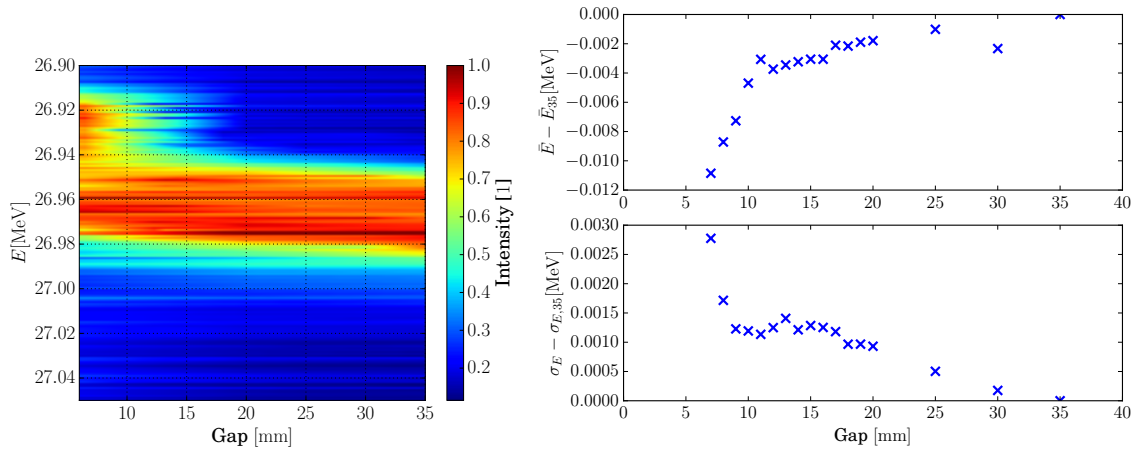
**Figure 6.7:** Normed intensities of the energy spectra of the particle bunch 2508_1_56 for different gap width of the dechirper. A broadening of the width of the spectrum for lower gap widths of the dechirper is clearly visible in the second high intensity peak at $\approx 26.93\,\mathrm{MeV}$ for lower gap widths. The general energy reduction induced by the dechirper can be seen in a shift of the non-zero areas of the spectra towards lower energies.

**Figure 6.8:** Average energies (top) and standard deviations (bottom) of the energy spectra of the particle bunch 2508_1_56 for different gap width of the dechirper compared to the open dechirper. As in the previous experimental series, the closing of the dechirper leads to a decrease of the average energy and an increase in the standard deviations of the spectra.

For another very similar example of the effect of the dechirper on the energy spectrum of an electron bunch measured at ELBE, see Fig. D.1 in Appendix D.

**Influence of the Bunch Charge**

Next to the gap width of the dechirper, the charge of the used particle bunch was the second quantity the effect of which has been of great interest during all experimental sessions at ELBE. For this purpose, bunches with the same characteristics (i.e. the same settings of the thermionic gun) but different total charges have been used in the experiments. The effect of the dechirper for a decreasing gap width has subsequently been measured for all of these series.

The first series of experiments discussed here was measured for three different bunch charges, 68 pC, 82 pC and 97 pC. The results for the average energy of the spectra and the corresponding standard deviation can be found in Fig. 6.9.

The figure shows the scaling of the effect of the dechirper for an increasing bunch charge in the case of the average energy of the different spectra: the maximum dechirp at a gap width of 6 mm is the highest for a bunch charge of 97 pC ($\approx 12\,\mathrm{keV}$) and lowest for the lowest bunch charge of 68 pC ($\approx 6\,\mathrm{keV}$). The scaling is nonlinear,
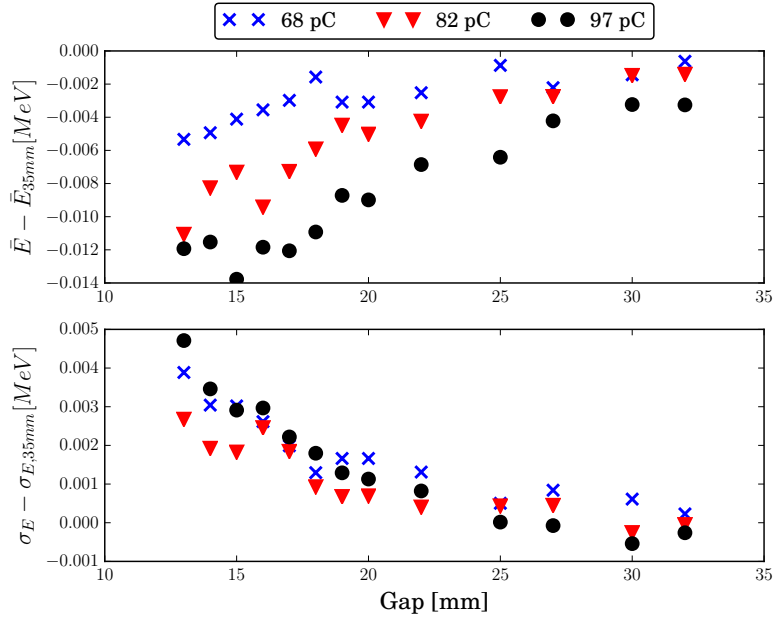
**Figure 6.9:** Progression of the average energy and the standard deviation of the energy spectra of particle bunches with different bunch charges from the series 2508_4 for different gap widths of the dechirper. The bunch charge clearly has an influence on the overall dechirp, seen in a stronger reduction of the average energy for the higher bunch charges compared to the lower ones. An effect on the standard deviation is also visible, though not as pronounced.

like predicted from theory, but it is clearly visible. For the standard deviations of the spectra, this dependence on the bunch charge is not as pronounced. First and foremost, all three series of measurements show the increase in the standard deviation for a decreasing gap width that has been predicted as one of the dechirpers main effects. There are also minimal differences visible for the different bunch charges. However, there is no clear scaling with the bunch charge visible; e.g. the middle bunch charge of 82 pC has the lowest maximum increase in the standard deviation for the minimum gap width ($\approx 3$ keV) and not, as would have been expected, the lowest measured bunch charge.

A second investigation of this scaling of the effect of the dechirper with the bunch charge can be seen in Fig. 6.10, which shows a series of measurements for the same bunch with now six differing total charges in the range from 29 pC to 98 pC. In this figure, it becomes even clearer that while there is some form of effect of the charge on the final dechirp, the theoretically expected scaling is hard to verify from these measurements. Again, the generally predicted overall behaviour of both the average energies and the standard deviation of the measured spectra can clearly be seen in the figure. Additionally, the experimental series studied for 98 pC shows the strongest

reduction of the average energy with decreasing gap widths and the strongest increase in the standard deviation, at least at the lowest gap width. However, there is no clear scaling identifiable from the other series with different bunch charges.
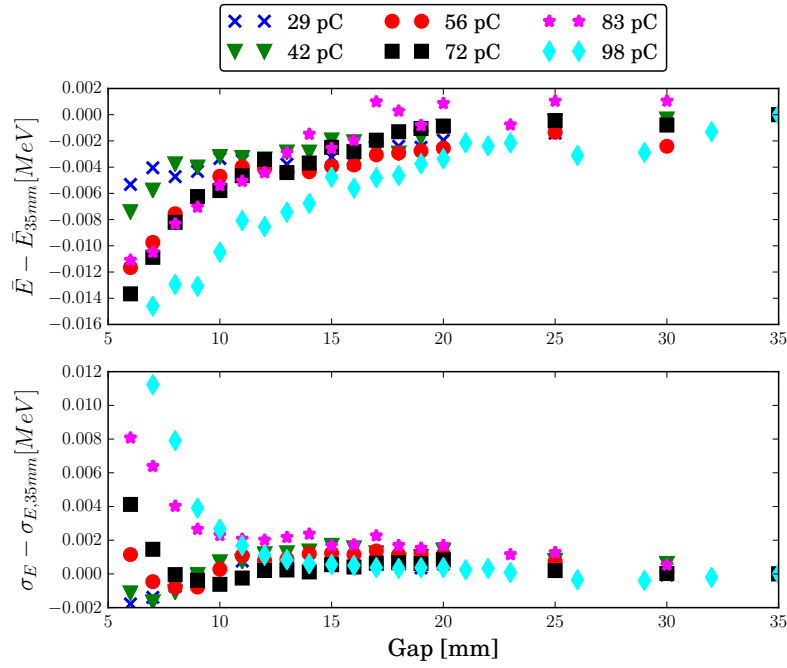


**Figure 6.10:** Progression of the average energy and the standard deviation of the energy spectra of particle bunches with different bunch charges from the series 2508_1 for different gap widths of the dechirper. While a variation of the effect of the dechirper for different bunch charges is clearly visible in this series, and, e.g., the highest reduction of the average energy is provided by the highest bunch charge measured, a clear scaling with the bunch charge cannot be seen neither for the average energy nor for the standard deviation of the energy spectra.

Similar effects could be observed in all other experimental series where different bunch charges have been tested for the same general bunch characteristics. As an intermediate conclusion, it can thus be said that while there generally is a qualitative effect of the bunch charge on the strength of the dechirper, the expected scaling could quantitatively not be verified.

There are multiple possible reasons for this. On the one hand, the measured bunch charges are comparatively close together, i.e. all in the same order of magnitude. In addition to the already small predicted effect of the dechirper, a small variation in the bunch charge does not lead to vastly different results. Other sources of errors that will be discussed in detail later and experimental limitations might already have a bigger influence on the measured qualitative effect of the dechirper compared to the variation of the bunch charge. This, once more, can be ascribed to technical

limitations at the accelerator site. The thermionic gun used for these experiments was not able to produce higher charges than a maximum of 100 pC. On the other hand, the thermionic gun is sensitive to changes in a sense that it could not be guaranteed that a variation of the bunch charge would not, even if only marginally, also change the phase space of the pulse. A different phase space might have led to a different pulse shape, which in turn would also influence the final dechirp and might account for changes in the range of a few keV. This is already in the same range as the expected effects of a change in the total charge, so there is a high relative insecurity of the measured data. Since the phase space could not be observed, there was no way to assess the qualitative changes to the bunch that the variation of the charge might have caused.

Another comparison of the behaviour of the dechirper for the same general bunch and different bunch charges can be found in Fig. D.3 in Appendix D.

## 6.3.2 Comparison to Semi-Analytical Calculations

As described earlier, a comparison of the experimental data to a semi-analytically predicted effect of the dechirper proves challenging because of the lack of knowledge about the phase space of the measured pulses. The pulse lengths could be recreated reasonably well using a form of phase space tomography, which can also give indicators for the unknown pulse shape function. For an example of such a phase space tomography, see appendix E. For more information on the details of this method, refer to [92].

To nevertheless compare the experimental data to references calculated with WIzaRD, the phase spaces of the measured pulses needed to be approximated. For that, the pulse shapes have been assumed to follow a double Gaussian (c.f. eqn. (5.3)) distribution for first comparisons, which is an educated guess based on the results of multiple phase space tomographies. The total length of the pulse was taken from the respective phase space tomography. With this information, a number of particles have been created within a Python programme which exhibit the given particle distribution. The energy distribution of the created particles is taken from the energy spectra of the open dechirper. The numerically generated particles were randomly assigned a position and an energy according to this distribution.

The so created test phase spaces were then subjected to the dechirps of the prototype for different gap widths. For this, the dechirp was calculated by multiplying the wake potential with the used pulse charge. The resulting curve of the dechirp (in dependence on the position $s$) was then interpolated over the region of the pulse so that a functional dependence of the dechirp from the position could be gained. In a next step, for each of the particles of the artificial phase space the dechirp was calculated with respect to the position of the particle. The determined dechirp per particle was then added to the original particle energy.

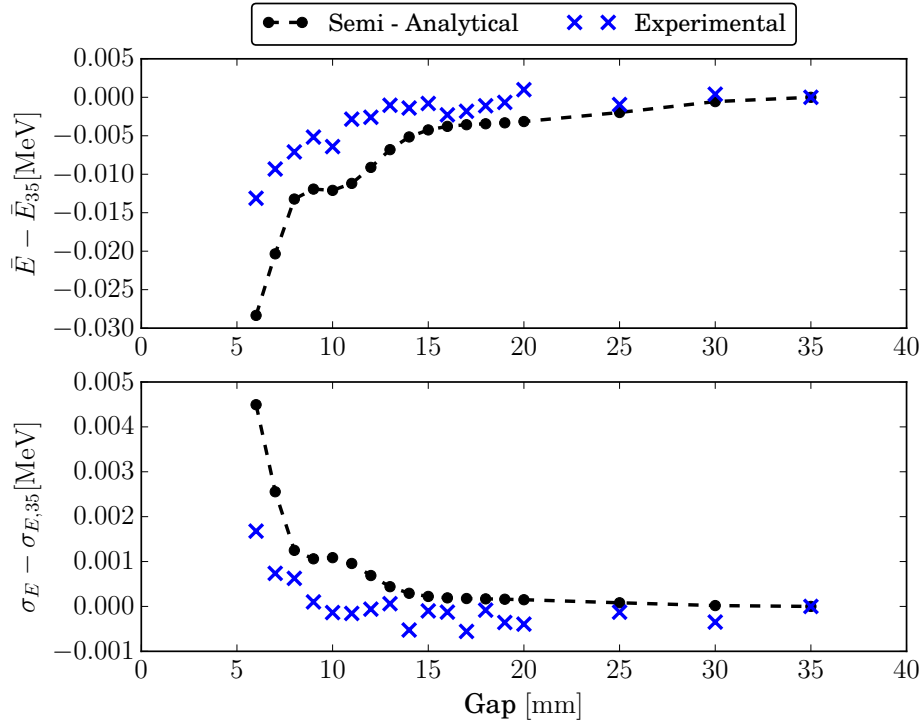Figure 6.11 shows a comparison between the experimentally determined average

**Figure 6.11:** Comparison between the theoretically predicted dechirp (dashed line) of the pulse 1008_1_54 (pulse shape: double Gaussian, length 2 mm) and the experimental data (x-shaped markers). The order of magnitude of the predicted dechirp clearly matches the experimental results, though both the average energy decrease and the increase in the standard deviation have been predicted as too large compared to the measured data.

energies and standard deviations of the energy spectra of pulse 1008_1_54 and their theoretically predicted pendants for different gap widths of the dechirper. First and foremost, the order of magnitude, i.e. changes in the range of a few 10 keV of the experimentally measured data is mirrored in the theoretical predictions. The non-linear dependence on the gap width is also highlighted by the theoretical data. When it comes to a quantitative agreement of the two methods, however, there are discrepancies. The absolute disagreement between both methods also grows for decreasing gap width. In case of the average energies, the difference of both methods is initially in the range of a few keV for the highest gap width. It grows to $\approx 5\,\text{keV}$ for gap width of 15 to 10 mm and lies at $\approx 15\,\text{keV}$ for the lowest gap width, 6 mm. Roughly rounded off, the theoretical predictions always seem to be about twice as large as the experimental values. A similar behaviour can be seen for the standard deviations. This apparent scaling, however, is assumed to be a coincidence, since other comparisons did not exhibit this behaviour.

A second comparison to a theoretical prediction of the effect of the dechirper for
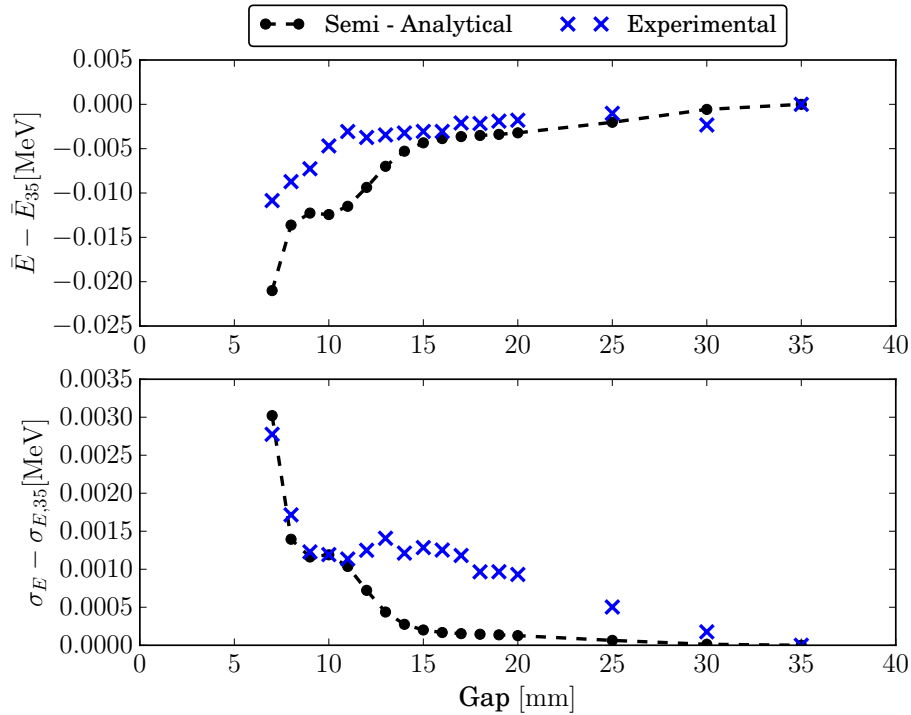
**Figure 6.12:** Comparison between the theoretically predicted dechirp (dashed line) of the pulse 2508_1_56 (pulse shape: double Gaussian, length 1.2 mm) and the experimental data (x-shaped markers). For the average energy, the chosen model is able to predict the experimental results accurately for gap width larger than 15 mm. For lower gap widths, the discrepancy is larger. In case of the standard deviation, the predicted effect of the dechirper is too low for most gap widths, though the order of magnitude of both results is still compliant.

the pulse 2508_1_56 generally confirms the previous findings. Figure 6.12 shows again that the theoretical prediction and the experimental results for both the average energy and the standard deviation of the observed pulse match in their order of magnitude, but also that there are quantitative differences. In this case, while the shift in the average energies is predicted as too strong compared to the actual measurements, the change in the standard deviation is predicted as too low apart for the region of the lowest gap width, in which prediction and experiment are actually in near perfect agreement. The apparent scaling with a factor of 2 that the previous comparison exhibited cannot be confirmed here, which supports the claim that this scaling was coincidence.

As a final statement it should be noted that due to the lack of knowledge of the real phase space of the ELBE beam the matching order of magnitude of all theoretical predictions should be treated as a success.

## 6.3.3 Influence of the Background Noise

### Reducing the Background Noise

Another aspect that needs to be taken into consideration when evaluating the experimental data becomes apparent when the energy spectra are studied more closely. Figure 6.13 shows two energy spectra (solid lines) from the series 2508_1_56. There is a clear offset in the intensities, a background of $\approx 10{,}000$ that is present throughout the measured region. Even measurements without an actual beam show this behaviour, it is thus part of the systematic error of the spectrometer and not inherit to the effect of the dechirper. This is especially problematic because this offset is not constant over the measured energy region, it is generally slightly larger in lower energy regions which can also be seen in Fig. 6.13.
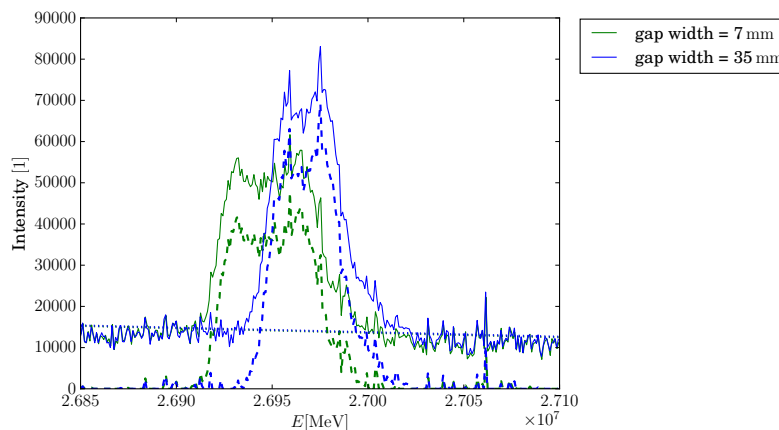


**Figure 6.13:** Energy spectra for the bunch 2508_1_56 and two different gap widths (solid line). The dotted line indicates the polynomials used to fit the background noise which have been subtracted from the raw data in the dashed spectra.

A strategy to reduce this background is also shown in this figure. The background is here fitted with a quadratic polynomial, excluding the high intensity region of the actual spectrum. Here,

$$I\left(E\right) = a \cdot E^2 + b \cdot E + c, \tag{6.1}$$

is the assumed relationship between the intensity $I$ of the spectrum and the energy $E$, and $a$, $b$ and $c$ are the fitting parameters which are consequently determined using a Python script.

The resulting polynomial function is then subtracted from the original spectra. This can lead to negative intensities, which are set to 0. The resulting spectra (dashed lines) show no offset. Due to the fitted polynomials generally not being constant, this background reduction is energy dependent and thus likely to influence the evaluated quantities, the average energy of the spectrum and the corresponding standard deviation.
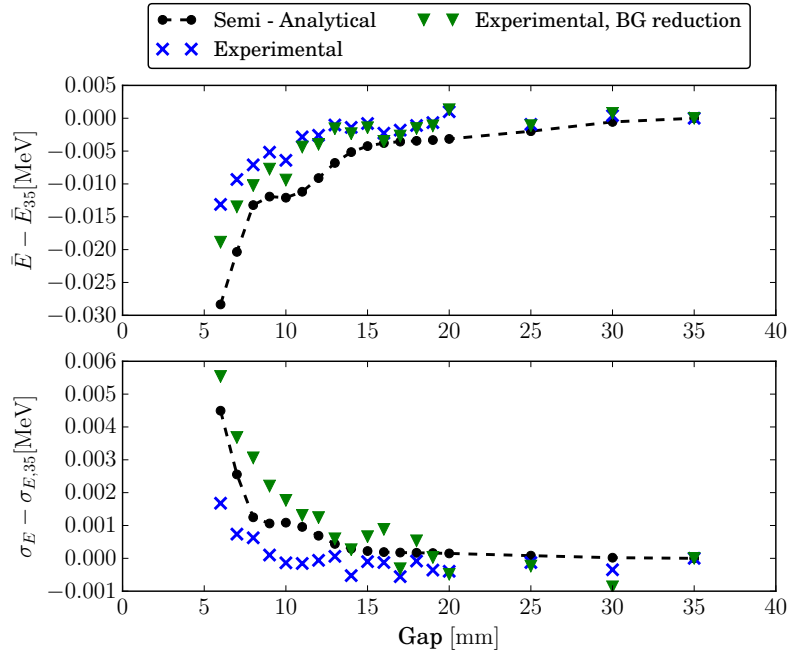
**Figure 6.14:** Influence of the background reduction on the average energy and the standard deviation of the energy spectra measured for the dechirping of bunch 1008_1_54. Reducing the background by subtracting the fitted quadratic function (triangular markers) increases the accordance between the theoretically calculated (dashed line) and experimentally measured results (x-shaped markers).

The influence of this background reduction on the experimental data, again in comparison to theoretical predictions, can be seen in Fig. 6.14 for the pulse 10_1_54. Both the decrease of the average energy and the increase of the standard deviation are more pronounced for the spectra after a reduction of the background with a quadratic polynomial. This leads to an increase of the maximum change in the average energy from $\approx -13\,\mathrm{keV}$ without the background reduction to $\approx -20\,\mathrm{keV}$ with this reduction. In the case of the maximum change in the standard deviation, the shift at 6 mm gap width increases from $\approx 1.5\,\mathrm{keV}$ without reduction to $\approx 5.5\,\mathrm{keV}$ with reduction. For both quantities, the changes introduced by the reduction of the background correspond to a scaling of the original curve, not to an offset; i.e. the influence of the background reduction is smaller for larger gap widths. In general, this modification of the raw experimental data seems to increase the accordance with the theoretical predictions for this pulse.

A similar investigation of the bunch 2508_1_56 also shows an improvement of the accordance of theory and experiment by using a quadratic background reduction on the experimental data. In case of the average energies of this series of experiments, the background reduction even leads to a very good qualitative agreement of both
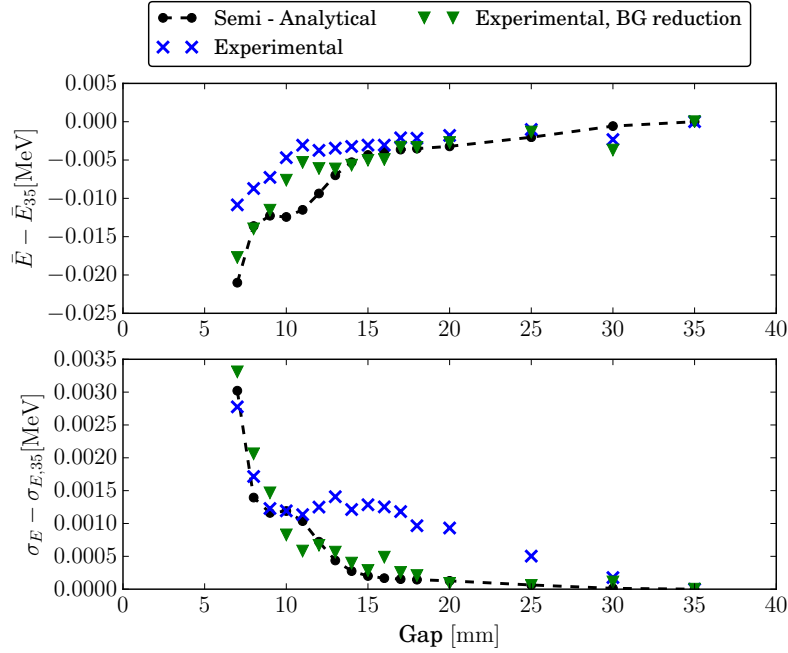
**Figure 6.15:** Influence of the background reduction on the average energy and the standard deviation of the energy spectra measured for the dechirping of bunch 2508_1_56. Reducing the background by subtracting the fitted quadratic function (triangular markers) increases the accordance between the theoretically calculated (dashed line) and experimentally measured results (x-shaped markers).

curves apart from a small region around the gap width 10 mm. Especially for the very low gap widths, the measured and calculated average energies of the spectra match very well. For the standard deviation, the increased accordance between prediction and experiment is especially apparent for gap widths larger than 10 mm where the discrepancies used to be the largest for the raw experimental data and the semi-analytical predictions.

Other experimental results underline these findings, compare to Fig. D.2 in Appendix D for a third example.

## 6.3.4 Influence of Experimental Limitations and Uncertainties on the Evaluated Quantities

All experimental data is subject to errors. To judge the quality of the obtained results, these errors need to be taken into account and evaluated regarding the used methods and devices.

In case of the experiments with the dechirper prototype conducted at ELBE, especially the methods used to postprocess the data and compare to theoretical

expectations are the source of uncertainties and thus, errors. These methods and quantities include the choice of the fitting function for the background reduction, the bunch length extracted from the phase space tomography and the choice of the bunch shape for the semi-analytical calculation of the dechirped phase space. These aspects, together with other possible sources of errors, are going to be discussed in this section.

### The Background Fitting Function

In the previous section, the background noise of the energy spectrum has been reduced by fitting it with a quadratic function and then subtracting this function from the raw experimental data. The choice of the function, however, was only empirical and based on experiences in dealing with the data. Instead of a quadratic polynomial, other functions might be used as well to represent the background.

In the following, next to the quadratic polynomial (c.f. eqn. (6.1)) also a linear function

$$I\left(E\right) = a \cdot E + b, \tag{6.2}$$

and a hyperbolic function

$$I\left(E\right) = a \cdot E^3 + b \cdot E^2 + c \cdot E + d, \tag{6.3}$$

will be used to represent the background. For the series 1008_1_54, the average energies and standard deviations consequently extracted from the modified experimental data can be found in Fig. 6.16.

The figure shows that the influence of the fitting function of the background is generally small. For this series of experiments, the linear and the hyperbolic fitting function deliver nearly exactly the same results for the average energy and the standard deviation. Only a fit with a quadratic function leads to slightly higher shifts in the standard deviation for lower gap widths. The difference to the results which utilised one of the other two fitting functions is only in the range of a maximum of $2\,\mathrm{keV}$ for the lowest gap width.

Figure 6.17 shows a similar behaviour for the series 2508_1_56. Any choice of the fitting function for the background noise delivers nearly the same results for the average energies of the dechirped spectra, with only minor variations. For the standard deviations, though, it is apparent that the choice of a linear function for the fitting of the background leads to vastly different results than the other two. In this case, it leads even to negative overall changes of the standard deviation for nearly all gap widths, which means that here, the standard deviation does actually *increase*, which fits neither the theoretical prediction, nor the extracted values from the raw data. Apparently, in this case, a fit with a linear function is unsuitable[2].

---

[2]Fitting the background with other theoretically possible functions usually does not lead to convergent results for the coefficients.
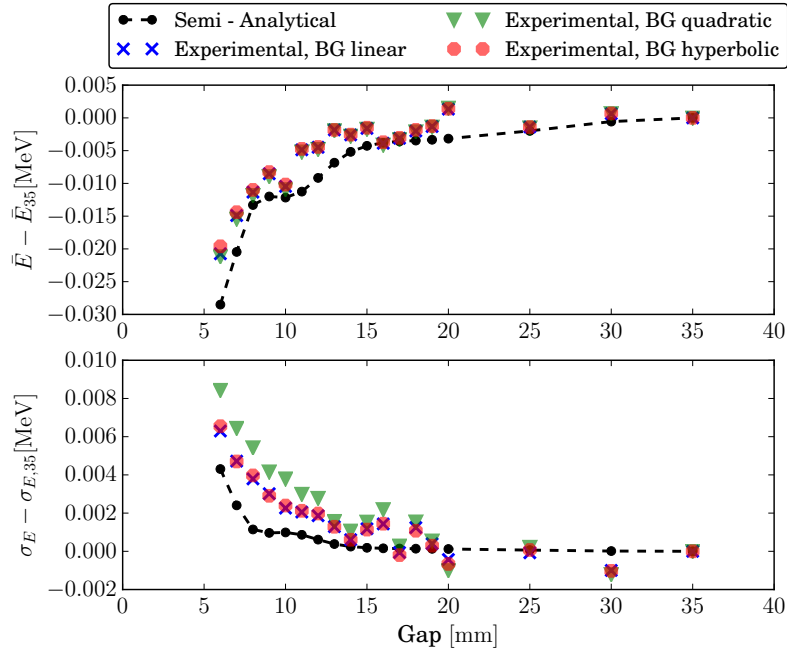
**Figure 6.16:** Influence of the choice of the function used to fit the background on the experimental data of the series 1008_1_54. The background has been fitted with a linear (blue), quadratic (green) and a hyperbolic polynomial (red), respectively. The average energies for different dechirper gap widths do not vary strongly with a change in the background function. For the standard deviation, the linear and the hyperbolic function deliver similar results, while the quadratic function leads to a stronger increase of this quantity for lower gap width.

To summarise, the choice of the function for the fitting of the background has only a minimal influence on the extracted quantities, the average energy and the standard deviation of the spectra. Therefore, the choice of the fitting function is also only a small source of uncertainties for these quantities. The choice of the background fitting function is, however, also not completely arbitrary as the series 2508_1_56 shows and should always be verified against a second or even third option.

**Uncertainties of the Bunch Length**

As stated in Section 6.2.2, the direct measurement of bunch characteristics like the length and shape was not possible at ELBE due to technical limitations. The bunch length, however, could be estimated using phase space tomography.

For comparisons to semi-analytical calculations of the dechirp, knowledge of the bunch characteristics is vital. To estimate which influence this lack of detailed knowledge has on the comparisons made in the previous sections, the previously estimated bunch lengths extracted from the phase space tomography are now varied.
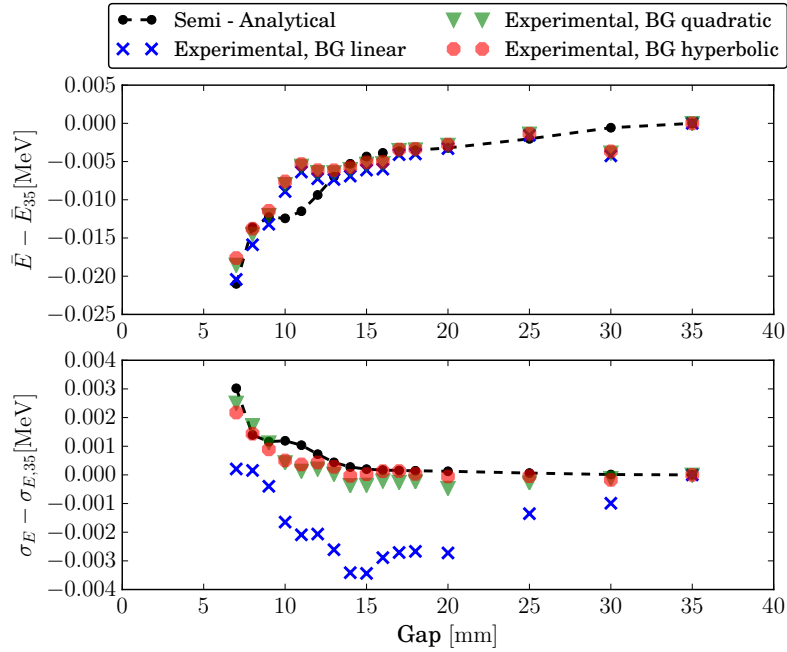
**Figure 6.17:** Influence of the choice of the function used to fit the background on the experimental data of the series 2508_1_56. The background has been fitted with a linear (blue), quadratic (green) and a hyperbolic polynomial (red), respectively. In this case, using the linear fit results in a stronger shift in the average energies for lower gap width compared to the higher order polynomials. Additionally, the evaluation of the standard deviation for the linear fit shows a decrease in this quantity for all gap widths, compared to the (predicted) increase that the use of a higher order polynomial shows.

With these differing bunch lengths, the semi-analytical calculations for the dechirp are repeated and the results are compared to each other, and to the experimentally obtained result. A background reduction of any kind has not been applied for the evaluations in this chapter. All theoretically modelled bunches use a double Gaussian bunch profile.

Figure 6.18 shows a comparison between the experimentally determined effect of the dechirper on the energy spectra for the series 1008_1_54 to semi-analytical predictions made for several different bunch lengths. Three bunch lengths have been used in the figure; 2 mm (red) as determined from the phase space tomography, 1 mm (green) and a vastly shorter length of 0.2 mm (blue). The figure shows that for the two bunch lengths which lie closest together, 2 mm and 1 mm, the results from the semi-analytical calculations do not differ significantly, neither the average energies, nor the standard deviations. However, reducing the estimated bunch length to a tenth of the original value, so to 0.2 mm, decreases the expected effect of the dechirper on the electron beam. Especially for the calculated average energies, the use of a smaller bunch length leads to a drop in the maximally expected effect of
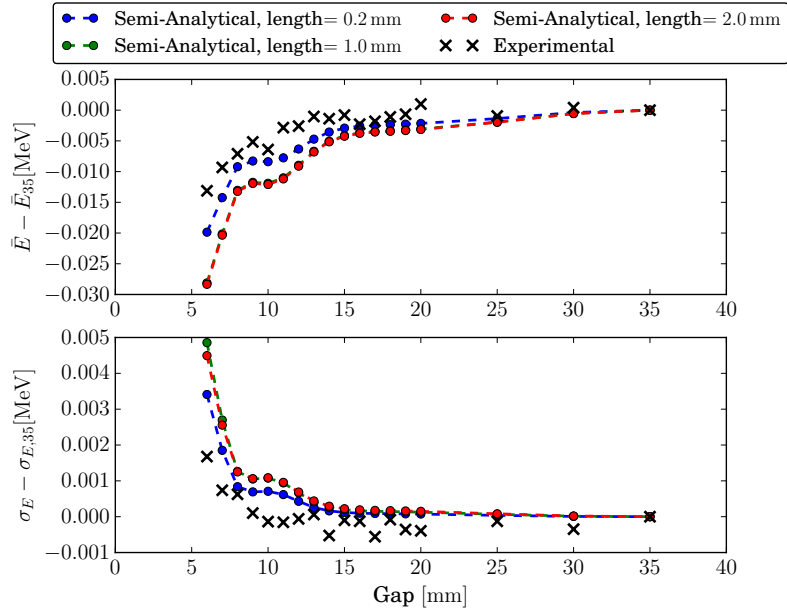
**Figure 6.18:** Comparison of the experimental series 1008_1_54 to semi-analytical calculations of the energy spectra after the dechirper for three different bunch lengths used in the generation of the test phase spaces for the semi-analytical studies. Shown are again the average energy and the standard deviation of the energy spectra for different gap widths of the dechirper. While there is no significant difference in the behaviour of both quantities when comparing the bunch lengths of 1 mm and 2 mm, the very short bunch length of 0.2 mm shows a drastically weaker overall effect of the dechirper.

the dechirper by nearly 10 keV for the lowest gap width, which is about one third of the expected effect for the bunch length estimated by phase space tomography. A similar effect, though on a smaller scale, can be observed for the standard deviations. This also moves the semi-analytical expectations closer to the actual experimental results.

These observations were again validated against a second series of experiments, the series 2508_1_56. The actual bunch length extracted from the phase space tomography for this series was 1.2 mm. In Fig. 6.19, the semi-analytically calculated dechirps for differing gap widths are plotted for three different bunch lengths, including the one extracted from the phase space tomography. Here it shows that the highest compliance between semi-analytical prediction and experiment in case of the average energies is reached for the shortest observed bunch length, 0.12 mm (blue), which is a tenth of the originally used length. For this bunch length, both methods are in nearly perfect agreement. Both higher bunch lengths, 1.2 mm (green) and 2.4 mm (red), deliver average energies of the spectra that are higher compared to the experimental results. The maximum difference between these curves, again reached for the minimal gap width of 6 mm, is more than 30 keV for the shortest and longest bunch,
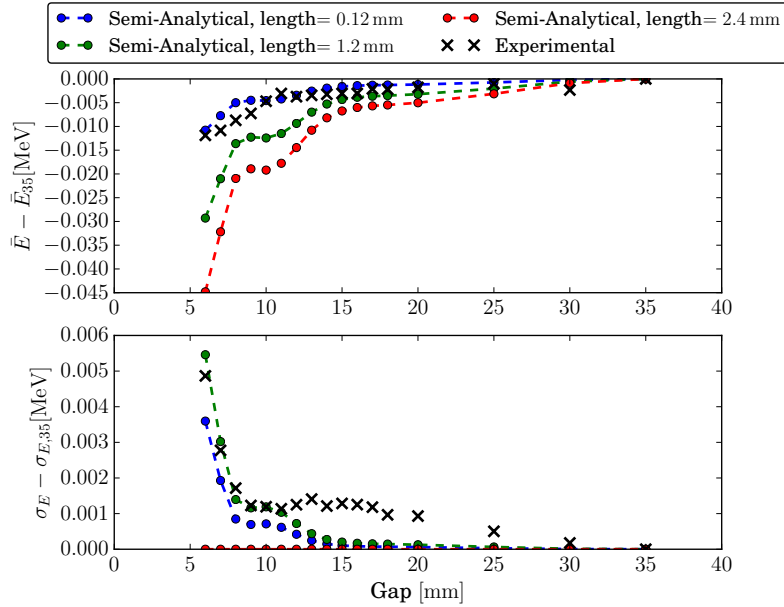
**Figure 6.19:** Comparison of the experimental series 2508_1_56 to semi-analytical calculations of the energy spectra after the dechirper for three different bunch lengths used in the generation of the test phase spaces for the semi-analytical studies. For the average energies, the lowest used bunch length of 0.12 mm (blue) leads to the highest accordance with the experimental data, while both larger bunch lengths predict the effect of the dechirper as too large. For the standard deviations, the bunch length extracted from the phase space tomography, 1.2 mm (green), delivers marginally better results. The third observed bunch length, 2.4 mm (red) does not lead to a satisfactory agreement with the experimental data.

respectively. With respect to the bunch length determined from the phase space tomography, the lower bunch length delivers a maximum dechirp at the lowest gap width of $\approx 30\%$ of the value for the estimated length, while the higher bunch length leads to a maximum dechirp of $\approx 150\%$ of that value. For both bunch lengths, this is a significant difference. For the standard deviation, it is easy to see in Fig. 6.19 that results obtained for the bunch length of 2.4 mm do not mirror the experimental results at all. Both other bunch lengths lead to shifts in the standard deviation that are significantly closer to the experimental value. The bunch length extracted from the phase space tomography shows the largest compliance here, though.

Overall, these comparisons show that the bunch length has a significant influence on the effect of the dechirper. An accurate knowledge of this quantity is thus needed to successfully model the bunch and perform the semi-analytical predictions. While especially the average energy of the spectra seems to be more robust against slight changes of the bunch length within the same order of magnitude, there are still shifts and variations in the predicted results in the range of a few keV. This is, however,

the same order of magnitude in which the increase or decrease of the gap width will change the overall effect of the dechirper, so that this lack of accurate knowledge about the bunch length will in any case complicate a qualitative comparison between theory and experiments. On the other hand, the most drastic changes in the predicted effect of the dechirper that result from a change in the bunch length are the two cases in which the bunch length has been reduced to a tenth of the original value, so in which the order of magnitude of the bunch length has been altered. It has to be mentioned here that these two are artificial test cases and that it is not expected that the uncertainty of the bunch length resulting from the use of the phase space tomography is that significant.

**The Semi-Analytical Dechirp for Different Bunch Shapes**

Next to the uncertainties regarding the bunch length, during the experiments carried out at ELBE, the bunch shape could also not directly be measured. The reconstruction of the unknown phase space of the bunch using phase space tomography and experiences with the thermionic gun suggest a Gaussian or double Gaussian behaviour, from which the latter has so far been used to artificially generate the pulses used for the semi-analytical prediction of the dechirp.

To estimate the influence the correct pulse shape has on the semi-analytical predictions, in this section these predictions have been carried out using bunches recreated for different bunch shapes of the same length; the double Gaussian shape that has already been used in the previous sections, the Gaussian, and the uniform (flat-top) pulse. The results are then compared to the raw experimental data without any background reduction. The bunch lengths chosen here are the ones determined by the phase space tomography.

Figure 6.20 shows the average energies and the standard deviations of the energy spectra for the raw experimental data of the series 1008_1_54 compared to semi-analytical studies made for bunches with the three named bunch shapes. The figure shows that the choice of the bunch shape has only a minor influence on these two quantities, especially the average energy. All three shapes deliver nearly the same results for the studied bunch shapes, only the use of flat-top pulse shape leads to a slight difference in the standard deviations of the energy spectra calculated for the lowest gap width. Figure 6.21 shows that the same holds true for the second experimental series studied, 2508_1_56.

To some extent, the only minimal variation between the characteristics of the energy spectra for the different bunch shapes seem counter-intuitive. However, both quantities studied here are averaged parameters of the whole bunch. In the cases observed here, the Figures 6.20 and 6.21 show that the shift of the particles' energies after the dechirper are the same *on average* for the different bunch shapes, and that overall, the spectra broadened by about the same amount for all observed bunch shapes. The effect of the dechirper on the actual longitudinal phase space distribution
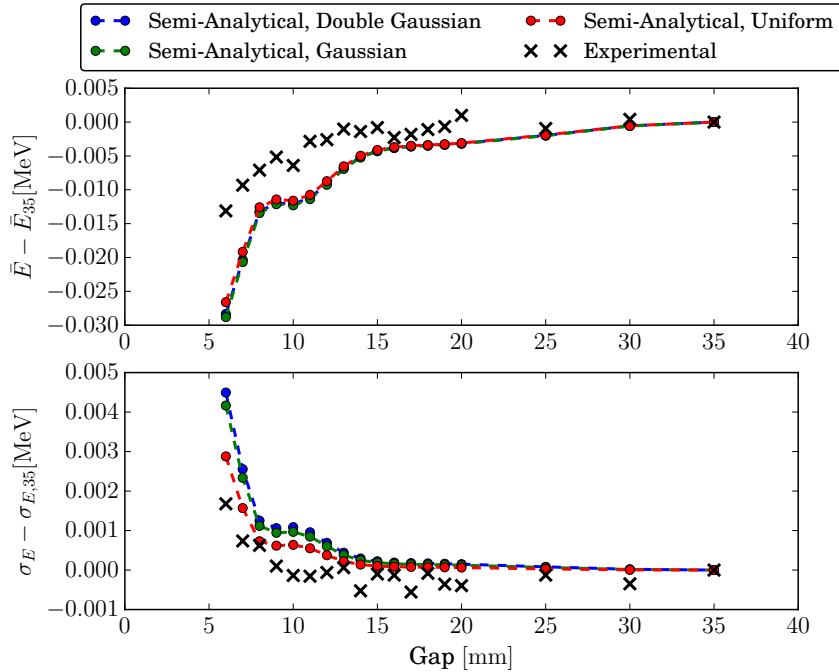
**Figure 6.20:** Comparison of the experimental series 1008_1_54 to semi-analytical calculations of the energy spectra after the dechirper for three different bunch shapes used in the generation of the test phase spaces for the semi-analytical studies. All bunch shapes deliver approximately the same changes in both the average energy and the standard deviation of the spectra for decreasing gap width. In case of the standard deviation, the uniform pulse (red) delivers a slightly lower shift for the lower gap width compared to the double Gaussian (blue) and the Gaussian pulse (green).

could not be studied, and is still expected to differ for the different bunch shapes. Additionally, Fig. 5.9 shows clearly that the maximum achievable strength of the wake potential over the pulse does not vary much for the different bunch shapes. The Gaussian and the flat-top pulse are also symmetrical to $s = 0$, so averaging the wake potential over the pulse shape would also lead to a very comparable result. This explains the similar results for the various bunch shapes.

## 6.3.5 The Actual Dechirping Effect

Apart from the inverse effect of the dechirper discussed in the previous sections, another series of experiments carried out on August 25, 2016 showed the actually desired effect of the dechirper, namely a reduction of the width of the energy spectrum (as opposed to a broadening). The series, referred to as 2508_2_65 from now on, used slightly modified settings for the thermionic gun compared to the series discussed previously. The bunch charge here was 65 pC.
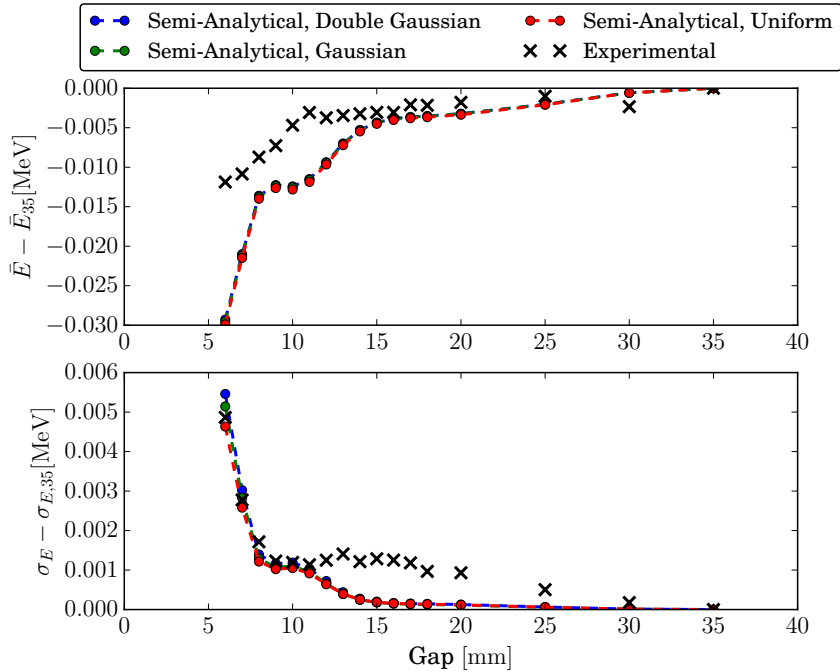
**Figure 6.21:** Comparison of the experimental series 2508_1_56 to semi-analytical calculations of the energy spectra after the dechirper for three different bunch shapes used in the generation of the test phase spaces for the semi-analytical studies. All three studied bunch shapes lead to similar behaviours of the average energy and the standard deviation for the different gap width.

Figure 6.22 shows the normalised intensities of the energy spectra recorded for the bunch after the dechirper using varying gap width. As in the Figures 6.5 and 6.7, the intensities have been interpolated for the gap widths that have not been measured.

The figure verifies again the energy reduction due to the effect of the dechirper: the high intensity peak at 26.92 MeV shifts towards lower energies for decreasing gap widths. This shift is especially strong for gap widths lower than 10 mm. But additionally, the figure illustrates an actual reduction of the width of the energy spectrum. There is a second peak of higher intensities in the spectra that is located at $\approx 26.96$ MeV. For decreasing gap widths, this peak does not only shift towards lower energies, its intensity also becomes less and less until it is nearly completely suppressed for gap widths lower than 10 mm. This suppression of the second high intensity peak leads to an overall reduction of the energy width.
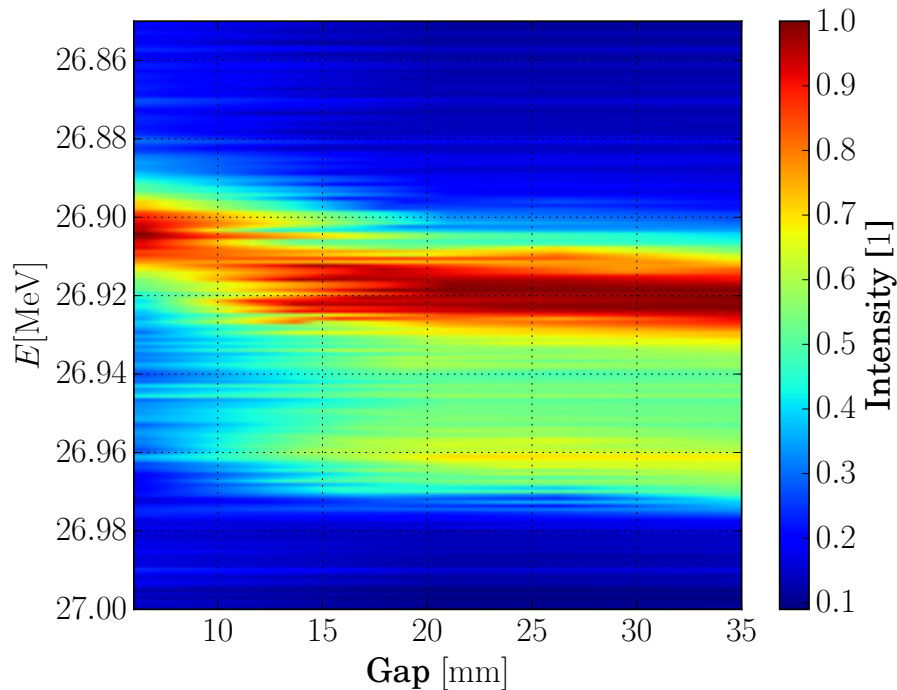
**Figure 6.22:** The actually desired dechirper effect measured in the series 2508_2_65. The shift of the spectrum towards lower energies for a decreasing gap width of the dechirper is seen in the high intensity peak at 26.92 MeV. The actually intended decrease in the width of the energy spectrum can be seen in the second energy peak at 26.96 MeV, which gets gradually suppressed for lower gap width.

## 6.4 Summary

Despite the technical and spatial limitations that only allowed for a dechirper proto-type with a relatively minor expected influence on the overall phase space of the electron beam, both the effect of the dechirper prototype could be shown in multiple series of experiments and are supported by similar findings in [1], [2] and [60] regarding the influence of the gap width and the overall strength of the dechirper.

Since the phase spaces of the electron beam could not directly be measured, the energy spectra of the beams after the dechirper were studied instead. The quantities that have been focussed on during the evaluation of the experimental data were the average energies and the standard deviations of the spectra. These quantities were extracted from the raw data for different gap widths of the dechirper, and the changes in these quantities were recorded with respect to the open dechirper, i.e. the dechirper setting with the highest achievable gap width.

The experiments were carried out for electron beams without an initial energy chirp. The operation of the dechirper in this case shows the inverse of the desired

effect: a widening of the spectrum instead of a reduction of the energy width that increases with a decreasing gap width. This was visible in all experimental results in an increase of the standard deviations of the spectra. The general energy reduction induced by the dechirper was also shown in all experimental series. The order of magnitude of the dechirp can be predicted reasonably well with the use of WIzaRD, however, and accurate prediction of the qualitative effect of the dechirper is difficult due to the lack of knowledge about the phase space of the electron beam. Both the bunch lengths and the approximate beam shape could be recreated using phase space tomography, and even though the data extracted from this procedure contains errors that are hard to estimate, small variations in both quantities do not change the predicted results drastically. The comparison between WIzaRD and the experiments remains still valid.

Another factor that has an influence on the agreement between theory and experiment is the background of the energy spectra. It has been shown that fitting this background with a simple polynomial and then subtracting it from the raw data generally helps to increase the agreement of both methods.

The influence of the bunch charge on the effect of the dechirper has also been studied. Here, measurements show that changing the bunch charge does influence the effect of the prototype in the expected order of magnitude, but the linear scaling that was predicted from theory was not observed. A reason for this is the relatively small range of charges that could be generated by the thermionic gun compared to the already small effect of the dechirper overall. Nevertheless, for future studies, this can easily be remedied when the ELBE SRF gun is ready for operation.

Overall, despite the technical limitations, the experiments can be treated as a success that gives a general proof of principle of the functionality of the dechirper. Especially the influence of the gap width was illustrated very well by all experimental series that have been carried out, and thus underlines the predicted versatility and adaptability of this particular dechirper type during operation.

Additionally, the actually desired effect of the dechirper - a reduction of the energy width of the beam - could also be measured in form of the suppression of a high energy peak in one of the experimental series.

# 7 Discussion, Summary and Outlook

The objective of this thesis has been a comprehensive study of the general properties and application of dielectrically lined rectangular waveguides for the purpose of dechirping electron bunches, specifically at the ELBE facility at the HZDR. The term dechirping in this context refers to a reduction of the energy width of the electron bunch. A particular point of interest has been the influence of the geometric parameters of the structure on the final wake potential and the resulting dechirping ability.

The final goal of the project work of this thesis has been set as the test of a prototype dechirper at the HZDR from the very beginning. This means that all the studies conducted for this thesis are heavily tied to the requirements at ELBE and the applicability of the considered concepts at this facility. This duality of theoretical research and practical applicability has been what first and foremost determined the prospective geometry of the dechirper as a rectangular waveguide with dielectric coatings. This particular type of dechirper promised an easy construction, and an additional experimental degree of freedom in form of the gap width of the dechirper, i.e. the distance between the upper and the lower dielectric plate which has later become an important focus of the experiments.

The initial choice of the structure of the dechirper provided another important advantage in its geometric simplicity and similarity to a plain, empty and uncoated rectangular waveguide. The only difference is that compared to the empty waveguide, the dechirper is coated with dielectric plates, which will lead to a varying permittivity in one transversal dimension of the dechirper.

This advantage has been exploited in the course of this work to gain an analytic expression of the wake function inside the dechirper using an eigenmode expansion. For this purpose, a Rayleigh-Ritz based formulation of the eigenmodes of these dechirpers, so-called LSE and LSM modes, has been established. These formulations use Fourier-sine and Fourier-cosine expansions to express the otherwise unknown behaviour of the eigenmodes in the direction of the changing permittivity; in the other dimensions, the eigenmode solutions are similar to those in an uncoated waveguide.

As a next step, the electric field of a point charge traversing the dechirper in longitudinal direction at the speed of light has been computed by expanding it into a series of eigenmodes. From the electric field, the wake function has been determined via integration. A simplification of the gained expression for the wake function lead to eqn. (3.56). This shows that the wake function can be expressed as the sum of contributions from each mode. The strength of these contributions

is measured by the loss factors (3.57) and (3.58), which in turn depend entirely on mode characteristics and geometric parameters of the structure. This means that for a practical calculation of the wake function, no previous knowledge of the electric field is necessary.

As a result of these considerations, an analytical expression of the eigenmodes and the wake function of a rectangular, dielectrically coated dechirper has been gained. However, the expansion coefficients of both the Fourier expansions used for the mode computations and the eigenmode expansion used to calculate the electric field cannot be calculated analytically for any reasonable number of expansion functions. Their computation needs to be carried out numerically, which renders the overall model semi-analytical for any practical application.

In the following step, the semi-analytical model has been implemented in Python. For this, the two Python modules *SymPy* and *NumPy* have been combined. As a first subroutine, the Python programme, dubbed WIzaRD, calculates the eigenmodes of the specified structure in a sense that it determines the expansion coefficients of the underlying Fourier expansions and computes the eigenfrequency of the mode. For these eigenmodes, the loss factors are then generated, which enables the superposition to obtain the wake function. To grant an efficient performance of WIzaRD, the modes are generated and superimposed following a certain scheme (c.f. Fig. 4.13) that exploits that a great number of eigenmodes does not contribute to the wake function due to symmetry reasons, and that only eigenmodes with a phase velocity close to the speed of light have a large influence on the wake function. All other modes are not considered and also not computed by WIzaRD. Additionally, the modes are calculated in ascending order with respect to their eigenfrequencies.

The algorithms and methods used in WIzaRD have been benchmarked against computations with CST PS and analysed with respect to their convergence. These studies show that especially for the short-range wake fields important in the field of dechirpers (i.e. the wakefields directly in the region of the particle pulse that generates them), WIzaRD shows a very good and fast convergence and delivers nearly the same results as CST PS. Over the course of these studies it was also illustrated that WIzaRD has several inherent advantages against purely numerical software. The most important advantage is that WIzaRD allows for a computation of the wake function, which serves as the Green's function for the calculation of wake potentials of arbitrary bunch shapes. In contrast, CST PS can only compute the wake potentials of Gaussian pulses. Additionally, the calculation of wake potentials of small pulses is difficult and computationally expensive because numerical simulation tools require a very fine spatial discretisation in these cases. Post-processing of wakefield data almost always uses particle tracking software, e.g. ELEGANT, to determine the effect of the wakefield on the generating and following particle bunches. This software requires the input of the wake function, which means that using the result of a numerical solver, i.e. the wake potential of a small Gaussian beam, is automatically the source of errors. WIzaRD enables the calculation of a Green's

function which avoids this source of error. Additionally, WIzaRD is not reliant on spatial or temporal grids since it is purely based on the analytical descriptions of the modes and the wake function. This allows for a computation of substantially higher order modes with nearly the same accuracy as modes of a lower order in the same amount of time.

As a next step, the programme package WIzaRD was used to perform parameter studies. In this section, all relevant geometric and dielectric parameters of the dechirper were varied based on the configuration that had been chosen for the prototype tested at ELBE. First, the known linear behaviour of the wake function with the length of the structure was observed and used as a benchmark for the accuracy and performance of WIzaRD. After this step, it was shown that the width of the dechirper only has an influence on the strength of the wake function in a certain, limited range. After this range, larger widths of the dechirper do not lead to higher amplitudes of the wake function. With respect to the dielectric parameters, it could be shown that lower dielectric constants are favourable for achieving higher wake function amplitudes, but that small variations of this parameter do not influence the amplitude of the wake function as strongly as variations in the length or of the gap width of the dechirper. A similar observation could be made regarding the thickness of the dielectric plates. The highest potential for influencing the wake function of a dechirper with a fixed length has the gap width of the rectangular dechirper, i.e. the distance between the upper and lower dielectric plate. It could be shown in this work that within a few centimetres of range the strength of the wake function can be reduced significantly. This also means that the dechirper can nearly be turned off completely by only increasing the gap width, which has several practical advantages. Here it likewise became clear that a tuning of the gap width can enable a later adjustment of the wakefield to the needs at the accelerator site.

During the experiments performed at ELBE, the focus was set on providing experimental proof of the tunability of the wake potential due to the mechanical variation of the gap width. An additional point of interest was the scaling of the effect of the dechirper with the total bunch charge, which, in theory, should be linear. Due to the parameter studies performed previously, it was already expected that the prototype dechirper would not be able to produce a dechirp that could counteract the usual chirp of the ELBE beam. This chirp is usually in the range of a few MeV, the dechirper was expected to be able to counteract $\approx 40\,\mathrm{keV}$. This effect is very small compared to the actual chirp. To be able to measure the effect of the dechirper without correlation to the chirp of the particle beam, the magnetic chicane and the second accelerating module at ELBE were not used in these experiments. As a result, the beams that were used in these experiments had no initial chirp. Thus, the dechirper, while it still would lower the overall energy of the bunch, was expected to broaden the energy width of the particle bunch. This could be measured in a decrease of the average energy of the energy spectrum and an increase in the respective standard deviation. Overall, the experiments showed exactly this

behaviour. Additionally, a stepwise decrease of the gap width of the dechirper lead in all measured experimental series to an increase in the effect of the dechirper which underlines the expected tunabilitiy of the rectangular dechirper type. When it came to analysing the behaviour of the dechirper for different bunch charges, it has to be said that while the bunch charge could be shown to have a qualitative influence on the effect of the dechirper, quantitatively this did not match the expected linear scaling. In one of the experiments performed it was also possible to generate a particle bunch that could actually be dechirped by the prototype, which became apparent in the measured spectra in form of the suppression of a high intensity peak at the higher end of the spectrum (c.f. Fig. 6.22).

Comparisons between the experimental results and theoretical predictions proved challenging because the technical limitations at the HZDR did not allow for a direct measurement of the longitudinal phase space of the observed particle bunches. Both the approximate bunch length and pulse shape could be extracted from additional measurements which enabled a phase space tomography. With this data, the particle bunches were artificially recreated in Python and then dechirped using the wake functions determined with WIzaRD during the parameter studies. The average energies and standard deviations of the energy distributions of these assumed particle bunches were then calculated and compared to the results of the experiments. Here it showed that while generally, the experiments and the theoretical computations show and predict the effect of the prototype in the same order of magnitude, which was in most cases a few 10 keV. However, the agreements of theory and raw experimental data was still not found to be very high within that order of magnitude. A reduction of the background of the experimental data by a fit with a quadratic polynomial increased this agreement, while it still not fully compensated the differences. Additional simulations performed to estimate the influence of the lack of detailed knowledge of the length and shape of the particle bunch showed that especially due to evaluating averaged quantities of the whole spectrum, variations of the beam shape and length within reasonable limits did not significantly change the outcome of the theoretical predictions. In other words, while the lack of detailed knowledge about the phase space inhibits the estimation of the effect of the dechirper on the phase space, for observations regarding the energy spectrum an approximation of the bunch shape and length seem sufficient.

However, a crucial point in all experimental investigations was the comparatively small effect of the dechirper on the particle bunch that is in the same order of magnitude as the effects that the variation of quantities like the bunch charge or pulse length have. A decorrelation of these effects to identify sources or errors in both the experimental setup and the theoretical predictions is thus very hard.

Notwithstanding these experimental challenges, in this work the rectangular dielectrically coated waveguide could be characterised in the use as a bunch dechirper from three different angles: first, an analytical foundation and subsequent semi-analytical implementation for the calculation of these wake functions could be found. Second,

the influence of the geometrical and dieletric properties of the dechirper could be analysed. And third, the effect of the dechirper could be shown in multiple series of experiments. From this point of view, the objective of reaching a comprehensive understanding of this dechirper type has been met, and it could be shown that this particular structure is suited for the application as a wakefield dechirper. The major advantages of this dechirper type lie in its simplicity and therefore the possibility to study its effect analytically; and in the tunability of the effect of the structure by adjusting the gap width, which is even possible after construction. The disadvantage is the comparatively weak effect of the dechirper, which, however, is also limited by the spatial requirements of the accelerator site ELBE and the limitations to the bunch charge.

In the future, these studies can provide the basics for additional, more detailed experiments regarding the dechirper prototype at ELBE. Once the ELBE SRF gun can be utilised for the bunch generation, higher bunch charges of up to $1\,\mathrm{nC}$ are possible, which would already increase the effect of the dechirper by a factor of ten and thus allow for observations of more pronounced shifts in the characteristics of the energy spectrum. Current research and construction projects at ELBE also focus on deflecting cavities and their application for the measurement of the complete longitudinal phase space. With these measurements at hand, the theoretical predictions of the effect of the dechirper could be significantly improved. Additionally, this would allow for an analysis of the effect of the dechirper on the complete phase space, not only the energy spectrum, which can give a vastly more detailed insight into the effect of the dechirper on the single particles. This type of investigation would then also allow for studies regarding the applicability of the dechirper in other fields; e.g. the here described effects of the bunch shape on the form of the dechirped particle bunch. This could, e.g. allow for a compensation of higher order correlations in the longitudinal phase space by applying a dechirper and using a particular bunch profile that creates a wake potential which counteracts this effects.

On a more theoretical sector this work can provide the groundwork for additional studies of other dechirper types. The algorithms discussed here can, with a few modifications, also be applied for cylindrical waveguides with a dielectric coating, which have also been suggested as dechirpers. Here, instead of having a varying permittivity in one transversal direction, the radius of the waveguide would be subjected to a varying permittivity due to the dielectric coating. Calculating eigenmodes and the resulting wake function from this should be possible analogously to the procedure described here. With a few more alterations, this methodology can also be used to compute the wake functions inside corrugated dechirpers. Here, the described methods to compute the eigenmodes have to be adjusted by employing, e.g., mode-matching techniques and Floquet's theorem. This would then enable the programming of an even more all-encompassing semi-analytical tool for the calculation of wake functions in every dechirper type studied so far.

# A Detailed Proof of the Orthogonality Relations

The proof of the orthogonality relations of LSE and LSM modes, due to their representation, is in large parts simply a matter of the familiar orthogonality relations of sine and cosine,

$$\int_0^a \sin(k_x x) \sin(k'_x x) \mathrm{d}x = \delta_{k_x k'_x} \left\{ \begin{array}{l} \frac{a}{2}, \text{ for } k_x \neq 0 \\ 0, \text{ for } k_x = 0 \end{array} \right. \tag{A.1}$$

$$\int_0^a \cos(k_x x) \cos(k'_x x) \mathrm{d}x = \delta_{k_x k'_x} \left\{ \begin{array}{l} \frac{a}{2}, \text{ for } k_x \neq 0 \\ a, \text{ for } k_x = 0 \end{array} \right. , \tag{A.2}$$

with equivalent relations in $z$-direction. Additionally, the relations (3.16) and (3.28) between two solutions of the same Sturm-Liouville problem as given in Chapter 3.2.2 will become important in the following derivations.

Perhaps the relation that is easiest to prove is the orthogonality of the magnetic flux densities of LSM modes (4.6). When solving $\int \underline{\mathbf{B}}_\mu(\mathbf{r}) \cdot \underline{\mathbf{B}}_{\mu'}(\mathbf{r}) \, \mathrm{d}V$, the integrations over the $x$- and $z$-components are simply following (A.1) and (A.2). Thus, the orthogonality relation simplifies to a proof of

$$\int \underline{\mathbf{B}}_\mu(\mathbf{r}) \cdot \underline{\mathbf{B}}_{\mu'}(\mathbf{r}) \, \mathrm{d}V = -A_\mu^2 \frac{\omega_\mu \omega_{\mu'}}{c_0^4} \frac{aL}{4} \left( k_x^2 + k_z^2 \right) \delta_{k_x,k'_x} \delta_{k_z,k'_z}$$

$$\cdot \int_0^b \left( \sum_{m=0}^N q_{\mu,m} \cos(k_{y,m} y) \right) \cdot \left( \sum_{m'=0}^N q_{\mu,m'} \cos(k_{y,m'} y) \right) \mathrm{d}y.$$

With this formulation it can be seen that if both modes differ in either $k_x$ or $k_z$, the integral vanishes. In this case, the functions $Q_{\mu,m}(y)$ and $Q_{\mu,m'}(y)$ do not belong to the same Sturm-Liouville problem and their orthogonality is not granted by (3.16). However, the solution to the remaining integration over the $y$-components is not necessary for the orthogonality in total, since $\delta_{k_x,k'_x} \delta_{k_z,k'_z} = 0$ already renders the expression 0.

Should $\delta_{k_x,k'_x} \delta_{k_z,k'_z} = 1$, the final integration needs to be carried out. Note that in this case, the $y$-components of both modes are derived from the same Sturm-Liouville problem (since $k_x = k'_x$ and $k_z = k'_z$), so that (3.16) is valid. Thus, the orthogonality

relation of the magnetic flux densities of LSM modes can be summarised as

$$\int \underline{\mathbf{B}}_\mu\left(\mathbf{r}\right) \cdot \underline{\mathbf{B}}_{\mu'}\left(\mathbf{r}\right) \mathrm{d}V = A_\mu^2 V_\mu \delta_{\mu,\mu'} \text{ with } V_\mu = -\frac{\omega_\mu^2}{c_0^4}\left(k_x^2 + k_z^2\right)\frac{aL}{4}\xi, \qquad \text{(A.3)}$$

with $\delta_{\mu,\mu'} = \delta_{k_x,k_x'}\delta_{k_z,k_z'}\delta_{m,m'}$.

The derivation of the orthogonality relation of the electric field of two LSE modes (4.2) follows the previous proof nearly analogously.

Due to the solutions of the Sturm-Liouville problem for LSE modes being orthogonal with respect to the relative permittivity (c.f. eqn. (3.28)), the same orthogonality is proven here for the electric fields. The only adaptation that needs to be made in comparison to the proceeding for the magnetic flux density of the LSM mode is the introduction of a case differentiation that accounts for the possibility of either one-dimensional wavenumber being zero, so that

$$\int \varepsilon_r(y)\underline{\mathbf{E}}_\lambda\left(\mathbf{r}\right) \cdot \underline{\mathbf{E}}_{\lambda'}\left(\mathbf{r}\right) \mathrm{d}V = A_\lambda^2 U_\lambda \delta_{\lambda,\lambda'} \text{ with } U_\lambda = \omega_\lambda^2\frac{aL}{2}T_{xz}\xi, \qquad \text{(A.4)}$$

with

$$T_{xz} = \begin{cases} \frac{1}{2}\left(k_x^2 + k_z^2\right) & \text{for } k_x \neq 0, k_z \neq 0 \\ k_x^2 & \text{for } k_x \neq 0, k_z = 0 \\ k_z^2 & \text{for } k_x = 0, k_z \neq 0 \end{cases}. \qquad \text{(A.5)}$$

Proving the orthogonality of the magnetic flux densities of LSE modes and the electric fields the LSM modes is more complex, and requires several 'detours'. This is caused by the $x$- and $z$-components of both fields being dependent on the first derivatives of their respective functions $Q(y)$, for which no orthogonality relations are known.

A detailed solution strategy is presented here for the orthogonality of the electric fields of two LSM modes (4.7): an obvious method to circumvent the first order derivatives of $Q_\mu(y)$ is to proof the orthogonality of the electric field with a vector where both the $x$- and $z$-component are zero anyway, e.g. the Hertzian potential (3.18). And indeed, the orthogonality of the electric fields of two modes can be reduced to the orthogonality of the electric field of one mode and the Hertzian potential of another mode using (3.12),

$$\int \varepsilon_r(y)\underline{\mathbf{E}}_\mu\left(\mathbf{r}\right) \cdot \underline{\mathbf{E}}_{\mu'}\left(\mathbf{r}\right) \mathrm{d}V = k_0^2 \int \varepsilon_r(y)\underline{\mathbf{E}}_\mu\left(\mathbf{r}\right) \cdot \mathbf{\Pi}_{\mu,\mu'}\left(\mathbf{r}\right) \mathrm{d}V$$
$$+ \int \varepsilon_r(y)\underline{\mathbf{E}}_\mu\left(\mathbf{r}\right) \cdot \nabla\left(\varepsilon_r^{-1}(y)\left(\nabla \cdot \mathbf{\Pi}_{\mu,\mu'}\left(\mathbf{r}\right)\right)\right) \mathrm{d}V,$$

where the first term is the desired formulation of the orthogonality relation and the second term is effectively zero, as will be proven now.

Inverting the product rule, the second term of the above integral can be rewritten as

$$\int \varepsilon_r(y)\underline{\mathbf{E}}_\mu(\mathbf{r}) \cdot \nabla \left(\varepsilon_r^{-1}(y)\left(\nabla \cdot \mathbf{\Pi}_{\mu,\mu'}(\mathbf{r})\right)\right) \mathrm{d}V$$

$$= \int \nabla \cdot \left(\varepsilon_r(y)\underline{\mathbf{E}}_\mu(\mathbf{r})\,\varepsilon_r^{-1}(y)\left(\nabla \cdot \mathbf{\Pi}_{\mu,\mu'}(\mathbf{r})\right)\right) \mathrm{d}V$$

$$- \int \underbrace{\nabla \cdot \left(\varepsilon_r(y)\underline{\mathbf{E}}_\mu(\mathbf{r})\right)}_{\propto \nabla \cdot \underline{\mathbf{D}}_\mu(\mathbf{r})=0}\varepsilon_r^{-1}(y)\left(\nabla \cdot \mathbf{\Pi}_{\mu,\mu'}(\mathbf{r})\right) \mathrm{d}V,$$

where the second term vanishes due to (3.6). The first term is now subjected to the Divergence Theorem, rewriting it into

$$\int \nabla \cdot \left(\varepsilon_r(y)\underline{\mathbf{E}}_\mu(\mathbf{r})\,\varepsilon_r^{-1}(y)\left(\nabla \cdot \mathbf{\Pi}_{\mu,\mu'}(\mathbf{r})\right)\right) \mathrm{d}V = \int \underline{\mathbf{E}}_\mu(\mathbf{r})\left(\nabla \cdot \mathbf{\Pi}_{\mu,\mu'}(\mathbf{r})\right)\mathbf{n}\,\mathrm{d}S = 0.$$

This expression vanishes on the PEC boundary, since $\nabla \mathbf{\Pi}_{\mu,\mu'}(\mathbf{r})\,\mathbf{n} = 0$ at this surface (with $\mathbf{n}$ representing a vector normal to the surface). This can be seen clearly when actually determining the gradient of the Hertzian potential,

$$\nabla \cdot \mathbf{\Pi}_{\mu,\mu'}(\mathbf{r}) = -A_\mu \sin(k_x x)\sum_{m=0}^{N} q_{\mu,m}k_{y,m}\sin(k_{y,m}y)\sin(k_z z),$$

and is caused by the symmetry of the sine functions.

In total, the orthogonality of the electric fields of LSM modes reduces to

$$\int \varepsilon_r(y)\underline{\mathbf{E}}_\mu(\mathbf{r}) \cdot \underline{\mathbf{E}}_{\mu'}(\mathbf{r})\,\mathrm{d}V = k_0^2 \int \varepsilon_r(y)\underline{\mathbf{E}}_\mu(\mathbf{r}) \cdot \mathbf{\Pi}_{\mu,\mu'}(\mathbf{r})\,\mathrm{d}V.$$

Note that the dependency of the electric field on the relative permittivity cancels out the permittivity in the volume integral, and the final proof of the orthogonality follows closely the statements made for the previous two proofs.

The final relation thus reads as

$$\int \varepsilon_r(y)\underline{\mathbf{E}}_\mu(\mathbf{r}) \cdot \underline{\mathbf{E}}_{\mu'}(\mathbf{r})\,\mathrm{d}V = k_0^2 \int \varepsilon_r(y)\underline{\mathbf{E}}_\mu(\mathbf{r}) \cdot \mathbf{\Pi}_{\mu,\mu'}(\mathbf{r})\,\mathrm{d}V = A_\mu^2 U_\mu \delta_{\mu,\mu'}$$

$$\text{with } U_\mu = k_0^2\left(k_x^2 + k_z^2\right)\frac{aL}{4}\xi.$$

(A.6)

A similar procedure can be applied for the magnetic field of LSE modes (4.3), substituting one of the fields employing eqn. (3.25) and proving the orthogonality of one magnetic flux density with another Hertzian potential instead:

$$\int \underline{\mathbf{B}}_\lambda(\mathbf{r})\cdot\underline{\mathbf{B}}_{\lambda'}(\mathbf{r})\,\mathrm{d}V = -jk_0^2\int \varepsilon_r\underline{\mathbf{B}}_\lambda(\mathbf{r})\cdot\mathbf{\Pi}_{\lambda,\lambda'}(\mathbf{r})\,\mathrm{d}V - j\int \underline{\mathbf{B}}_\lambda(\mathbf{r})\cdot\nabla\left(\nabla \cdot \mathbf{\Pi}_{\lambda,\lambda'}(\mathbf{r})\right)\,\mathrm{d}V.$$

The first term on the right-hand side is the desired formulation of the orthogonality relation, while the second term needs to be zero. To proof this, the same strategy as before is used. Reversing the product rule, the second term on the right-hand side can be written as

$$\int \underline{\mathbf{B}}_\lambda (\mathbf{r}) \cdot \nabla (\nabla \cdot \mathbf{\Pi}_{\lambda,\lambda'} (\mathbf{r}))\, \mathrm{d}V = - \int \underbrace{(\nabla \cdot \underline{\mathbf{B}}_\lambda (\mathbf{r}))}_{=0} (\nabla \cdot \mathbf{\Pi}_{\lambda,\lambda'} (\mathbf{r}))\, \mathrm{d}V$$
$$+ \int \nabla \cdot (\underline{\mathbf{B}}_\lambda (\mathbf{r}) (\nabla \cdot \mathbf{\Pi}_{\lambda,\lambda'} (\mathbf{r})))\, \mathrm{d}V,$$

where the first term vanishes due to (3.9).

The remaining term is rewritten using the Divergence Theorem,

$$\int \nabla \cdot (\underline{\mathbf{B}}_\lambda (\mathbf{r}) (\nabla \cdot \mathbf{\Pi}_{\lambda,\lambda'} (\mathbf{r})))\, \mathrm{d}V = \int \underline{\mathbf{B}}_\lambda (\mathbf{r}) (\nabla \cdot \mathbf{\Pi}_{\lambda,\lambda'} (\mathbf{r}))\, \mathbf{n}\, \mathrm{d}S = 0,$$

which vanishes because $\underline{\mathbf{B}}_\lambda (\mathbf{r})\, \mathbf{n} = 0$ according to the PEC boundary conditions.

All in all this means that it is sufficient for the orthogonality of the magnetic flux densities of two LSE modes to proof the orthogonality of one field with the Hertzian potential, which, again, follows the same general thoughts as all examples before. The final result reads

$$\int \underline{\mathbf{B}}_\lambda (\mathbf{r}) \cdot \underline{\mathbf{B}}_{\lambda'} (\mathbf{r})\, \mathrm{d}V = -jk_0^2 \int \varepsilon_r \underline{\mathbf{B}}_\lambda (\mathbf{r}) \cdot \mathbf{\Pi}_{\lambda,\lambda'} (\mathbf{r})\, \mathrm{d}V = A_\lambda^2 V_\lambda \delta_{\lambda,\lambda'}$$
$$\text{with } V_\lambda = -\frac{aL}{2} k_0^2 T_{xz} \xi. \tag{A.7}$$

For the sake of completeness, also the orthogonality of LSE and LSM modes amongst themselves shall be proven here.

Due to the case discrimination regarding the one-dimensional wavenumbers $k_x$ and $k_z$ for the LSE modes, the same differentiation is necessary here. For the moment, $k_x \neq 0$ and $k_z \neq 0$ is assumed. In this case, the volume integral over the scalar product of the electric fields of the modes reads as

$$\int \varepsilon_r(y) \underline{\mathbf{E}}_\lambda (\mathbf{r}) \cdot \underline{\mathbf{E}}_\mu (\mathbf{r})\, \mathrm{d}V = A_\lambda A_\mu \omega_\lambda \frac{aL}{4} \delta_{k_{x,\lambda},k_{x,\mu}} \delta_{k_{z,\lambda},k_{z,\mu}} \cdot$$
$$\int_0^b Q_\lambda(y) \left( \frac{\mathrm{d}}{\mathrm{d}y} Q_\mu(y) \right) \mathrm{d}y \cdot (-k_{x,\mu} k_{z,\lambda} + k_{x,\lambda} k_{z,\mu}) \,.$$

If $\delta_{k_{x,\lambda},k_{x,\mu}} \delta_{k_{z,\lambda},k_{z,\mu}} = 0$, the above expression is zero. If $\delta_{k_{x,\lambda},k_{x,\mu}} \delta_{k_{z,\lambda},k_{z,\mu}} \neq 0$, which is the case only for $k_{x,\lambda} = k_{x,\mu}$ and $k_{z,\lambda} = k_{z,\mu}$, the parenthesised expression on the right-hand side consists of two terms with identical absolute value and different signs and thus vanishes. So in total, the integral is always zero.

If $k_{x,\lambda} = 0$ and $k_{z,\lambda} \neq 0$, the electric field of an LSE mode will only be non-zero in the $x$-component. The $x$-dependency in this component simplifies to $\cos(k_{x,\lambda}x) = 1$. The orthogonality integral reads

$$
\int \varepsilon_r(y)\underline{\mathbf{E}}_\lambda(\mathbf{r}) \cdot \underline{\mathbf{E}}_\mu(\mathbf{r})\,\mathrm{d}V = A_\lambda A_\mu \omega_\lambda k_{z,\lambda}\frac{L}{2}\delta_{k_{z,\lambda},k_{z,\mu}} \cdot
$$

$$
\int_0^b Q_\lambda(y)\left(\frac{\mathrm{d}}{\mathrm{d}y}Q_\mu(y)\right)\mathrm{d}y \cdot \underbrace{\int_0^a \cos(k_{x,\mu})\mathrm{d}x}_{=0} = 0,
$$

where the integral over the single cosine is zero, and thus the total expression is, as well. The same argumentation applies for the case $k_{x,\lambda} \neq 0$ and $k_{z,\lambda} = 0$, and thus the orthogonality

$$
\int \varepsilon_r(y)\underline{\mathbf{E}}_\lambda(\mathbf{r}) \cdot \underline{\mathbf{E}}_\mu(\mathbf{r})\,\mathrm{d}V = 0 \tag{A.8}
$$

is proven.

The orthogonality proof for the magnetic flux density follows the same argumentation and case discrimination. For $k_{x,\lambda} \neq 0$ and $k_{z,\lambda} \neq 0$ the volume integral results in two expressions with different signs and the same absolute value; while in the other two cases a one-dimensional integral over a single cosine each renders the total integral zero. Thus, also for the magnetic flux densities of the two modes, the orthogonality

$$
\int \underline{\mathbf{B}}_\lambda(\mathbf{r}) \cdot \underline{\mathbf{B}}_\mu(\mathbf{r})\,\mathrm{d}V = 0 \tag{A.9}
$$

is proven.

# B Integrals over the Charge Density and the Current Density

For the general solution of the integral

$$I = -\frac{c_0^2}{A_i^2 U_i} \left( \underbrace{\int \nabla \left( \frac{\rho\left(\mathbf{r}, t\right)}{\varepsilon_r(y)\varepsilon_0} \right) \cdot \mathbf{A}(\mathbf{r}, t)\mathrm{d}V}_{I_1} + \underbrace{\int \mu_0 \frac{\partial \mathbf{J}\left(\mathbf{r}, t\right)}{\partial t} \cdot \mathbf{A}(\mathbf{r}, t)\mathrm{d}V}_{I_2} \right), \quad \text{(B.1)}$$

where $\mathbf{A}(\mathbf{r}, t)$ is any arbitrary vector field, an explicit formulation of $\nabla\left(\frac{\rho(\mathbf{r},t)}{\varepsilon_r(y)\varepsilon_0}\right)$ and $\frac{\partial \mathbf{J}(\mathbf{r},t)}{\partial t}$ is needed.

The integral $I_1$ splits into two terms using the quotient rule

$$I_1 = \underbrace{\int \frac{1}{\varepsilon_r(y)\varepsilon_0} \left(\nabla\rho\left(\mathbf{r}, t\right)\right) \cdot \mathbf{A}\left(\mathbf{r}, t\right)\mathrm{d}V}_{I_{11}} + \underbrace{\int \frac{\rho\left(\mathbf{r}, t\right)}{\varepsilon_0\varepsilon_r^2(y)} \left(\nabla\varepsilon_r(y)\right) \cdot \mathbf{A}\left(\mathbf{r}, t\right)\mathrm{d}V}_{I_{12}}. \quad \text{(B.2)}$$

By the definition of the charge and current densities in (3.37) and (3.38), any form of derivative of these two quantities will contain first order derivatives of Dirac distribution. The derivative of the Dirac distribution $\delta(\zeta)$ with respect to the quantity $\zeta$ will in the following be referred to as $\delta'_\zeta(\zeta)$. The time derivative of the current density thus reads

$$\frac{\partial}{\partial t}\mathbf{J}\left(\mathbf{r}, t\right) = qc\delta\left(x - \frac{a}{2}\right)\delta\left(y - \frac{b}{2}\right)\delta'_t\left(z - ct\right)\mathbf{e}_z, \quad \text{(B.3)}$$

while the gradient of the charge density is given as

$$\nabla\rho\left(\mathbf{r}, t\right) = \begin{pmatrix} \partial/\partial x \\ \partial/\partial y \\ \partial/\partial z \end{pmatrix} q\delta\left(x - \frac{a}{2}\right)\delta\left(y - \frac{b}{2}\right)\delta\left(z - ct\right), \quad \text{(B.4)}$$

$$= q \begin{pmatrix} \delta'_x\left(x - \frac{a}{2}\right)\delta\left(y - \frac{b}{2}\right)\delta\left(z - ct\right) \\ \delta\left(x - \frac{a}{2}\right)\delta'_y\left(y - \frac{b}{2}\right)\delta\left(z - ct\right) \\ \delta\left(x - \frac{a}{2}\right)\delta\left(y - \frac{b}{2}\right)\delta'_z\left(z - ct\right) \end{pmatrix}. \quad \text{(B.5)}$$

To solve the integral $I_{12}$, knowledge of the gradient of the relative permittivity is required. Due to the piecewise-nature of the permittivity function defined in (3.1),

it becomes clear that the derivative of this function is going to contain a sum of two Dirac distributions at the jump discontinuities. Additionally, a derivative is only non-zero with respect to $y$. Thus, the gradient of the relative permittivity reads

$$\nabla \varepsilon_r(y) = N\left(\delta(y - (b - d)) + \delta(y - d)\right)\mathbf{e}_y, \tag{B.6}$$

where $N$ is an arbitrary proportionality factor that does not need to be determined any further. Most importantly, it is to note here that the gradient of the relative permittivity is zero everywhere, except at the jump discontinuities.

With these definitions settled, the three integrals can be solved separately now, starting with

$$I_{12} = \int\limits_0^b \int\limits_0^a \int\limits_0^L \frac{\rho(\mathbf{r}, t)}{\varepsilon_0 \varepsilon_r^2}\left(\nabla \varepsilon_r(y)\right) \cdot \mathbf{A}(\mathbf{r}, t)\, \mathrm{d}z \mathrm{d}x \mathrm{d}y.$$

The integrations over $x$ and $z$ can be carried out without any complications, taking into account the Dirac distributions from the charge density. The product of the gradient and the general vector field will only amount to a non-zero result in the $y$-component. Thus, the integral can be reformulated as

$$I_{12} = \int\limits_0^b \frac{N}{\varepsilon_0 \varepsilon_r(y)^2}\delta\left(y - \frac{b}{2}\right)\left(\delta(y - (b - d)) + \delta(y - d)\right)A_y\left(\frac{a}{2}, y, ct\right)\mathrm{d}y.$$

An integration over $y$ means that the Dirac distributions arising from the gradient will be evaluated at $y = b/2$, where both are zero. As a result, the whole integrand is zero, and thus, the integral itself is

$$I_{12} = 0. \tag{B.7}$$

The integral $I_{11}$ basically separates again into three different terms:

$$I_{11} = \int \frac{1}{\varepsilon_r(y)\varepsilon_0}\left(\nabla \rho(\mathbf{r}, t)\right) \cdot \mathbf{A}(\mathbf{r}, t)\, \mathrm{d}V$$

$$= \int\limits_0^L \int\limits_0^b \int\limits_0^a \frac{1}{\varepsilon_r(y)\varepsilon_0}\begin{array}{l}\left(\left(\nabla \rho(\mathbf{r}, t)\right)_x A_x(\mathbf{r}, t) + \left(\nabla \rho(\mathbf{r}, t)\right)_y A_y(\mathbf{r}, t)\right.\\ \left. + \left(\nabla \rho(\mathbf{r}, t)\right)_z A_z(\mathbf{r}, t)\right)\end{array}\mathrm{d}x\, \mathrm{d}y\, \mathrm{d}z.$$

Inserting the components of (B.5) now and carrying out all simple integrals over ordinary Delta distributions yields

$$I_{11} = \frac{q}{\varepsilon_0}\int\limits_0^a \delta_x'\left(x - \frac{a}{2}\right)A_x\left(x, \frac{b}{2}, c_0 t\right)\mathrm{d}x + \frac{q}{\varepsilon_0}\int\limits_0^b \frac{1}{\varepsilon_r}\delta_y'\left(y - \frac{b}{2}\right)A_y\left(\frac{a}{2}, y, ct\right)\mathrm{d}y$$

$$+ \frac{q}{\varepsilon_0}\int\limits_0^L \delta_z'\left(z - c_0 t\right)A_z\left(\frac{a}{2}, \frac{b}{2}, z\right)\mathrm{d}z.$$

Here it was used that $\varepsilon_r\left(\frac{b}{2}\right) = 1$, and thus $c\left(\frac{b}{2}\right) = c_0$.

Further calculations require knowledge of the behaviour of the derivative of the Dirac distribution when integrated. The integration rule reads as $\int \delta'_x\left(x - r\right) f(x)\mathrm{d}x = -\frac{\mathrm{d}}{\mathrm{d}x}f(x)\big|_{x=r}$ and is used to further specify $I_{11}$, resulting in

$$I_{11} = -\frac{q}{\varepsilon_0}\frac{\partial}{\partial x}A_x\left(x, \frac{b}{2}, c_0 t\right)\bigg|_{x=\frac{a}{2}} - \frac{q}{\varepsilon_0}\frac{\partial}{\partial z}A_z\left(\frac{a}{2}, \frac{b}{2}, z\right)\bigg|_{z=c_0 t}$$
$$-\frac{q}{\varepsilon_0}\frac{\partial}{\partial y}\left(\frac{1}{\varepsilon_r}A_y\left(\frac{a}{2}, y, ct\right)\right)\bigg|_{y=\frac{b}{2}}.$$

Here, the last addend requires closer consideration. At first, the quotient rule is applied so that

$$-\frac{q}{\varepsilon_0}\frac{\partial}{\partial y}\left(\frac{1}{\varepsilon_r(y)}A_y\left(\frac{a}{2}, y, ct\right)\right)\bigg|_{y=\frac{b}{2}} = -\frac{q}{\varepsilon_0}\underbrace{\frac{\partial}{\partial y}\frac{1}{\varepsilon_r(y)}\bigg|_{y=\frac{b}{2}}}_{=0}A_y\left(\frac{a}{2}, \frac{b}{2}, c_0 t\right)$$
$$-\frac{q}{\varepsilon_0}\frac{\partial}{\partial y}A_y\left(\frac{a}{2}, y, ct\right)\bigg|_{y=\frac{b}{2}},$$

again using $\varepsilon_r\left(\frac{b}{2}\right) = 1$. To evaluate this term, the application of the chain rule is necessary due to the $y$-dependence of the speed of light. This, however, will lead to a term containing $\frac{\mathrm{d}}{\mathrm{d}y}c(y)\big|_{y=b/2}$, which is zero since $\frac{\mathrm{d}}{\mathrm{d}y}\varepsilon_r(y)\big|_{y=b/2} = 0$. Thus, the final result for integral $I_{11}$ is

$$I_{11} = -\frac{q}{\varepsilon_0}\left(\frac{\partial}{\partial x}A_x\left(x, \frac{b}{2}, c_0 t\right)\bigg|_{x=\frac{a}{2}} - \frac{\partial}{\partial y}A_y\left(\frac{a}{2}, y, c_0 t\right)\bigg|_{y=\frac{b}{2}}\right.$$
$$\left.- \frac{\partial}{\partial z}A_z\left(\frac{a}{2}, \frac{b}{2}, z\right)\bigg|_{z=c_0 t}\right). \tag{B.8}$$

When calculating the term $I_2$, the vector field $\mathbf{A}\left(\mathbf{r}\right)$ is projected to the $z$-axis by the dependency of the current density, and the integrations over $x$ and $y$ can be carried out right away:

$$I_2 = \int \mu_0 \frac{\partial |\mathbf{J}\left(\mathbf{r}, t\right)|}{\partial t}A_z(x, y, z)\mathrm{d}V$$
$$= \mu_0 q c_0 \int_0^L \delta'_t(z - c_0 t)A_z\left(\frac{a}{2}, \frac{b}{2}, z\right)\mathrm{d}z.$$

Next, the coordinate transformation $\eta = z - c_0 t$ is employed,

$$I_2 = -\frac{q}{\varepsilon_0}\int_{-c_0 t}^{L-c_0 t} \delta'_\eta\left(\eta\right) A_z\left(\frac{a}{2}, \frac{b}{2}, \eta + c_0 t\right)\mathrm{d}\eta,$$

using $\frac{\partial \eta}{\partial t} = -c_0$, $\frac{\partial \eta}{\partial z} = 1$ and $\mu_0 c_0^2 = \mu_0 (\mu_0 \varepsilon_0)^{-1} = \varepsilon_0^{-1}$.

The result of the last equation is readily determined as

$$I_2 = \frac{q}{\varepsilon_0} \frac{\partial}{\partial \eta} A_z \left( \frac{a}{2}, \frac{b}{2}, \eta + c_0 t \right) \bigg|_{\eta=0} ,$$

and resubstituting $z = \eta + c_0 t$ the final result for the auxiliary integral is

$$I_2 = \frac{q}{\varepsilon_0} \frac{\partial}{\partial z} A_z \left( \frac{a}{2}, \frac{b}{2}, z \right) \bigg|_{z=c_0 t} . \tag{B.9}$$

The summation of $I_{11}$, $I_{12}$ and $I_2$ cancels out the terms dependent on the $z$-component of the field, so that the final result of eqn. (B.1) is

$$I = \frac{q c_0^2}{A_i^2 U_i \varepsilon_0} \left( \frac{\partial}{\partial x} A_x \left( x, \frac{b}{2}, c_0 t \right) \bigg|_{x=\frac{a}{2}} - \frac{\partial}{\partial y} A_y \left( \frac{a}{2}, y, c_0 t \right) \bigg|_{y=\frac{b}{2}} \right) . \tag{B.10}$$

# C  The Wakefield Integral

This chapter is dedicated to the procedure finding the solution of the double integral

$$I(s) = \int\limits_0^L \int\limits_0^{T^*} \underbrace{\sin\left(k_z c_0 t'\right) \sin\left(\omega\left(\frac{z+s}{c_0} - t'\right)\right) \cos\left(k_z z\right)}_{\Psi(z,s,t')} \mathrm{d}t' \mathrm{d}z \qquad \text{(C.1)}$$

as used in Chapter 3.4.

For the solution, a differentiation of cases depending on the position of the test charge and the exciting charge to each other is necessary. This derivation follows closely the procedure shown in [31].

1. The distance between the two charges is larger than the waveguide length $L$ ($s > L$). Accordingly, the test charge only enters the guide when the exciting charge has already left, and thus $c_0 T^* = \min\left(z+s, L\right) = L$ is the upper boundary of the time integral.

2. The distance between the two charges is positive, but smaller than the length of the guide ($0 < s < L$). As long as $z + s < L$, both charges will be in the guide simultaneously, and thus, $c_0 T^* = z + s$. However, when the exciting charge leaves the guide, the test charge still has to travel a distance of $s$, which will give rise to a second term of the integral with $c_0 T^* = L$.

3. Both charges are virtually at the same place, i.e. $s = 0$.

4. The test charge travels through the guide in front of the exciting charge, $s < 0$. In this case, as a consequence of the principle of causality, the wakefield must be zero.

These cases will now be evaluated one by one.

The first case is probably the simplest. Refining the upper boundary leads to

$$I_1(s) = \int\limits_0^L \int\limits_0^{L/c_0} \Psi\left(z, s, t'\right) \mathrm{d}t' \mathrm{d}z.$$

Carrying out the two integrations delivers

$$I_1(s) = -\frac{c_0^2 k_z \omega \left(2 - 2e^{jl\pi} \cos\left(k_0 L\right)\right) \cos\left(k_0 s\right)}{\left(c_0 k_z - \omega\right)^2 \left(c_0 k_z + \omega\right)}. \qquad \text{(C.2)}$$

For the second case, the integral is split into two terms according to

$$I_2(s) = \int\limits_0^{L-s} \int\limits_0^{(z+s)/c_0} \Psi\left(z, s, t'\right) \mathrm{d}t'\mathrm{d}z + \int\limits_{L-s}^{L} \int\limits_0^{L/c_0} \Psi\left(z, s, t'\right) \mathrm{d}z\mathrm{d}t'.$$

The boundaries of these double integrals are now transformed so that the final version contains the same limits as the integral $I_1(s)$:

$$I_2(s) = \int\limits_0^{L} \int\limits_0^{L/c_0} \Psi\left(z, s, t'\right) \mathrm{d}t'\mathrm{d}z + \int\limits_0^{L-s} \int\limits_{(z+s)/c_0}^{L/c_0} \Psi\left(z, s, t'\right) \mathrm{d}z\mathrm{d}t' = I_1(s) - K(s).$$

So, while the solution of $I_1(s)$ is already known, the solution to $K(s)$ has to be determined now. For that, the 'artificial' case 4 is considered now.

In the fourth case, the test charge is always in front of the exciting charge. This case is obviously unphysical, because there can be no wakefield if the test charge is in front of the field generating charge. However, the case is useful for the purpose of further defining $K(s)$. Only the situation $0 > s$ and $|s| < L$ needs to be treated, which does not change the fact that the wakefield here must be zero. In this case, $c_0 T^* = z + s$ always holds. The double integral reads here

$$I_4(s) = \int\limits_0^{L} \int\limits_0^{(z+s)/c_0} \Psi\left(z, s, t'\right) \mathrm{d}t'\mathrm{d}z \overset{!}{=} 0.$$

As far as the integral over $z$ is concerned, expanding it up until $L - s$ will not change the result, because the point $L - s$, in this case, is behind the guide where no wakefield is generated:

$$I_4(s) = \int\limits_0^{L-s} \int\limits_0^{(z+s)/c_0} \Psi\left(z, s, t'\right) \mathrm{d}t'\mathrm{d}z \overset{!}{=} 0.$$

The boundaries of this integral are transformed, so that they reflect the boundaries of $K(s)$:

$$I_4(s) = \underbrace{\int\limits_0^{L-s} \int\limits_0^{L/c_0} \Psi\left(z, s, t'\right) \mathrm{d}t'\mathrm{d}z}_{=0} - \int\limits_0^{L-s'} \int\limits_{(z+s)/c_0}^{L/c_0} \Psi\left(z, s, t'\right) \mathrm{d}t'\mathrm{d}z \overset{!}{=} 0.$$

The first part of this integral must be zero, since it reflects the case $z + s > L$, which is only the case if $z > L$, and $L - s$, again, is already outside the cavity. So the first

part of the integral basically is the expression for a case in which also the generating charge, located at $z$, is already outside the cavity. Without an exciting charge, there is no wakefield, so obviously, the integral must be zero.

What remains is an integral that on first glance looks identical to $K(s)$; but for $K(s)$, $s$ was defined as positive, whereas in this case, it is negative. Considering the absolute values, however, both integrals are defined in the same (absolute) domain. Thus, $I_4(s) = -K(-s) = 0$.

Additionally, $K(s)$ is an even function: $\Psi(z, s, t')$ is a product of two sines and thus even, its integral will therefore be odd. Multiplying this by a cosine does not change that, as the cosine is an even function. Integrating again over said odd function will result in $K(s)$, the final result, being even. Thus, $K(s) = K(-s) = 0$.

Coming back to the second case, $I_2(s)$, this means that in

$$I_2(s) = I_1(s) - K(s),$$

$K(s)$ can now safely be assumed to be zero, so that

$$I_2(s) = I_1(s) \tag{C.3}$$

is the final result for the wakefield integral in the second stated case.

The only remaining case is the third now, where $s = 0$. Here, the fundamental theorem of beam loading (see, e.g., [13]) can be applied. It states that a charge sees the half of the voltage induced by itself, and thus, half its own wakefield. Therefore, the solution of the integral (C.1) can be finalised as

$$I(s) = -\frac{c_0^2 k_z \omega \left(2 - 2e^{jl\pi} \cos\left(k_0 L\right)\right) \cos\left(k_0 s\right)}{\left(c_0 k_z - \omega\right)^2 \left(c_0 k_z + \omega\right)} \begin{cases} 1 & s > 0 \\ \frac{1}{2} & s = 0 \\ 0 & s < 0 \end{cases} \tag{C.4}$$

# D Additional Experimental Results

This section of the appendix introduces the experimental results of the series 0311_1_60 as supplementary material for the data presented in Chapter 6.

The data in this section has been measured in the same manner as the previous two series of results. The energy spectra of the used particle bunch have been measured after the dechirper for different gap widths. From the spectra, the average energy and the standard deviation were calculated, and the results for the maximum gap width of 35 mm were taken as a reference. The total bunch charge amounted to 60 pC in this case.

For the recreation of the phase space of the bunch used in the semi-analytical predictions of the results, a double Gaussian bunch profile was employed. The length of the particle bunch has been extracted from phase space tomography once more, and is assumed to be 3.6 mm throughout this section.

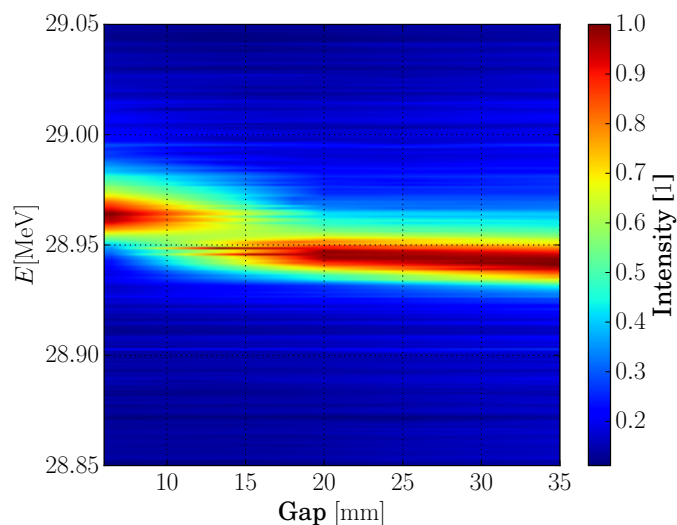For the reduction of the background, a quadratic polynomial was used in Fig. D.2.



**Figure D.1:** Normed total intensities of the energy spectra recorded for the bunch 0311_1_60 plotted over the gap width of the dechirper. The data has been interpolated for the gap widths that have not been measured. The figure shows clearly the energy reduction induced by the dechirper in the shift of the high intensity peak at $\approx 28.95$ keV towards lower energies for decreasing gap width. An increase in the width of the spectrum is not easily visible.
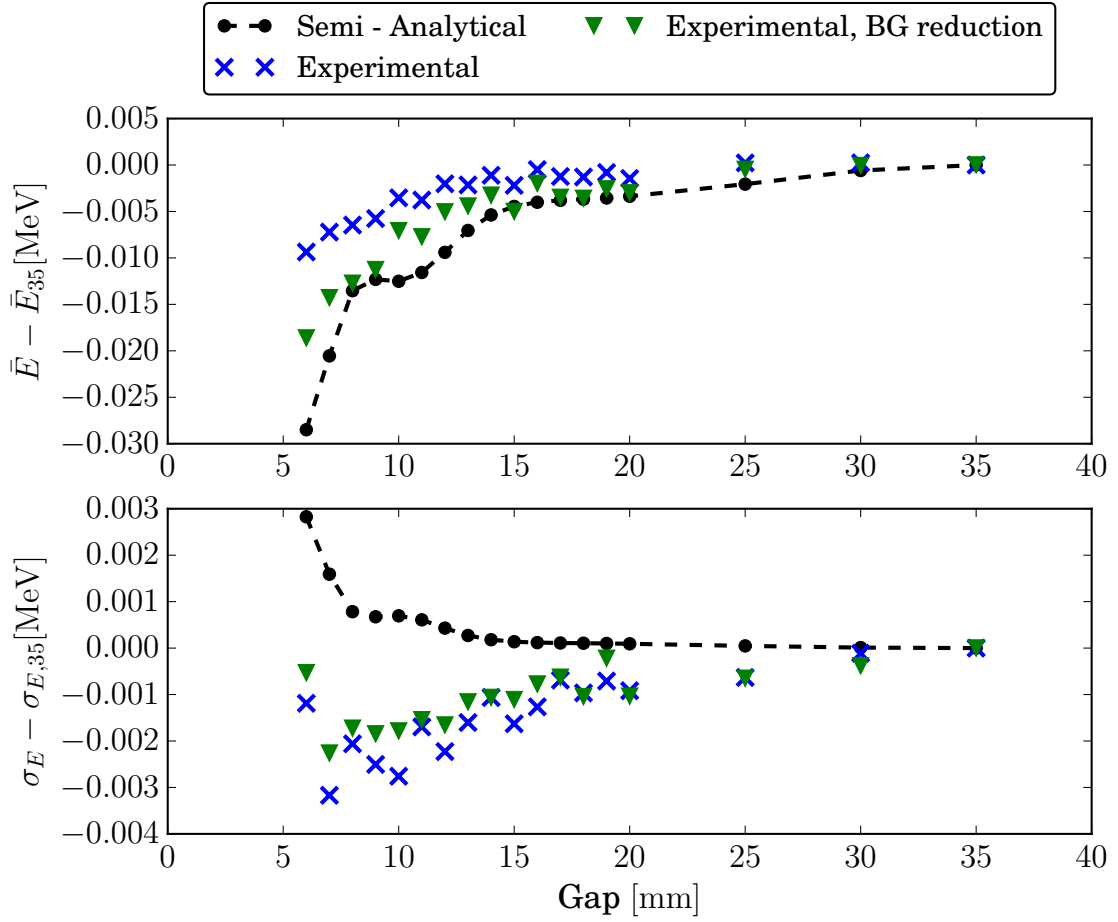
**Figure D.2:** Progression of the average energies and the standard deviations of the energy spectra of the bunch 0311_1_60 measured for different gap width of the dechirper. The figure shows the raw experimental data (x-shaped markers), the experimental data after a reduction of the background by a quadratic polynomial (triangular markers) and the semi-analytical predictions carried out for the extracted bunch length and assumed bunch shape of a double Gaussian (dashed lines).

Like in Chapter 6, the semi-analytically predicted shift in the average energies for lower gap width is, while in the same order of magnitude, lower than the experimentally shift. The discrepancy between both curves is highest for gap widths lower than 10 mm. When the background of the spectra is fitted and subtracted, the accordance of the experimental and semi-analytical results can be increased.

For the standard deviations, the experimental results do not match the semi-analytical predictions. Both the raw data and the data after the background reduction suggest a minimal increase of the standard deviation of the spectrum, while the semi-analytically calculated results suggest a decrease of the width of the spectrum in the range, which would be in better accordance with the generally expected effect of the dechirper. However, both shifts are only in the range of a few keV and thus very minimal.
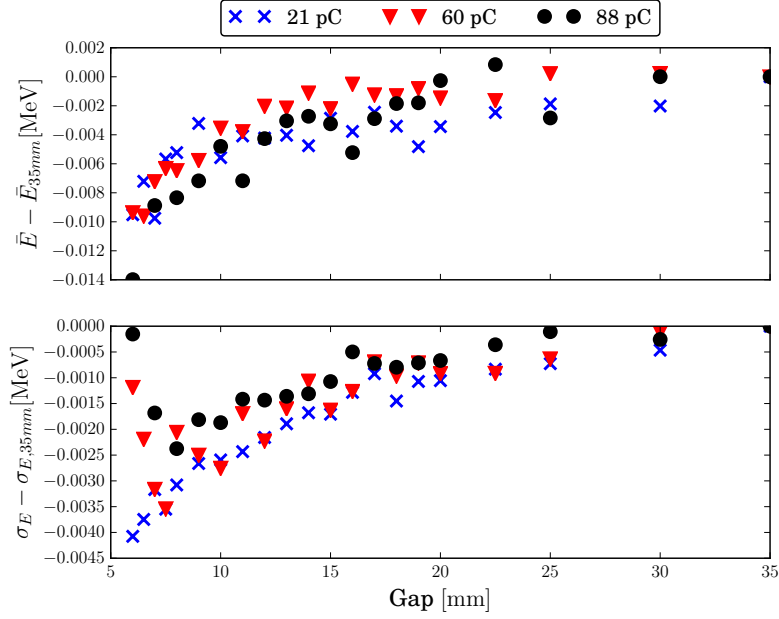
**Figure D.3:** Average energies and standard deviations of the energy spectra recorded for three different bunch charges, but the same overall settings like the bunch 0311_1_60. Both quantities were extracted from the raw experimental data. While slight variations of the observed quantities with the change in the bunch charge can be observed, the clear scaling of the effect of the dechirper with the bunch charge is not visible from the given data. This is also in accordance with the results presented in Chapter 6.

In addition to the decrease in the average energies for decreasing gap widths of the dechirper, the figure also shows that all three observed bunches show a slight decrease in the standard deviations for decreasing gap widths, which would indicate a decrease in the width of the energy spectrum. This is against the predictions presented in Fig. D.2, but the small order of magnitude in which these changes occur and the overall unknown phase space of the particle bunch can explain this discrepancy.

# E Supplementary Material Regarding Phase Space Tomography

The lack of a possibility to directly measure the longitudinal phase space of the studied particle bunches at ELBE makes it necessary to approximate this very important quantity in other ways.
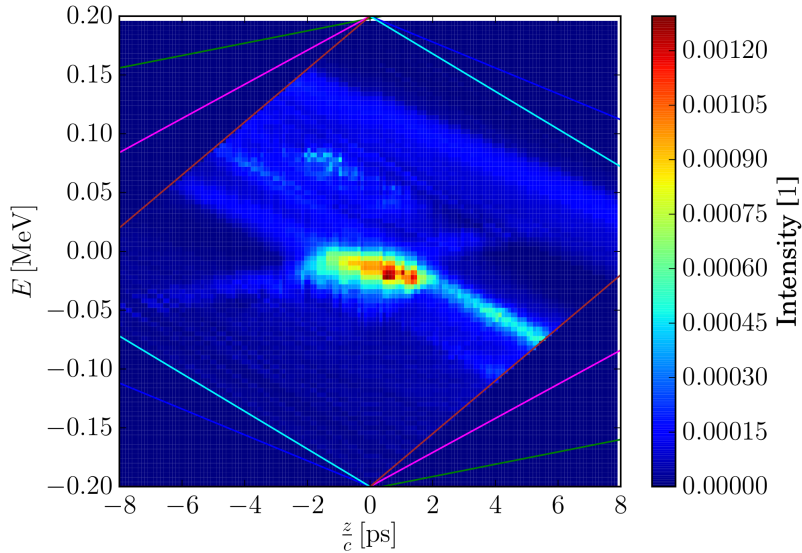


**Figure E.1:** Underlying longitudinal phase space distribution of the series of pulses 2508_1, measured at 80 pC and recreated employing phase space tomography. The majority of the pulse is located in a range of $\pm 2$ ps around zero, which corresponds to an approximate pulse length of 4 ps (roughly 1.2 mm). The intensity around the centre of the pulse indicates two maxima, which would correspond well with the double Gaussian pulse profile.

One way is the so-called phase space tomography. In general, tomographic techniques allow for a recreation of an $n$-dimensional object from a number of $(n-1)$-dimensional projections of this object. In this specific case this term refers to the recreation of the two-dimensional longitudinal phase space; a depiction of the longitudinal position of each particle and its energy, with the help of the one-dimensional projections of the phase space. These projections are here energy spectra; depictions of the energy distribution of the particle beam. For the underlying reconstruction algorithm to work, it is necessary that a number of energy spectra is measured for

different projection angles, which can be adjusted using a quadrupole magnet. For a detailed description of this method and its limitations refer to [92].

Figure E.1 shows such a reconstruction of the phase space for the series 2508_1 measured at 80 pC. For this, as mentioned above, the energy spectra were measured for different projection angles which are indicated in the figure by the solid coloured lines[1]. From the intensity shown in the figure, it can be deduced that the pulse extends from $\approx -2\,\mathrm{ps}$ to $\approx 2\,\mathrm{ps}$. This corresponds to a total bunch length of $\approx 4\,\mathrm{ps}$, which corresponds to roughly 1.2 mm. This is the bunch length assumed for the pulse 25_1_54 in Chapter 6, assuming that a change in the charge of the pulse will not significantly alter the phase space. Additionally, the figure indicates that the pulse does indeed have an approximately double Gaussian profile, as in the non-zero area of the pulse there are two high intensity peaks (located in the centre of the pulse between 0 ps and 2 ps), which has been used to generate the model pulses in Chapter 6.

---

[1]The reconstruction was computed employing a Python programme courtesy of U. Lehnert, HZDR

# Bibliography

[1] S. Antipov, S. Baturin, C. Jing, M. Fedurin, A. Kanareykin, C. Swinson, P. Schoessow, W. Gai, and A. Zholents, "Experimental demonstration of energy-chirp compensation by a tunable dielectric-based structure," *Phys. Rev. Lett.*, vol. 112, p. 114801, 2014.

[2] S. Antipov, C. Jing, S. Baryshev, A. Kanareykin, S. Stoupin, W. Gai, A. Zholents, S. Baturin, M. Fedurin, and C. Swinson, "Experimental Test of Semiconductor Dechirper," in *Proceedings of the Int. Part. Accel. Conf. 2015*, Richmond, USA, 2015, p. TUPMA043. [Online]. Available: http://accelconf.web.cern.ch/AccelConf/IPAC2015/papers/tupma043.pdf

[3] F. Reimann, U. van Rienen, P. Michel, and U. Lehnert, "Wakefield-based dechirper structures for ELBE," in *Proceedings of the Internat. Part. Accel. Conf. 2014*, Dresden, Germany, 2014.

[4] F. Reimann, U. van Rienen, P. Michel, and U. Lehnert, "A dielectrically lined rectangular waveguide as a wakefield dechirper for ELBE," in *2015 Intl. Conf. on Electromagnetics in Advanced Applications*, Torino, Italy, 2015.

[5] S. Myers, "The LEP Collider, from design to approval and commissioning," 1991, delivered at CERN, 26 Nov 1990. [Online]. Available: http://cds.cern.ch/record/226776

[6] T. S. Pettersson and P. Lefèvre, "The Large Hadron Collider: Conceptual design," 1995.

[7] The ATLAS Cooperation, "Observation of a new particle in the search for the standard model Higgs boson with the ATLAS detector at the LHC," *Physics Letters B*, vol. 716, no. 1, pp. 1 – 29, 2012.

[8] K. Balewski, W. Brefeld, W. Decking, H. Franz, R. Rohlsberger, and E. Weckert, "PETRA III: A low emittance synchrotron radiation source. Technical design report," 2004.

[9] J. Arthur *et al.*, "Linac coherent light source (LCLS) conceptual design report," 2002.

[10] The XFEL Collaboration, "The technical design report of the European XFEL," 01 2006.

[11] P. Michel, "The Rossendorf IR-FEL ELBE," in *Proceedings of the Free Electron Laser Conf. 2006*, BESSY, Berlin, Germany, 2006.

[12] T. Wangler, *RF Linear Accelerators.* Weinheim: Wiley-VCH, 2008.

[13] A. W. Chao, *Physics of Collective Beam Instabilities in High Energy Accelerators.* New York: John Wiley & Sons, Inc., 1993.

[14] S. Humphries, *Principles of Charged Particle Acceleration.* New York: Wiley, 1986.

[15] F. Hinterberger, *Physik der Teilchenbeschleuniger und Ionenoptik.* Berlin Heiderlberg: Springer-Verlag, 2008.

[16] H. Wiedemann, *Particle accelerator physics; 3rd ed.* Berlin: Springer, 2007.

[17] D. Umstadter, J. K. Kim, and E. Dodd, "Laser injection of ultrashort electron pulses into wakefield plasma waves," *Phys. Rev. Lett.*, vol. 76, pp. 2073–2076, Mar 1996.

[18] C. Geddes, C. Toth, J. Van Tilborg, E. Esarey, C. Schroeder, D. Bruhwiler, C. Nieter, J. Cary, and W. Leemans, "High-quality electron beams from a laser wakefield accelerator using plasma-channel guiding," *Nature*, vol. 431, no. 7008, pp. 538–541, 2004.

[19] W. Leemans, B. Nagler, A. Gonsalves, C. Toth, K. Nakamura, C. Geddes, E. Esarey, C. Schroeder, and S. Hooker, "GeV electron beams from a centimetre-scale accelerator," *Nature physics*, vol. 2, no. 10, pp. 696–699, 2006.

[20] V. Malka, S. Fritzler, L. E., M.-M. Aleonard, F. Burgy, J.-P. Chambaret, J.-F. Chemin, K. Krushelnick, G. Malka, S. Mangles, Z. Najmudin, M. Pittman, J.-P. Rousseau, J.-N. Scheurer, B. Walton, and A. Dangor, "Electron acceleration by a wake field forced by an intense ultrashort laser pulse," *Science*, vol. 298, pp. 1596–1600, 2002.

[21] D. Hopkins, A. Sessler, and J. Wurtele, "The two-beam accelerator," *Nuclear Instruments and Methods in Physics Research Section A: Accelerators, Spectrometers, Detectors and Associated Equipment*, vol. 228, no. 1, pp. 15 – 19, 1984.

[22] S. Y. Kazakov, S. V. Kuzikov, Y. Jiang, and J. L. Hirshfield, "High-gradient two-beam accelerator structure," *Phys. Rev. ST Accel. Beams*, vol. 13, p. 071303, Jul 2010.

[23] W. Barletta, J. Bisognano, J. N. Corlett, P. Emma, Z. Huang, K.-J. Kim, R. Lindberg, J. B. Murphy, G. Neil, D. Nguyen, C. Pellegrini, R. Rimmer, F. Sannibale, G. Stupakov, R. Walker, and A. Zholents, "Free electron lasers: Present status and future challenges," vol. 618, pp. 69–96, 06 2010.

[24] Y. Kim, K. Flöttmann, T. Limberg, M. Dohlus, D. Son, and Y. Kim, "Injector and bunch compressor for European XFEL," in *Proceedings of the Europ. Part. Accel. Conf. 2004*, Lucerne, Switzerland, 2004, pp. 342–344.

[25] H. Weise, "The TESLA XFEL project," in *Proceedings of the Europ. Part. Accel. Conf. 2004*, Lucerne, Switzerland, 2004, pp. 11–16.

[26] J. Corlett, K. Baptise, J. Byrd, P. Denes, R. Falcone, J. Feng, M. Graves, J. Kirz, D. Li, H. Padmore, C. Papadopoulous, G. Penn, J. Qiang, D. Robin, R. Ryne, F. Sannibale, R. Schoenlein, J. Staples, C. Steier, T. Veccione, M. Venturini, W. Wan, R. Wells, R. Wilcox, and J. Wurtele, "Design studies for a VUV-soft X-ray FEL facility at LBNL," in *Proceedings of the Internat. Part. Accel. Conf. 2010*, Kyoto, Japan, 2010, pp. 2639–2641.

[27] B. Zotter and S. Kheifetz, "Impedances and wakes in high-energy particle accelerators," *World Scientific*, p. 405, 1997.

[28] T. Weiland, "Transverse beam cavity interaction. Part I: Short range forces," *Nuclear Instruments and Methods in Physics Research*, vol. 212, no. 1–3, pp. 13–21, 1983.

[29] G. A. Voss and T. Weiland, "The Wake Field Acceleration Mechanism," *eConf*, vol. C8209271, p. 287, 1982.

[30] W. Bialowons, H. D. Bremer, F.-J. Decker, M. v. Hartrott, H. C. Lewin, G.-A. Voss, T. Weiland, P. Wilhelm, X. Chengde, and K. Yokoya, *Wake Field Acceleration.* Boston, MA: Springer US, 1987, pp. 29–44.

[31] K. Bane, P. Wilson, and T. Weiland, "Wake fields and wake field acceleration," *SLAC-Pub. 3528*, 1984.

[32] T. Weiland and R. Wanzenberg, *Wake fields and impedances.* Berlin, Heidelberg: Springer Berlin Heidelberg, 1992.

[33] R. Klatt and T. Weiland, "Wake field calculations with three-dimensional BCI code," in *Proceedings of the Internat. Linac Conf. 2010*, Stanford, USA, 1986, pp. 282–285.

[34] R. Klatt, W.-R. Krawczyk, C. Novender, T. Weiland, and B. Steffen, "MAFIA - a three-dimensional electromagnetic CAD system for magnets, RF structures,

and transient wake-field calculations," in *Proceedings of the Internat. Linac Conf. 2010*, Stanford, USA, 1986, pp. 276–278.

[35] *CST Studio Suite* ®. Darmstadt, Germany: CST AG.

[36] I. Zagorodnov and T. Weiland, "TE/TM scheme for computation of electromagnetic fields in accelerators," *J. Comput. Phys.*, vol. 207, pp. 69–91, 2005.

[37] I. Zagorodnov and T. Weiland, "TE/TM field solver for particle beam simulations without numerical Cherenkov radiation," *Phys. Rev. ST Accel. Beam*, vol. 8, p. 042001, 2005.

[38] U. van Rienen and T. Weiland, "Impedance calculation with URMEL-I using multigrid methods," *IEEE Transactions on Magnetics*, vol. 26, no. 2, pp. 743–746, Mar 1990.

[39] T. Weiland, "On the computation of resonant modes in cylindrically symmetric cavities," *Nuclear Instruments and Methods in Physics Research*, vol. 216, no. 3, pp. 329 – 348, 1983.

[40] U. van Rienen and T. Weiland, "Triangular discretization method for the evaluation of rf fields in waveguides and cylindrically symmetric cavities," *Part. Accel.*, vol. 20, p. 239, 1987.

[41] M. Borland, *User's Manual for ELEGANT*.

[42] K. Floettmann, *ASTRA - A Space Charge Tracking Algorithm*. Hamburg, Germany: DESY.

[43] W. Bialowons, M. Bieler, H. Bremer, F. Decker, H. Lewin, G. Voss, R. Wanzenberg, T. Weiland, and P. Schutt, "Computer simulations of the wake field transformer experiment at DESY," in *European particle accelerator conference*, 1988.

[44] O. Napoly, "The luminosity for beam distributions with error and wakefield effects in linear colliders," *Part. Accel.*, vol. 40, no. CLIC-Note-173, pp. 181–203, 1992.

[45] R. Nagaoka, "Study of resistive-wall effects on SOLEIL," in *Proceedings of Europ. Part. Accel. Conf.*, Lucerne, Switzerland, 2004, pp. 2038–2040.

[46] P. Craievich, "Short-range longitudinal and tranverse wakefield effects in FERMI@Elettra FEL project," Ph.D. dissertation, University of Trieste, 2010.

[47] T. Sipahi, S. Milton, and S. Biedron, "Wakefield excitation in power extraction cavity (PEC) of colinear X-band energy booster (CXEB) in time domain with ACE3P," in *Proceedings of the Int. Part. Accel. Conf. 2016*, Busan, Korea, 2016, pp. 477–479.

[48] T. Weiland and B. Zotter, "Wake potentials of a relativistic current in a cavity," *Particle Accelerator*, vol. 11, pp. 143–151, 1981.

[49] S. Ratschow and T. Weiland, "Analytical calculation of the wake potential of a spherical resonator," *Phys. Rev. ST Accel. Beam*, vol. 5, p. 052001, 2002.

[50] A. Novokhatski and A. Mosnier, "Wakefield dynamics in quasi periodic structures," in *Proceedings of the Part. Accel. Conf. 1997*, Vancouver, Canada, 1997, pp. 467–469.

[51] A. W. Chao, "Coherent instabilities of a relativistic bunched beam," *AIP Conference Proceedings*, vol. 105, no. 1, pp. 353–523, 1983.

[52] H. Henke and O. Napoly, "Wake fields between two parallel resistive plates," in *Proceedings of the Int. Part. Accel. Conf. 1990*, Nice, France, 1990, pp. 1046–1048.

[53] A. Novokhatski and A. Mosnier, "Wakefields of short bunches in the canal covered with thin dielectric layer," in *Proceedings of the Part. Accel. Conf. 1997*, Vancouver, Canada, 1997, pp. 1661–1663.

[54] M. Rosing and J. Simpson, "Passive momentum spread reduction, the wakefield silencer," in *Argonne Wakefield Accelerator Note WF - 144 (unpublished)*, 1990.

[55] K. Bane, "Corrugated pipe as a beam dechirper," *SLAC-PUB-14925*, 2012.

[56] P. Emma, M. Venturini, K. Bane, G. Stupakov, H.-S. Kang, M. Chae, J. Hong, C.-K. Min, H. Yang, T. Ha, W. Lee, C. Park, S. Park, and I. Ko, "Experimental demonstration of energy-chirp control in relativistic electron bunches using a corrugated pipe," *Phys. Rev. Lett.*, vol. 112, no. 3, p. 034801, 2014.

[57] H. Deng *et al.*, "Experimental demonstration of longitudinal beam phase space linearizer in a free-electron laser facility by corrugated structures," *Phys. Rev. Lett.*, vol. 113, no. 25, p. 254802, 2014.

[58] P. Craievich, "Passive longitudinal phase space linearizer," *Phys. Rev. ST Accel. Beams*, vol. 13, p. 034401, 2010.

[59] S. Antipov, "Passive momentum spread compensation by a "wakefield silencer"," in *Proceedings of the Internat. Part. Accel. Conf. 2012*, New Orleans, USA, 2012.

[60] S. Antipov, C. Jing, M. Fedurin, W. Gai, A. Kanareykin, K. Kusche, P. Schoessow, V. Yakimenko, and A. Zholents, "Experimental observation of energy modulation in electron beams passing through terahertz dielectric wakefield structures," *Phys. Rev. Lett.*, vol. 108, p. 144801, 2012.

[61] S. Antipov, C. Jing, P. Schoessow, A. Kanareykin, M. Fedurin, W. Gai, C. Swinson, S. Baturin, and A. Zholents, "A tunable energy chirp correction," in *Proceedings of the Part. Accel. Conf. 2013*, Pasadena, USA, pp. 279–281.

[62] Y. Nie, G. Xia, and T. Pacey, "Simulations of an energy dechirper based on dielectric lined waveguides," *Nucl. Instrum. Meth.*, vol. A909, pp. 271–275, 2018.

[63] A. Tremaine, J. Rosenzweig, and P. Schoessow, "Electromagnetic wake-fields and beam stability in dielectric slab structures," *Phys. Rev. E*, vol. 56, pp. 7204–7216, 1997.

[64] R. Collin, *Field Theory of Guided Waves*. IEEE Press, 1991.

[65] D. Mihalcea, P. Piot, and P. Stoltz, "Three-dimensional analysis of wakefields generated by flat electron beams in planar dielectric-loaded structures," *Phys. Rev. ST Accel. Beams*, vol. 15, p. 081304, Aug 2012.

[66] S. Baturin, I. Sheinman, A. Altmark, and A. Kanareykin, "Transverse operator method for wakefields in a rectangular dielectric loaded accelerating structure," *Phys. Rev. ST Accel. Beams*, vol. 16, 2013.

[67] S. Baturin and A. Kanareykin, "Cherenkov radiation from short relativistic bunches; general approach," *Phys. Rev. Lett.*, vol. 113, p. 21480, 2014.

[68] L. Xiao, W. Gai, and X. Sun, "Field analysis of a dielectric-loaded rectangular waveguide accelerating structure," *Phys. Rev. E*, vol. 65, p. 016505, 2001.

[69] C. Jing, W. Liu, L. Xiao, W. Gai, P. Schoessow, and T. Wong, "Dipole-mode wakefields in dielectric-loaded rectangular waveguide accelerating structures," *Phys. Rev. E*, vol. 68, p. 016502, 2003.

[70] K.-Y. Ng, "Wake fields in a dielectric-lined waveguide," *Phys. Rev. D*, vol. 42, pp. 1819–1828, 1990.

[71] C. Wang and J. L. Hirshfield, "Theory for wakefields in a multizone dielectric lined waveguide," *Phys. Rev. ST Accel. Beams*, vol. 9, p. 031301, Mar 2006.

[72] G. Stupakov and K. L. F. Bane, "Surface impedance formalism for a metallic beam pipe with small corrugations," *Phys. Rev. ST Accel. Beams*, vol. 15, p. 124401, 2012.

[73] B. Podobedov and G. Stupakov, "Point-charge wakefield calculations from finite length bunch wake potentials," *Phys. Rev. ST Accel. Beam*, vol. 16, p. 024401, 2013.

[74] J. Maxwell, *A Treatise on Electricity and Magnetism*. Cambridge: Cambridge University Press, 2010.

[75] F. Reimann and U. van Rienen, "Wakefields - an overview," *CERN Yellow Reports: School Proceedings*, vol. 1, no. 0, 2018.

[76] P. Morse and H. Feshbach, *Methods of Theoretical Physics*. New York: McGraw-Hill, 1953.

[77] G. Lehner, *Elektromagnetische Feldtheorie*. Berlin: Springer, 1996.

[78] F. Reimann, U. van Rienen, P. Michel, and U. Lehnert, "Rayleigh-Ritz based expansion method for wakefields in dielectrically lined rectangular waveguides," *Journal of Computational Physics*, pending.

[79] F. Gardiol, "Higher-order modes in dielectrically loaded rectangular waveguides," *IEEE Transactions on Microwave Theory and Techniques*, vol. MTT-16, pp. 919–924, 1968.

[80] V. Ledoux, M. V. Daele, and G. V. Berghe, "Efficient computation of high index Sturm-Liouville eigenvalues for problems in physics," *Computer Physics Communications*, vol. 180, no. 2, pp. 241 – 250, 2009.

[81] G. van Rossum, *Python tutorial*, 1995.

[82] U. van Rienen, *Numerical Methods in Computational Electrodynamics*, ser. Lecture Notes in Computational Science and Engineering. Berlin: Springer, 2001, vol. 12.

[83] A. Meurer, C. P. Smith, M. Paprocki, O. Čertík, S. B. Kirpichev, M. Rocklin, A. Kumar, S. Ivanov, J. K. Moore, S. Singh, T. Rathnayake, S. Vig, B. E. Granger, R. P. Muller, F. Bonazzi, H. Gupta, S. Vats, F. Johansson, F. Pedregosa, M. J. Curry, A. R. Terrel, v. Roučka, A. Saboo, I. Fernando, S. Kulal, R. Cimrman, and A. Scopatz, "Sympy: symbolic computing in Python," *PeerJ Computer Science*, vol. 3, p. e103, Jan. 2017. [Online]. Available: https://doi.org/10.7717/peerj-cs.103

[84] E. Jones, T. Oliphant, P. Peterson *et al.*, "SciPy: Open source scientific tools for Python," 2001–. [Online]. Available: http://www.scipy.org/

[85] *Mathematica 8.0*. Wolfram Research, Inc., 2010.

[86] E. Süli and D. F. Mayers, *Eigenvalues and eigenvectors of a symmetric matrix.* Cambridge University Press, 2003, pp. 133—-178.

[87] E. Süli and D. F. Mayers, *Solution of equations by iteration.* Cambridge University Press, 2003, pp. 1—-38.

[88] J. R. Aguilar, M. Beadle, P. T. Thompson, and M. W. Shelley, "The microwave and rf characteristics of FR4 substrates," in *IEE Colloquium on Low Cost Antenna Technology (Ref. No. 1998/206)*, 1998, pp. 2/1–2/6.

[89] MACOR. Corning inc. [Online]. Available: http://glassfab.com/wp-content/uploads/2015/08/Corning-Macor.pdf

[90] H. Sakaue, N. Yoshimura, S. Shingubara, and T. Takahagi, "Low dielectric constant porous diamond films formed by diamond nanoparticles," *Applied Physics Letters*, vol. 83, no. 11, pp. 2226–2228, 2003.

[91] S. Baturin, A. Altmark, I. Sheinman, and A. Kanareykin, "Parameter optimization of a rectangular dielectric based wakefield accelerating structure," in *Proceedings of the Russ. Part. Accel. Conf. 2012*, St. Petersburg, Russia, 09 2012, pp. 260–262.

[92] J. Rudolph, "Instruments and techniques for analysing the time-resolved transverse phase space distribution of high-brightness electron beams," Ph.D. dissertation, University of Rostock, 2012.

# Selbstständigkeitserklärung

Hiermit erkläre ich, dass ich die vorliegende Dissertation mit dem Titel "Dielectrically Lined Rectangular Waveguides as Wakefield Based Dechirper Structures" selbstständig und ohne fremde Hilfe und nur unter Verwendung der von mir angegebenen Quellen und Hilfsmittel verfasst habe.

Rostock,

Franziska Reimann